

UNIVERSITY OF CALIFORNIA

San Diego

A Study of Inclusive Kaon Charge Exchange

in the Triple Regge Region

A dissertation submitted in partial satisfaction of the

requirements for the degree Doctor of Philosophy

in Physics

by

Randall Evans Pitt

Committee in charge:

Professor Robert A. Swanson, Chairman

Professor Hugh Bradner

Professor William R. Frazer

Professor Hans G. E. Kobrak

Professor Robert G. Linck

Professor George E. Masek

1980

TABLE OF CONTENTS

	Page
List of Figures	v
List of Tables	x
Acknowledgments	xii
Vita and Publications	xiii
Abstract	xiv
I. Introduction	1
II. Theory	4
III. Experimental Apparatus	14
IV. Analysis	19
V. Comparison between Data and Theory	22
VI. Concluding Remarks	26
References	113
Appendix I. Hadron Beam	115
Appendix II. Cerenkov Counter	120
Appendix III. Beam Spectrometer	127
Appendix IV. Liquid Hydrogen Target	132
Appendix V. Multiwire Proportional Chamber	135
Appendix VI. Wire Spark Chambers	144
Appendix VII. Trigger Counters and Logic	151
Appendix VIII. Pattern Recognition/Track Fitting	157



	Page
Appendix IX. Event Selection	168
Appendix X. Monte Carlo	186
Appendix XI. Calculation of the Cross-Section	206
Appendix XII. Measurement Errors	212
Appendix XIII. Data Acquisition System	224

LIST OF FIGURES

Figure		Page
1	Direct and Cross Channels for $A + B \rightarrow C + D$	47
2	Contour C with Regge Poles and a Branch Cut	47
3	Contour C'	47
4	Beam Spectrometer	49
5	Forward Spectrometer	51
6.1 -		
6-8	Differential Cross-Sections for the 68 GeV/c Data	
	Figure 6.1	53
	Figure 6.2	54
	Figure 6.3	55
	Figure 6.4	56
	Figure 6.5	57
	Figure 6.6	58
	Figure 6.7	59
	Figure 6.8	60
6.9 -		
6.21	Cross-Sections for the 116 GeV/c Data of this Experiment	
	Figure 6.9	62
	Figure 6.10	63
	Figure 6.11	64
	Figure 6.12	65
	Figure 6.13	66
	Figure 6.14	67
	Figure 6.15	68
	Figure 6.16	69
	Figure 6.17	70
	Figure 6.18	71
	Figure 6.19	72
	Figure 6.20	73
	Figure 6.21	74

Figure		Page
6.22 - 6.36	Cross-Sections for the 176 GeV/c Data of this Experiment	
	Figure 6.22	76
	Figure 6.23	77
	Figure 6.24	78
	Figure 6.25	79
	Figure 6.26	80
	Figure 6.27	81
	Figure 6.28	82
	Figure 6.29	83
	Figure 6.30	84
	Figure 6.31	85
	Figure 6.32	86
	Figure 6.33	87
	Figure 6.34	88
	Figure 6.35	89
	Figure 6.36	90
7	Comparison of the Regge Trajectories for this Experiment	92
8.1 - 8.7	Comparison between Differential Cross-Sections at Given Values of x and t , for Different Values of s	
	Figure 8.1	94
	Figure 8.2	95
	Figure 8.3	96
	Figure 8.4	97
	Figure 8.5	98
	Figure 8.6	99
	Figure 8.7	100
9	Regge Trajectories ($\alpha_E(s, t)$)	102
10	Comparison between $\alpha_E(s, t)$, the Effective Regge Trajectory for this Experiment at 116 GeV/c, and $\alpha_0(t)$ and $\alpha_A(t)$, the Regge Trajectories from Pion Charge ² Exchange	104
11	Effective Regge Trajectory, $\alpha_E(s, t)$, Compared with Prediction from Pion Charge Exchange	106

Figure	Page
12.1 -	Comparison of Some of our Cross-Sections at
12.5	$s = 232 \text{ GeV}^2$ with the Corresponding Predictions
	using the Pion Charge Exchange Cross-Sections
	at $s = 200 \text{ GeV}^2$
Figure 12.1	108
Figure 12.2	109
Figure 12.3	110
Figure 12.4	111
Figure 12.5	112

APPENDIX I

I.1	The M4 Beam Line	119
-----	------------------	-----

APPENDIX II

II.1	Details of the Cherenkov Counter Optics	124
II.2	Response of the Cherenkov Counter to the M4 Beam	126

APPENDIX III

III.1	Beam Spectrometer	131
-------	-------------------	-----

APPENDIX IV

IV.1	Liquid Hydrogen Target	134
------	------------------------	-----

APPENDIX V

V.1	"Termination" of Sense Wire Planes	141
V.2	Proportional Wire Chamber Readout Logic	143

APPENDIX VI

VI.1	High Voltage Pulser for the Spark Chamber	150
------	---	-----

Figure	Page
--------	------

APPENDIX VII

VII. 1	Trigger Logic	156
--------	-------------------------	-----

APPENDIX IX

IX. 1 -	Geometric and Kinematical Acceptance Criteria	
IX-10	for 116 GeV/c Data	
	Figure IX. 1	176
	Figure IX. 2	177
	Figure IX. 3	178
	Figure IX. 4	179
	Figure IX. 5	180
	Figure IX. 6	181
	Figure IX. 7	182
	Figure IX. 8	183
	Figure IX. 9	184
	Figure IX. 10	185

APPENDIX X

X. 1	Coordinate Systems used in the Analysis of this Experiment	190
X. 2 -	Comparison between Our Data and the Predictions	
X. 15	from the Monto Carlo Computations for the Same Total Number of Events	
	Figure X. 2	192
	Figure X. 3	193
	Figure X. 4	194
	Figure X. 5	195
	Figure X. 6	196
	Figure X. 7	197
	Figure X. 8	198
	Figure X. 9	199
	Figure X. 10	200
	Figure X. 11	201
	Figure X. 12	202
	Figure X. 13	203
	Figure X. 14	204
	Figure X. 15	205

Figure

Page

APPENDIX XII

XII. 1 - Calculated Measurement Resolutions

XII. 3

Figure XII. 1	219
Figure XII. 2	219
Figure XII. 3	219

XII. 4 - Calculated Measurement Resolutions

XII. 7

Figure XII. 4	221
Figure XII. 5	221
Figure XII. 6	221
Figure XII. 7	221

XII. 8 - Calculated Measurement Resolutions

XII. 10

Figure XII. 8	223
Figure XII. 9	223
Figure XII. 10	223

LIST OF TABLES

Table		Page
I	M4 Beam Phase Space and Fluxes	29
II. 1	Differential Cross-Sections - $t = -0.05$	30
II. 2	$t = -0.15$	31
II. 3	$t = -0.25$	32
II. 4	$t = -0.35$	33
II. 5	$t = -0.45$	34
II. 6	$t = -0.55$	35
II. 7	$t = -0.65$	36
II. 8	$t = -0.75$	37
II. 9	$t = -0.85$	38
II. 10	$t = -0.95$	39
II. 11	$t = -1.05$	40
II. 12	$t = -1.15$	41
II. 13	$t = -1.25$	42
II. 14	$t = -1.35$	43
II. 15	$t = -1.45$	44
III	Effective Regge Trajectories	45

APPENDIX I

I	The Charged M4 Beam	117
---	-------------------------------	-----

APPENDIX II

I	Useful Relations	122
II	Operating Parameters	122

APPENDIX III

I	Beam Chamber Spectrometer Resolutions	129
---	---	-----

APPENDIX IV

I	132
---	-----------	-----

Table		Page
APPENDIX VI		
I	Spark Chamber Efficiencies	148
APPENDIX VII		
I	Cumulative Signal Counts	154
APPENDIX IX		
I	Variable Names	172
II	Event Selection Criteria	173
III	Event Selection History	174
APPENDIX XI		
I	Corrections to Cross-Section	208
APPENDIX XII		
I	Systematic Error in α_E Due to a Mistake of 1% in the Momentum Calibration of the Beam Spectrometer	216
II	Measurement Errors	217

ACKNOWLEDGMENTS

First, I want to express my deep appreciation to Bob Swanson and Hans Kobrak. Whatever I am, as a physicist, they have made.

Thanks also the rest of E-383-Maris Abolins, Ken Edwards, Bill Francis, and especially Werner de Rosario, Bob Smythe and Phil Yager who made all those night shifts bearable.

Without the Fermilab staff, mainly the Meson Lab crew and the computer operators, none of this would have possible, and I would be doing something more mundane.

I would also like to thank Peggy Haven and Annetta Whiteman who typed this tome. Neither of them knew quite what they were letting themselves in for. Without their cheerful work, this thesis could not have been completed.

Finally, my thanks to my wife, Phyllis. Now that this is over, I hope she remembers who I am.

This work was supported by the National Science Foundation.

VITA

- 1974- A. B. , University of California, San Diego
- 1974-1975 Regents Fellow, Department of Physics,
University of California, San Diego
- 1975-1980 Research Assistant, Department of Physics,
University of California, San Diego
- 1980- Doctor of Philosophy
University of California, San Diego

PUBLICATIONS

- "Charged M4 Beam Line" (with H. Kobrak and R. A. Swanson),
Fermilab TM-597 (1975).
- "Coherent Regeneration of K_s^0 's by Carbon as a Test of Regge-
Pole Exchange Theory" (with J. Roehrig, A. Gsponer,
W. R. Molzon, E. I. Rosenberg, V. L. Telegdi,
B. D. Winstein, H. G. E. Kobrak, R. A. Swanson),
Phys. Rev. Lett. 38, 1116 (1977).
- "Coherent K_s^0 Regeneration from Protons in the Momentum Range
30 to 130 GeV/c" (with G. Bock et al.), Bull. Am. Phys.
Soc. 23, 634 (1978).
- "Coherent K_s^0 Regeneration on Protons from 30 to 130 GeV/c"
(with G. J. Bock et al.), Phys. Rev. Lett. 42, 350 (1979).

ABSTRACT OF THE DISSERTATION

A Study of Inclusive Kaon Charge Exchange
in the Triple Regge Region

by

Randall Evans Pitt

Doctor of Philosophy in Physics

University of California, San Diego, 1980

Professor Robert A. Swanson, Chairman

The reaction $K^- + p \rightarrow \bar{K}^0 + X$ has been studied in the
kinematic range

$$133 < s < 350 \text{ GeV}^2$$

$$0.3 < X_F < 1$$

$$t_{\min} < -t < 1.3 (\text{GeV}/c)^2$$

In an experiment performed at Fermilab, 110,000 \bar{K}^0 's were recorded by the detection of the decay $K_S \rightarrow \pi^+ + \pi^-$. From these, the differential cross-section, $d^2\sigma(s, \mathbf{x}, t)/d\mathbf{x}dt$, has been calculated. 21,000 \bar{K}^0 's are in the kinematic region appropriate to an analysis

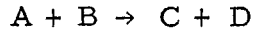
in the framework of Triple Regge theory. Effective Regge trajectories have been extracted from these at each value of s and t . The differential cross-sections have been compared with predictions relating them to pion inclusive charge exchange differential cross-sections in the Triple Regge region.

There is good agreement between the results of this analysis and the predictions of Triple Regge theory.

I. INTRODUCTION

This thesis describes an experiment which studied inclusive kaon charge exchange for incident kaon momenta of 68, 116 and 176 GeV/c. Differential cross-sections ($d^2\sigma/dx dt$) have been measured over the entire kinematic range accessible to our apparatus. In the limited kinematic range of Feynman x near 1, these data have been analyzed in the framework of Triple Regge theory.

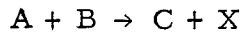
Regge theory¹ has been a successful framework for the interpretation of a variety of exclusive reactions:



Total cross-sections,² kaon regeneration³ and pion charge exchange⁴ are examples of processes which are well described by the exchange of Regge poles.

However, cross-sections for exclusive reactions fall rapidly with increasing energy while total cross-sections remain constant. Thus, it becomes more and more difficult to isolate a given exclusive channel from the large number of other processes.

Mueller⁵ extended Regge theory to cover interactions:



where "C + X" represents all possible final states containing at least one particle of type C. The cross-section for such an inclusive interaction is much larger than that of the corresponding exclusive

reaction. Also, it is much easier to measure, as only particles of type C must be detected.

Using Mueller's work, de Tar et al.⁶ first derived an expression for the inclusive cross-section in the kinematic region characterized by large s and Feynman x near 1, the "Triple Regge Region." Their prediction was

$$\frac{d^2\sigma}{dx dt} = \sum_{i, j, k} F_{ijk}(t)(1-x)^{\alpha_k(0) - \alpha_i(t) - \alpha_j(t)} s^{\alpha_k(0) - 1}$$

where s and t are the usual Mandelstam variables and the subscripts (i, j, k) represent the allowed Regge pole exchanges. The α 's are the trajectories associated with the exchanged poles while $F_{ijk}(t)$ describes the interaction amongst poles and between the poles and the particles A, B, and C.

The first tests of this prediction with good statistical accuracy were the measurements of $p+p \rightarrow p+X$ at the CERN ISR and at Fermilab. These experiments were the subject of a detailed analysis by Field and Fox,¹³ who found that the large number of possible exchanges ($\pi, \rho, \omega, A_2, f, P$) called for simplifying assumptions (they assumed that all mesons, except pions, have the same trajectory). Even so, they note that several choices for the relative contributions of the various Triple Regge terms fit the data equally well.

There are very few interactions which have a small number of allowed exchanges and which are experimentally feasible. The three

most simple are:

$$\pi^- + p \rightarrow \pi^0 + X \quad (1)$$

$$\pi^- + p \rightarrow \eta + X \quad (2)$$

$$K^- + p \rightarrow \overline{K^0} + X \quad (3)$$

Reactions (1) and (2) are being studied by E-350⁷ at Fermilab. This experiment studies (3). Below, we review the theoretical predictions for these processes.

Inclusive kaon charge exchange has been studied in bubble chambers for incident kaon momenta between 5 and 32 GeV/c.⁸ For these experiments, the detection efficiency for the decay $K_s^+ \rightarrow \pi^+ + \pi^-$ falls with increasing x because high energy K_s 's are more likely to leave the bubble chamber before decaying. Some Triple Regge analyses have been made of these data,⁹ but the low detection efficiency in the kinematic range of interest (high x) reduced the size of their data sample, and hence their statistical power is severely limited.¹⁶

In this experiment the detection efficiency was a maximum at large x and for incident momenta of 116 and 176 GeV/c it was nearly uniform in the kinematic region of interest for Triple Regge theory.

II. THEORY

We interpret the results of this experiment in the framework of Triple Regge theory. This theory is an extension of Regge theory to inclusive reactions of the form

$$A + B \rightarrow C + X$$

where $C+X$ represents the sum of all possible final states containing at least one particle of type C . Using the ideas of Regge theory, we will derive the high energy limit of the scattering amplitude, $A(s, t)$ for the reaction

$$A + B \rightarrow C + D \quad (\text{direct channel})$$

from the low energy behavior of the reaction

$$A + \bar{C} \rightarrow \bar{B} + D \quad (\text{cross channel})(\text{see Fig. 1})$$

If P_a , P_b , and P_c are the four-momenta of particles A , B and C , then we define the usual Mandelstam variables.

$$s = (P_a + P_b)^2$$

$$t = (P_a - P_c)^2$$

In its earliest form, Regge theory¹ attempted to explain direct channel bound states and resonances by the effect of poles in the scattering amplitude, $A(E, \cos \theta)$, where E is the center-of-mass energy and θ is the center-of-mass angle between A and C .

First, $A(E, \cos \theta)$ is written as a partial wave series

$$A(E, \cos \theta) = \sum_{\ell=0}^{\infty} (2\ell+1) a_{\ell}(E) P_{\ell}(\cos \theta) \quad (1)$$

where the $P_{\ell}(\cos \theta)$ are the Legendre functions. $a_{\ell}(E)$ is defined only for non-negative integer values of ℓ . We assume the existence of a function, $a'(\ell, E)$, which is analytic in the complex ℓ -plane and

$$a'(\ell, E) = a_{\ell}(E) \quad \ell = 0, 1, 2, 3 \dots$$

Regge showed that $a'(\ell, E)$ has poles, "Regge poles," at $\ell = \alpha(E)$, where $\alpha(E)$ depends on the form of the interaction.

The imaginary part of $\alpha(E)$ determines the effect of such a pole on $a_{\ell}(E)$ at $\text{Re} \{\alpha(E)\} = \ell$. $\text{Im} \{\alpha(E)\} = 0$ implies a pole in $a_{\ell}(E)$, or a bound state. $\text{Im} \{\alpha(E)\} \ll 1$ implies an enhancement in $a_{\ell}(E)$, or a resonance.

To apply these ideas to high energy scattering, we first rewrite (1) in the cross channel ¹²

$$A(t, \cos \theta_t) = \sum_{\ell=0}^{\infty} (2\ell+1) a_{\ell}(t) P_{\ell}(\cos \theta_t) \quad (2)$$

where t is the square of the center-of-mass energy and θ_t is the center-of-mass angle between A and \bar{B} .

$$\cos \theta_t = \frac{t^2 + t(2s - \Sigma) + (m_A^2 - m_B^2)(m_C^2 - m_D^2)}{\{[t - (m_A + m_B)^2][t - (m_A - m_B)^2][t - (m_C + m_D)^2][t - (m_C - m_D)^2]\}^{1/2}} \quad (3)$$

with

$$\Sigma \equiv m_A^2 + m_B^2 + m_C^2 + m_D^2 .$$

Assuming the analyticity of $a'(l, t)$ we use the Watson-Sommerfeld transformation to change the sum to a contour integral in the complex l -plane enclosing poles at $l = 0, 1, 2, 3, 4 \dots$ (see Figure 2).

$$A(t, \cos \theta_t) = \frac{1}{2i} \oint_C (2l+1) \frac{a'(l, t)}{\sin \pi l} P_l(-\cos \theta_t) \quad (4)$$

The contour can be deformed (see Figure 3) to lie at $\text{Re} \{l\} = -1/2$ giving

$$A(t, \cos \theta_t) = \frac{1}{2i} \oint_{C'} (2l+1) \frac{a'(l, t)}{\sin \pi l} P_l(-\cos \theta_t) - \pi \sum_n \frac{(2\alpha_n(t)+1)}{\sin \pi \alpha_n(t)} b_n(t) P_{\alpha_n(t)}(-\cos \theta_t) \quad (5)$$

+ cut contributions

where $b_n(t)$ is the residue of the Regge pole at $l = \alpha_n(t)$. For the rest of the derivation, we assume the cut contributions are negligible.¹⁰

We are interested in

$$\lim_{\cos \theta_t \rightarrow \infty} A(t, \cos \theta_t)$$

so we use the limiting form of the Legendre function

$$\lim_{Z \rightarrow \infty} P_{\alpha(t)}(Z) = C(\alpha(t)) Z^{\alpha(t)}$$

to rewrite (5)

$$\begin{aligned} \lim_{\cos \theta_t \rightarrow \infty} A(t, \cos \theta_t) &= \frac{1}{2i} \oint_{C'} (2l+1) \frac{\alpha'(\ell, t)}{\sin \pi \ell} C(\ell) (-\cos \theta_t)^{-1/2} (-\cos \theta_t)^{\text{Im}(\ell)} \\ &- \pi \sum_n \frac{(2\alpha_n(t)+1)}{\sin \alpha_n(t) \pi} C(\alpha_n(t)) b_n(t) (-\cos \theta_t)^{\alpha_n(t)} \end{aligned} \quad (6)$$

The first term, the "background integral," vanishes in the limit.

In potential theory, the presence of an exchange potential leads to two separate Schrödinger equations, one for ℓ even and one for ℓ odd. A factor is needed to prevent a Regge pole from producing resonances at both even and odd ℓ . This factor, the "signature factor" is

$$S(t) = 1 + \tau e^{i\pi\alpha_n(t)} \quad (7)$$

where

$$\tau = 1 \text{ for "even" poles (no resonance at odd } L)$$

$$\tau = -1 \text{ for "odd" poles (no resonance at even } L)$$

Including this factor in (6), we get

$$A(t, \cos \theta_t) = -\pi \sum_n \frac{1 + \tau e^{i\pi\alpha_n(t)}}{2 \sin \pi\alpha_n(t)} b_n(t) C(\alpha_n(t)) (-\cos \theta_t)^{\alpha_n(t)} \quad (8)$$

Finally, from (3)

$$\lim_{S \rightarrow \infty} (-\cos \theta_t) \propto S$$

So,

$$A(s, t) = \sum_n \frac{1 + \tau e^{i\pi\alpha_n(t)}}{\sin \pi\alpha_n(t)} B_n(t) S^{\alpha_n(t)} \quad (9)$$

where $b_n(t)$ and all factors of $2, \pi$, etc. have been combined into $B_n(t)$.

As a Feynman diagram, equation (9) is ¹¹

$$A(s, t) = \sum_n \begin{array}{c} A \quad C \\ \diagdown \quad / \\ \text{wavy line} \\ / \quad \diagdown \\ B \quad D \end{array} \alpha_n(t) \quad (10)$$

For inclusive reactions, Mueller's generalized Optical Theorem relates the differential cross-section to the imaginary part of the forward three-body amplitude.⁶

$$\frac{d^2\sigma}{dx dt} = \frac{1}{S} \sum_X \begin{array}{c} A \quad C \\ \diagdown \quad / \\ \text{circle} \\ / \quad \diagdown \\ B \quad X \end{array}^2 = \frac{1}{S} \text{Disc} \left| \begin{array}{c} A \rightarrow \quad \left(\text{circle} \right) \quad \rightarrow A \\ C \leftarrow \quad \left(\text{circle} \right) \quad \leftarrow C \\ B \rightarrow \quad \left(\text{circle} \right) \quad \rightarrow B \end{array} \right| \quad (11)$$

Mueller

with

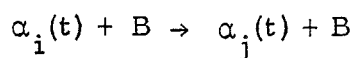
$$M_X^2 = (P_a + P_b - P_c)^2$$

$$x \equiv 1 - \frac{M_X^2}{S}$$

For $S/M_X^2 \gg 1$, this amplitude can be expanded by the simple Regge methods outlined above.

$$\lim_{\substack{S \rightarrow \infty \\ M_X^2 \rightarrow \infty}} \frac{d^2 \sigma}{dx dt} = \frac{1}{S} \text{ Disc} \left\{ \sum_{i,j} \left(\begin{array}{c} \text{A} \rightarrow \text{C} \\ \alpha_i(t) \\ \text{B} \rightarrow \text{C} \\ \alpha_j(t) \\ \text{B} \rightarrow \text{A} \\ \alpha_j(t) \\ \text{B} \rightarrow \text{B} \end{array} \right) \right\} \quad (12)$$

If we then take $M_X^2 \gg 1$, the reaction



can be expanded by Regge methods

$$\lim_{\substack{S \rightarrow \infty \\ M_X^2 \rightarrow \infty}} \frac{d^2 \sigma}{dx dt} = \frac{1}{S} \sum_{i,j,k} \text{Im} \left[\begin{array}{c} \text{A} \rightarrow \text{C} \\ \alpha_i(t) \\ \text{B} \rightarrow \text{C} \\ \alpha_j(t) \\ \text{B} \rightarrow \text{A} \\ \alpha_k(0) \\ \text{B} \rightarrow \text{B} \end{array} \right] \quad (13)$$

This kinematic region, $S \gg M_X^2 \gg 1$, is known as the Triple-Regge region. This Triple Regge diagram corresponds to

$$\frac{d^2\sigma}{dx dt} = \sum_{ijk} F_{ijk}(t)(1-x)^{\alpha_k(0) - \alpha_i(t) - \alpha_j(t)} s^{\alpha_k(0) - 1} \quad (14)$$

where

$$F_{ijk}(t) = \gamma_{AC}^i(t) \gamma_{AC}^j(t) \gamma_{ij}^k(0) \gamma_{BB}^k(0) S_i(t) S_j^*(t) \quad (11)$$

By assuming that k can be either a pomeron, P , with $\alpha_k(0) \approx 1$ or a meson with $\alpha_k \approx 0.5$, (14) becomes

$$\begin{aligned} \frac{d^2\sigma}{dx dt} = & \sum_{ij} F_{ijP}(t)(1-x)^{1 - \alpha_i(t) - \alpha_j(t)} \\ & + \sum_{ij} F_{ijM}(t)(1-x)^{0.5 - \alpha_i(t) - \alpha_j(t)} s^{-1/2} \end{aligned} \quad (15)$$

The Triple Regge cross-section is expected to be dominated by the energy independent term.

For the process

$$K^- + p \rightarrow \overline{K^0} + X \quad (16)$$

conservation rules limit the choices of i , j , and k to

\underline{i}	\underline{j}	\underline{k}
ρ	ρ	P
A_2	A_2	P
ρ	ρ	$(\rho + f)$
A_2	A_2	$(\rho + f)$
ρ	A_2	A_2
A_2	ρ	A_2

Assuming $\alpha_\rho(0) = \alpha_f(0)$, equation (14) becomes

$$\begin{aligned}
 \frac{d^2 \sigma}{dx dt} \Big|_{K^0 x} &= \frac{\gamma_{KK}^\rho(t)^2}{\cos^2\left(\frac{\pi}{2} \alpha_\rho(t)\right)} \left(\gamma_{pp}^P(0) \gamma_{\rho\rho}^P(0)(1-x)^{1-2\alpha_\rho(t)} \right. \\
 &\quad \left. + \gamma_{pp}^{\rho+f}(0) \gamma_{\rho\rho}^{\rho+f}(0)(1-x)^{\alpha_\rho(0) - 2\alpha_\rho(t)} s^{\alpha_\rho(0) - 1} \right) \\
 &+ \frac{\gamma_{KK}^{A_2}(t)^2}{\sin^2\left(\frac{\pi}{2} \alpha_{A_2}(t)\right)} \left(\gamma_{pp}^P(0) \gamma_{A_2 A_2}^P(0)(1-x)^{1-2\alpha_{A_2}(t)} \right. \\
 &\quad \left. + \gamma_{pp}^{\rho+f}(0) \gamma_{A_2 A_2}^{\rho+f}(0)(1-x)^{\alpha_\rho(0) - 2\alpha_{A_2}(t)} s^{\alpha_\rho(0) - 1} \right) \\
 &+ \gamma_{KK}^\rho(t) \gamma_{KK}^{A_2}(t) \gamma_{\rho A_2}^{A_2}(0) \gamma_{pp}^{A_2}(0)(1-x)^{\alpha_{A_2}(0) - \alpha_\rho(t) - \alpha_{A_2}(t)} s^{\alpha_{A_2}(0) - 1} \\
 &\quad \times \sin \pi(\alpha_\rho(t) - \alpha_{A_2}(t)) \tag{17}
 \end{aligned}$$

Equation (17) is the Triple Regge prediction for reaction (16).

The third term, "interference term," is commonly neglected, both because of its s -dependence and because $(\alpha_\rho(t) - \alpha_{A_2}(t))$ is small.

Combining Triple Regge theory and SU(3) we can derive a relation between our cross-section and those of the reactions

$$\pi^- + p \rightarrow \pi^0 + X \tag{18}$$

$$\pi^- + p \rightarrow \eta + X \tag{19}$$

The Triple Regge prediction for reaction (18) is

$$\frac{d^2\sigma}{dx dt} \Big|_{\pi^0 X} = \frac{\gamma_{\pi\pi}^\rho(t)^2}{\cos^2 \frac{\pi}{2} \alpha_\rho(t)} \left(\gamma_{pp}^P(0) \gamma_{\rho\rho}^P(0)(1-x)^{1-2\alpha_\rho(t)} \right. \\ \left. + \gamma_{pp}^{\rho+f}(0) \gamma_{\rho\rho}^{\rho+f}(0)(1-x)^{\alpha_\rho(0)-2\alpha_\rho(t)} s^{\alpha_\rho(0)-1} \right) \quad (20)$$

and for reaction (19) is

$$\frac{d^2\sigma}{dx dt} \Big|_{\eta X} = \frac{\gamma_{\pi\pi}^{A_2}(t)^2}{\sin^2 \frac{\pi}{2} \alpha_{A_2}(t)} \left(\gamma_{pp}^P(0) \gamma_{A_2 A_2}^P(0)(1-x)^{1-2\alpha_{A_2}(t)} \right. \\ \left. + \gamma_{pp}^{\rho+f}(0) \gamma_{A_2 A_2}^{\rho+f}(0)(1-x)^{\alpha_\rho(0)-2\alpha_{A_2}(t)} s^{\alpha_\rho(0)-1} \right) \quad (21)$$

From SU(3), we get the relations ⁽¹⁴⁾

$$\gamma_{KK}^\rho(t)^2 = \frac{1}{2} \gamma_{\pi\pi}^\rho(t)^2 \quad (22)$$

$$\gamma_{KK}^{A_2}(t) = \frac{3}{2} \gamma_{\pi\pi}^{A_2}(t)^2 \quad (23)$$

So, combining (20) - (23), and neglecting the interference term, equation (16) can be rewritten

$$\frac{d^2\sigma}{dx dt} \Big|_{K^0 K} = \frac{1}{2} \frac{d^2\sigma}{dx dt} \Big|_{\pi^0 X} + \frac{3}{2} \frac{d^2\sigma}{dx dt} \Big|_{\eta X} \quad (24)$$

To summarize, the predictions which we check in our analysis

are

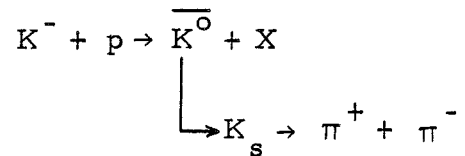
1) $\frac{d^2 \sigma}{dx dt}$ is s-independent.

2) $\gamma_{KK}^{\rho}(t)^2 = \frac{1}{2} \gamma_{\pi\pi}^{\rho}(t)^2$; $\gamma_{KK}^{A_2}(t)^2 = \frac{3}{2} \gamma_{\pi\pi}^{A_2}(t)^2$

3) $\alpha_{\rho}(t)$ and $\alpha_{A_2}(t)$ are the same for kaon and pion charge exchange.

III. EXPERIMENTAL APPARATUS

To study the reaction



in the framework of the above theory, it is necessary to identify the incident K^- and measure its vector momentum (necessary for the calculation of x , s , and t). The identification was done by a Cherenkov counter; the momentum was measured by a beam spectrometer. To reconstruct the K_s , it was necessary to measure the vector momentum of the pions downstream of the interaction point. No particle identification was made. This meant that neutral decays found during the off-line analysis could be either kaons or lambdas; requirements on the kinematics of the decay discriminated between the two possibilities. The layout of the experimental apparatus is shown in Figures 4 and 5.

A. BEAM

This experiment was performed in the M4 beam line at Fermilab. The 7.25 milliradian angle between this beam line and the incident proton beam resulted in an enhanced kaon to pion ratio but a reduced flux relative to the more forward beam lines. During our data taking, we used fluxes from 0.5×10^5 to 1.0×10^6 particles

per spill. The average kaon content was 5%. Table I and Appendix I describe the beam in detail.

B. CHERENKOV COUNTER

A differential Cherenkov counter distinguished kaons from the other particles (mostly pions) in the beam. The counter had two phototubes. Under normal operating conditions, one tube recorded kaons while the other recorded pions (as well as muons and electrons, if present); anti-protons were below threshold and were not recorded. The output of the kaon tube was used in the event trigger. The output of each tube was analyzed by an analog-to-digital converter (ADC) and recorded. This allowed us to monitor the operation of the counter. In Appendix II the counter and its operation are described in detail.

C. BEAM SPECTROMETER

The vector momentum of an incident particle was measured in a beam spectrometer consisting of four pairs of small proportional chambers and two dipole magnets. The magnet excitation was set so that a particle left the spectrometer with its momentum vector unchanged, but displaced 150 mm in X. This displacement, with the 1 mm wire spacing of the chambers, gave a typical momentum resolution of 0.4% and a typical angular resolution of 30 μ rad. Appendix III describes this spectrometer.

D. LIQUID HYDROGEN TARGET

When full, the liquid hydrogen target had approximately 31×10^{23} protons/cm², of which 92% were in the liquid hydrogen. The probability for a K⁻ interaction in the target was 6%. The target is described in Appendix IV.

E. SWEEPING MAGNET

Immediately downstream of the target was a sweeping magnet and the vacuum decay region. The magnet swept the beam away from the center of the forward spectrometer, and swept most charged secondaries out of the spectrometer entirely. The vacuum decay region following the sweeping magnet was 14.75 m long, with a diameter of 30.5 cm at the upstream end and 90.8 cm at the downstream end.

F. FORWARD SPECTROMETER

Charged tracks downstream of the target were detected by a spectrometer consisting of six multiwire proportional chamber (PWC) planes with 2 mm wire spacing, 24 magnetostrictive spark chamber planes with 1 mm wire spacing, and an analysis magnet (see Appendix V, for a description of the PWC's and Appendix VI for a description of the spark chambers). The analysis magnet had a useful aperture of 1.25 m by 0.59 m and a field integral of 6.87 kG-m. With this spectrometer, we achieved a position resolution of 1 mm at

the center of the analysis magnet and a momentum resolution of 1.5% for 75 GeV/c pions.

G. TRIGGER COUNTERS AND LOGIC

Scintillation counters were installed to help identify the occurrence of a possible charge exchange event. In the beam spectrometer, three small counters in the beam and one larger counter surrounding the beam were mounted and used to define an incident beam particle, unaccompanied by a particle outside the beam region (halo). A small counter was centered on the beam at the most upstream chamber station of the forward spectrometer. This was used to veto potential triggers due to diffractive dissociation of the K^- . A counter hodoscope, measuring 1.5 m by 1.2 m with an opening for the beam, was located downstream of the last chamber station in the forward spectrometer. This was used to identify events with at least one charged track outside the beam region downstream of the target.

Three trigger levels were defined. The first defined K^- 's which arrived while the experiment was "live." These were counted and used in the normalization of our cross-section. The second level defined events with no charged track inside and at least one charged track outside the beam region of the forward spectrometer. The final step, using the proportional chambers, defined events with at least two charged tracks outside the beam at every PWC station. Because of the late arrival of the proportional chamber signal, the

second trigger level was used to latch our ADC's and coincidence registers. The final trigger level began the data acquisition process which recorded the states of the various detectors on magnetic tape for further analysis. About 3.4% of these events contained a reconstructable kaon or lambda (see Appendix VII).

IV. ANALYSIS

A. PATTERN RECOGNITION AND EVENT SELECTION

The first step of the analysis consisted of reformatting the data written onto tape on-line, and converting chamber information into hit locations in the coordinate system of the experiment. Pattern recognition/track finding programs were then used to construct track segments out of the recorded hits. (See Appendix VIII for details.) Events which were not consistent with the decay of any known neutral particle were rejected. The final cuts were applied to eliminate lambdas and events with tracks in regions of the apparatus where the detection efficiency was hard to calculate (near the trigger counters, for example). Appendix IX describes the event selection.

B. CROSS-SECTION

For the calculation of the detection efficiency, Monte Carlo events were generated to simulate, as closely as possible, the data. These events were processed by the same pattern recognition and reconstruction programs as the data (for details on the Monte Carlo simulation of the data, see Appendix X). From the accepted event distribution, efficiencies, and measured incident K^- flux, cross-sections were calculated. Corrections were made for the effects of x and t resolution, double-interactions in the target, K^- decay before the target, K^- , $\overline{K^0}$ and pion absorption, beam phase cuts and false vetoes by the trigger logic. Appendix XI contains the details

of the calculation of the cross-section. The differential cross-sections are listed in Table II.

C. REGGE TRAJECTORIES

From these cross-sections, we have extracted an effective Regge trajectory, $\alpha_E(s, t)$, for each t -bin at each of the three values of s .

The function

$$\frac{d^2\sigma}{dx dt} = \frac{f(t)}{\cos^2\left(\frac{\pi}{2}\alpha_E(s, t)\right)} (1-x)^{1-2\alpha_E(s, t)} \quad (1)$$

was fit to the data by the minimization program MINUIT.¹⁵ $\alpha_E(s, t)$ was the only free parameter. The normalization, $f(t)$, was fixed by the requirement that the total number of events predicted by summing (1) over the x -bins used in the fit be the same as the total number of events actually found in those bins. MINUIT calculated the chi-squared (χ^2) for the fit at different values of $\alpha_E(s, t)$. The result of the fit was that value of $\alpha_E(s, t)$ which minimized χ^2 . Table III lists $\alpha_E(s, t)$. Figure 6 shows the calculated differential cross-sections in each t -bin and value of s . Also shown on these figures are the fitted curves with $\alpha_E(s, t)$, $f(t)$ and χ^2 . The quoted error in $\alpha_E(s, t)$ is the change in $\alpha_E(s, t)$ which increases χ^2 by 1, using a parabolic approximation for $\chi^2(\alpha_E(s, t))$ near its minimum. While the χ^2 per degree of freedom is higher than would be the case for "perfect" agreement between theory and data, there does not

seem to be any systematic deviation from the prediction of power law behavior in $(1-x)$.

The range in M_X^2 assumed in the derivation of the Triple Regge formula was

$$1 \ll M_X^2 \ll s$$

$X = 0.975$ was chosen as the upper limit for these fits. This choice was a compromise between the needs for satisfying the above assumption and for statistical power of the fits. $X = 0.975$ corresponds to

$$M_X^2 = 3.8 (\text{GeV}/c^2)^2 \text{ for } P_{\text{BEAM}} = 68 \text{ GeV}/c$$

$$M_X^2 = 9 (\text{GeV}/c^2)^2 \text{ for } P_{\text{BEAM}} = 176 \text{ GeV}/c$$

Fits made using lower values of x as upper limits showed that our calculation of $\alpha_E(s, t)$ is not sensitive to this choice. To select the lower limit in x , several fits to the data were made using different limiting values of x . From the invariance of the resulting α_E , we decided on $x = 0.7$ as a good choice for this limit. Figure 7 shows $\alpha_E(s, t)$ for different choices of this limit.

V. COMPARISON BETWEEN DATA AND THEORY

A. s DEPENDENCE

With the approximations made in the derivation in Chapter II, Triple Regge theory predicts that:

1. Cross-sections are independent of s .
2. The values of α ("Regge trajectories") are independent of s .

Figure 8 displays $d^2\sigma/dxdt$, our experimental cross-section, as a function of x , s and t . A small systematic s -dependence is apparent. Cross-sections at $s = 133 \text{ GeV}^2$ ($P_{\text{beam}} = 68 \text{ GeV}/c$) are approximately 20% higher than cross-sections at $s = 346 \text{ GeV}^2$ ($P_{\text{beam}} = 176 \text{ GeV}/c$), with cross-sections for $s = 228 \text{ GeV}^2$ ($P_{\text{beam}} = 116 \text{ GeV}/c$) generally in between. This trend, which holds over a range in x and t where the cross-sections change by a factor of 100, is well outside our experimental errors.

Figure 9 displays our results for $\alpha_E(s, t)$ for our three values of s . While there is no difference between the values of α_E for $s = 133 \text{ GeV}^2$ and $s = 228 \text{ GeV}^2$, the values for $s = 346 \text{ GeV}^2$ are consistently lower.

The most obvious candidates for systematic experimental errors which could cause the above s -dependences are errors in either the measurements of x or of ϕ_K , the incident K^- flux (a systematic error in x could be caused by a miscalibration of the momentum scale in the beam spectrometer). The deviations of our data

from the theory are not consistent with either of these explanations. The x - and t -dependence of the observed deviations are quite different from those expected for such systematic errors. Even at a given (x, t) point, attempting to explain the deviations by an error in the measurement of x requires errors three times larger than the upper limit derived from the consistency checks discussed in Appendix XII.

The details of the small s dependence are not consistent with the expected effect of the s dependent terms which were neglected in the derivations in Chapter II. The background integral, the Regge-Regge-Regge and interference terms are expected fall as $s^{-1/2}$ or faster. One expects then that the cross-section difference between 68 and 116 GeV/c would be larger than that between 116 and 176 GeV/c. Also, since the s dependent terms are expected to have a different $(1-x)$ power law behavior than the s independent terms, one would expect that the effective Regge trajectory for 176 GeV/c would be closer to that at 116 GeV/c, with the 68 GeV/c trajectory above the other two.

It is possible that the observed s dependence is due to a combination of the effects of neglecting some s dependent terms in deriving the predictions and of some systematic error in this experiment. We do not think it likely that our systematic errors are large enough to support such an explanation. It is also possible that the observed effects are due to the effects of other terms which were

neglected in the derivations, cut contributions for example. We do not know what their effect on the form of the cross-sections for inclusive reactions should be.

To summarize, the estimated systematic errors in our experiment are too small to cause the observed s dependence. Also, even if the errors were much larger than we estimate, the effects of such errors disagree, in detail, with the observed s dependence. Similarly, the s dependent terms which were neglected in the derivation of the predicted cross-section would give a different dependence than that observed. The difference between our measurements and the theoretical predictions used in our analysis appears to point to the limits of the validity of that theory.

B. COMPARISON BETWEEN KAON AND PION CHARGE EXCHANGE

A Triple Regge analysis of the reactions

$$\pi^- + p \rightarrow \pi^0 + X$$

and $\pi^- + p \rightarrow \eta + X$

at 100 GeV/c is described in Ref. 7.

In Chapter II, the following prediction was derived

$$\frac{d^2\sigma}{dx dt} \Big|_{K^0 X} = \frac{1}{2} \frac{d^2\sigma}{dx dt} \Big|_{\pi^0 X} + \frac{3}{2} \frac{d^2\sigma}{dx dt} \Big|_{\eta X}$$

For this relationship to be true, the Regge trajectories for

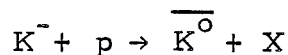
kaon and pion charge exchange must be the same. On Fig. 10, $\alpha_E(s, t)$ at 116 GeV/c is shown, along with $\alpha_\rho(t)$ and $\alpha_{A_2}(t)$ from Ref. 7.

From the parameterized cross-sections given in Ref. 7, a predicted cross-section for kaon charge exchange was calculated using the above relationship. Using the predicted cross-sections as input, effective $\alpha(t)$'s were extracted by the method described above. The comparisons between these values of $\alpha(t)$ and our values of $\alpha_E(s, t)$ at 116 GeV/c are shown in Fig. 11.

Figure 12 shows some predicted and measured cross-sections. The remarkable agreement between these at all values of t is striking evidence for the validity of Triple Regge theory and for the SU(3) relations between coupling constants which was used to derive the predicted cross-sections for kaon charge exchange.

VI. CONCLUDING REMARKS

We have measured the cross-section for the inclusive process



in the kinematic range

$$136 < s < 352 \text{ GeV}^2$$

$$0.3 < x < 1.0$$

$$t_{\min} < |t| < 1 \text{ (GeV/c)}^2$$

From our total sample of 110,000 "good kaons," the subset in the region $0.7 < x < 0.975$ (21,000 events) has been used to test the following predictions of Triple Regge theory:

- 1) $\frac{d^2\sigma}{dx dt} = c(t)(1-x)^{1-2\alpha(t)}$, independent of s
- 2) $\alpha(t)$ is given in terms of similar parameters for reactions
 $\pi^- + p \rightarrow \pi^0 + x$ and $\pi^- + p \rightarrow \eta + x$
- 3) $\left. \frac{d^2\sigma}{dx dt} \right|_{K^0} = \frac{1}{2} \left. \frac{d^2\sigma}{dx dt} \right|_{\pi^0} + \frac{3}{2} \left. \frac{d^2\sigma}{dx dt} \right|_{\eta}$

everywhere in the "Triple Regge region."

Here the first cross-section refers to our kaon charge exchange reaction while the others refer to the above two pion charge exchange reactions.

When deriving these predictions in Chapter II, the following assumptions were made.

- 1) The background integral was neglected.
- 2) Any cut contributions were neglected.
- 3) Only the leading term was kept in the expansion of $P_{\alpha}(\cos \theta_t)$.
- 4) The s -dependent Regge-Regge-Regge and interference terms were neglected.
- 5) $\alpha_P(0) = 1$ was assumed.

We find a small systematic s dependence in our cross-sections and Regge trajectories. We conclude that these differences point to a failure of our simplified form of the Triple Regge theory to accurately describe the data. This is possibly due to the effects of assumptions 1, 3 and 4 above, but the exact form of the disagreement is not consistent with the expected effect of such terms.

There is excellent agreement between our data and the second and third predictions above. In the Triple Regge region, the kaon charge exchange cross-section is that predicted from the pion charge exchange data.

In view of the wide kinematic range considered, the other reactions with which our data has been compared and the drastic approximations in the derivation of the theoretical expressions, the agreement between our data and theory is quite remarkable. The results of this and other high statistics experiments will prompt, we hope, the theoretical work needed to refine an already quite successful treatment of inclusive reactions. Should more pion

charge exchange cross-sections become available, especially at energies different from that which has been published, further efforts on the comparison between kaon and pion charge exchange cross-sections will clearly be needed.

The "low x " ($0.3 < x < 0.7$) subset of our data can be used to test theoretical proposals which derive features of "soft" (low t) hadronic processes from the expected behavior of basic hadron constituents. Interactions in this kinematic region for (charged particle \rightarrow charged particle) have been studied in Experiment 118 at Fermilab. It will be of great interest to compare their results with the results of a similar analysis of our "low x " data.

TABLE I

M4 Beam Phase Space and Fluxes

Momentum (GeV/c)	68	116	176	
σ_x (mm)	6.7	6.6	6.1	
σ_x (r)	81	92	66	
σ_y (mm)	5.4	6.3	5.2	
σ_y (r)	71	70	67	
$\delta p/p$ (%)	19	8.7	10	(1)
K ⁻ content (%)	4.2	6.2	5.7	
Total beam	216 K	145 K	40800	(2)

Notes:

- (1) $\delta p/p$ is the full width at half maximum.
 (2) Total beam is the number of beam particles for 10^{12} protons on the meson target.

TABLE II. 1

Differential Cross-Sections (millibarns/(GeV/c)²)

t = -0.05

(1-x)	68 GeV/c		116 GeV/c		176 GeV/c	
	σ	$\delta\sigma$	σ	$\delta\sigma$	σ	$\delta\sigma$
.0125	2.30	(.16)	2.88	(.17)	1.99	(.17)
.0375	3.12	(.21)	2.77	(.17)	2.33	(.19)
.0625	3.27	(.23)	2.84	(.19)	2.60	(.20)
.0875	3.90	(.25)	3.33	(.20)	2.89	(.22)
.1125	4.00	(.26)	4.34	(.23)	3.64	(.24)
.1375	5.28	(.31)	4.10	(.22)	4.63	(.27)
.1627	5.08	(.31)	4.77	(.25)	4.26	(.26)
.1875	5.37	(.33)	4.95	(.25)	4.89	(.27)
.2125	5.95	(.36)	4.60	(.24)	4.36	(.26)
.2375	5.80	(.38)	5.05	(.25)	4.60	(.26)
.2625	5.74	(.39)	4.48	(.24)	4.93	(.27)
.2875	5.10	(.39)	4.18	(.23)	4.04	(.24)
.3125	5.9	(.4)	4.28	(.24)	3.55	(.23)
.3375	4.3	(.4)	3.81	(.23)	4.06	(.24)
.3625	4.0	(.4)	3.46	(.22)	3.83	(.24)
.3875	4.4	(.5)	2.51	(.21)	2.68	(.24)
.4125	2.9	(.4)	1.96	(.18)	1.26	(.19)
.4375	2.0	(.5)	1.05	(.16)	.78	(.12)
.4625	.14	(.24)	.13	(.08)	.03	(.06)

TABLE II. 2

 $t = -0.15$

(1-x)	68 GeV/c		116 GeV/c		176 GeV/c	
	σ	$\delta\sigma$	σ	$\delta\sigma$	σ	$\delta\sigma$
.0125	1.42	(.14)	1.10	(.11)	.82	(.11)
.0375	1.78	(.17)	1.48	(.13)	1.31	(.13)
.0625	1.82	(.18)	1.65	(.14)	1.53	(.14)
.0875	2.46	(.22)	1.79	(.14)	1.37	(.14)
.1125	2.82	(.24)	2.38	(.17)	2.05	(.17)
.1375	2.44	(.23)	2.56	(.17)	2.55	(.19)
.1675	2.26	(.23)	2.43	(.17)	1.87	(.16)
.1875	3.94	(.32)	3.07	(.19)	3.18	(.21)
.2125	3.71	(.32)	3.25	(.20)	3.03	(.20)
.2375	5.1	(.4)	3.51	(.21)	3.77	(.23)
.2625	4.7	(.4)	3.74	(.21)	3.61	(.22)
.2875	4.7	(.4)	3.91	(.22)	4.08	(.24)
.3125	6.3	(.5)	5.05	(.27)	4.86	(.26)
.3375	6.1	(.6)	5.30	(.26)	5.26	(.26)
.3625	6.7	(.6)	6.09	(.28)	6.23	(.29)
.3875	7.9	(.7)	5.52	(.30)	6.51	(.28)
.4125	9.3	(.9)	6.86	(.32)	4.88	(.30)
.4375	10.3	(1.0)	7.63	(.35)	6.95	(.32)
.4625	12.0	(1.2)	7.67	(.35)	7.99	(.34)
.4875	9.9	(1.3)	7.86	(.39)	7.82	(.34)
.5125	8.0	(1.5)	6.36	(.37)	6.15	(.31)
.5375	8.4	(1.7)	3.68	(.29)	4.46	(.28)
.5625	3.1	(1.3)	1.30	(.19)	1.56	(.19)
.5875	---	---	.010	(.024)	---	---

TABLE II. 3

$$t = -0.25$$

(1-x)	68 GeV/c		116 GeV/c		176 GeV/c	
	σ	$\delta\sigma$	σ	$\delta\sigma$	σ	$\delta\sigma$
.0125	.78	(.12)	.45	(.07)	.45	(.08)
.0375	.80	(.13)	.75	(.09)	.60	(.10)
.0625	1.11	(.16)	.80	(.09)	.65	(.09)
.0875	1.03	(.16)	1.15	(.12)	1.06	(.11)
.1125	1.94	(.24)	1.27	(.12)	1.49	(.14)
.1375	2.00	(.25)	1.40	(.12)	1.38	(.14)
.1625	2.29	(.30)	1.58	(.13)	1.74	(.15)
.1875	2.71	(.32)	1.69	(.14)	1.71	(.15)
.2125	2.84	(.36)	2.09	(.16)	2.51	(.19)
.2374	3.07	(.38)	2.73	(.18)	2.98	(.20)
.2625	2.66	(.37)	2.65	(.18)	2.86	(.20)
.2875	4.2	(.5)	2.67	(.19)	3.12	(.20)
.3125	4.6	(.6)	3.48	(.22)	2.94	(.20)
.3375	4.5	(.6)	3.64	(.23)	3.35	(.21)
.3625	4.4	(.6)	4.56	(.25)	3.96	(.24)
.3875	5.6	(.8)	3.97	(.26)	4.67	(.24)
.4125	4.1	(.8)	4.72	(.27)	3.09	(.25)
.4375	6.9	(1.1)	5.49	(.31)	5.20	(.27)
.4625	6.3	(1.2)	5.41	(.32)	6.44	(.30)
.4875	11.1	(1.8)	6.86	(.37)	7.05	(.32)
.5125	13.6	(2.5)	8.5	(.4)	8.26	(.35)
.5375	15.3	(3.0)	7.9	(.4)	8.41	(.35)
.5675	11.7	(2.9)	9.5	(.5)	9.89	(.39)
.5875	9.0	(3.2)	9.0	(.5)	10.7	(.4)
.6125	8.2	(4.5)	6.7	(.5)	8.17	(.38)
.6375	---	---	2.27	(.39)	1.73	(.20)

TABLE II. 4

$$t = -0.35$$

(1-x)	68 GeV/c		116 GeV/c		176 GeV/c	
	σ	$\delta\sigma$	σ	$\delta\sigma$	σ	$\delta\sigma$
.0125	.35	(.10)	.23	(.05)	.056	(.030)
.0375	.51	(.13)	.31	(.05)	.44	(.08)
.0625	.56	(.14)	.56	(.08)	.36	(.06)
.0875	.73	(.17)	.77	(.09)	.51	(.09)
.1125	1.11	(.22)	.82	(.10)	.63	(.09)
.1375	1.20	(.25)	.86	(.10)	.91	(.11)
.1625	.98	(.22)	1.46	(.13)	.95	(.12)
.1875	1.79	(.33)	1.25	(.12)	1.08	(.12)
.2125	1.50	(.30)	1.51	(.13)	1.54	(.14)
.2375	1.61	(.35)	1.65	(.15)	2.12	(.17)
.2625	2.6	(.5)	1.84	(.15)	1.72	(.15)
.2875	2.8	(.6)	1.78	(.16)	2.13	(.17)
.3125	3.4	(.6)	2.33	(.18)	2.41	(.18)
.3375	3.5	(.7)	2.43	(.19)	2.59	(.18)
.3625	3.7	(.8)	3.48	(.23)	3.14	(.20)
.3875	2.7	(.8)	2.96	(.22)	3.87	(.22)
.4125	5.7	(1.3)	3.69	(.25)	2.57	(.23)
.4375	7.5	(1.8)	4.00	(.28)	4.09	(.24)
.4625	4.6	(1.5)	3.84	(.28)	5.03	(.27)
.4875	5.2	(1.8)	5.25	(.35)	5.65	(.29)
.5125	7.5	(2.8)	6.22	(.39)	6.11	(.28)
.5375	8.5	(3.4)	6.1	(.4)	7.30	(.34)
.5625	16.9	(5.9)	7.5	(.5)	7.24	(.34)
.5875	4.9	(3.4)	8.2	(.5)	7.76	(.35)
.6125	12.6	(5.6)	9.8	(.6)	10.2	(.4)
.6375	12.5	(10.2)	9.1	(.7)	10.5	(.4)
.6625	---	---	9.2	(.8)	9.3	(.4)

TABLE II. 5

 $t = -0.45$

(1-x)	68 GeV/c		116 GeV/c		176 GeV/c	
	σ	$\delta\sigma$	σ	$\delta\sigma$	σ	$\delta\sigma$
.0125	.09	(.06)	.084	(.032)	.08	(.04)
.0375	.25	(.09)	.34	(.06)	.19	(.05)
.0625	.94	(.21)	.33	(.06)	.32	(.07)
.0875	.70	(.19)	.55	(.08)	.45	(.08)
.1125	.73	(.20)	.51	(.08)	.55	(.08)
.1375	1.09	(.27)	.54	(.08)	.75	(.10)
.1625	.63	(.22)	.74	(.09)	.79	(.11)
.1875	1.30	(.32)	.90	(.11)	.86	(.10)
.2125	2.1	(.4)	1.16	(.12)	1.39	(.13)
.2375	2.3	(.5)	1.39	(.14)	1.01	(.12)
.2625	3.1	(.7)	1.46	(.14)	1.42	(.14)
.2875	1.4	(.5)	1.84	(.16)	1.99	(.16)
.3125	1.0	(.4)	2.01	(.17)	1.88	(.15)
.3375	2.5	(.8)	1.87	(.17)	2.07	(.16)
.3625	3.0	(1.0)	2.59	(.20)	3.00	(.20)
.3875	3.0	(1.2)	2.83	(.23)	3.39	(.20)
.4125	1.1	(.9)	3.28	(.25)	2.47	(.22)
.4375	8.4	(2.4)	3.16	(.26)	2.90	(.19)
.4625	5.4	(1.8)	4.03	(.31)	3.82	(.23)
.4875	4.4	(2.7)	4.10	(.32)	5.42	(.27)
.5125	12.3	(4.0)	4.32	(.35)	5.59	(.29)
.5375	2.2	(2.5)	5.5	(.4)	6.03	(.29)
.5625	26.2	(12.6)	6.6	(.5)	6.91	(.32)
.5875	7.2	(8.8)	8.0	(.6)	7.40	(.34)
.6125	29.2	(12.4)	8.3	(.7)	9.15	(.39)
.6375	13.5	(13.5)	7.4	(.7)	9.6	(.4)
.6625	---	---	11.1	(1.0)	11.5	(.5)
.6875	---	---	10.7	(1.1)	12.6	(.5)
.7125	---	---	6.8	(1.2)	7.3	(.5)
.7375	---	---	.27	(.36)	.75	(.19)

TABLE II.6

$$t = -0.55$$

(1-x)	68 GeV/c		116 GeV/c		176 GeV/c	
	σ	$\delta\sigma$	σ	$\delta\sigma$	σ	$\delta\sigma$
.0125	.05	(.04)	.063	(.026)	.04	(.04)
.0375	.05	(.05)	.155	(.039)	.18	(.05)
.0625	.20	(.11)	.23	(.06)	.11	(.04)
.0875	.59	(.18)	.25	(.05)	.21	(.05)
.1125	.70	(.24)	.49	(.08)	.44	(.08)
.1375	.75	(.25)	.41	(.07)	.46	(.08)
.1625	.68	(.24)	.67	(.09)	.52	(.08)
.1875	.60	(.25)	.61	(.09)	.58	(.09)
.2125	1.0	(.4)	1.01	(.12)	.90	(.10)
.2375	2.1	(.6)	1.06	(.13)	.95	(.11)
.2625	2.2	(.7)	1.06	(.13)	1.39	(.13)
.2875	1.6	(.6)	1.37	(.15)	1.30	(.13)
.3125	1.3	(.6)	1.61	(.16)	1.50	(.14)
.3375	2.9	(1.0)	1.57	(.16)	1.92	(.15)
.3625	3.9	(1.8)	1.92	(.18)	1.98	(.16)
.3875	1.6	(.9)	2.15	(.22)	2.15	(.16)
.4125	4.8	(2.4)	2.77	(.24)	1.85	(.19)
.4375	4.4	(2.8)	3.35	(.29)	2.51	(.18)
.4625	4.2	(2.6)	3.33	(.30)	3.55	(.22)
.4875	5.8	(6.4)	3.17	(.31)	4.13	(.24)
.5125	----	----	3.71	(.34)	3.81	(.23)
.5375	----	----	4.4	(.4)	5.01	(.27)
.5625	----	----	5.6	(.5)	5.52	(.29)
.5875	----	----	6.8	(.6)	5.27	(.29)
.6125	----	----	8.6	(.8)	7.58	(.37)
.6375	----	----	6.8	(.8)	8.38	(.39)
.6625	----	----	8.2	(1.0)	9.0	(.4)
.6875	----	----	10.6	(1.3)	10.8	(.5)
.7125	----	----	13.2	(1.7)	12.6	(.6)
.7375	----	----	9.7	(2.0)	11.4	(.7)
.7625	----	----	----	----	.86	(.34)

TABLE II. 7

 $t = -0.65$

(1-x)	68 GeV/c		116 GeV/c		176 GeV/c	
	σ	$\delta\sigma$	σ	$\delta\sigma$	σ	$\delta\sigma$
.0125	---	---	.050 (.025)		.017 (.025)	
.0375	.11 (.11)		.050 (.022)		.074 (.034)	
.0625	.18 (.11)		.15 (.04)		.122 (.038)	
.0875	.39 (.20)		.116 (.035)		.17 (.05)	
.1125	.34 (.17)		.27 (.07)		.19 (.05)	
.1375	.36 (.18)		.43 (.08)		.44 (.08)	
.1625	.67 (.37)		.33 (.06)		.44 (.07)	
.1875	1.2 (.4)		.40 (.08)		.54 (.09)	
.2125	.43 (.33)		.57 (.09)		.86 (.10)	
.2375	.9 (.4)		.74 (.10)		.89 (.10)	
.2625	.3 (.4)		.59 (.10)		.75 (.10)	
.2875	.7 (.5)		1.22 (.15)		1.10 (.11)	
.3125	1.7 (1.1)		1.27 (.15)		1.26 (.13)	
.3375	3.2 (1.6)		1.34 (.17)		1.49 (.13)	
.3625	2.6 (1.4)		1.34 (.17)		1.92 (.16)	
.3875	1.2 (1.6)		1.91 (.23)		2.06 (.16)	
.4125	2.3 (2.1)		2.00 (.23)		1.74 (.18)	
.4375	4.3 (3.0)		1.85 (.23)		2.45 (.18)	
.4675	4.0 (7.2)		2.53 (.29)		3.17 (.19)	
.4875	6.1 (6.1)		2.57 (.33)		3.17 (.21)	
.5125	---	---	4.0 (.4)		3.68 (.23)	
.5375	---	---	3.3 (.4)		4.50 (.26)	
.5625	---	---	5.1 (.6)		4.20 (.26)	
.5875	---	---	5.6 (.6)		4.54 (.29)	
.6125	---	---	7.4 (.9)		6.64 (.34)	
.6375	---	---	7.0 (.9)		7.54 (.39)	
.6625	---	---	8.9 (1.3)		8.66 (.4)	
.6875	---	---	7.7 (1.5)		9.37 (.5)	
.7125	---	---	8.3 (1.9)		10.2 (.5)	
.7375	---	---	11.2 (2.8)		12.7 (.7)	
.7625	---	---	---	---	10.2 (.8)	

TABLE II. 8

 $t = -0.75$

(1-x)	68 GeV/c		116 GeV/c		176 GeV/c	
	σ	$\delta\sigma$	σ	$\delta\sigma$	σ	$\delta\sigma$
.0125	---	---	.013 (.013)		---	---
.0375	---	---	.10 (.04)		.057 (.029)	
.0625	.15 (.15)		.11 (.03)		.016 (.015)	
.0875	.79 (.26)		.13 (.05)		.20 (.05)	
.1125	---	---	.25 (.06)		.25 (.06)	
.1375	.11 (.18)		.30 (.06)		.27 (.06)	
.1625	2.0 (1.1)		.11 (.04)		.35 (.07)	
.1875	1.3 (.5)		.26 (.07)		.49 (.08)	
.2125	.7 (.4)		.42 (.08)		.39 (.07)	
.2375	.41 (.36)		.56 (.10)		.61 (.09)	
.2625	1.2 (.9)		.68 (.11)		.93 (.11)	
.2875	2.3 (1.0)		.78 (.12)		.90 (.11)	
.3125	.5 (.8)		.72 (.12)		.82 (.10)	
.3375	---	---	1.02 (.14)		1.14 (.12)	
.3625	4.4 (4.4)		1.11 (.17)		1.64 (.14)	
.3875	---	---	1.45 (.20)		1.72 (.14)	
.4125	3.8 (5.7)		1.71 (.23)		1.40 (.16)	
.4375	---	---	2.02 (.26)		2.07 (.17)	
.4625	---	---	1.84 (.27)		1.94 (.16)	
.4875	---	---	2.25 (.33)		2.82 (.19)	
.5125	---	---	2.40 (.36)		3.06 (.22)	
.5375	---	---	2.58 (.39)		3.61 (.24)	
.5625	---	---	2.5 (.5)		4.20 (.26)	
.5875	---	---	4.3 (.7)		4.57 (.28)	
.6125	---	---	6.2 (.9)		5.74 (.34)	
.6375	---	---	5.7 (1.1)		5.87 (.36)	
.6625	---	---	6.5 (1.4)		6.7 (.4)	
.6875	---	---	4.4 (1.3)		7.4 (.5)	
.7125	---	---	7.8 (2.4)		7.9 (.5)	
.7375	---	---	7.4 (2.8)		11.3 (.7)	
.7625	---	---	---	---	10.8 (.8)	

TABLE II. 9

 $t = -0.85$

(1-x)	68 GeV/c		116 GeV/c		176 GeV/c	
	σ	$\delta\sigma$	σ	$\delta\sigma$	σ	$\delta\sigma$
.0125	---	---	.018 (.023)		.013 (.011)	
.0375	---	---	.045 (.024)		.009 (.015)	
.0625	---	---	.065 (.029)		.15 (.04)	
.0875	.9	(.5)	.075 (.038)		.15 (.05)	
.1125	.36	(.35)	.17 (.05)		.093 (.032)	
.1375	.22	(.12)	.19 (.05)		.085 (.034)	
.1625	.8	(1.0)	.21 (.06)		.23 (.05)	
.1875	1.3	(1.1)	.28 (.07)		.38 (.07)	
.2125	.8	(.5)	.41 (.08)		.33 (.06)	
.2375	1.0	(1.2)	.61 (.11)		.40 (.07)	
.2625	.9	(1.6)	.75 (.12)		.58 (.09)	
.2875	---	---	.78 (.14)		.70 (.10)	
.3125	---	---	1.04 (.16)		.62 (.08)	
.3375	4.2	(3.2)	1.00 (.16)		.97 (.11)	
.3625	---	---	1.24 (.19)		1.14 (.12)	
.3875	---	---	1.41 (.23)		1.83 (.15)	
.4125	---	---	1.12 (.20)		1.06 (.13)	
.4375	---	---	1.18 (.21)		1.31 (.14)	
.4625	---	---	1.81 (.28)		2.36 (.18)	
.4875	---	---	2.03 (.35)		2.54 (.19)	
.5125	---	---	2.8	(.5)	3.48 (.24)	
.5375	---	---	2.8	(.5)	3.08 (.23)	
.5625	---	---	4.0	(.6)	3.83 (.25)	
.5875	---	---	3.5	(.7)	4.01 (.28)	
.6125	---	---	5.1	(.9)	5.32 (.33)	
.6375	---	---	5.5	(1.3)	5.48 (.37)	
.6125	---	---	7.8	(1.7)	6.3	(.4)
.7125	---	---	6.2	(2.1)	8.0	(.5)
.7125	---	---	7.9	(2.9)	7.4	(.5)
.7375	---	---	9.5	(4.2)	8.9	(.6)
.7625	---	---	---	---	9.9	(.8)

TABLE II. 10

 $t = -0.95$

(1-x)	68 GeV/c		116 GeV/c		176 GeV/c	
	σ	$\delta\sigma$	σ	$\delta\sigma$	σ	$\delta\sigma$
.0125	----	----	----	----	----	----
.0375	----	----	.010 (.008)		.024 (.018)	
.0625	----	----	.045 (.025)		.051 (.031)	
.0875	----	----	.070 (.033)		----	----
.1125	----	----	.15 (.04)		.073 (.032)	
.1375	----	----	.21 (.05)		.20 (.05)	
.1625	----	----	.25 (.06)		.29 (.06)	
.1875	----	----	.15 (.06)		.22 (.06)	
.2125	----	----	.52 (.11)		.39 (.06)	
.2375	----	----	.31 (.08)		.30 (.06)	
.2625	----	----	.40 (.09)		.44 (.08)	
.2875	----	----	.40 (.10)		.47 (.07)	
.3125	----	----	.34 (.09)		.69 (.10)	
.3375	----	----	.92 (.18)		.66 (.09)	
.3625	----	----	1.10 (.19)		1.33 (.13)	
.3875	----	----	.62 (.17)		1.17 (.11)	
.4125	----	----	1.56 (.25)		.93 (.14)	
.4325	----	----	.78 (.20)		1.43 (.14)	
.4625	----	----	1.36 (.27)		1.86 (.16)	
.4875	----	----	1.34 (.30)		2.17 (.18)	
.5125	----	----	2.4 (.5)		2.05 (.18)	
.5375	----	----	2.0 (.4)		2.82 (.21)	
.5625	----	----	2.7 (.6)		2.98 (.25)	
.5875	----	----	4.7 (.9)		3.28 (.26)	
.6125	----	----	3.7 (.9)		3.83 (.29)	
.6375	----	----	4.6 (1.4)		4.68 (.35)	
.6625	----	----	3.0 (1.3)		5.58 (.40)	
.6875	----	----	8.6 (3.2)		5.5 (.4)	
.7125	----	----	1.8 (1.7)		6.9 (.6)	
.7375	----	----	2.6 (2.8)		7.0 (.6)	

TABLE II.11

t = -1.05

(1-x)	68 GeV/c		116 GeV/c		176 GeV/c	
	σ	$\delta\sigma$	σ	$\delta\sigma$	σ	$\delta\sigma$
.0125	----	----	----	----	.011	(.033)
.0375	----	----	.016	(.016)	.031	(.033)
.0625	----	----	.011	(.012)	.027	(.018)
.0875	----	----	.058	(.024)	.047	(.026)
.1125	----	----	.06	(.04)	.099	(.040)
.1375	----	----	.04	(.03)	.17	(.05)
.1625	----	----	.13	(.05)	.14	(.04)
.1875	----	----	.16	(.06)	.28	(.06)
.2125	----	----	.18	(.07)	.19	(.05)
.2375	----	----	.45	(.10)	.39	(.06)
.2625	----	----	.65	(.14)	.24	(.05)
.2875	----	----	.49	(.12)	.53	(.08)
.3125	----	----	.64	(.14)	.56	(.08)
.3375	----	----	.69	(.15)	.60	(.08)
.3625	----	----	.61	(.15)	.83	(.10)
.3875	----	----	.55	(.18)	1.08	(.11)
.4125	----	----	2.06	(.37)	.87	(.12)
.4375	----	----	.83	(.20)	1.24	(.13)
.4625	----	----	2.1	(.4)	1.57	(.15)
.4875	----	----	1.77	(.33)	2.47	(.19)
.5125	----	----	2.0	(.4)	1.74	(.18)
.5375	----	----	3.2	(.6)	2.46	(.20)
.5675	----	----	1.7	(.6)	2.18	(.20)
.5875	----	----	3.5	(1.0)	3.22	(.27)
.6125	----	----	3.4	(1.1)	3.73	(.32)
.6325	----	----	1.3	(.9)	3.71	(.31)
.6625	----	----	5.3	(2.2)	4.19	(.38)
.6875	----	----	4.6	(2.6)	5.4	(.5)
.7125	----	----	4.4	(3.8)	5.1	(.5)
.7125	----	----	9.6	(10.2)	7.2	(.7)

TABLE II. 12

t = -1.15

(1-x)	68 GeV/c		116 GeV/c		176 GeV/c	
	σ	$\delta\sigma$	σ	$\delta\sigma$	σ	$\delta\sigma$
.0125	---	---	.006 (.006)		---	---
.0375	---	---	.005 (.010)		---	---
.0625	---	---	---	---	---	---
.0875	---	---	.042 (.027)		.031 (.021)	
.1125	---	---	.055 (.033)		.066 (.026)	
.1375	---	---	.082 (.040)		.006 (.007)	
.1625	---	---	.17 (.06)		.097 (.032)	
.1875	---	---	.15 (.06)		.19 (.05)	
.2125	---	---	.51 (.12)		.23 (.05)	
.2375	---	---	.31 (.10)		.32 (.06)	
.2625	---	---	.34 (.10)		.34 (.06)	
.2875	---	---	.33 (.10)		.26 (.06)	
.3125	---	---	.33 (.10)		.45 (.07)	
.3375	---	---	.40 (.12)		.58 (.08)	
.3625	---	---	.91 (.19)		.85 (.10)	
.3875	---	---	.91 (.22)		.92 (.10)	
.4125	---	---	1.39 (.33)		.76 (.11)	
.4375	---	---	.48 (.19)		1.00 (.12)	
.4625	---	---	.83 (.24)		1.38 (.15)	
.4875	---	---	1.07 (.34)		1.46 (.15)	
.5125	---	---	2.0 (.5)		1.64 (.18)	
.5375	---	---	2.3 (.6)		1.98 (.19)	
.5625	---	---	1.8 (.6)		2.53 (.24)	
.5875	---	---	.9 (.5)		2.87 (.26)	
.6125	---	---	2.2 (1.0)		3.38 (.29)	
.6375	---	---	2.0 (1.1)		3.00 (.31)	
.6625	---	---	---	---	4.3 (.4)	
.6875	---	---	6.2 (4.3)		4.0 (.4)	
.7125	---	---	13.3 (8.3)		5.1 (.6)	
.7375	---	---	---	---	6.0 (.7)	

TABLE II. 13

 $t = -1.25$

(1-x)	68 GeV/c		116 GeV/c		176 GeV/c	
	σ	$\delta\sigma$	σ	$\delta\sigma$	σ	$\delta\sigma$
.0125	---	---	---	---	---	---
.0375	---	---	---	---	---	---
.0625	---	---	---	---	.037	(.025)
.0875	---	---	---	---	.027	(.018)
.1125	---	---	.063	(.035)	.054	(.028)
.1375	---	---	.05	(.05)	.072	(.030)
.1625	---	---	.09	(.05)	.057	(.022)
.1875	---	---	---	---	.17	(.06)
.2125	---	---	.13	(.05)	.21	(.05)
.2375	---	---	.05	(.04)	.21	(.05)
.2625	---	---	.13	(.07)	.21	(.05)
.2875	---	---	.41	(.12)	.25	(.06)
.3125	---	---	.40	(.12)	.43	(.08)
.3375	---	---	.62	(.20)	.47	(.08)
.3625	---	---	.69	(.18)	.80	(.10)
.3875	---	---	.61	(.17)	.85	(.11)
.4125	---	---	.50	(.16)	.58	(.11)
.4375	---	---	.96	(.27)	.84	(.11)
.4625	---	---	.98	(.31)	1.06	(.13)
.4875	---	---	.87	(.30)	1.56	(.16)
.5125	---	---	.88	(.35)	1.65	(.18)
.5375	---	---	1.1	(.5)	1.75	(.19)
.5625	---	---	1.9	(.7)	1.87	(.19)
.5875	---	---	2.3	(1.2)	2.36	(.26)
.6125	---	---	---	---	3.07	(.30)
.6375	---	---	3.0	(2.4)	2.89	(.32)
.6625	---	---	---	---	3.98	(.40)
.6876	---	---	---	---	3.7	(.4)
.7125	---	---	---	---	4.7	(.6)
.7375	---	---	---	---	4.3	(.6)

TABLE II. 14

 $t = -1.35$

(1-x)	68 GeV/c		116 GeV/c		176 GeV/c	
	σ	$\delta\sigma$	σ	$\delta\sigma$	σ	$\delta\sigma$
.0125	---	---	---	---	---	---
.0375	---	---	---	---	.026	(.013)
.0625	---	---	---	---	.011	(.038)
.0875	---	---	---	---	.025	(.031)
.1125	---	---	.05	(.04)	.059	(.034)
.1375	---	---	.07	(.05)	.076	(.026)
.1625	---	---	.06	(.05)	.068	(.028)
.1875	---	---	.20	(.07)	.22	(.05)
.2125	---	---	.17	(.06)	.147	(.040)
.2375	---	---	.16	(.07)	.26	(.06)
.2625	---	---	.11	(.07)	.23	(.05)
.2875	---	---	.17	(.08)	.42	(.07)
.3125	---	---	.31	(.10)	.31	(.07)
.3375	---	---	.24	(.12)	.36	(.07)
.3625	---	---	.79	(.20)	.52	(.08)
.3875	---	---	.29	(.15)	.91	(.11)
.4125	---	---	.91	(.27)	.45	(.10)
.4375	---	---	.39	(.18)	.64	(.10)
.4625	---	---	1.7	(.4)	.84	(.11)
.4875	---	---	1.2	(.4)	1.46	(.16)
.5125	---	---	1.5	(.6)	1.57	(.18)
.5375	---	---	1.2	(.5)	2.13	(.21)
.5625	---	---	2.4	(1.1)	1.81	(.22)
.5875	---	---	3.8	(1.7)	1.95	(.24)
.6125	---	---	1.1	(1.1)	2.08	(.23)
.6375	---	---	2.7	(3.7)	2.43	(.34)
.6875	---	---	8.7	(5.8)	2.94	(.36)
.7125	---	---	---	---	2.74	(.37)
.7375	---	---	23.4	(15.6)	3.8	(.6)
.7625	---	---	---	---	4.3	(.7)

TABLE II. 15

t = -1.45

(1-x)	68 GeV/c		116 GeV/c		176 GeV/c	
	σ	$\delta\sigma$	σ	$\delta\sigma$	σ	$\delta\sigma$
.0125	---	---	---	---	---	---
.0375	---	---	---	---	---	---
.0625	---	---	---	---	---	---
.0875	---	---	---	---	---	---
.1125	---	---	.027	(.027)	---	---
.1375	---	---	.021	(.023)	.045	(.031)
.1625	---	---	.09	(.04)	.039	(.024)
.1875	---	---	.13	(.07)	.14	(.05)
.2125	---	---	.04	(.04)	.065	(.031)
.2375	---	---	.14	(.06)	.134	(.035)
.2625	---	---	.13	(.10)	.122	(.037)
.2875	---	---	.56	(.16)	.23	(.05)
.3125	---	---	.14	(.09)	.21	(.05)
.3375	---	---	.45	(.15)	.32	(.07)
.3625	---	---	.38	(.15)	.55	(.08)
.3875	---	---	1.01	(.28)	.74	(.10)
.4125	---	---	.32	(.18)	.37	(.09)
.4375	---	---	1.02	(.35)	.72	(.11)
.4625	---	---	.71	(.35)	1.19	(.16)
.4875	---	---	.60	(.32)	.84	(.12)
.5125	---	---	.25	(.26)	1.20	(.17)
.5375	---	---	1.7	(1.1)	1.78	(.21)
.5625	---	---	2.1	(1.3)	1.98	(.23)
.5875	---	---	1.3	(1.4)	1.55	(.21)
.6125	---	---	2.9	(1.9)	2.36	(.29)
.6375	---	---	---	---	2.64	(.31)
.6675	---	---	---	---	3.7	(.5)

TABLE III

Effective Regge Trajectories

$$\alpha_E(s, t) \text{ for } 0.7 < x < 0.975$$

t	68 GeV/c			116 GeV/c			176 GeV/c		
	α	($\delta\alpha$)	χ^2/DF	α	($\delta\alpha$)	χ^2/DF	α	($\delta\alpha$)	χ^2/DF
-0.05	0.329(.016)		16/11	0.351(.013)		36/11	0.325(.016)		35/11
-0.15	0.227(.026)		40/11	0.231(.020)		11/11	0.162(.024)		44/11
-0.25	0.107(.037)		12/11	0.124(.027)		17/11	0.029(.030)		18/11
-0.35	0.079(.064)		9/11	0.078(.031)		10/11	-.066(.042)		23/11
-0.45	0.037(.067)		23/11	-.039(.049)		22/11	-.057(.046)		18/11
-0.55	-.225(.105)		10/11	-.104(.054)		11/11	-.240(.060)		15/11
-0.65	0.022(.175)		4/9	-.227(.070)		18/11	-.238(.064)		11/11
-0.75	0.470(.177)		7/7	-.218(.121)		34/11	-.627(.127)		13/7
-0.85				-.418(.121)		6/11	-.469(.118)		20/10
-0.95				-.299(.078)		13/11	-.244(.097)		8/10
-1.05				-.898(.194)		10/9	-.316(.108)		14/10
-1.15				-.459(.160)		8/9	-.399(.140)		6/8
-1.25				0.012(.340)		11/6	-.447(.166)		6/10
-1.35				-.066(.288)		4/8	-.557(.202)		11/9
-1.45							-.691(.333)		5/7

Figure 1. Direct and Cross Channels for $A + B \rightarrow C + D$.

Figure 2. Contour C with Regge Poles and a Branch Cut.

Figure 3. Contour C'.

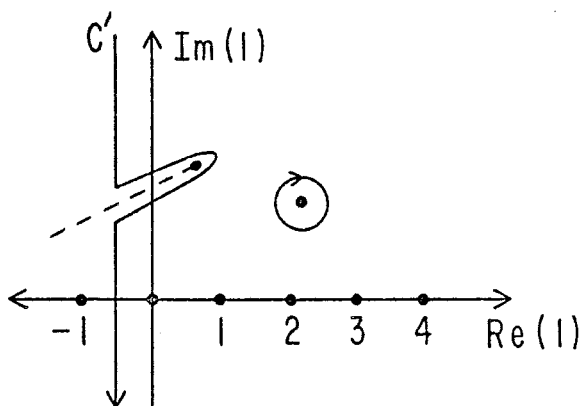
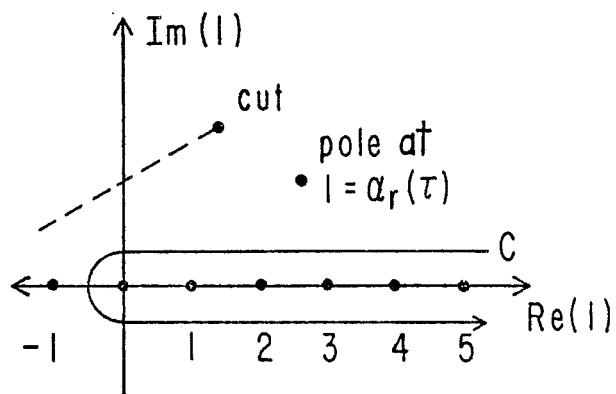
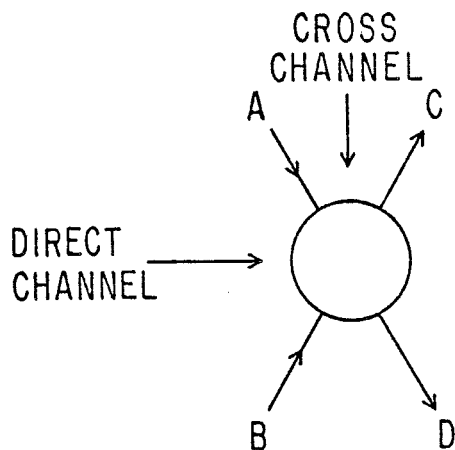
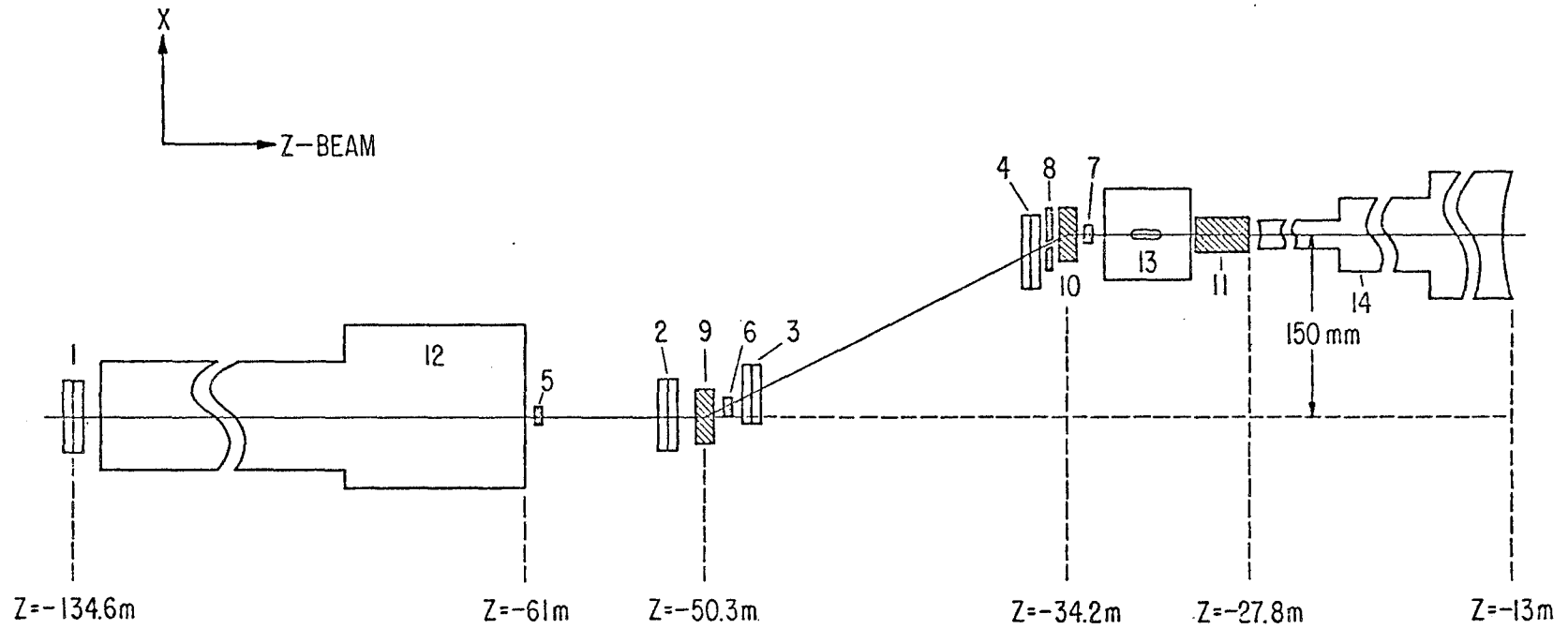


Figure 4. Beam Spectrometer.

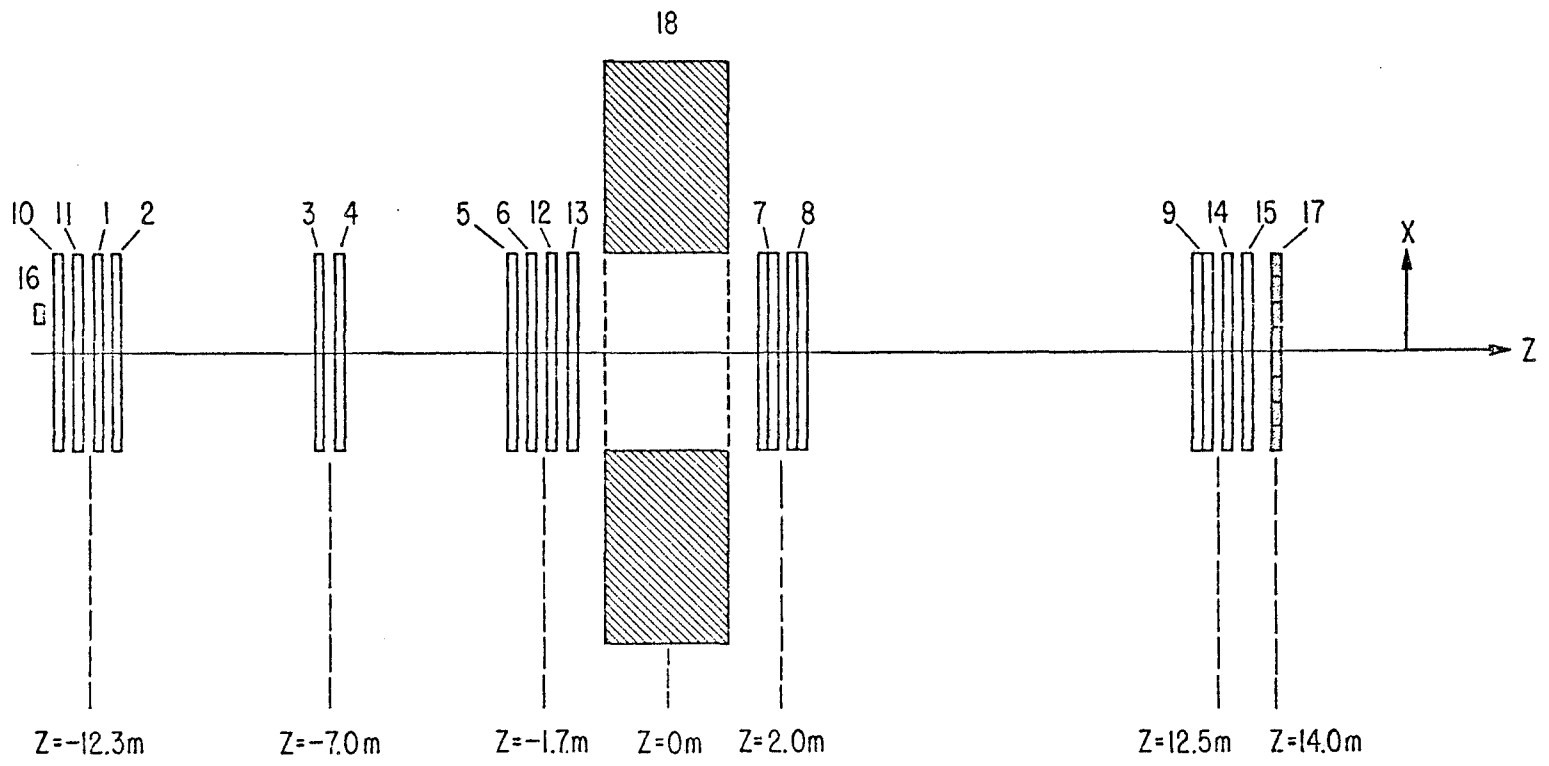
1-4	(X, Y) proportional wire chambers
5	B1 counter
6	B2 counter
7	B3 counter
8	Halo counter
9, 10	EPB magnets
11	Sweeping magnet
12	Cherenkov counter
13	Hydrogen target
14	Vacuum decay pipe



BEAM SPECTROMETER (Plan View)

Figure 5. Forward Spectrometer.

1-6	Small (X, Y) spark chambers
7-9	Large (X, Y, U, V) spark chambers
10, 11	(U, V) proportional wire chamber
12, 13	(X, Y) proportional wire chamber
14, 15	(X, Y) proportional wire chamber
16	B5 counter
17	I-counters
18	Analysis magnet



FORWARD SPECTROMETER (Plan View)

Figures 6.1 - 6.8. Differential Cross-Sections ($d^2\sigma/dxdt$) for the
68 GeV/c ($s = 136 \text{ GeV}^2$) Data.

The straight line is the best fit of the data to

$$\frac{d^2\sigma}{dx dt} = F(t) \frac{1 - 2\alpha_E(s, t)}{\cos^2\left(\frac{\pi}{2} \alpha_E(s, t)\right)}$$

with the constraint:

$$N_E = \left(\int_{x(\text{low})}^{x(\text{high})} dx \frac{d^2\sigma}{dx dt} \right) (t(\text{high}) - t(\text{low})) NL\rho$$

where N_E : Number of events within the (x, t) range of this fit;

$NL\rho$: Number of protons per cm^2 in the target on the figure;

$A(t)$: Average value of $\alpha_E(t)$ in the range:

Figure 6.1: $-0.1 < t < 0.0 \text{ (GeV/c)}^2$

Figure 6.2: $-0.2 < t < -0.1 \text{ (GeV/c)}^2$

Figure 6.3: $-0.3 < t < -0.2 \text{ (GeV/c)}^2$

Figure 6.4: $-0.4 < t < -0.3 \text{ (GeV/c)}^2$

Figure 6.5: $-0.5 < t < -0.4 \text{ (GeV/c)}^2$

Figure 6.6: $-0.6 < t < -0.5 \text{ (GeV/c)}^2$

Figure 6.7: $-0.7 < t < -0.6 \text{ (GeV/c)}^2$

Figure 6.8: $-0.8 < t < -0.7 \text{ (GeV/c)}^2$

Figure 6.1: $-0.1 < t < 0.0$ (GeV/c)²

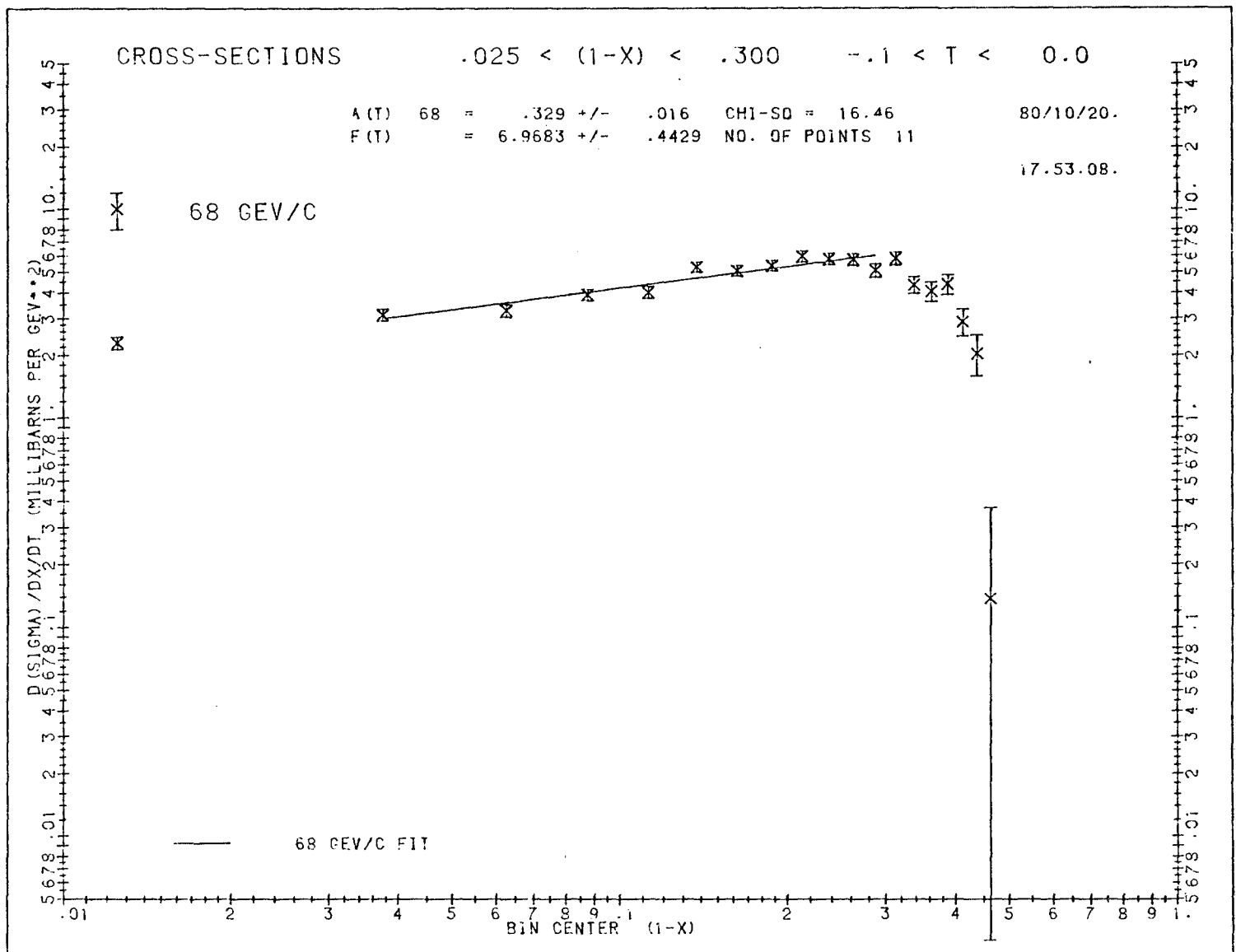


Figure 6.2: $-0.2 < t < -0.1$ (GeV/c)²

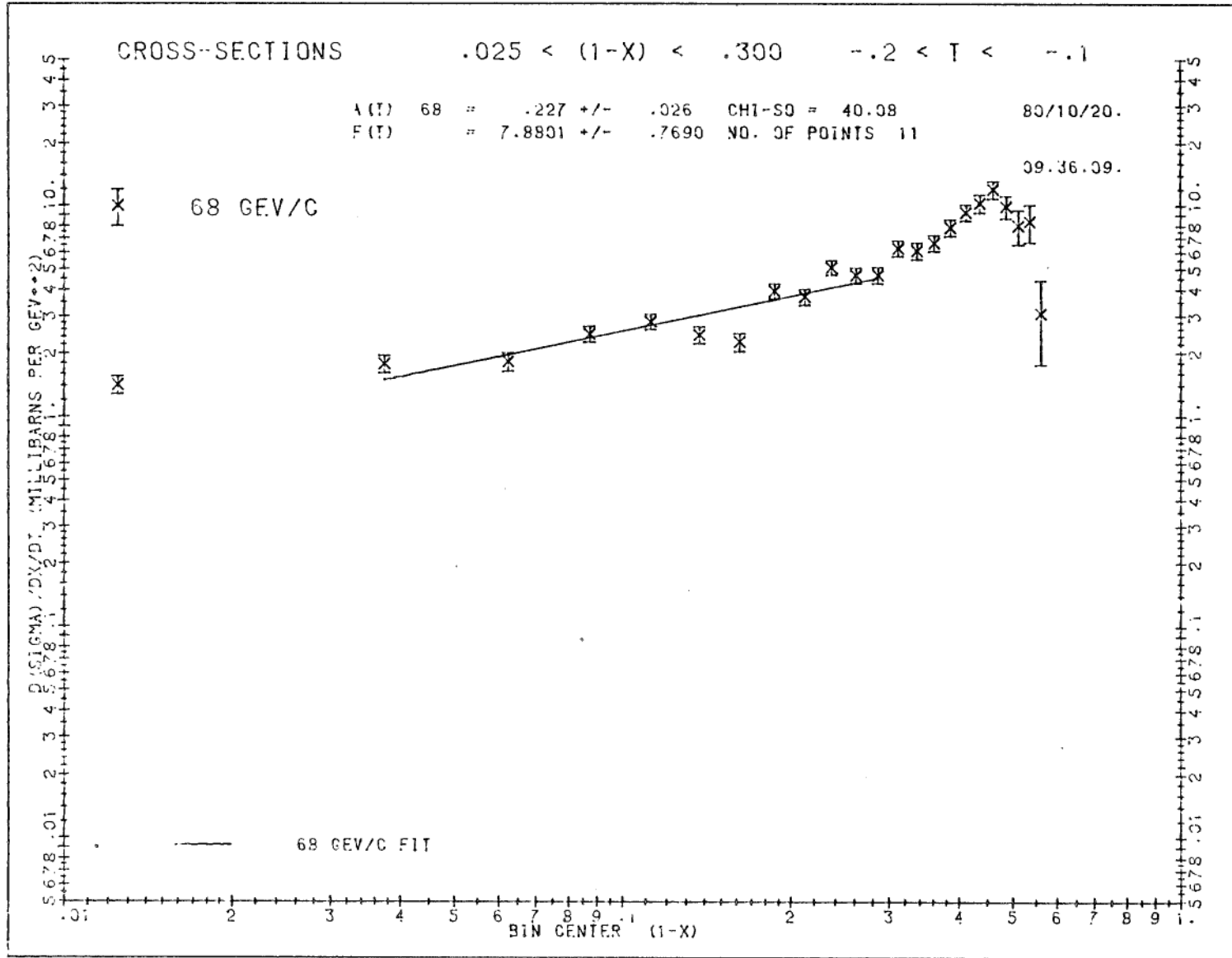


Figure 6.3: $-0.3 < t < -0.2$ (GeV/c)²

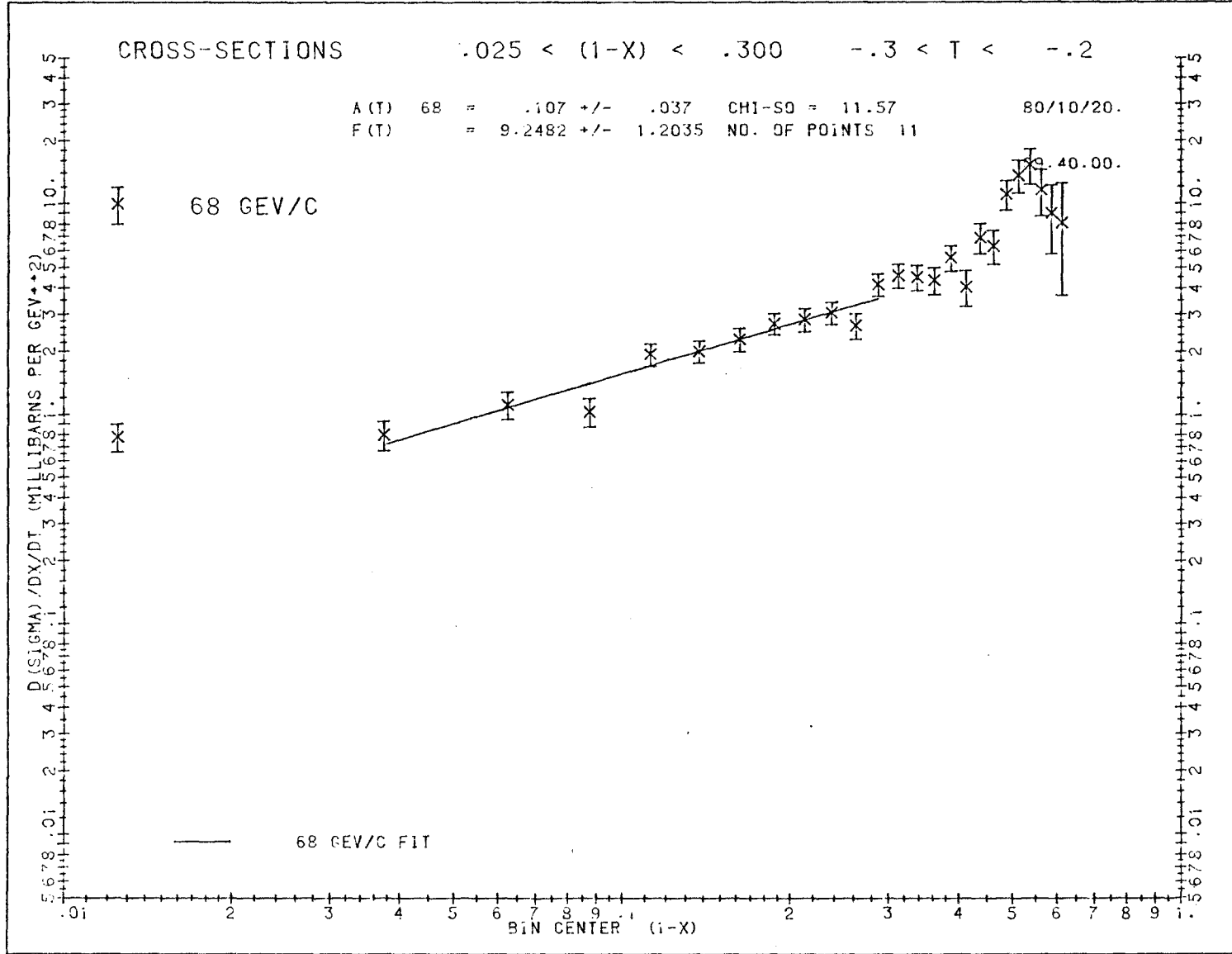


Figure 6.4: $-0.4 < t < -0.3$ (GeV/c)²

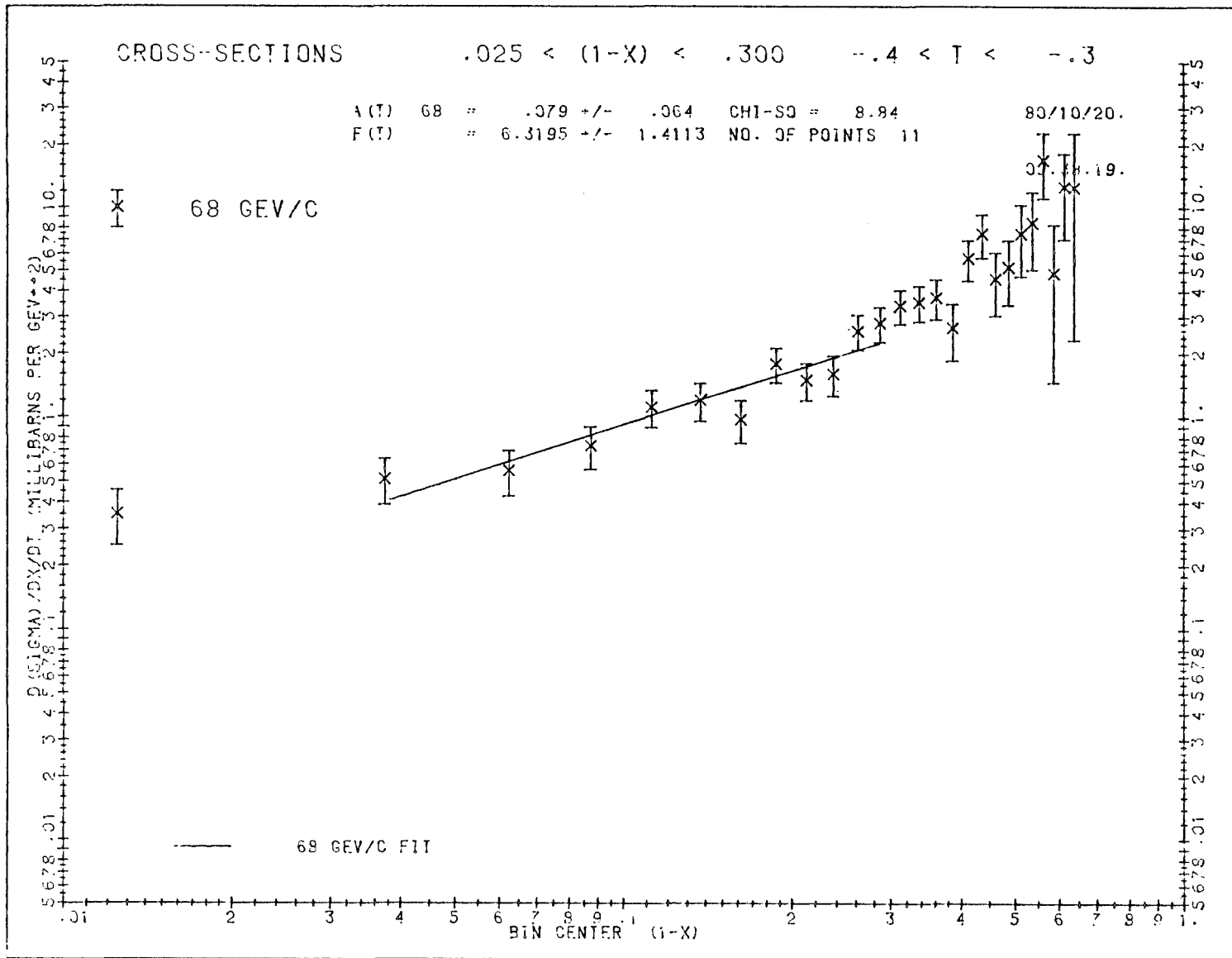
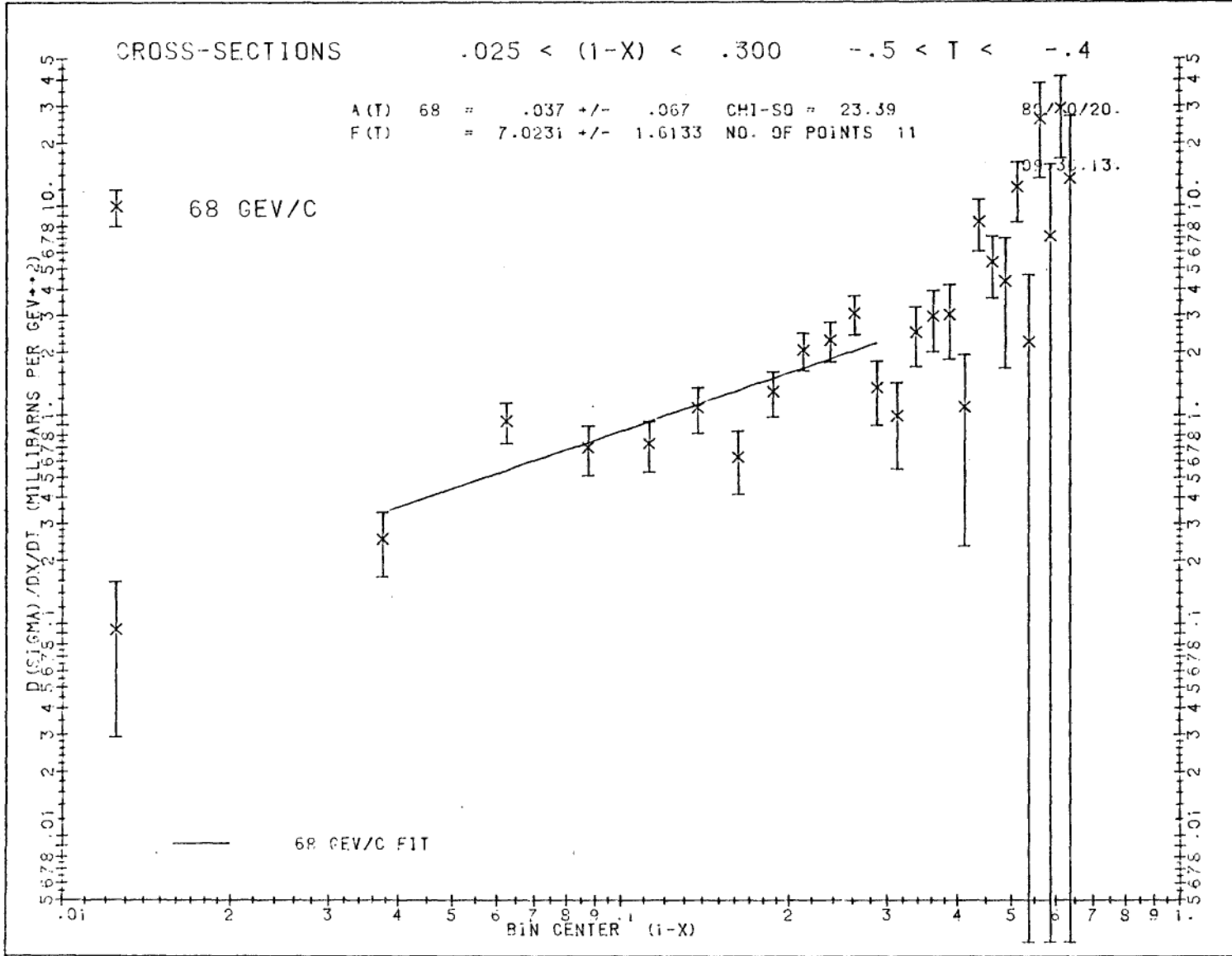


Figure 6.5: $-0.5 < t < -0.4$ (GeV/c)²



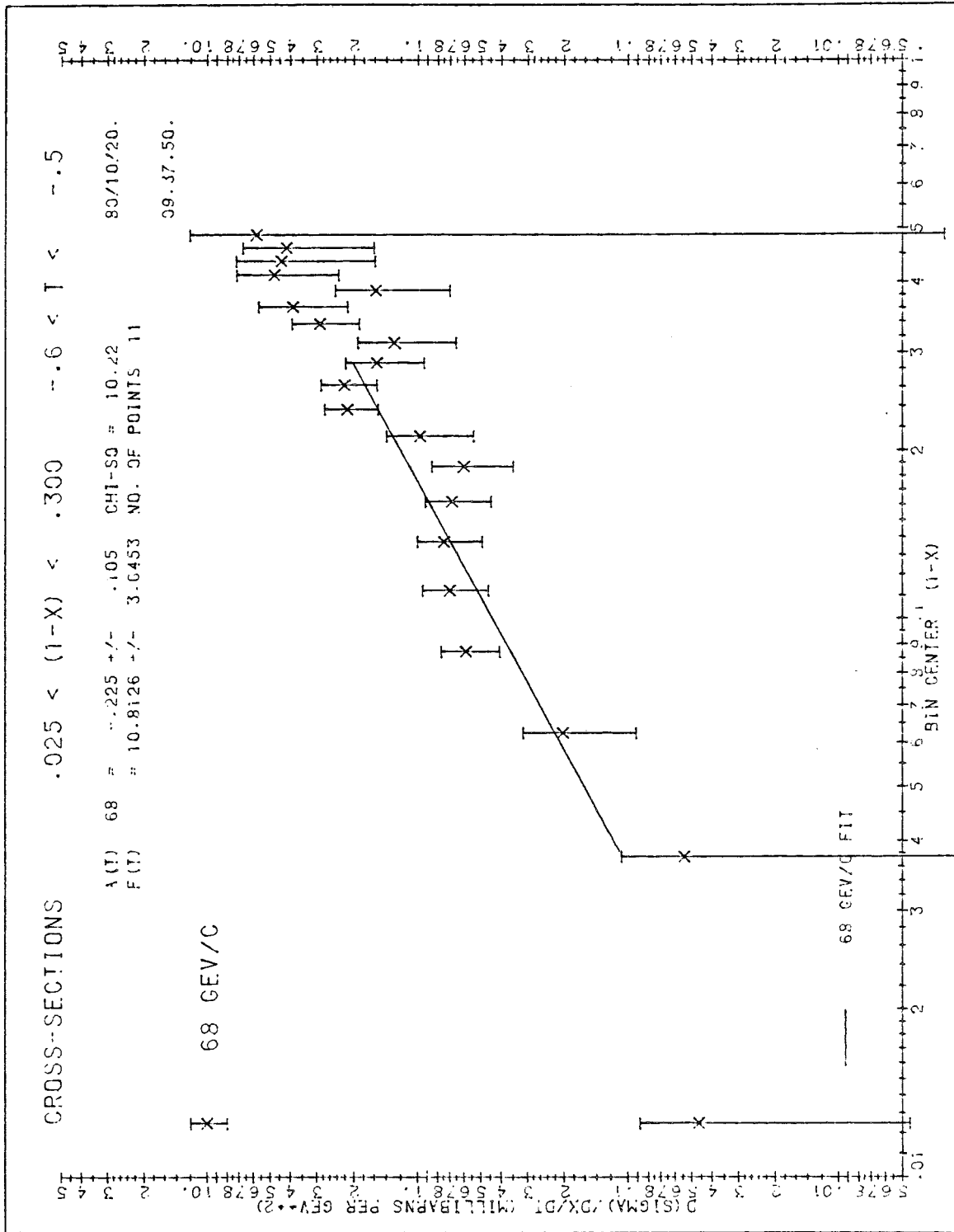
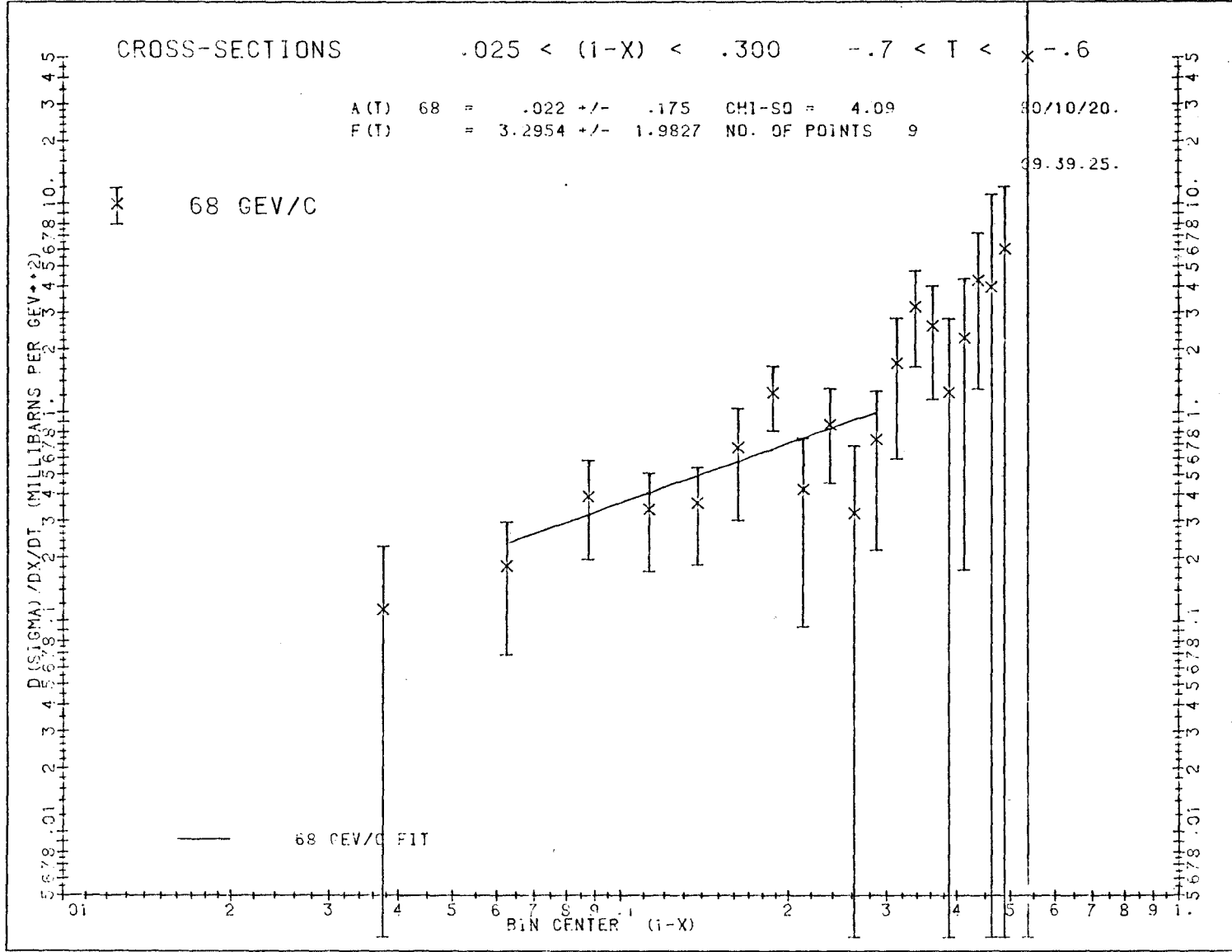


Figure 6.6: $-0.6 < t < -0.5$ (GeV/c)²

Figure 6.7: $-0.7 < t < -0.6$ (GeV/c)²



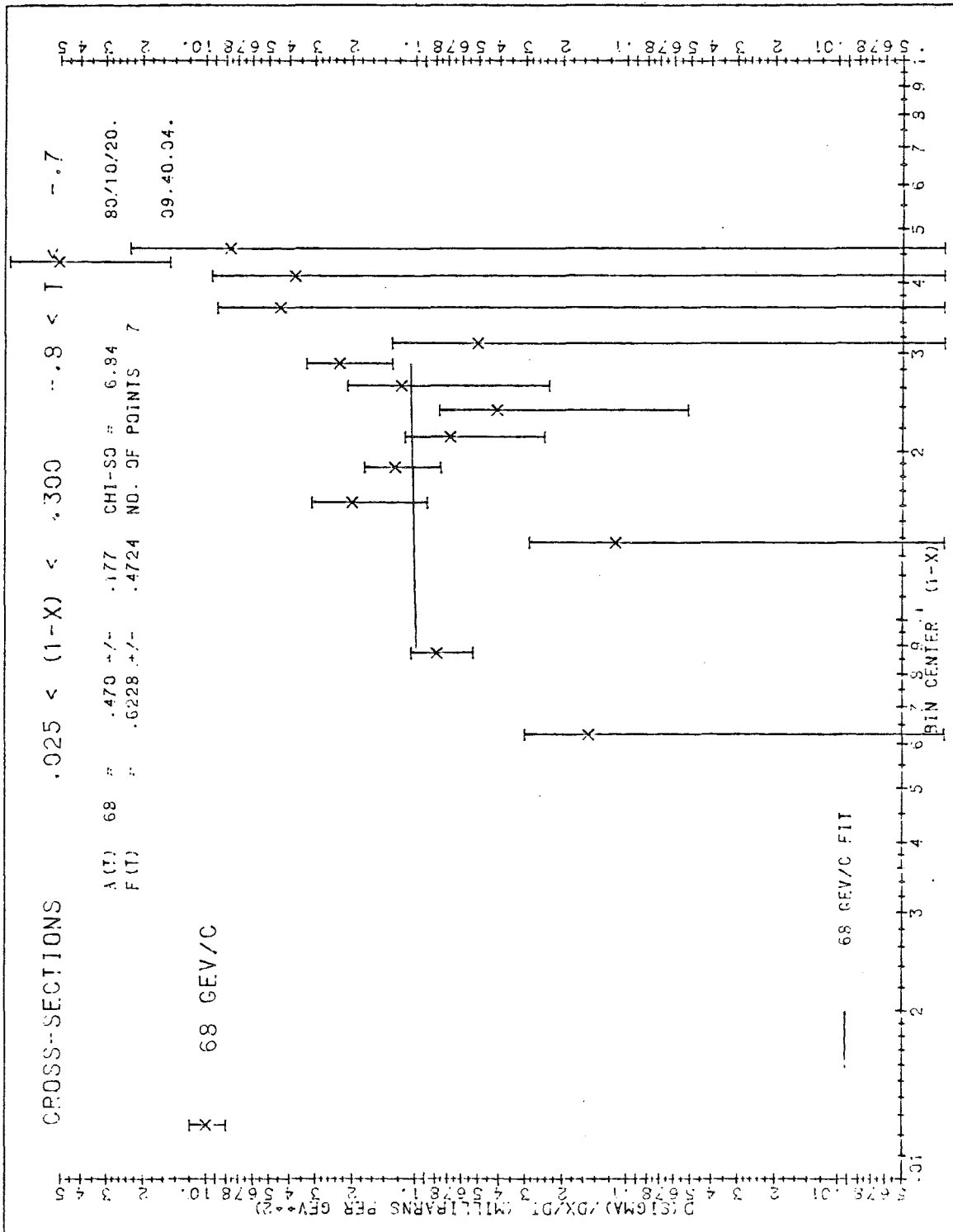


Figure 6.8: $-0.8 < t < -0.7$ (GeV/c)²

Figures 6.9 - 6.21. Cross-Sections ($d^2\sigma/dxdt$) for the 116 GeV/c
Data ($s = 232 \text{ GeV}^2$) of this Experiment.

The straight line is the best fit of the data to

$$\frac{d^2\sigma}{dx dt} = F(t) \frac{1 - 2\alpha_E(t)}{\cos^2\left(\frac{\pi}{2} \alpha_E(t)\right)}$$

with the constraint

$$N_E = \left(\int_{x(\text{low})}^{x(\text{high})} dx \frac{d^2\sigma}{dx dt} \right) (t(\text{high}) - t(\text{low})) NL\rho$$

where N_E : Number of events within the (x, t) range of this fit

$NL\rho$: Number of protons per cm^2 in the target on the figure

$A(t)$: Average value of $\alpha_E(t)$ in the range:

Figure 6.9: $-0.1 < t < 0.0 \text{ (GeV/c)}^2$

Figure 6.10: $-0.2 < t < -0.1 \text{ (GeV/c)}^2$

Figure 6.11: $-0.3 < t < -0.2 \text{ (GeV/c)}^2$

Figure 6.12: $-0.4 < t < -0.3 \text{ (GeV/c)}^2$

Figure 6.13: $-0.5 < t < -0.4 \text{ (GeV/c)}^2$

Figure 6.14: $-0.6 < t < -0.5 \text{ (GeV/c)}^2$

Figure 6.15: $-0.7 < t < -0.6 \text{ (GeV/c)}^2$

Figure 6.16: $-0.8 < t < -0.7 \text{ (GeV/c)}^2$

Figure 6.17: $-0.9 < t < -0.8 \text{ (GeV/c)}^2$

Figure 6.18: $-1.0 < t < -0.9 \text{ (GeV/c)}^2$

Figure 6.19: $-1.1 < t < -1.0 \text{ (GeV/c)}^2$

Figure 6.20: $-1.2 < t < -1.1 \text{ (GeV/c)}^2$

Figure 6.21: $-1.3 < t < -1.2 \text{ (GeV/c)}^2$

Figure 6.9: $-0.1 < t < 0.0$ (GeV/c)²

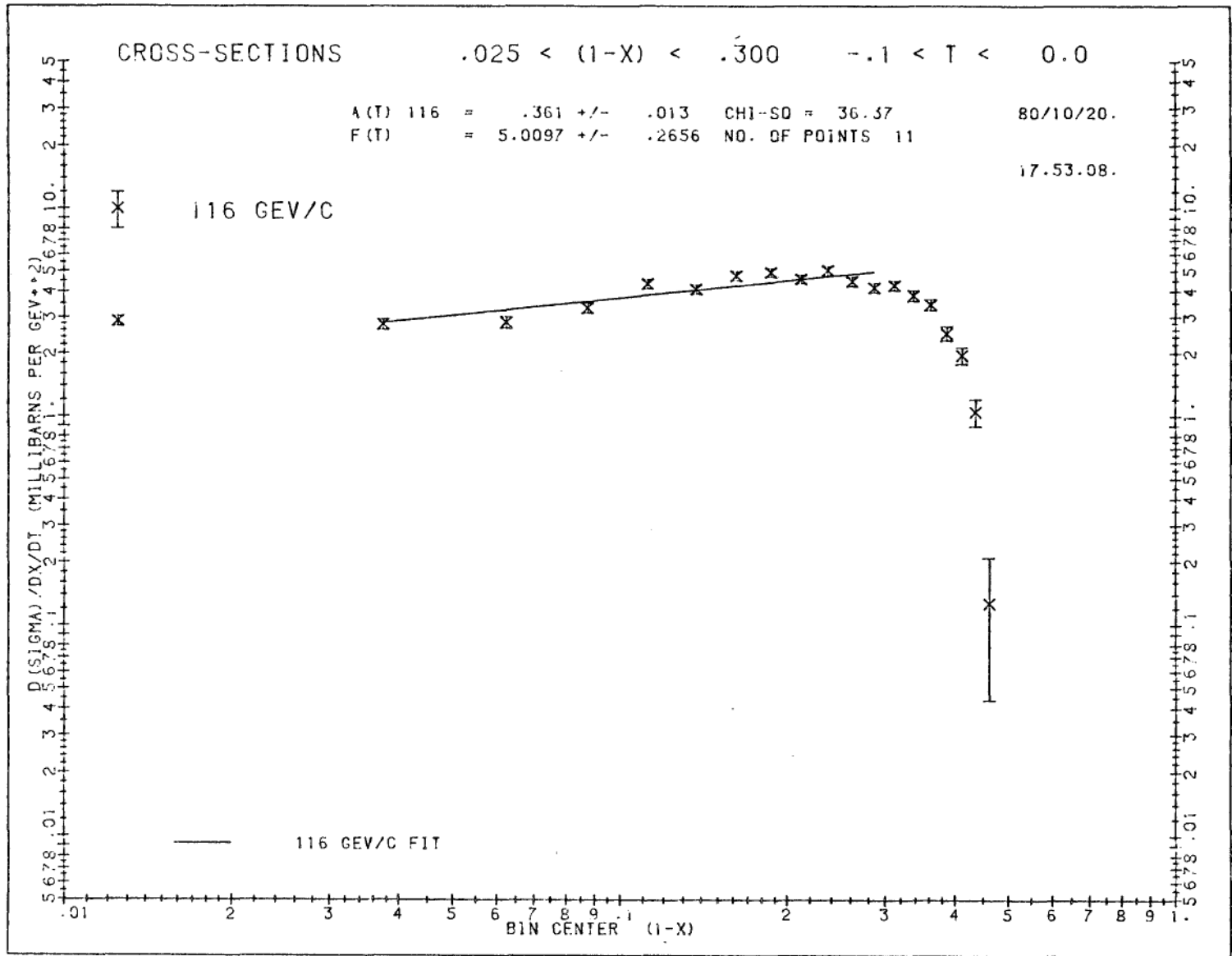


Figure 6. 10: $-0.2 < t < -0.1$ (GeV/c)²

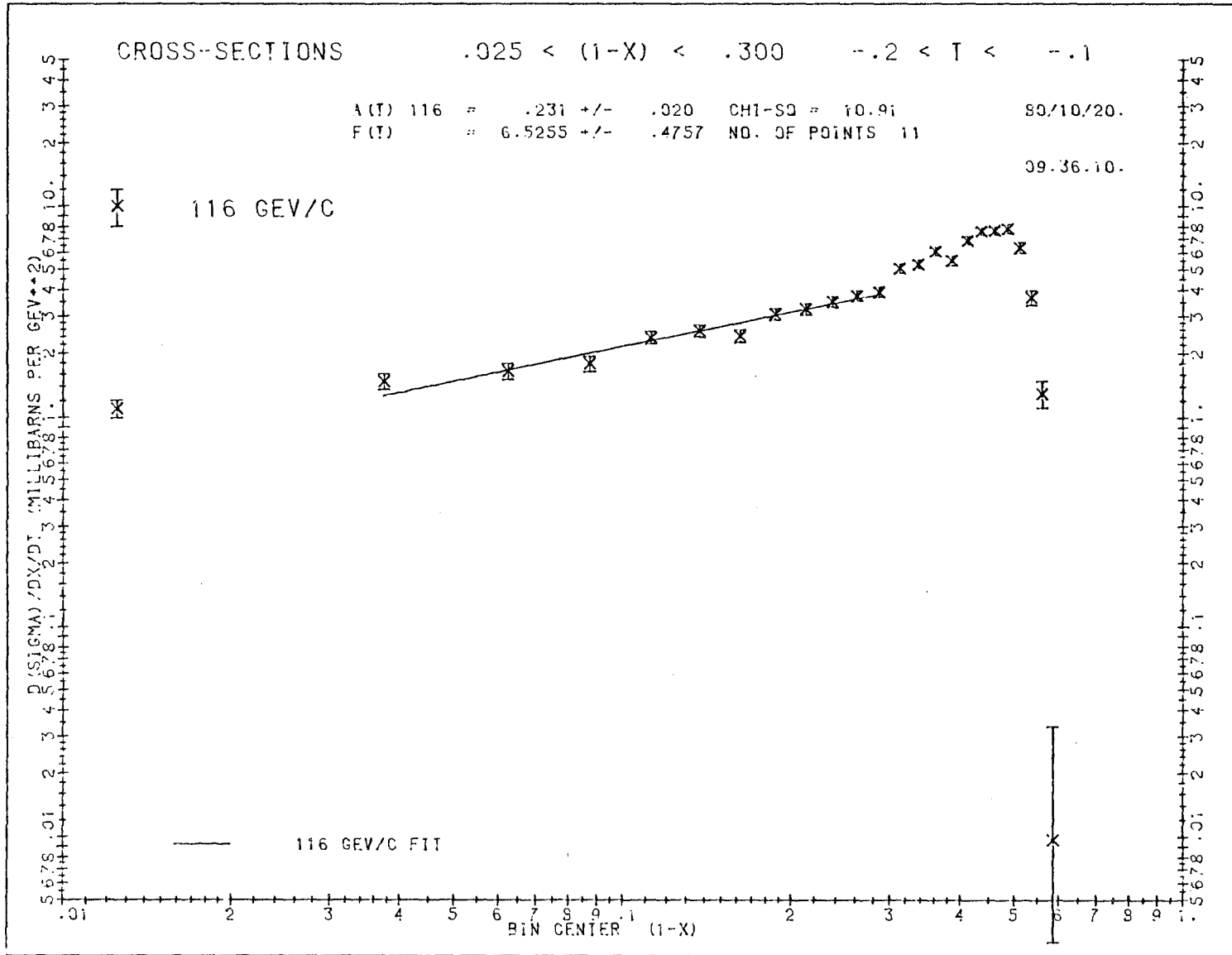


Figure 6.11: $-0.3 < t < -0.2$ (GeV/c)²

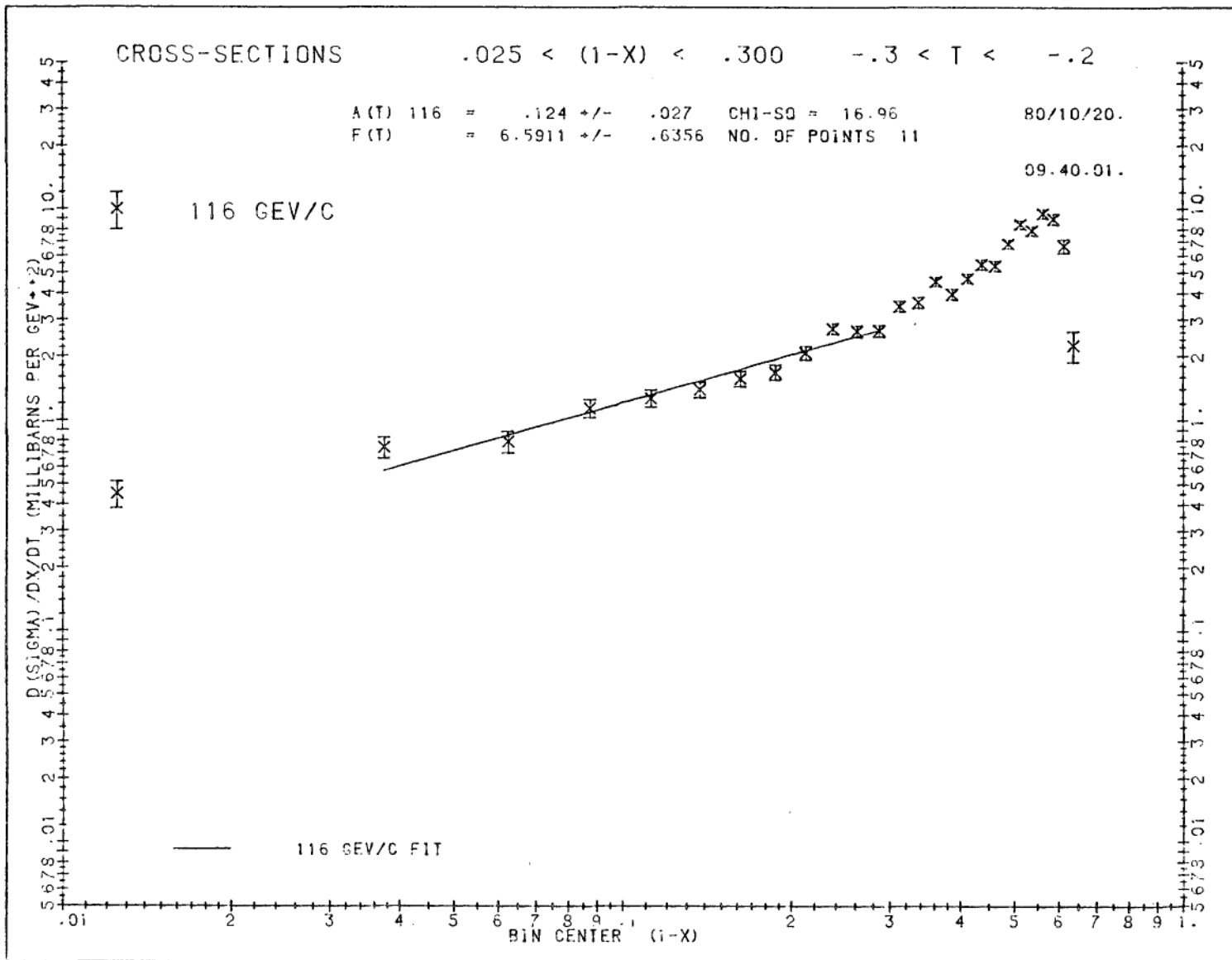


Figure 6.12: $-0.4 < t < -0.3$ (GeV/c)²

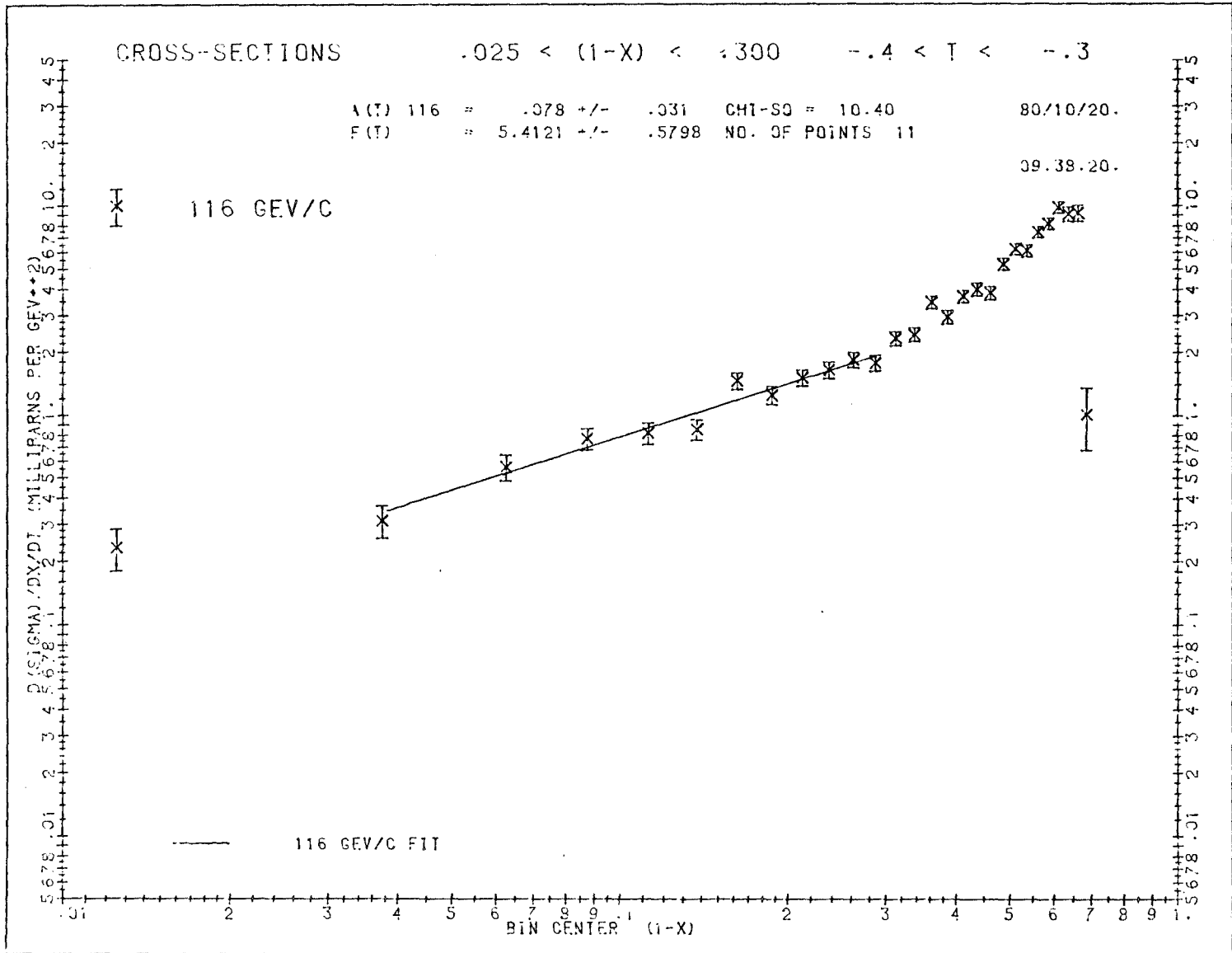
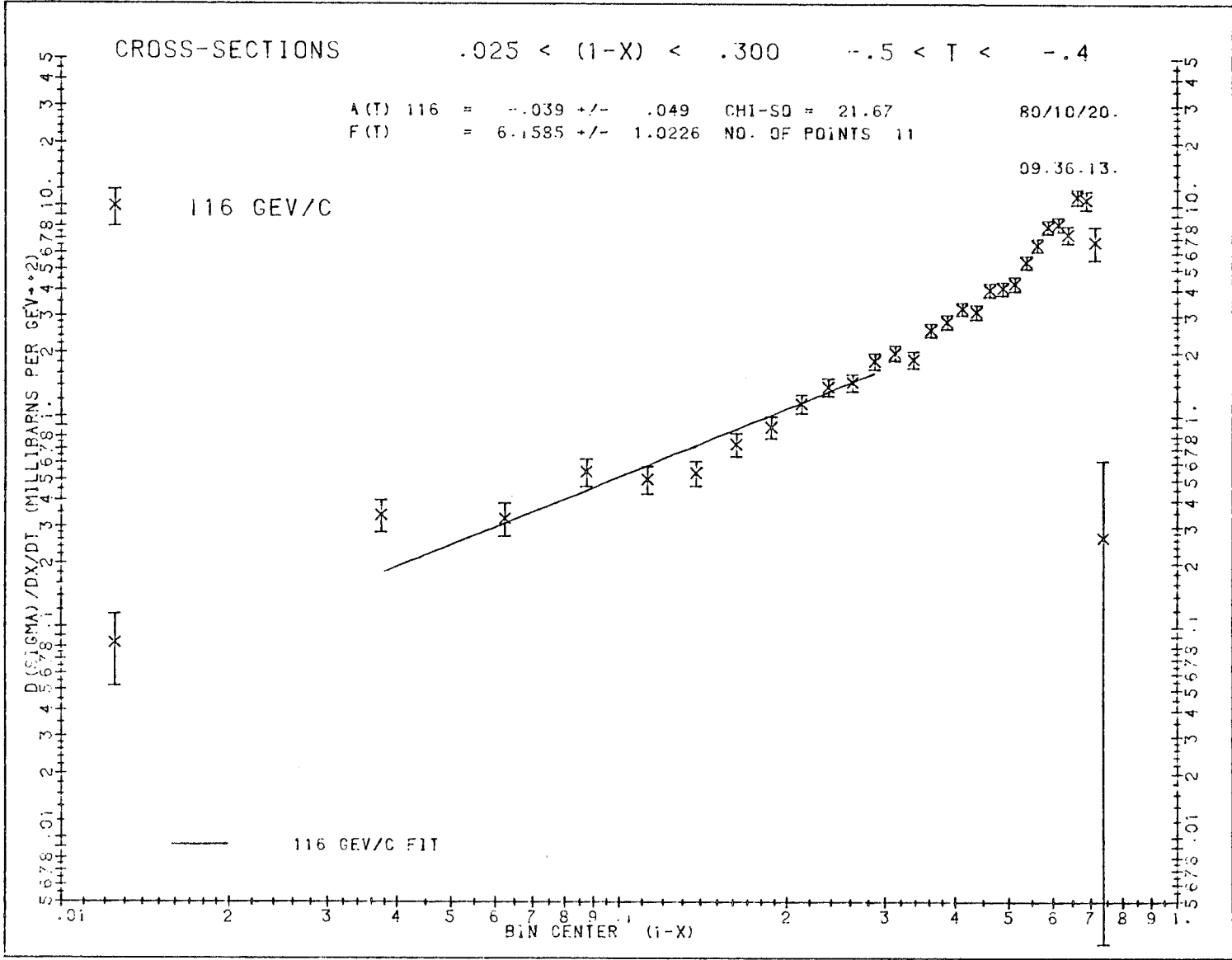


Figure 6.13: $-0.5 < t < -0.4$ (GeV/c)²



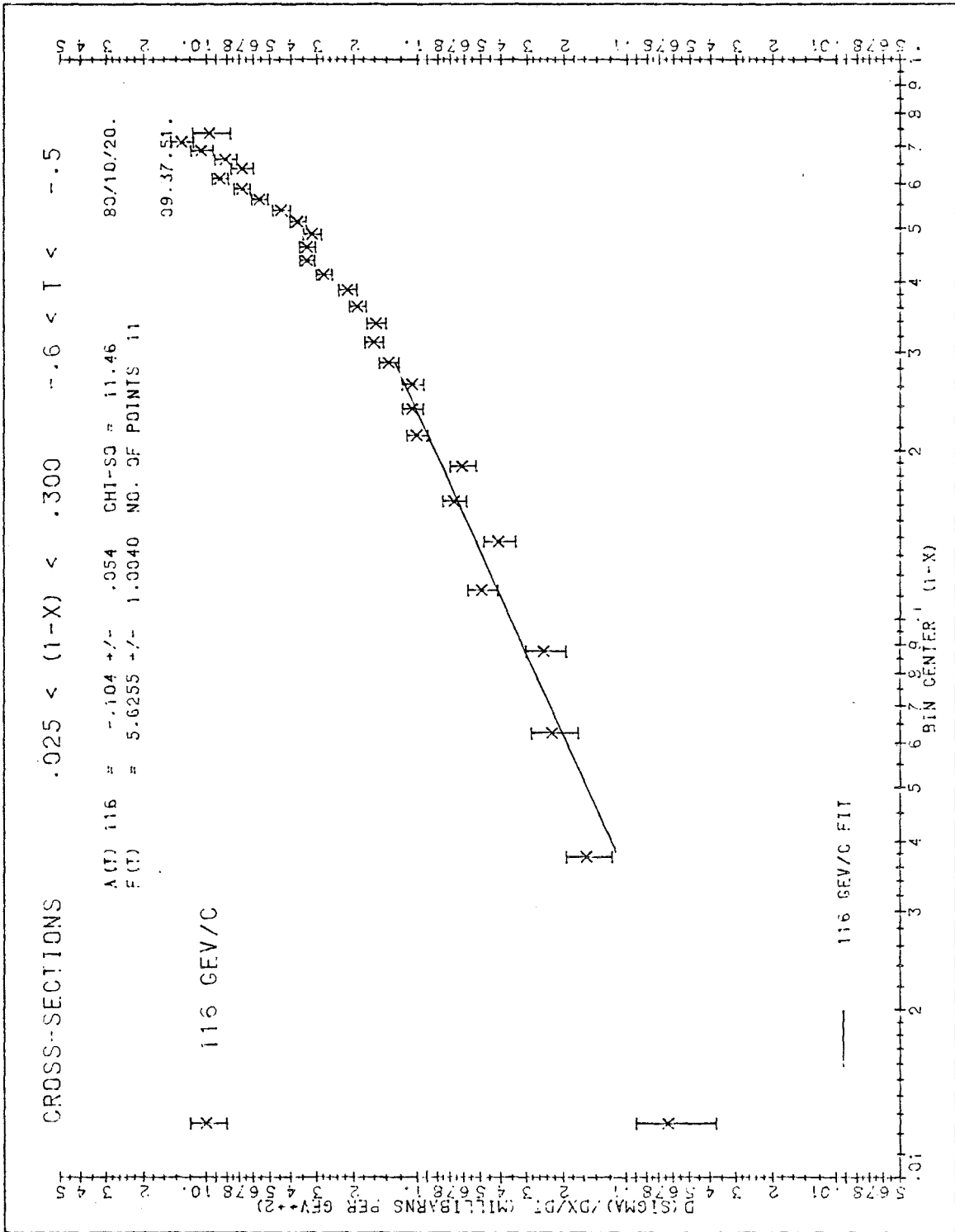


Figure 6.14: $-0.6 < t < -0.5$ (GeV/c)²

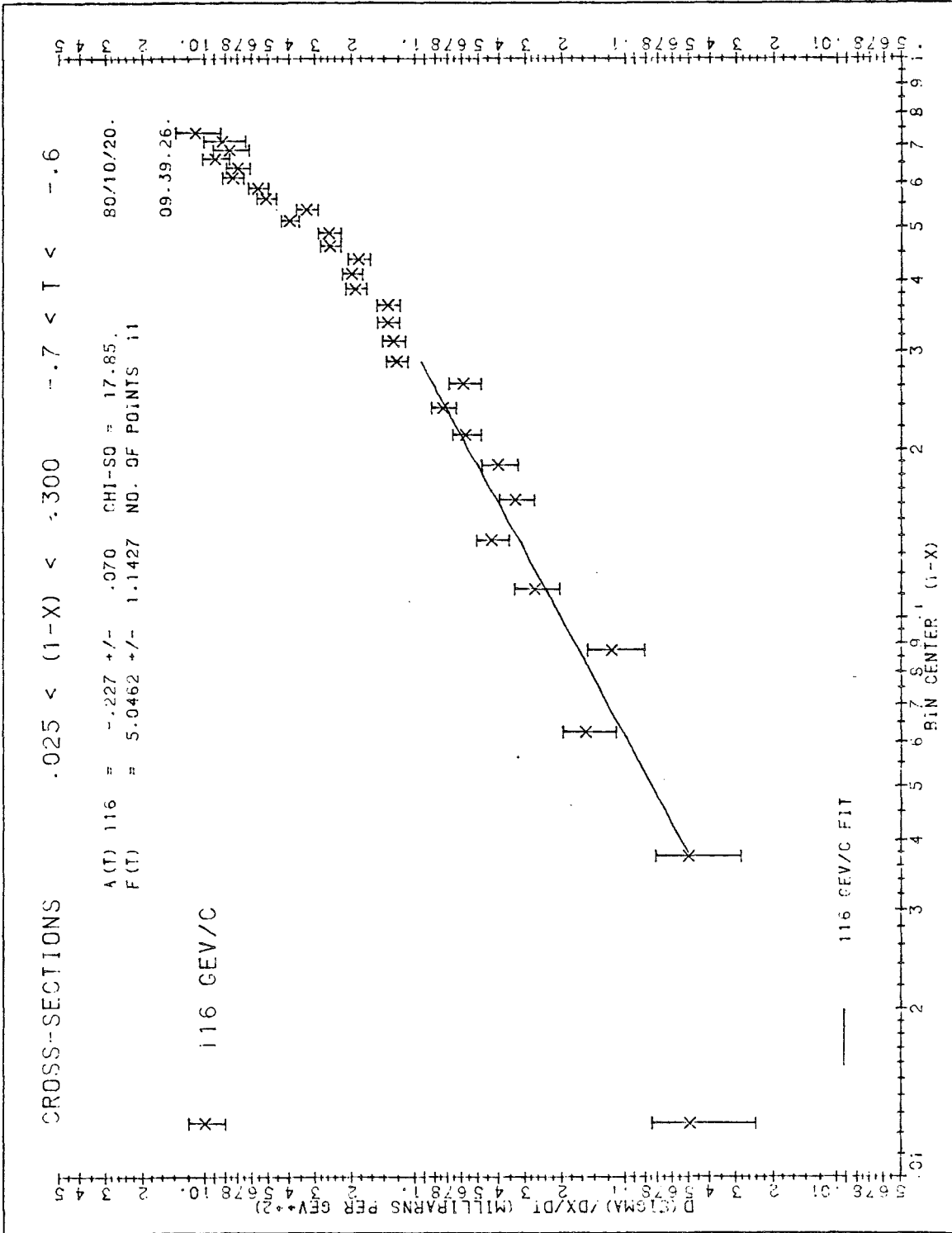


Figure 6.15: $-0.7 < t < -0.6$ (GeV/c)²

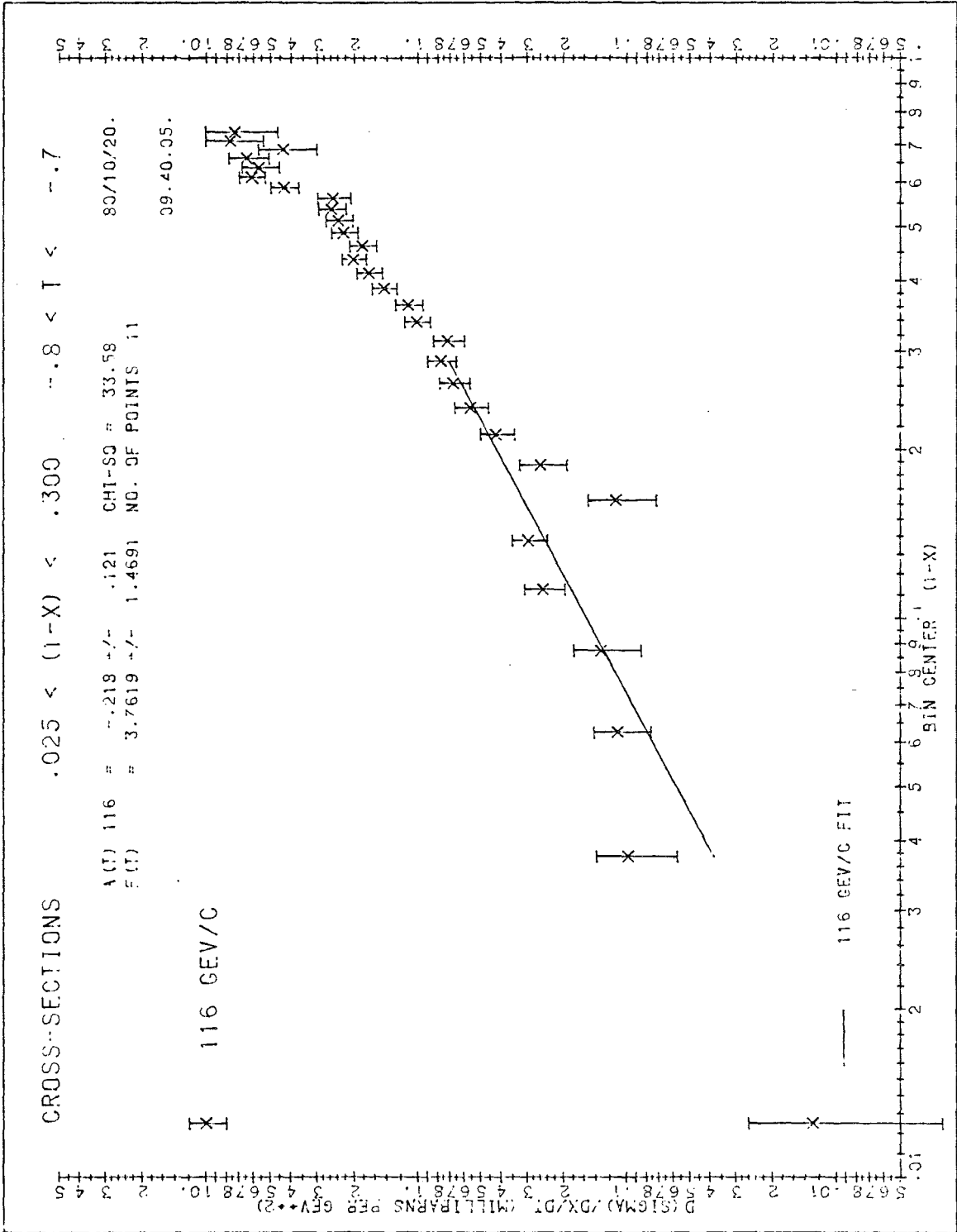


Figure 6.16: $-0.8 < t < -0.7$ (GeV/c)²

Figure 6.17: $-0.9 < t < -0.8$ (GeV/c)²

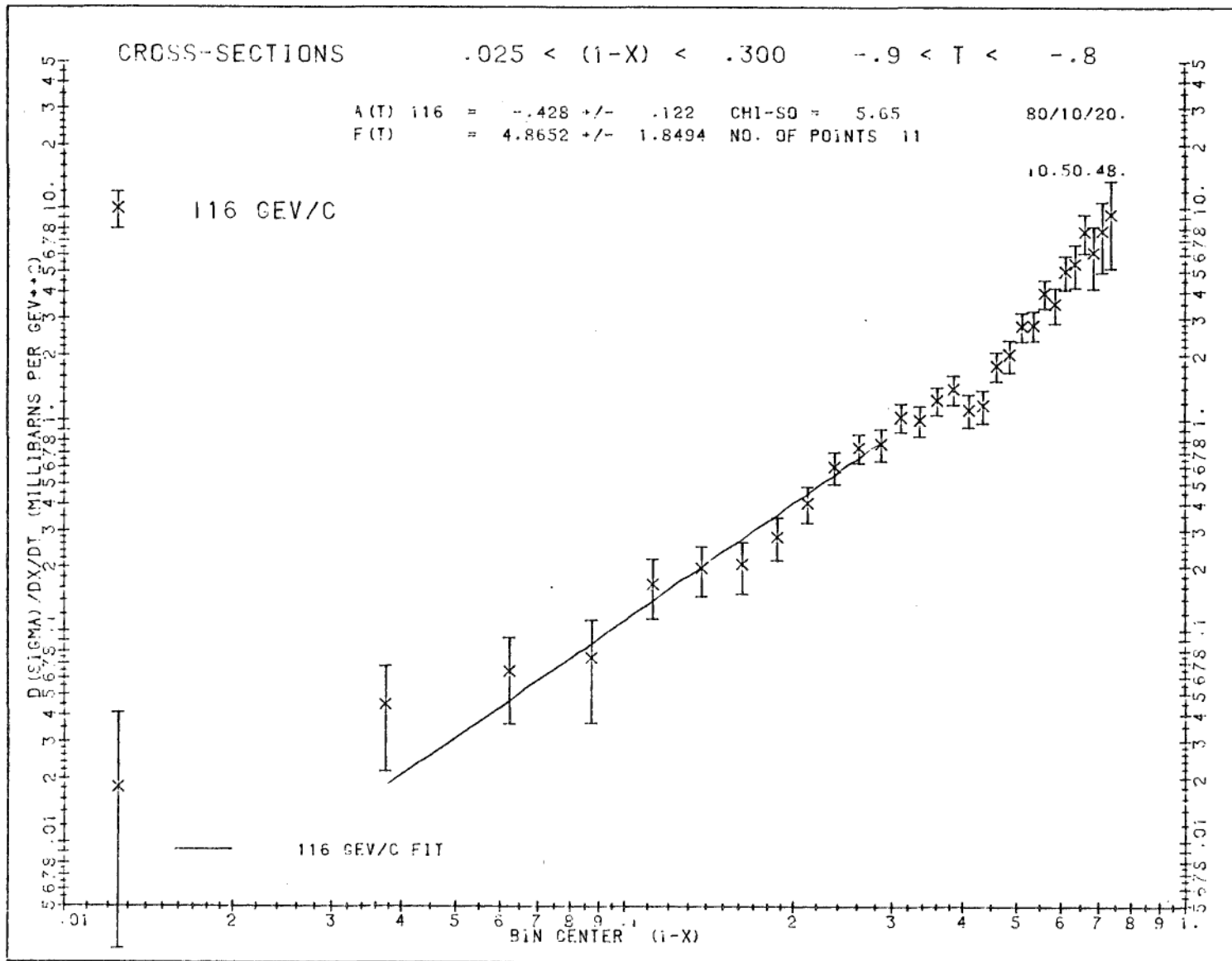


Figure 6.18: $-1.0 < t < -0.9$ (GeV/c)²

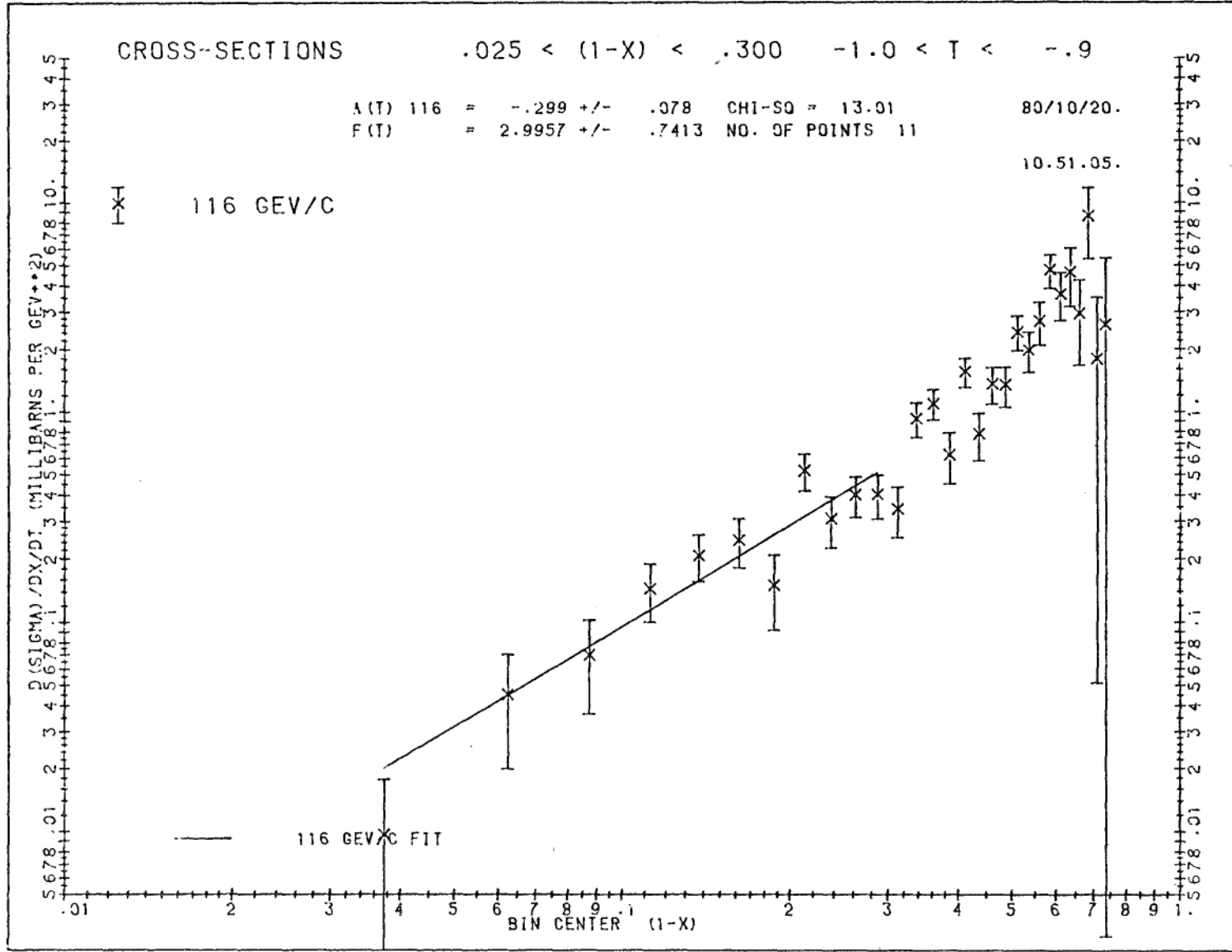


Figure 6.19: $-1.1 < t < -1.0$ (GeV/c)²

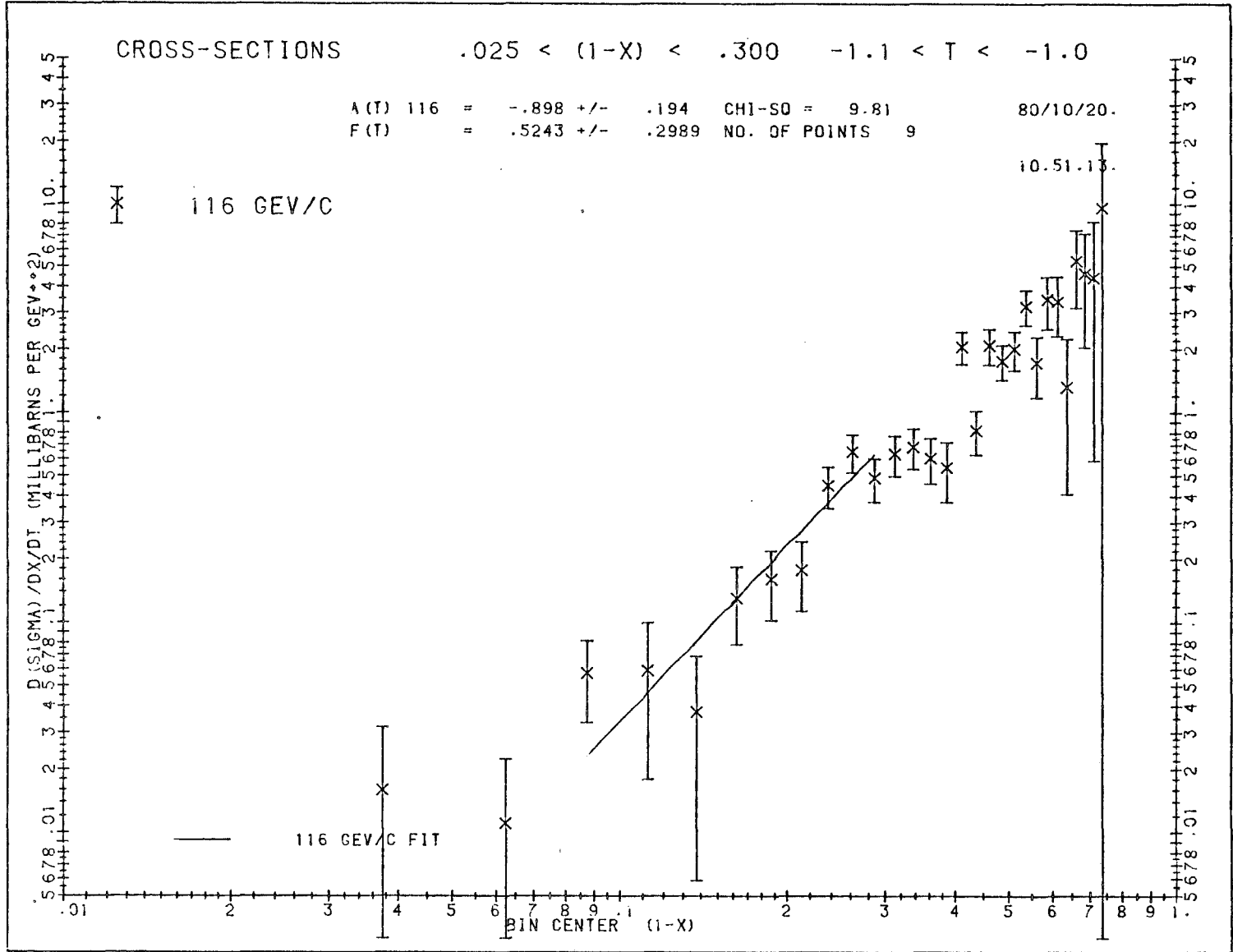


Figure 6.20: $-1.2 < t < -1.1$ (GeV/c)²

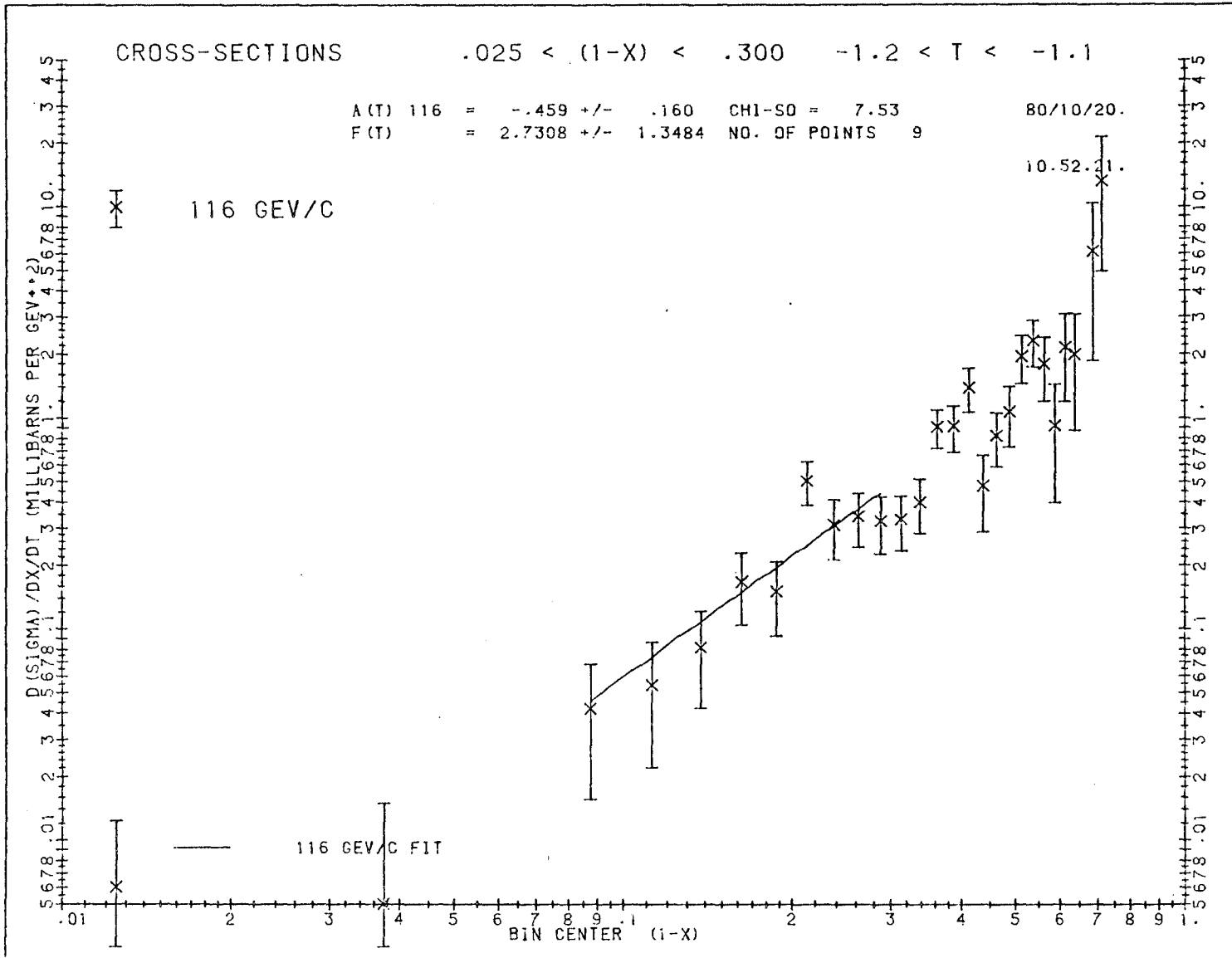
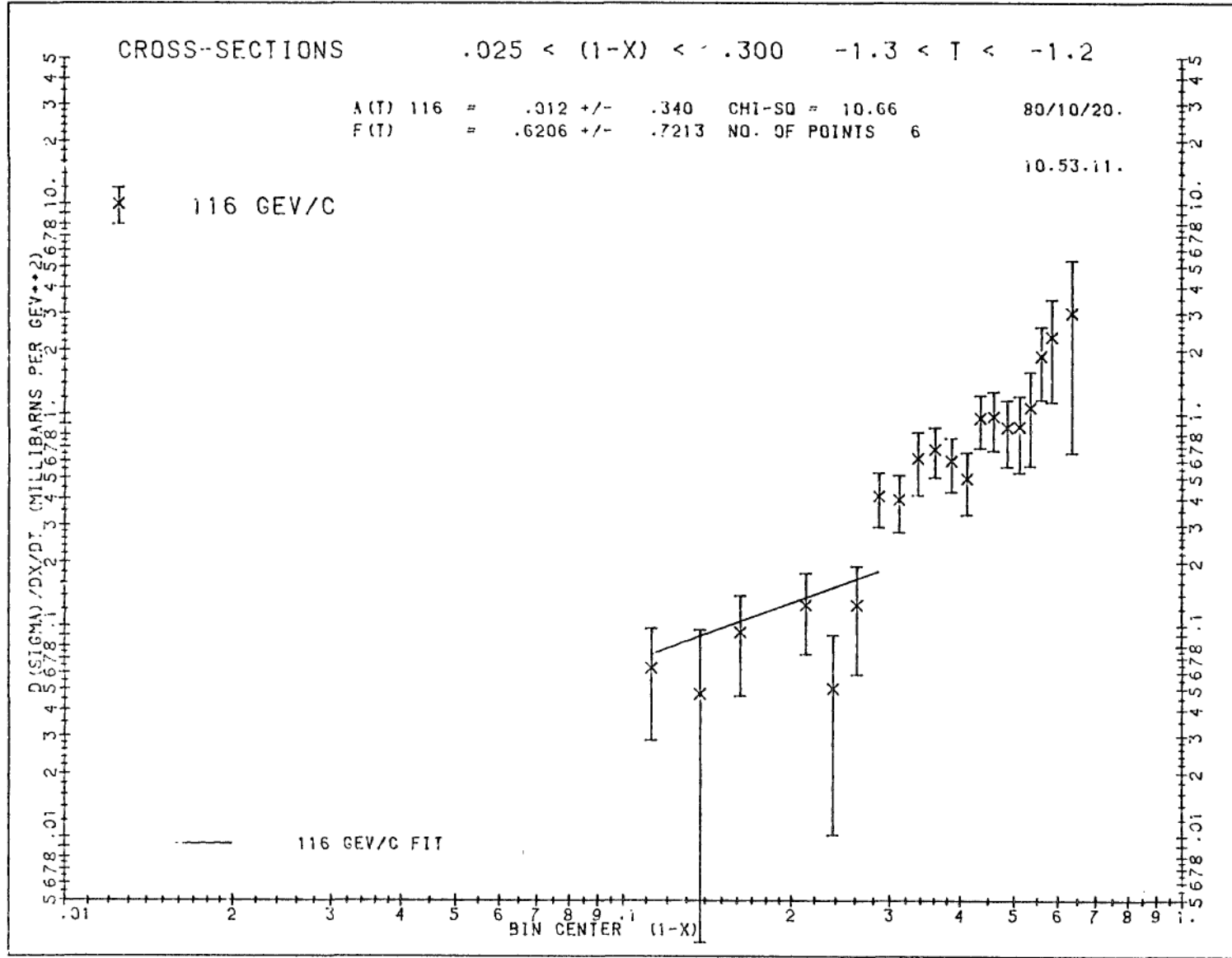


Figure 6.21: $-1.3 < t < -1.2$ (GeV/c)²



Figures 6.22 - 6.36. Cross-Sections ($d^2\sigma/dx dt$) for the 176 GeV/c
Data ($s = 363 \text{ GeV}^2$) of this Experiment

The straight line is the best fit of the data to

$$\frac{d^2\sigma}{dx dt} = F(t) \frac{1-2\alpha_E(t)}{\cos^2\left(\frac{\pi}{2}\alpha_E(t)\right)}$$

with the constraint

$$N_E \left(\int_{x(\text{low})}^{x(\text{high})} dx \frac{d^2\sigma}{dx dt} \right) (t(\text{high}) - t(\text{low})) NL_p$$

where N_E : Number of events within the (x, y) range of this fit

NL_p : Number of protons per cm^2 in the target on the figure

$A(t)$: Average value of $\alpha_E(t)$ in the range:

Figure 6.22: $-0.1 < t < 0.0 \text{ (GeV/c)}^2$

Figure 6.23: $-0.2 < t < -0.1 \text{ (GeV/c)}^2$

Figure 6.24: $-0.3 < t < -0.2 \text{ (GeV/c)}^2$

Figure 6.25: $-0.4 < t < -0.3 \text{ (GeV/c)}^2$

Figure 6.26: $-0.5 < t < -0.4 \text{ (GeV/c)}^2$

Figure 6.27: $-0.6 < t < -0.5 \text{ (GeV/c)}^2$

Figure 6.28: $-0.7 < t < -0.6 \text{ (GeV/c)}^2$

Figure 6.29: $-0.8 < t < -0.7 \text{ (GeV/c)}^2$

Figure 6.30: $-0.9 < t < -0.8 \text{ (GeV/c)}^2$

Figure 6.31: $-1.9 < t < -0.9 \text{ (GeV/c)}^2$

Figure 6.32: $-1.1 < t < -1.0 \text{ (GeV/c)}^2$

Figure 6.33: $-1.2 < t < -1.1 \text{ (GeV/c)}^2$

Figure 6.34: $-1.3 < t < -1.2 \text{ (GeV/c)}^2$

Figure 6.35: $-1.4 < t < -1.3 \text{ (GeV/c)}^2$

Figure 6.36: $-1.5 < t < -1.4 \text{ (GeV/c)}^2$

Figure 6.22: $-0.1 < t < 0.0$ (GeV/c)²

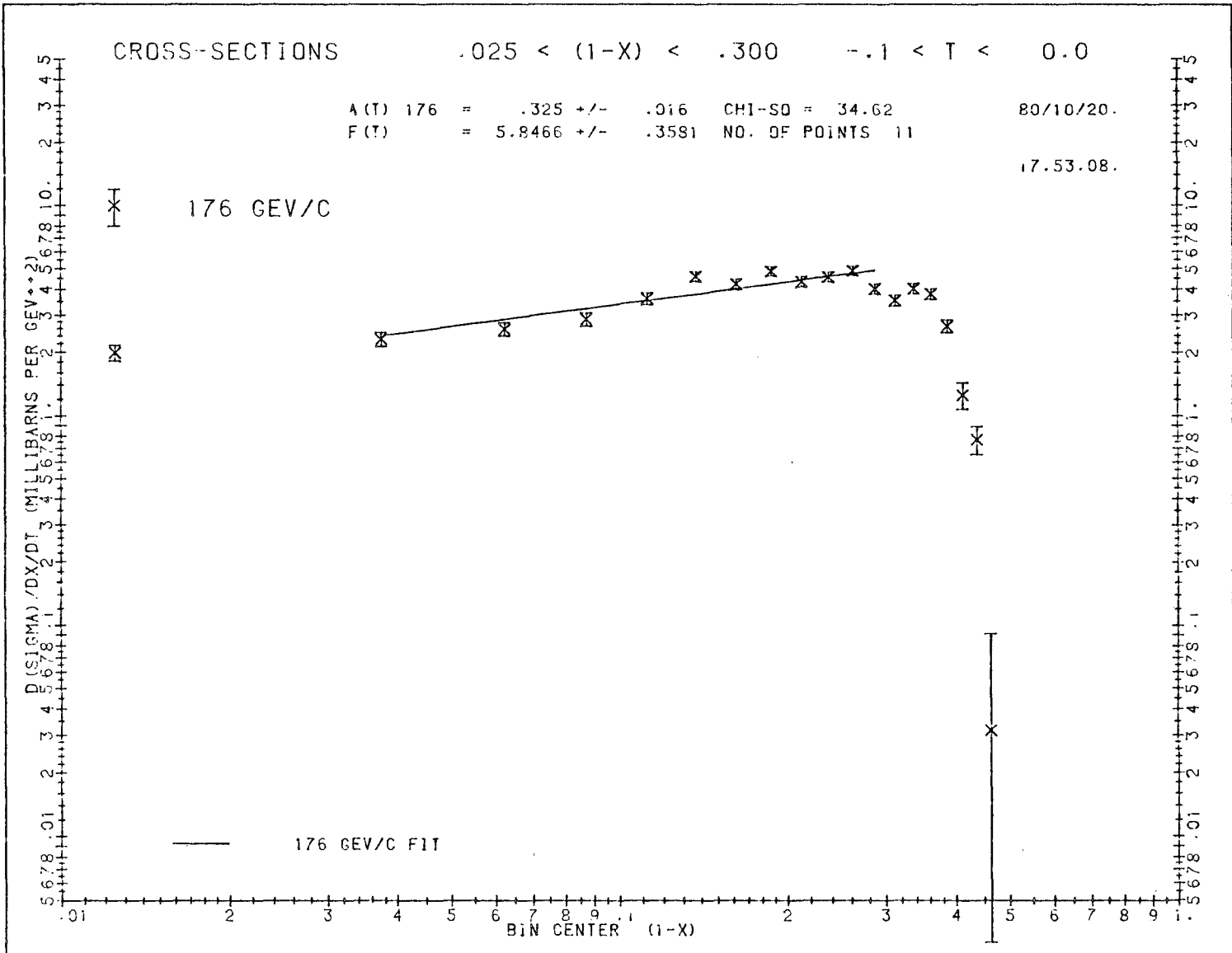


Figure 6.23: $-0.2 < t < -0.1$ (GeV/c)²

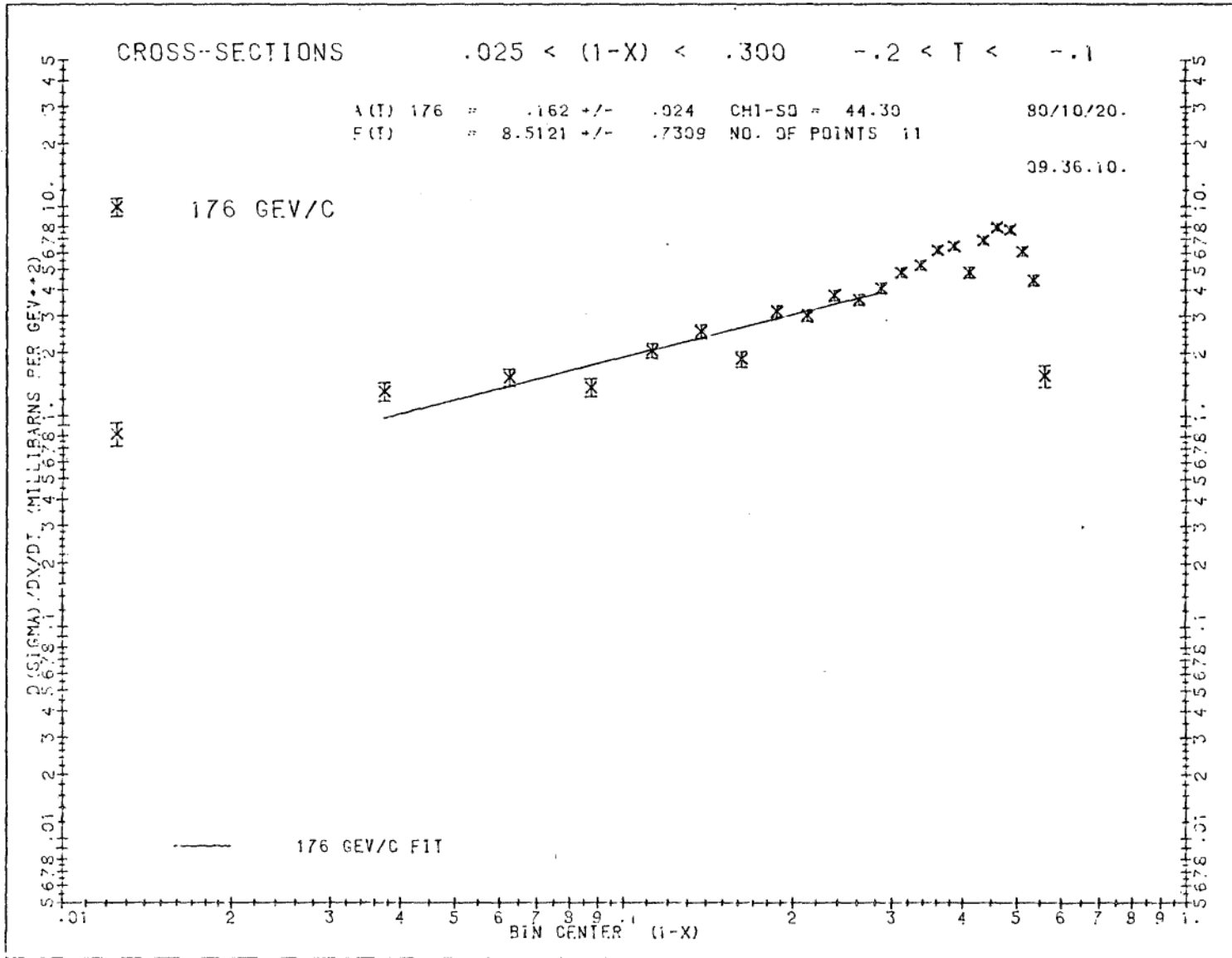


Figure 6.24: $-0.3 < t < -0.2$ (GeV/c)²

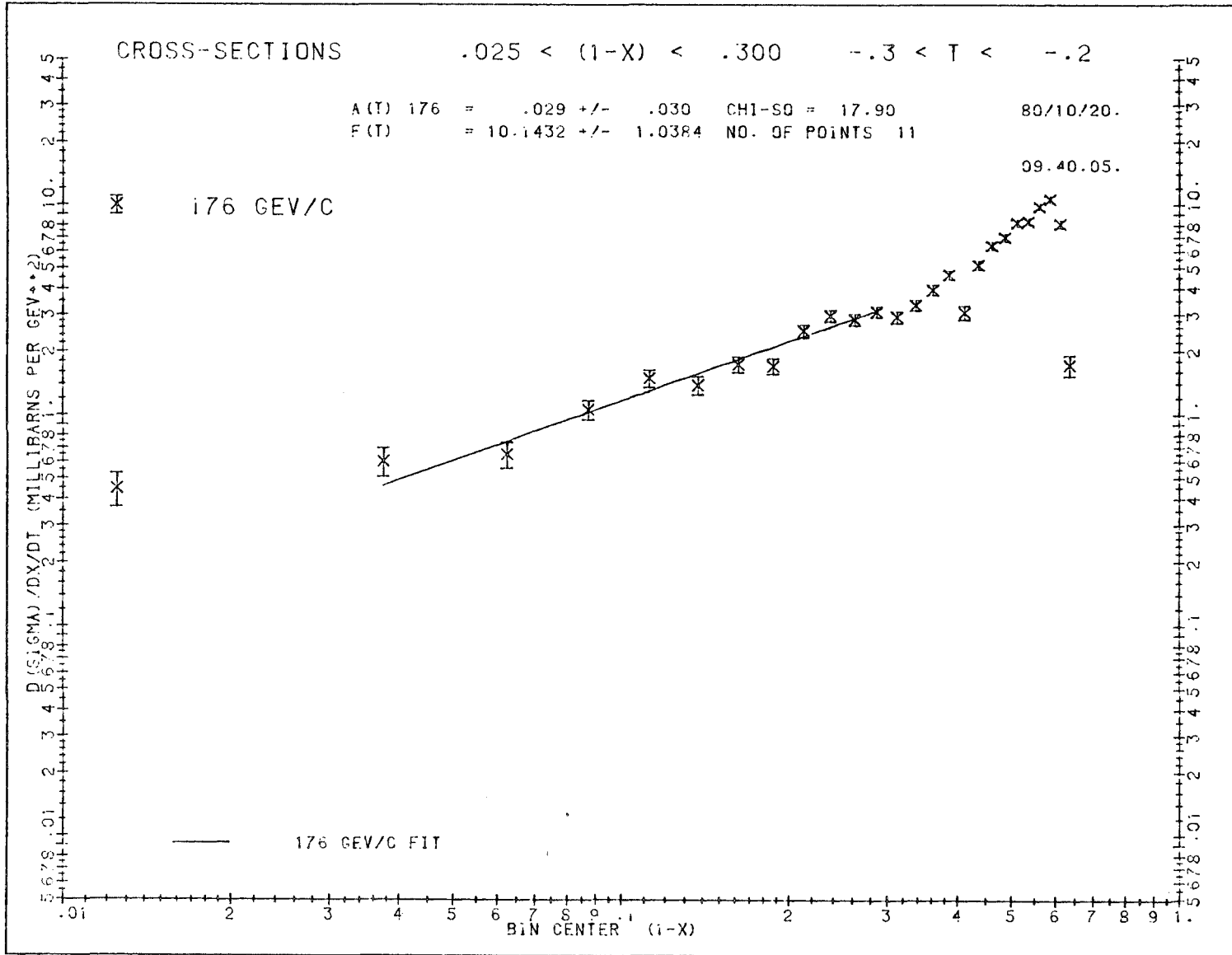
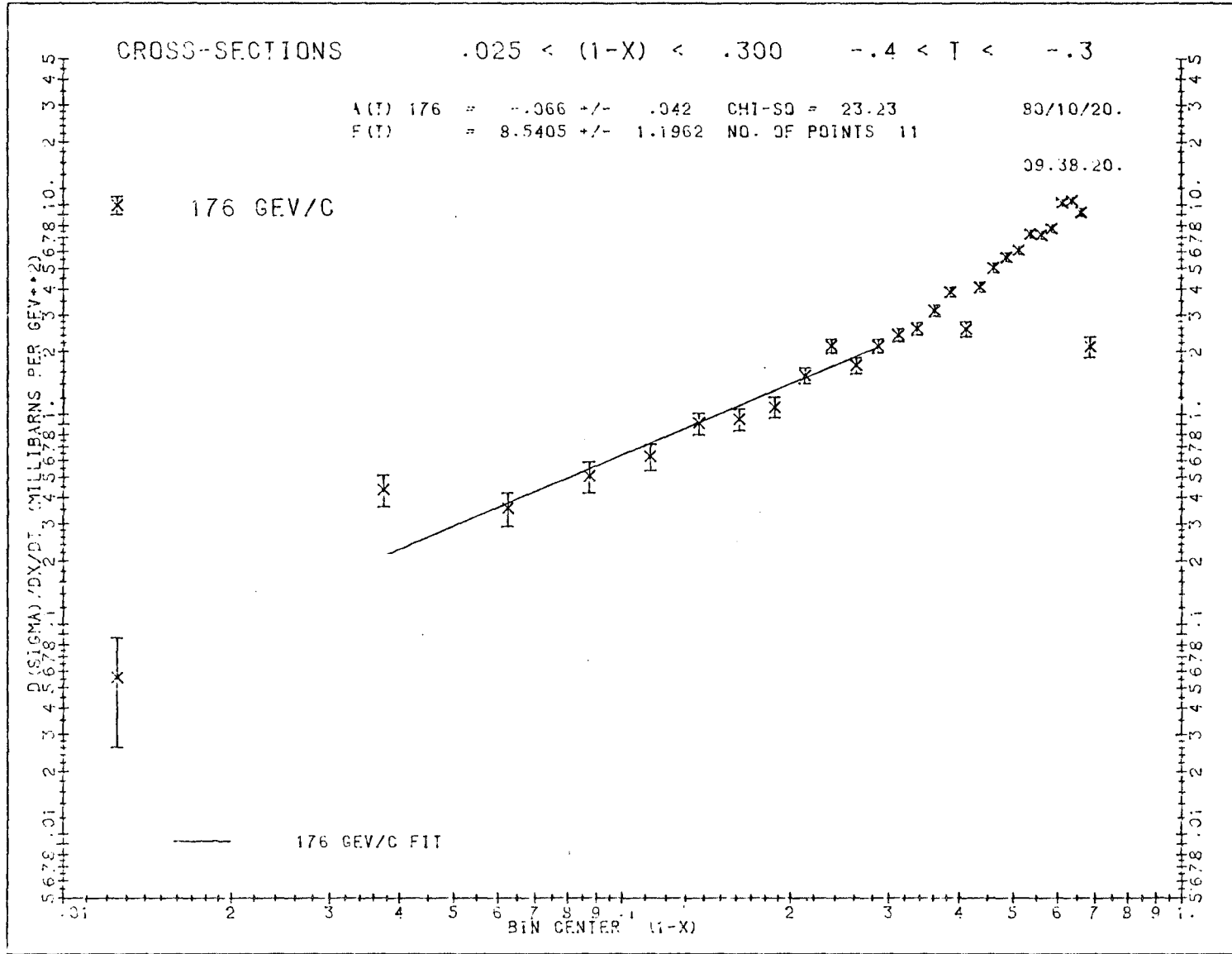


Figure 6.25: $-0.4 < t < -0.3$ (GeV/c)²



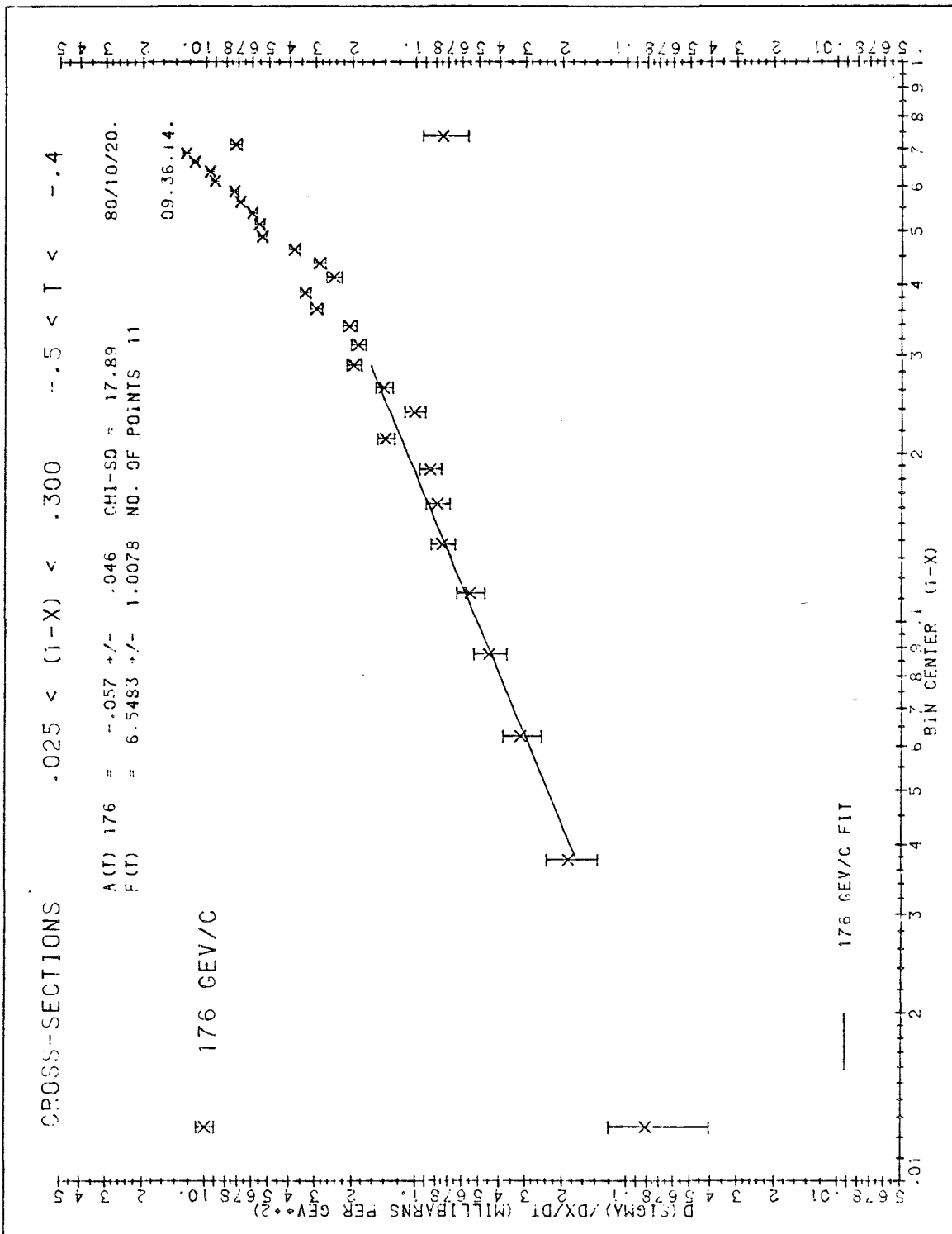


Figure 6.26: $-0.5 < t < -0.4 \text{ (GeV/c)}^2$

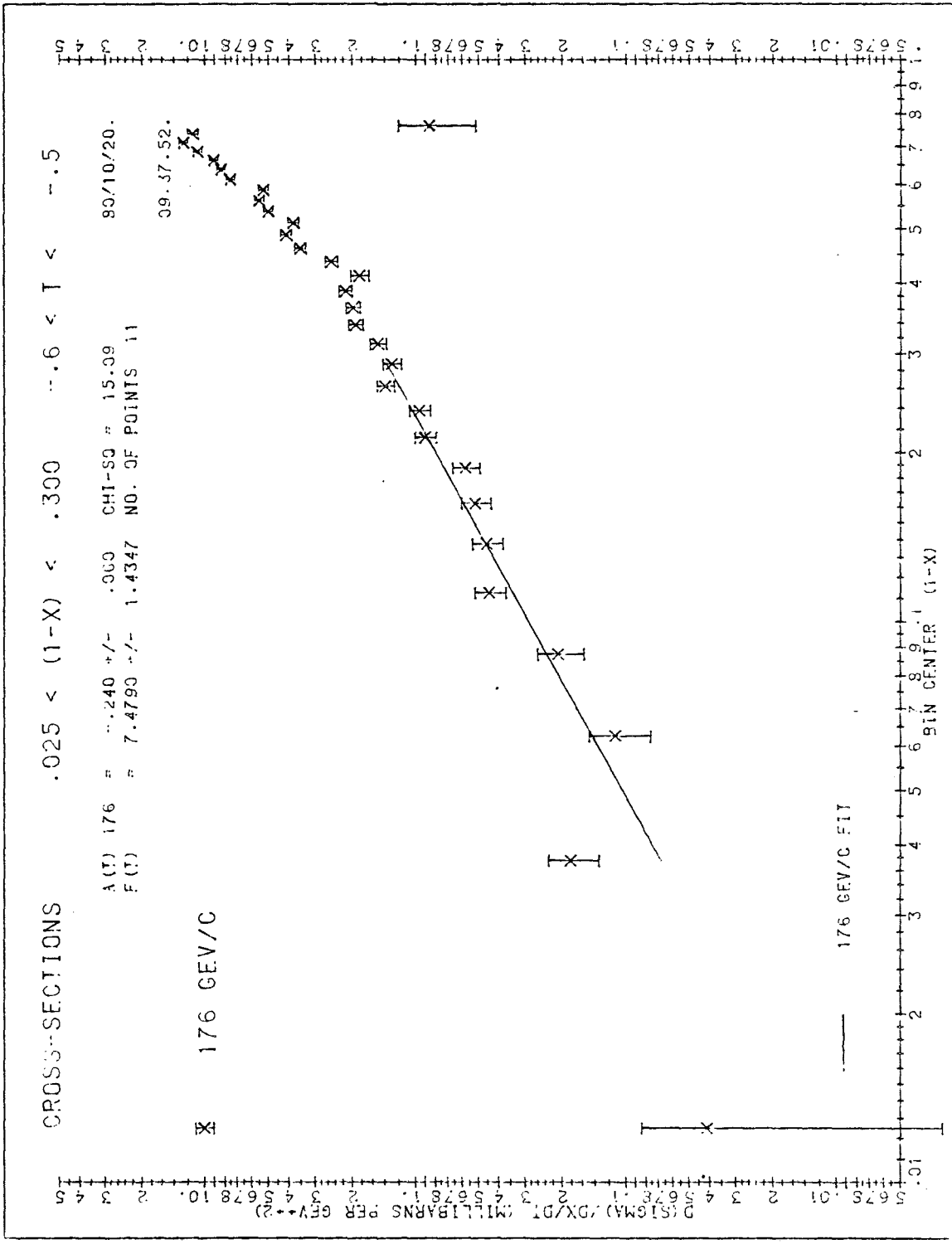


Figure 6.27: $-0.6 < t < -0.5 \text{ (GeV/c)}^2$

Figure 6.28: $-0.7 < t < -0.6$ (GeV/c)²

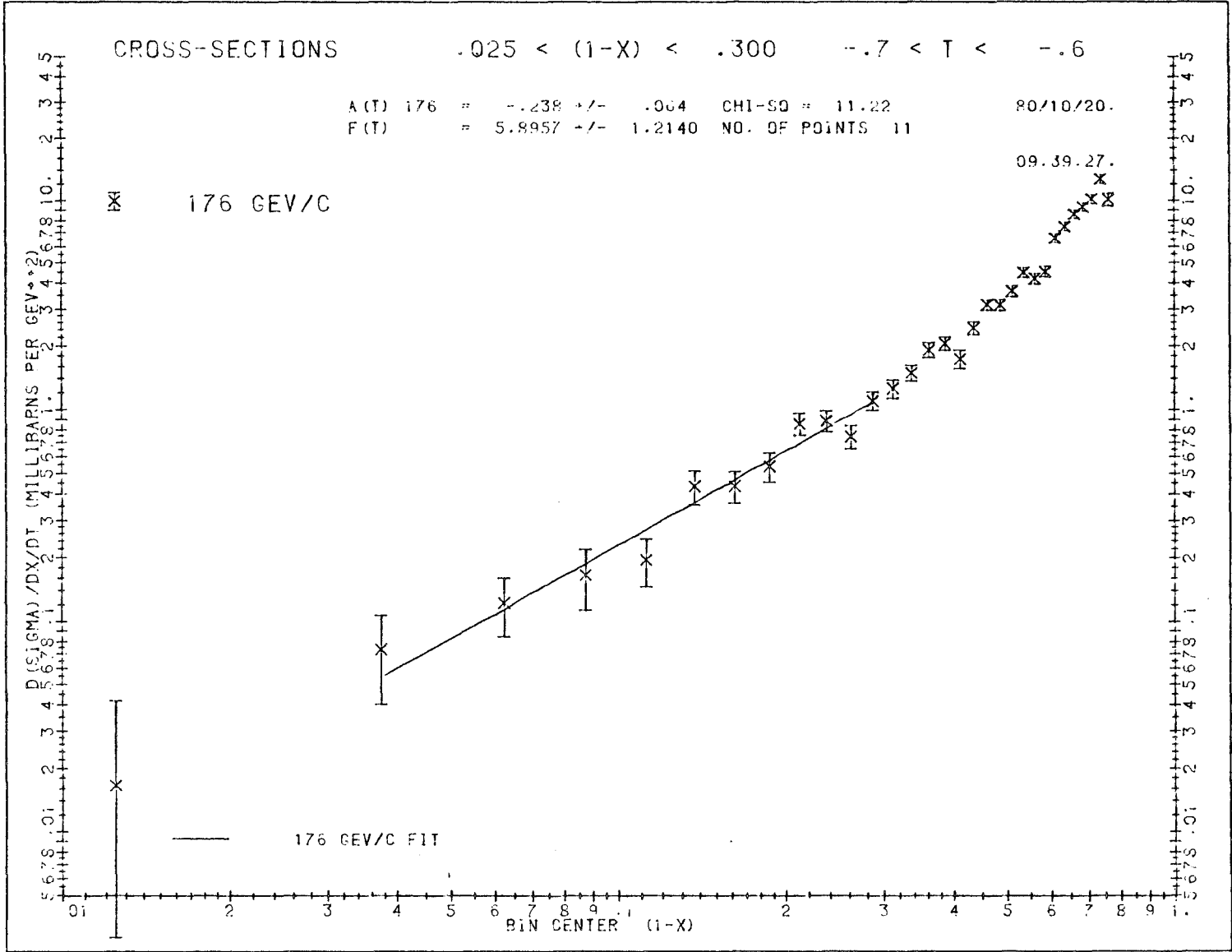


Figure 6.29: $-0.8 < t < -0.7$ (GeV/c)²

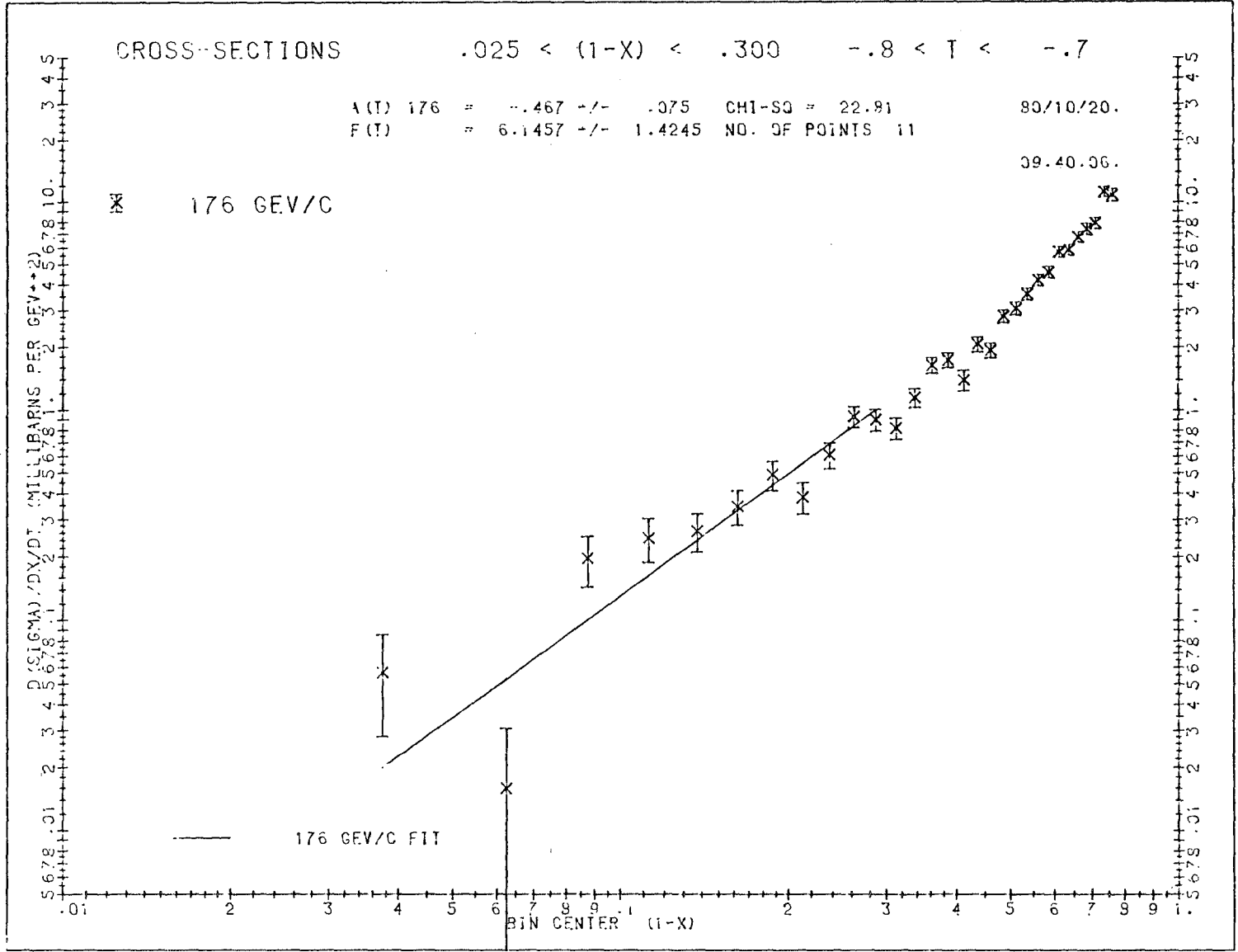
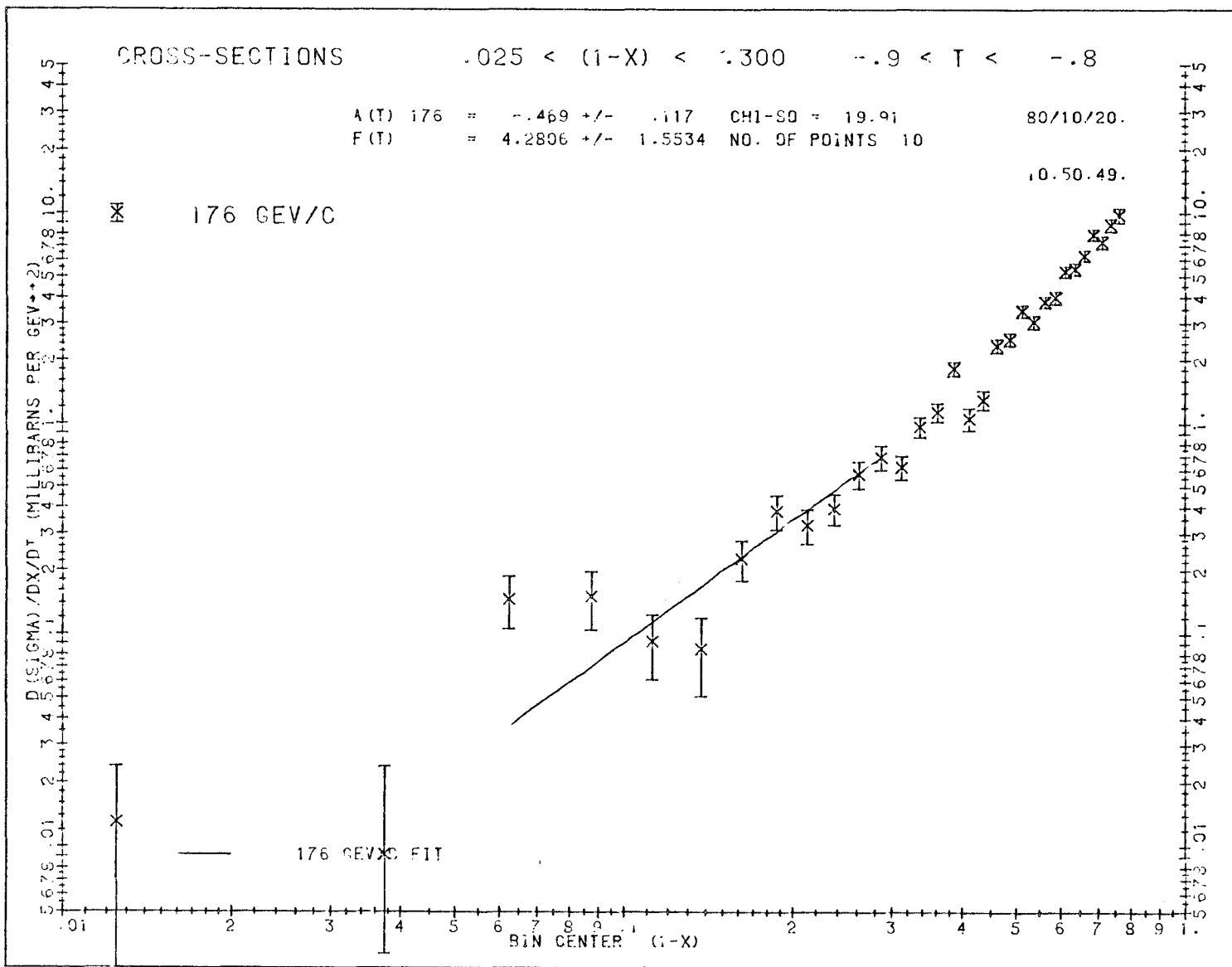


Figure 6.30: $-0.9 < t < -0.8$ (GeV/c)²



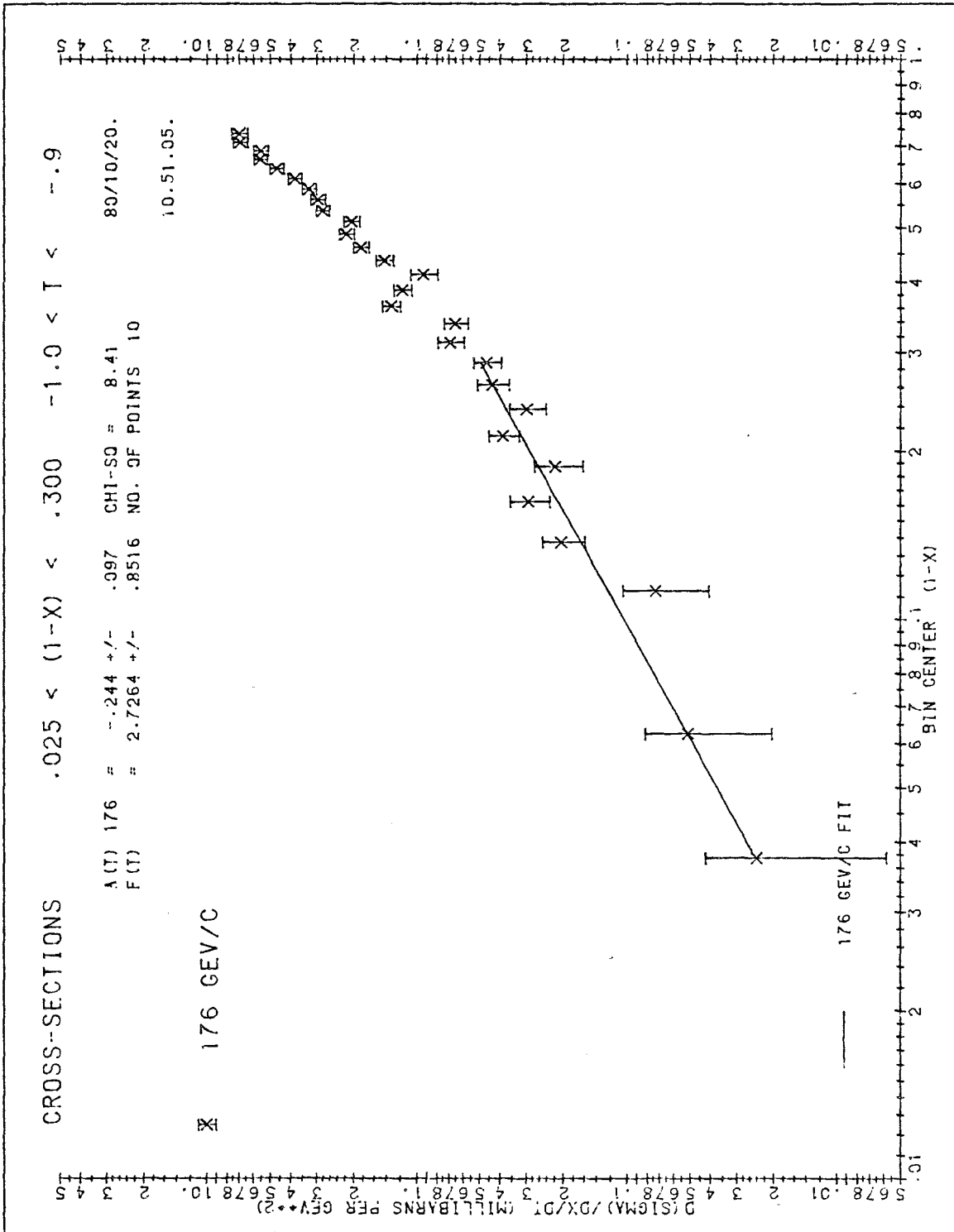


Figure 6.31: $-1.0 < t < -0.9 \text{ (GeV/c)}^2$

Figure 6.32: $-1.1 < t < -1.0$ (GeV/c)²

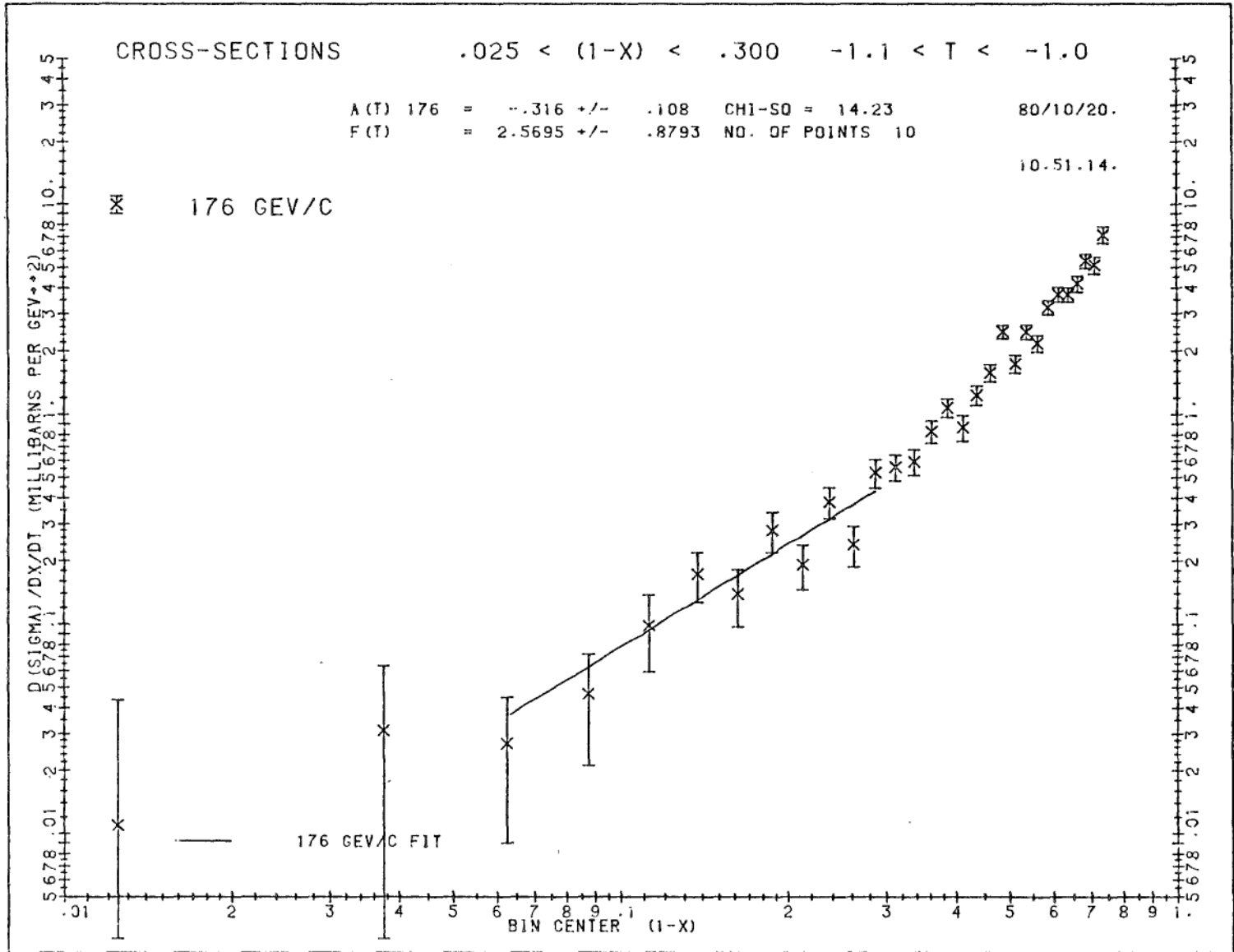
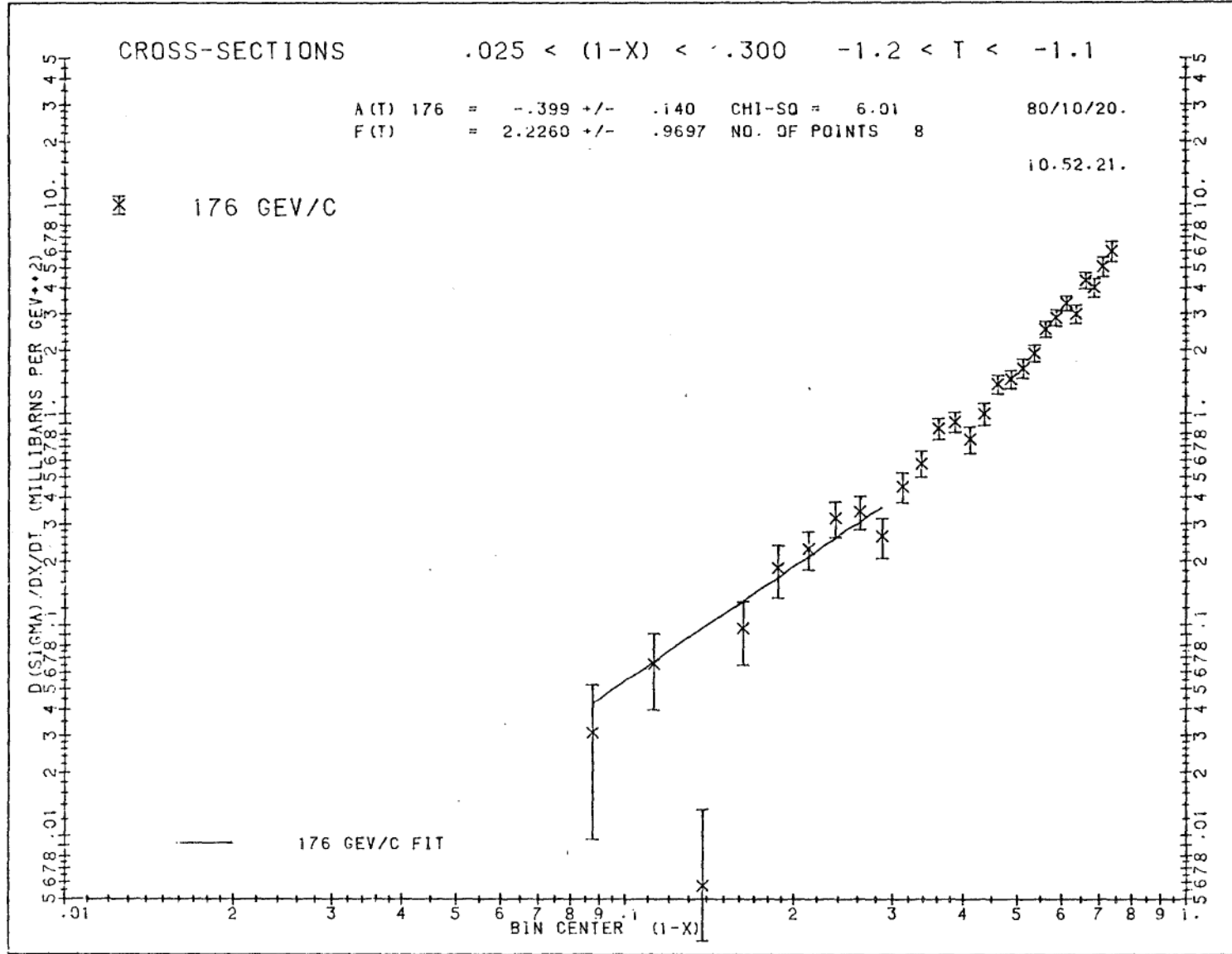


Figure 6.33: $-1.2 < t < -1.1$ (GeV/c)²



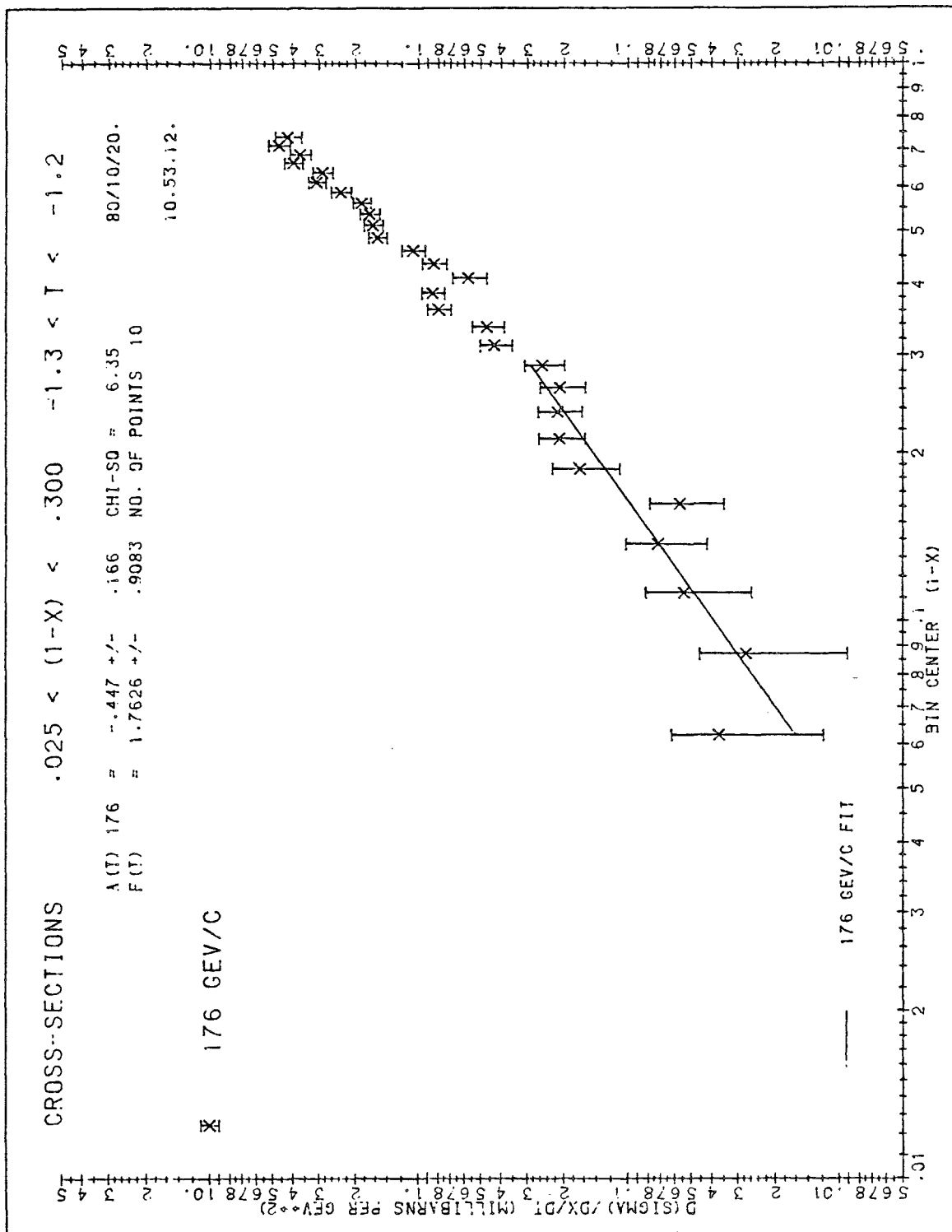


Figure 6.35: $-1.4 < t < -1.3$ (GeV/c)²

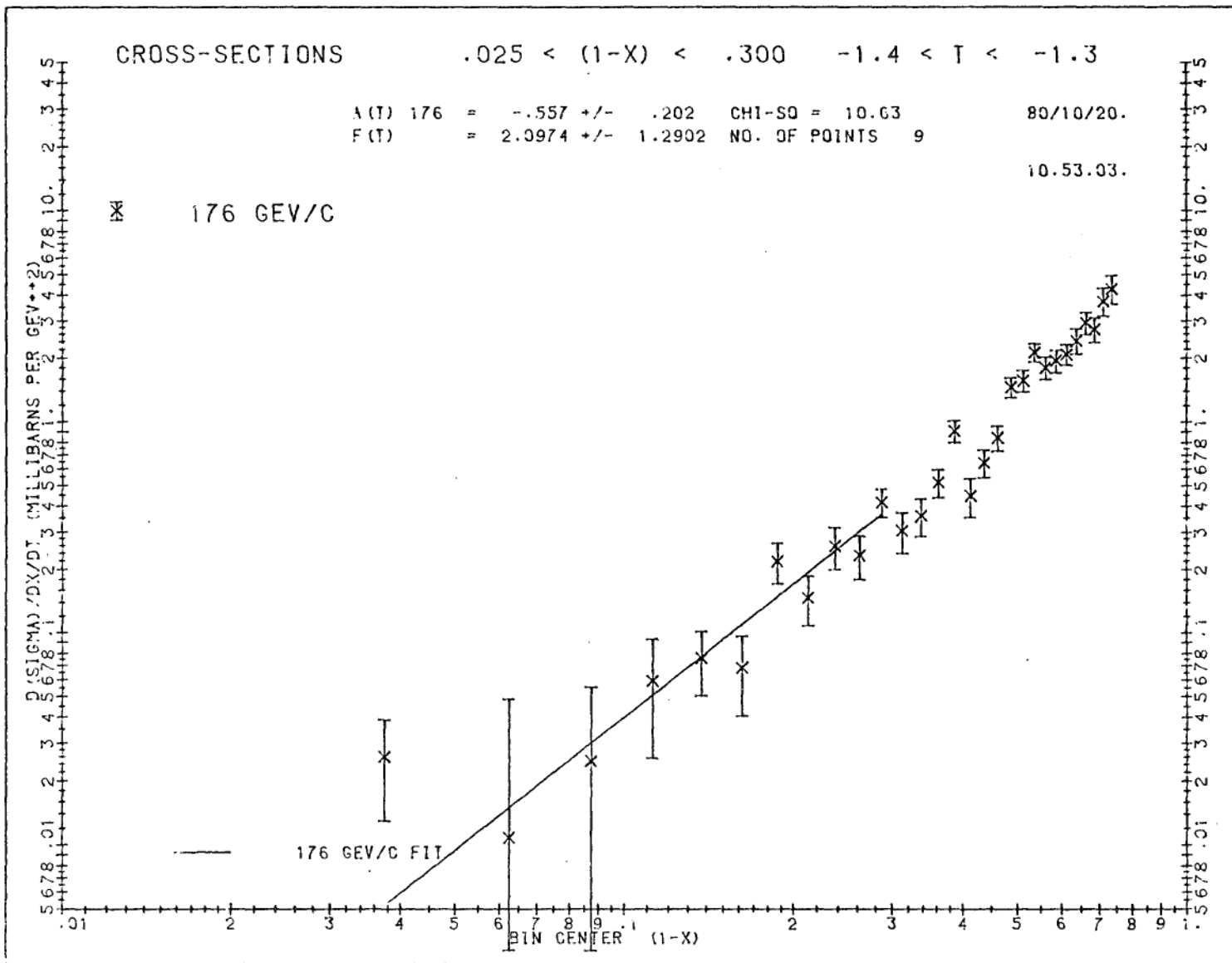


Figure 6.36: $-1.5 < t < -1.4$ (GeV/c)²

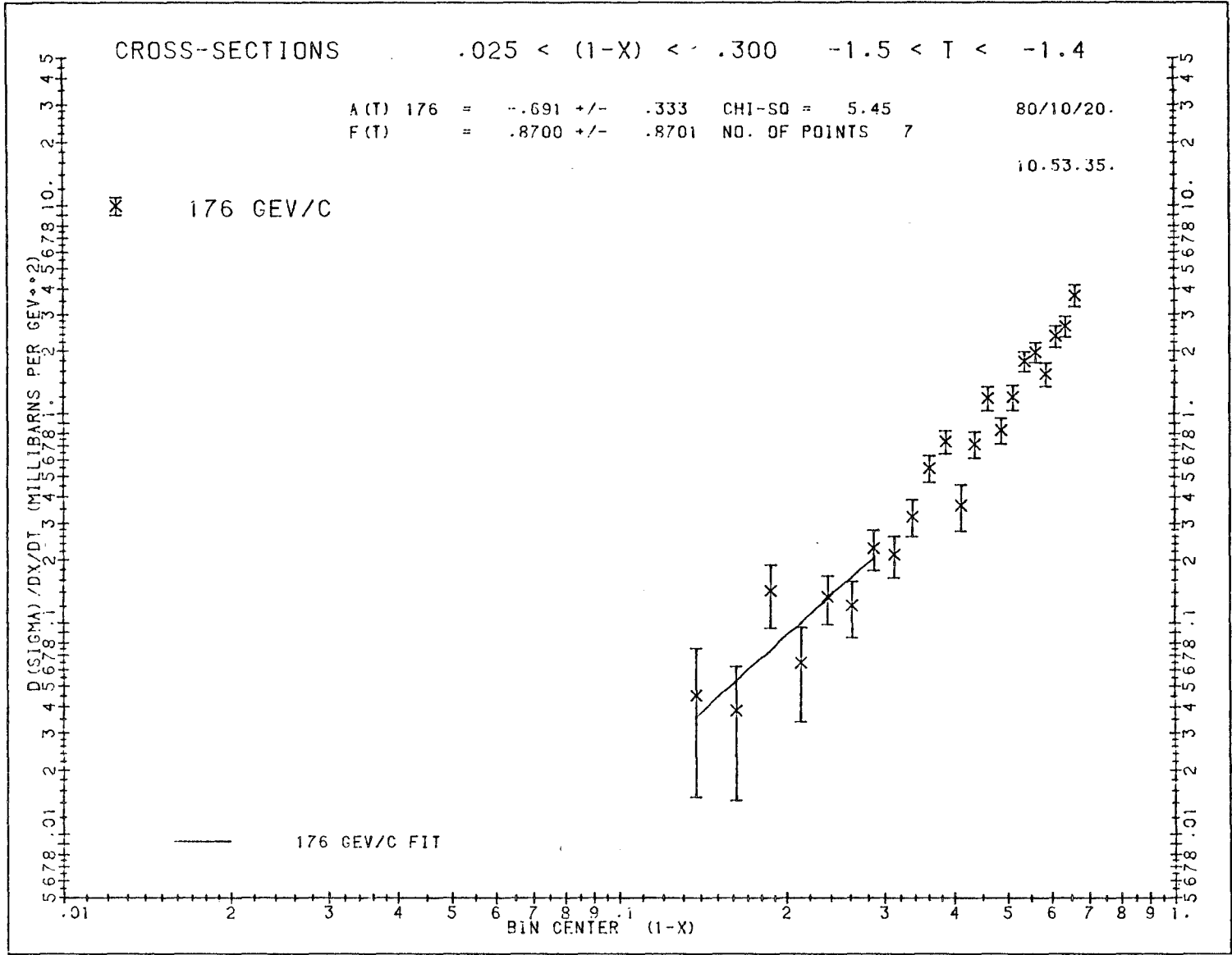
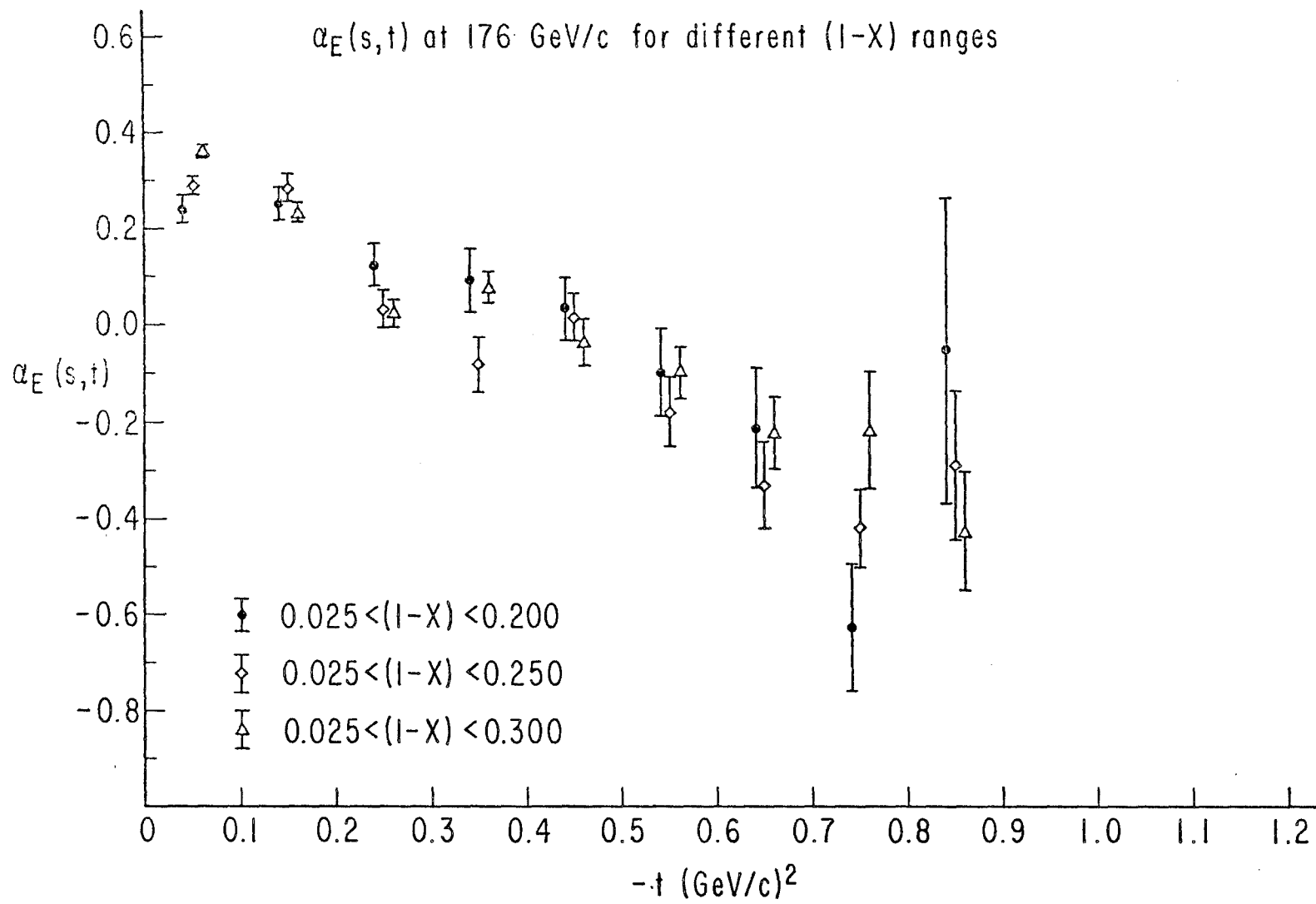


Figure 7. Comparison of the Regge Trajectories for this Experiment, Obtained by Fitting Subsets of Data Corresponding to Different Ranges in $(1-x)$.



Figures 8.1 - 8.7. Comparison between Differential Cross-Sections ($d^2\sigma/dx dt$), at Given Values of x and t , for Different Values of s (Beam Momentum).

Figure 8.1: $-0.1 < t < 0.0$

Figure 8.2: $-0.2 < t < -0.1$

Figure 8.3: $-0.3 < t < -0.2$

Figure 8.4: $-0.4 < t < -0.3$

Figure 8.5: $-0.5 < t < -0.4$

Figure 8.6: $-0.6 < t < -0.5$

Figure 8.7: $-0.7 < t < -0.6$

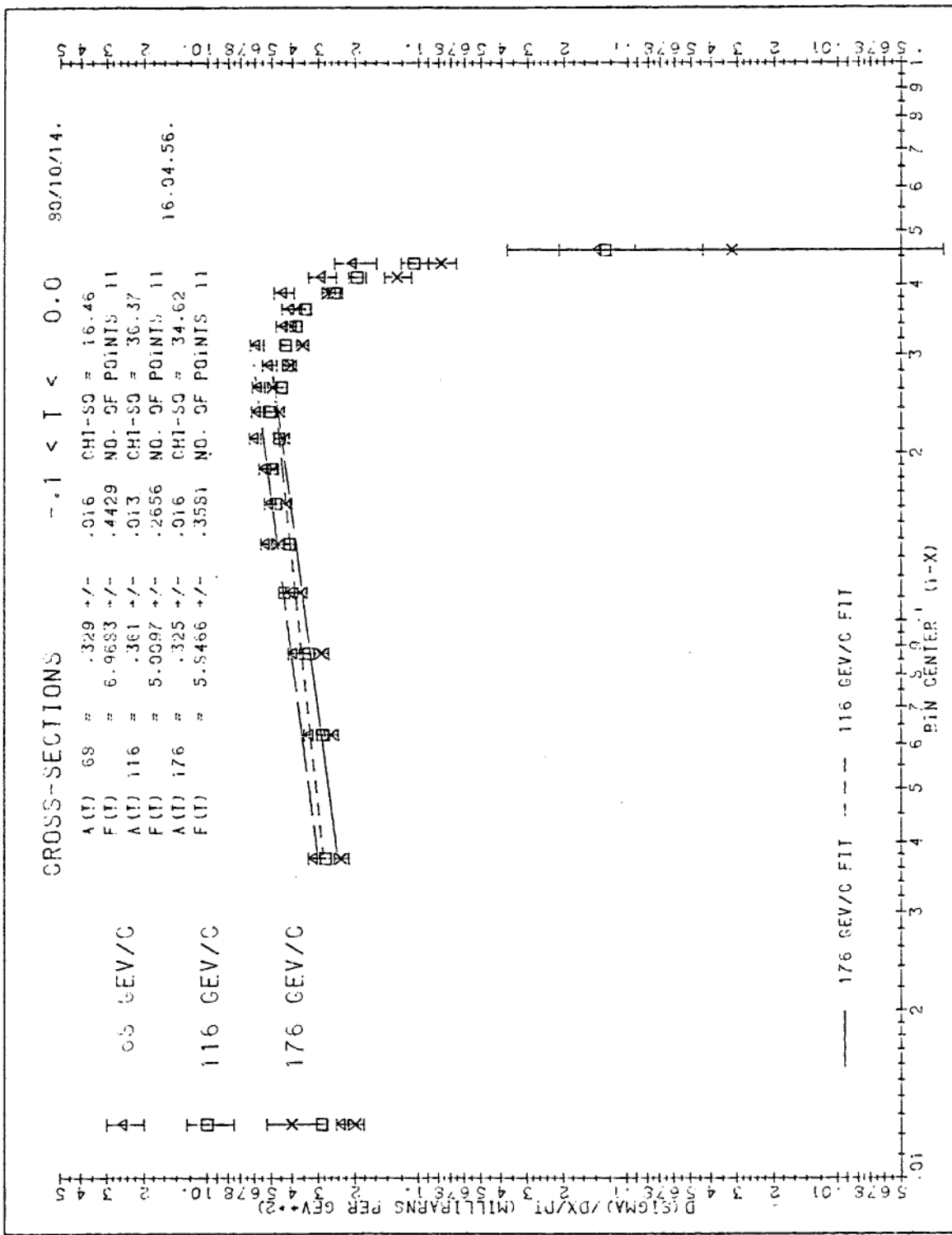


Figure 8.1: $-0.1 < t < 0.0$ (GeV/c)²

Figure 8.2: $-0.2 < t < -0.1$ (GeV/c)²

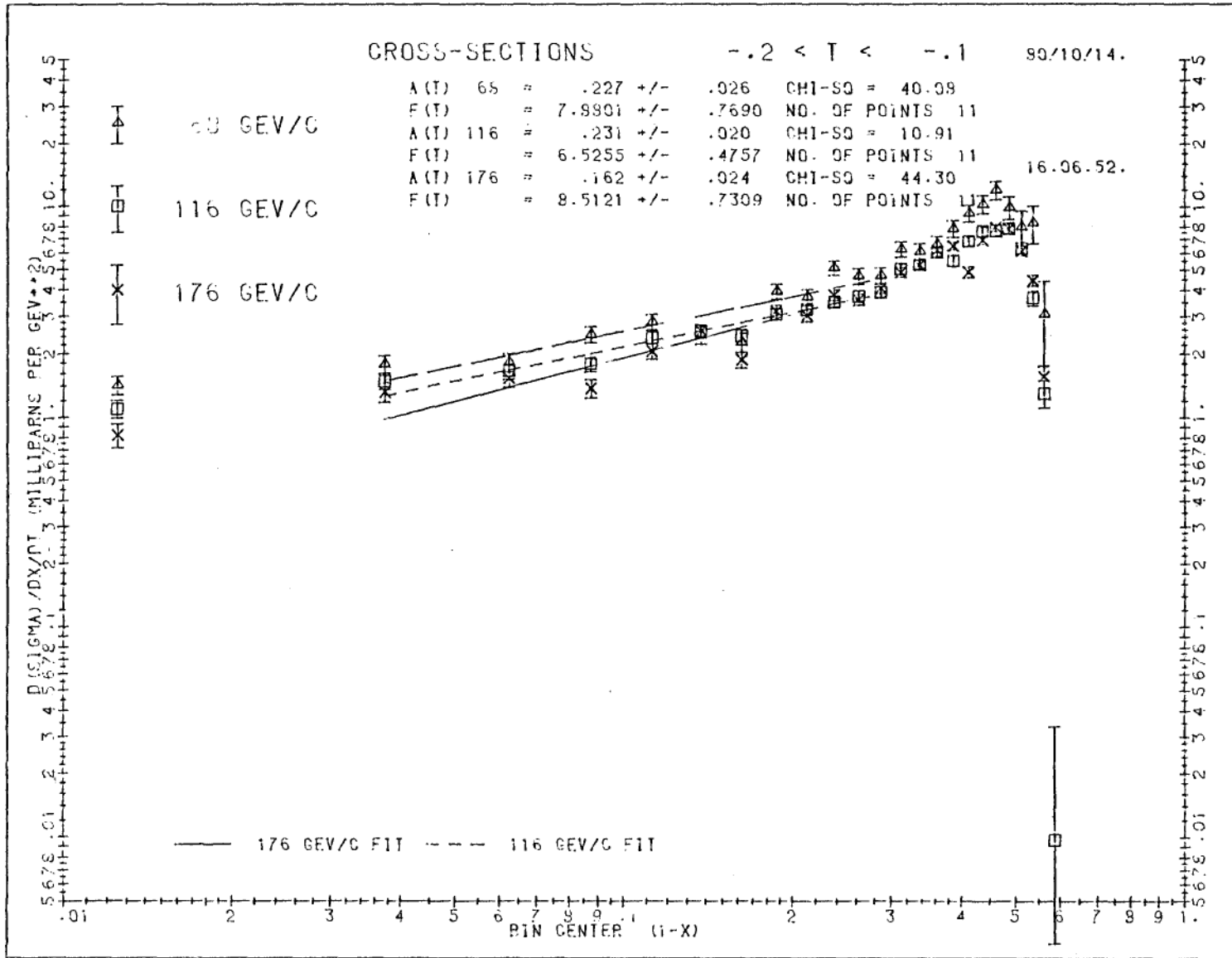
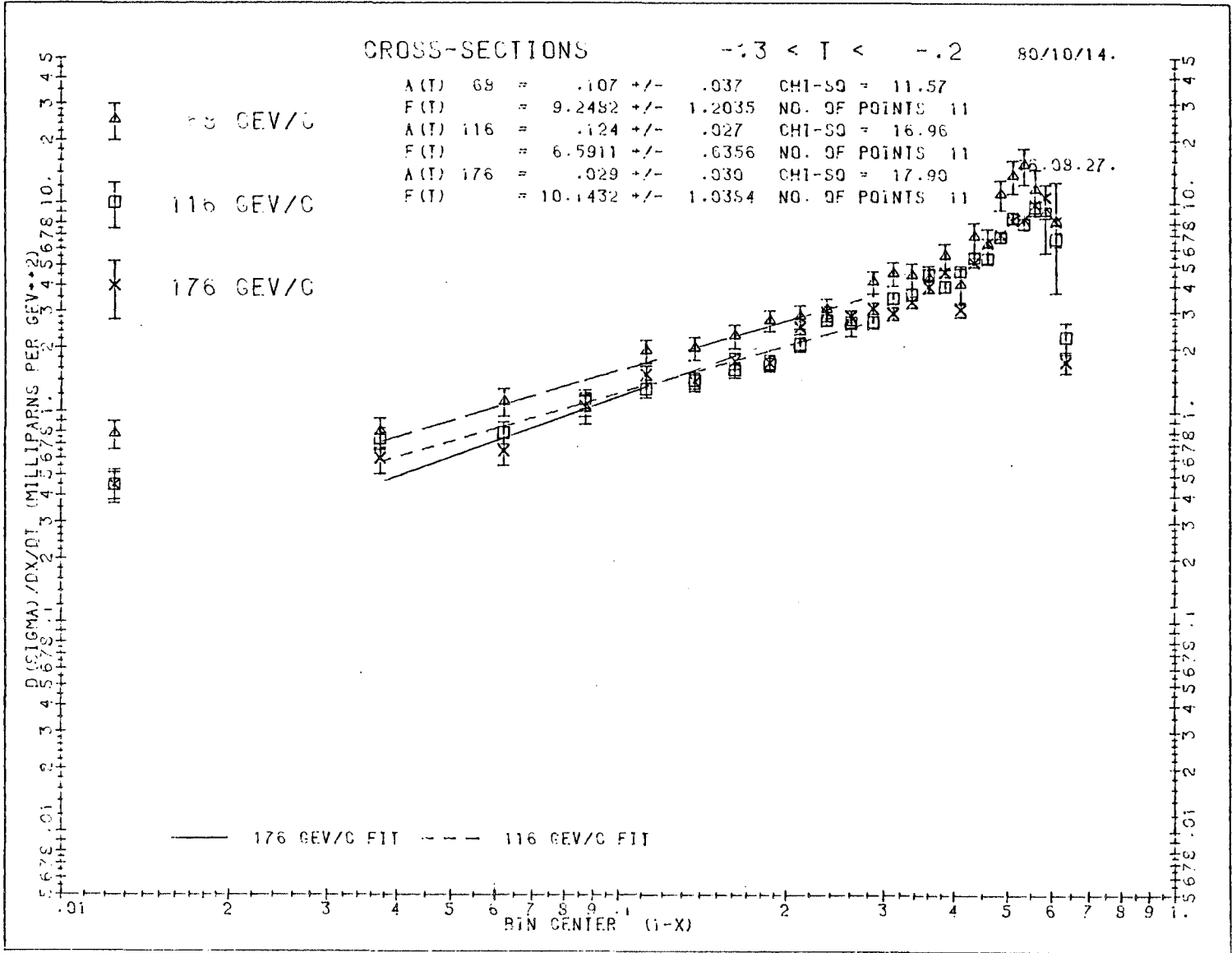


Figure 8.3: $-0.3 < t < -0.2$ (GeV/c)²



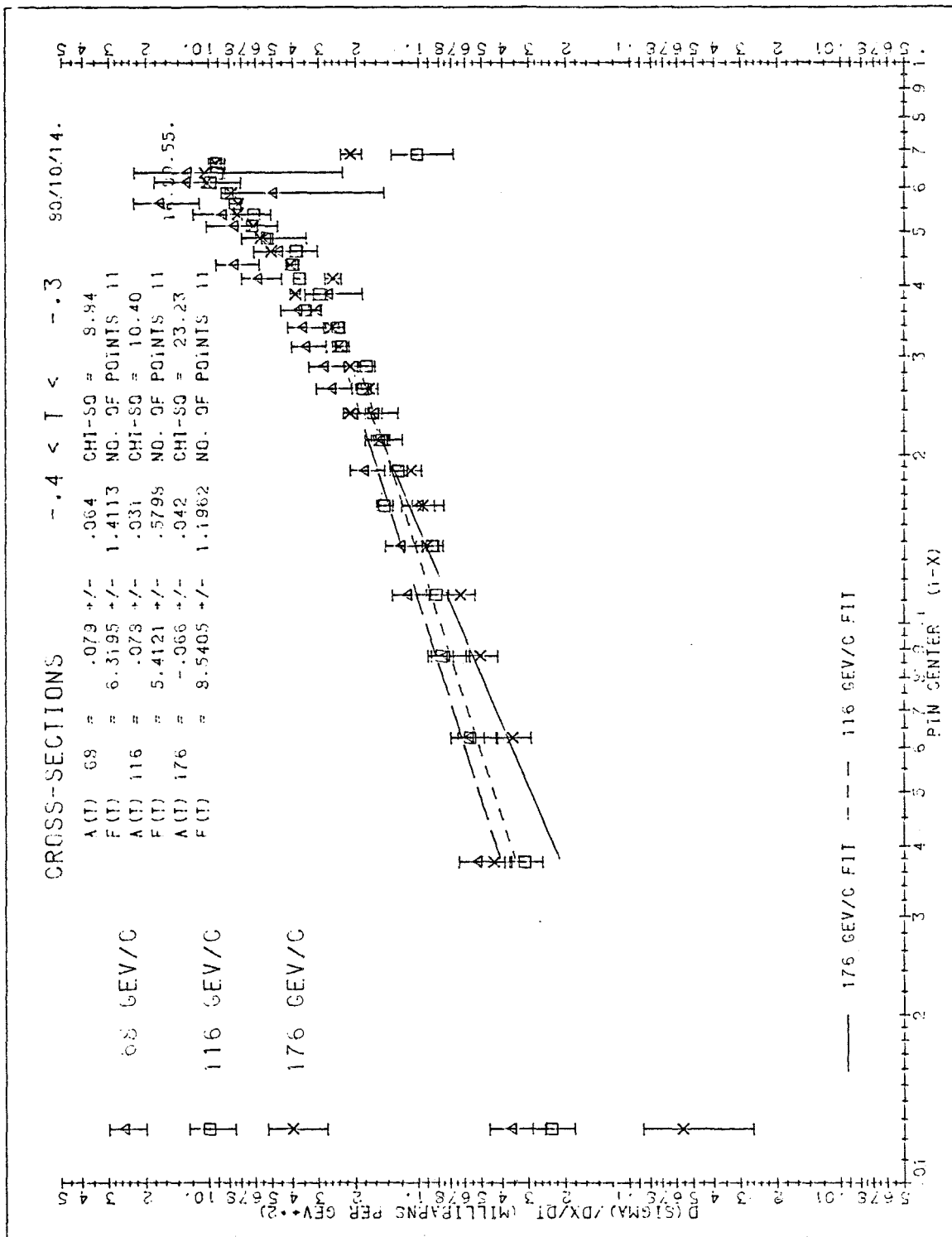


Figure 8.4: $-0.4 < t < -0.3$ (GeV/c)²

Figure 8.5: $-0.5 < t < -0.4$ (GeV/c)²

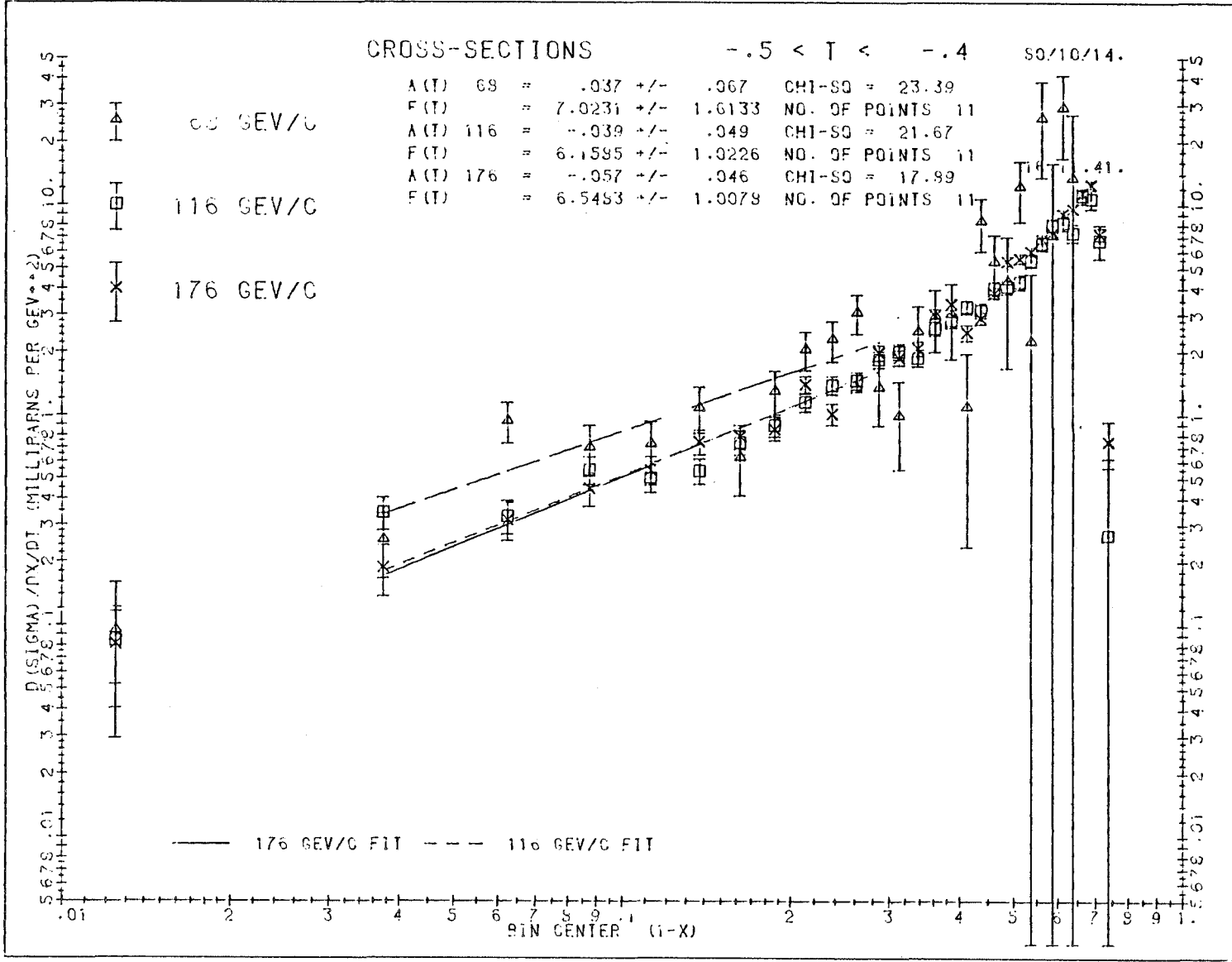
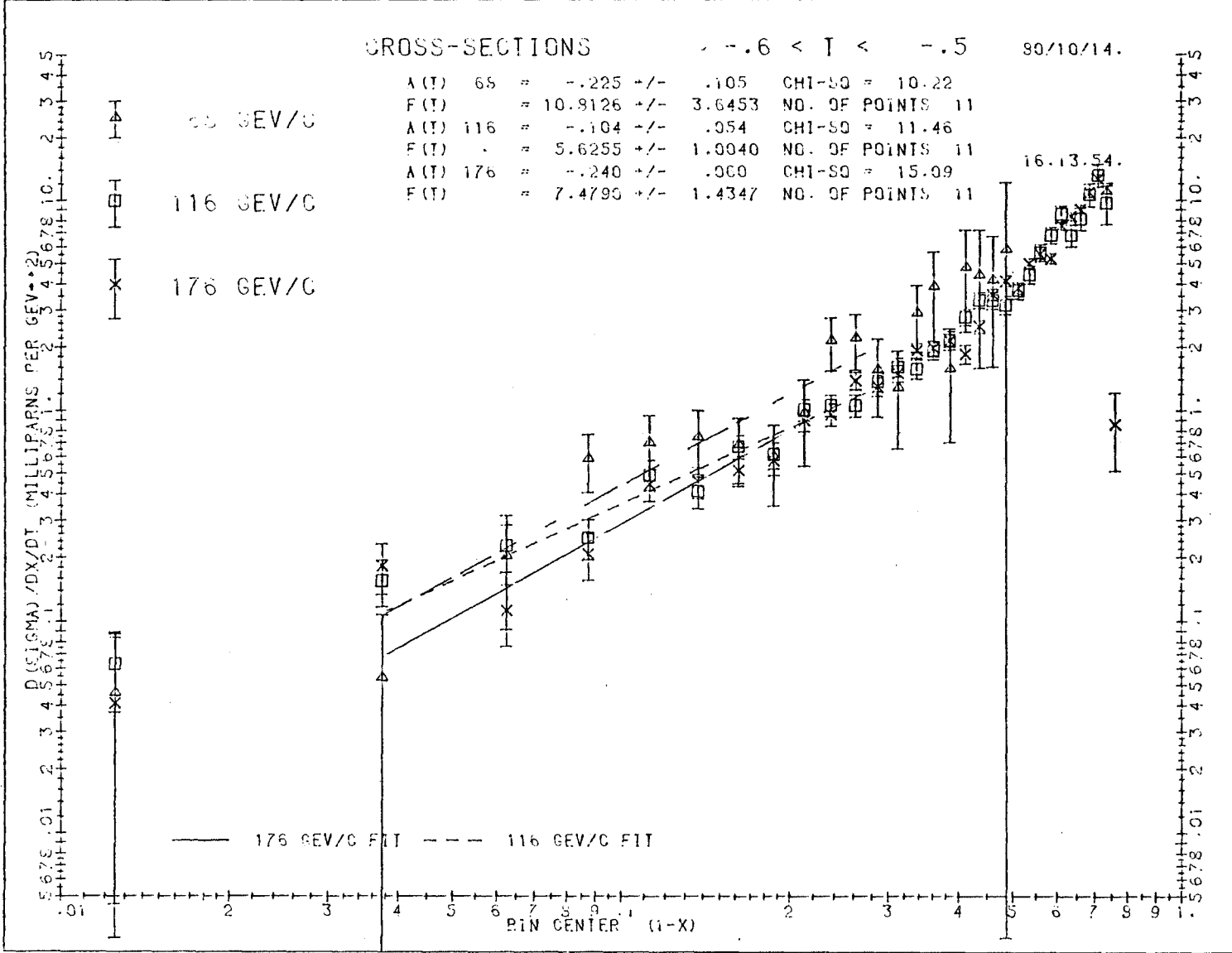


Figure 8.6: $-0.6 < t < -0.5$ (GeV/c)²



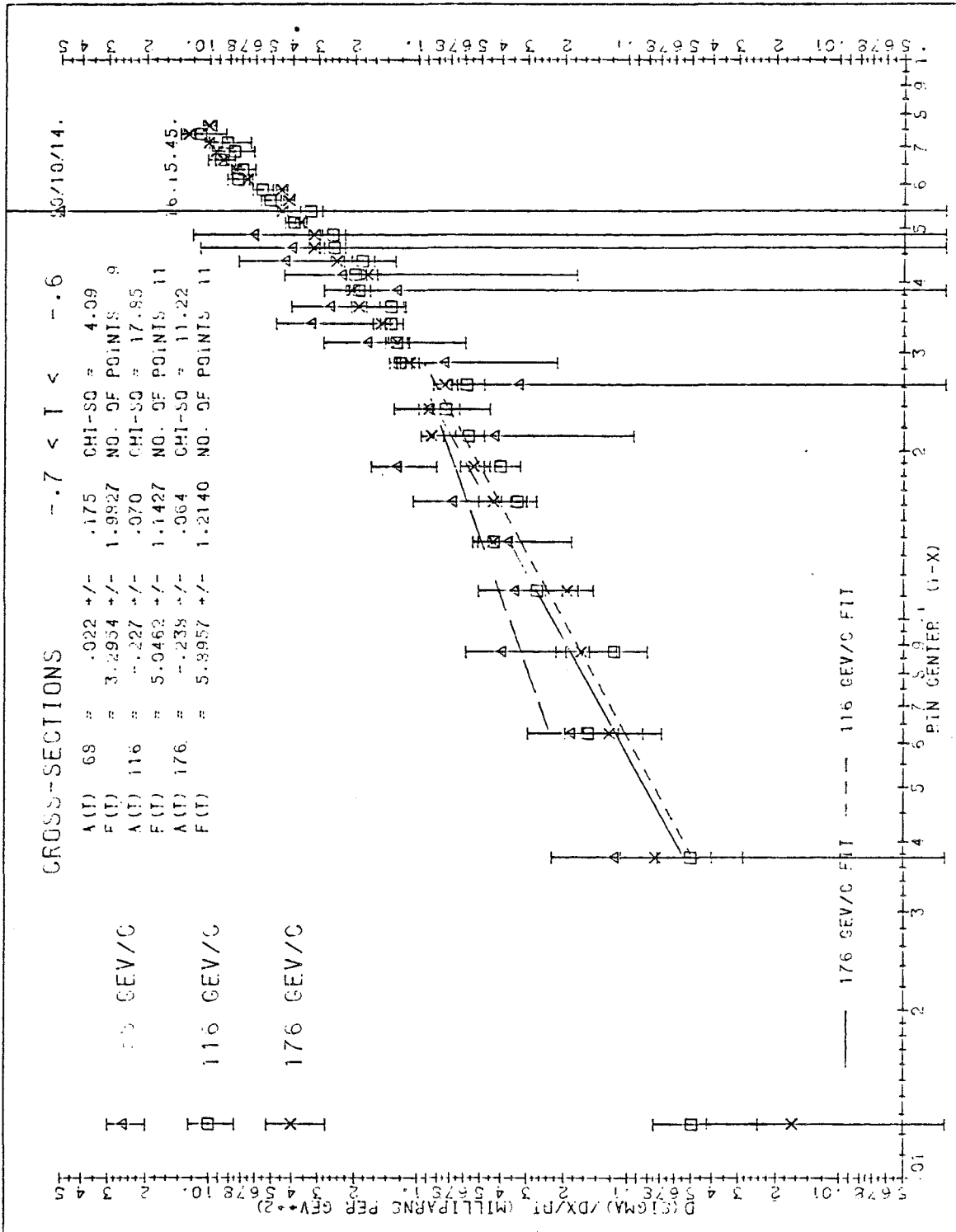


Figure 8.7: $-0.7 < t < -0.6 \text{ (GeV/c)}^2$

Figure 9. Regge Trajectories ($\alpha_E(s, t)$). Extracted from the data in this experiment by fitting over the range $0.025 < (1-x) < 0.300$.

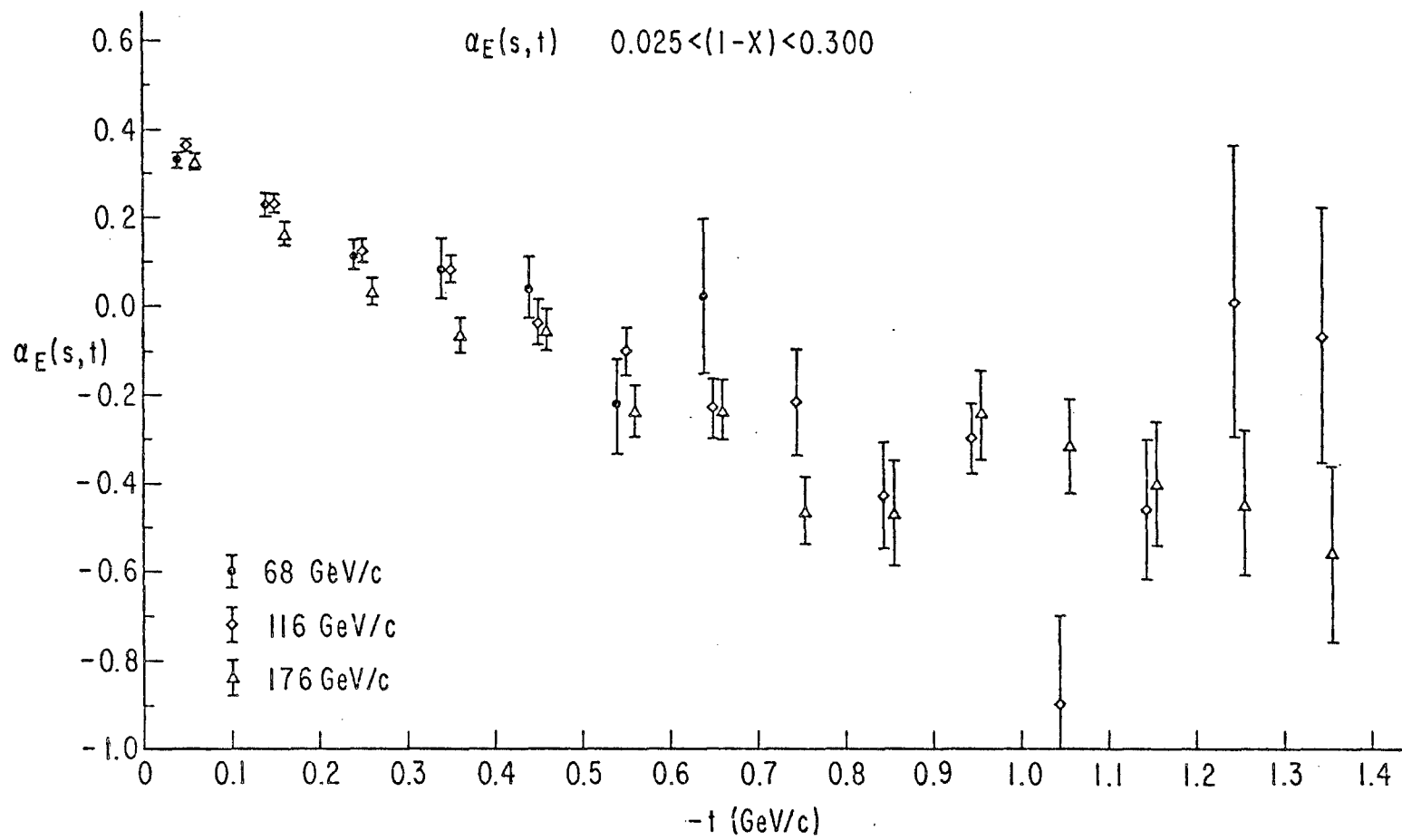


Figure 10. Comparison between $\alpha_E(s, t)$, the Effective Regge Trajectory for this Experiment at 116 GeV/c, and $\alpha_\rho(t)$ and $\alpha_{A_2}(t)$, the Regge Trajectories from Pion Charge Exchange.⁷

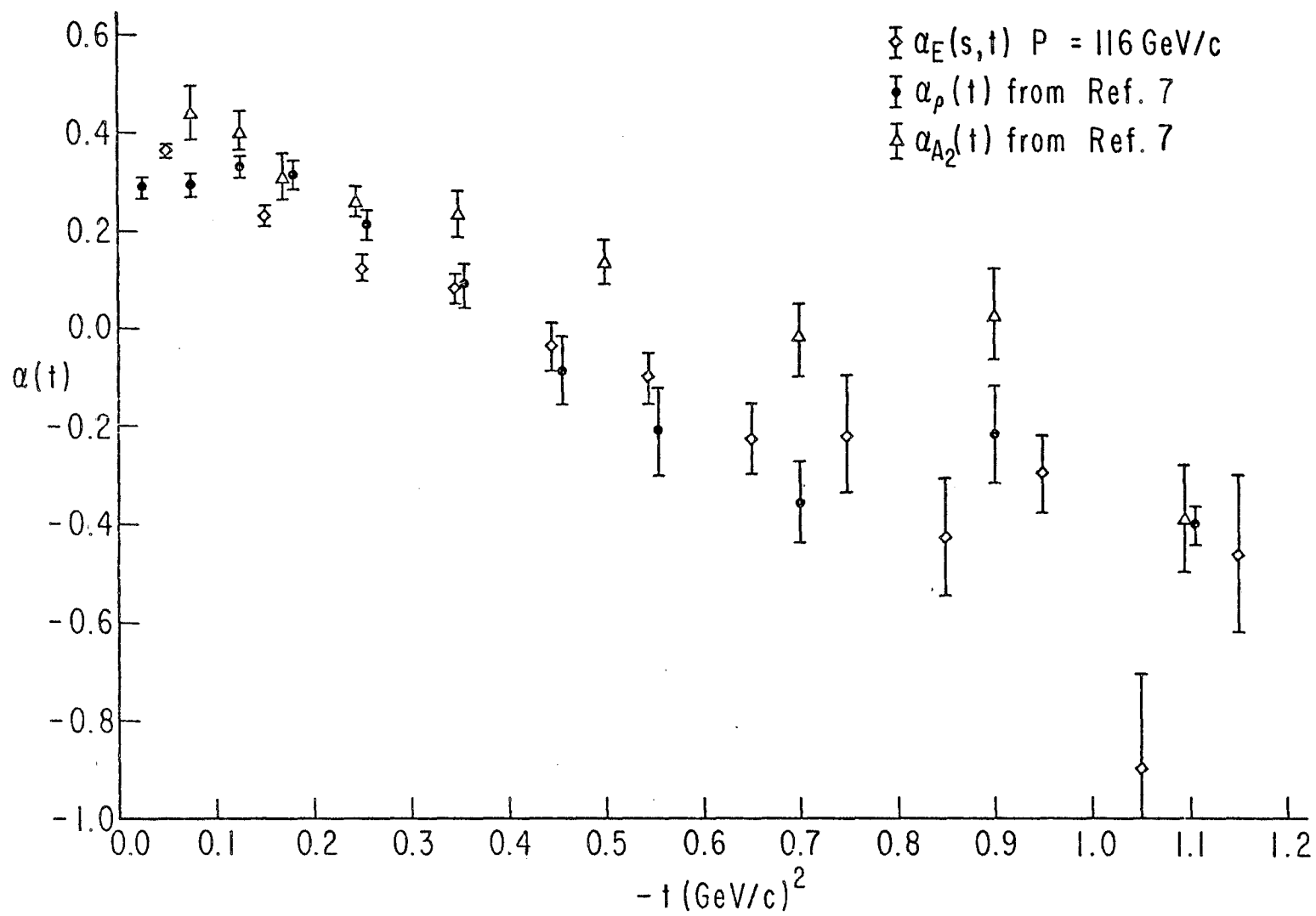
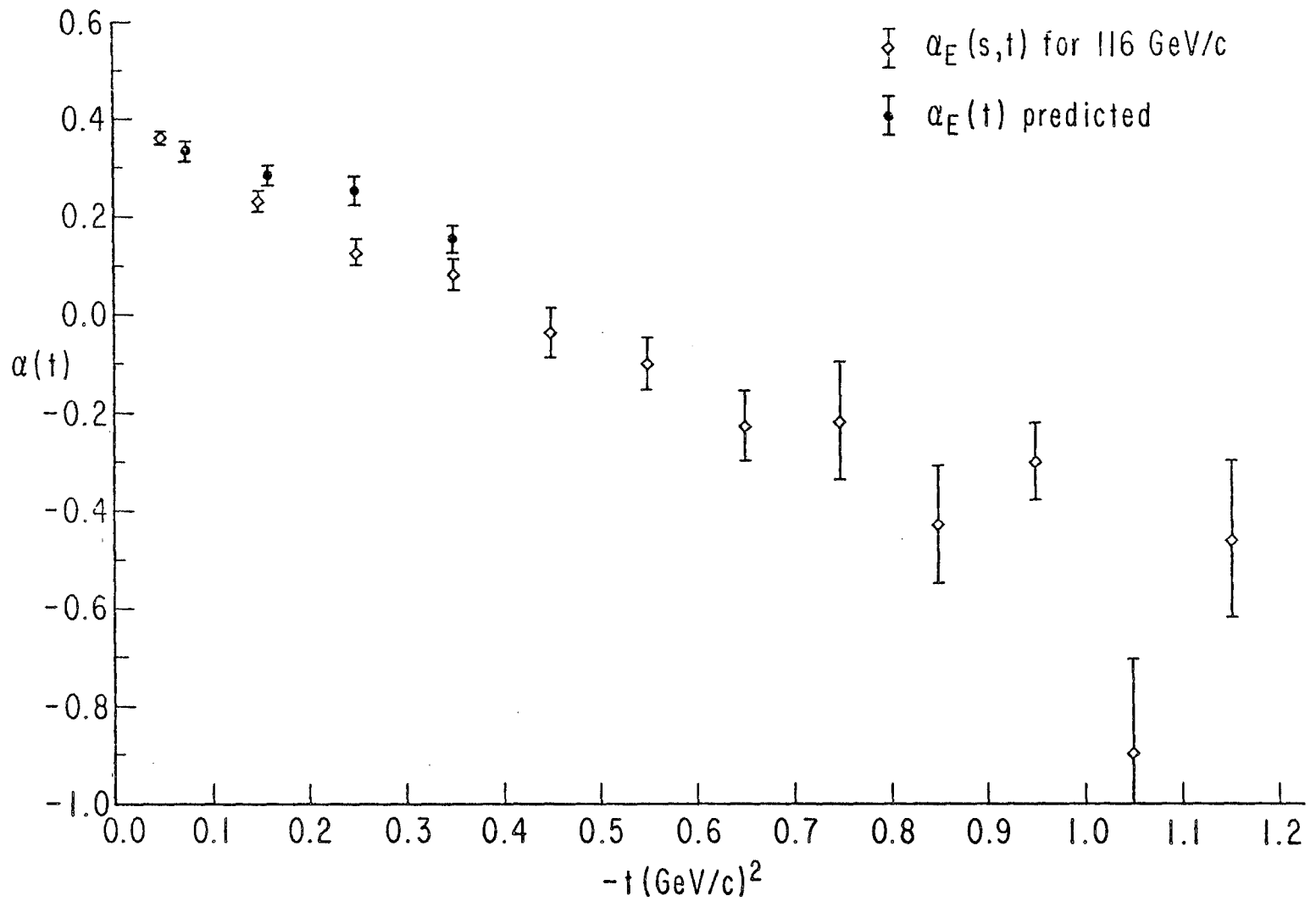


Figure 11. Effective Regge Trajectory, $\alpha_E(s, t)$, Compared with Prediction from Pion Charge Exchange.



Figures 12.1 - 12.5. Comparison of Some of our Cross-Sections at $s = 232 \text{ GeV}^2$ with the Corresponding Predictions using the Pion Charge Exchange Cross-Sections⁷ at $s = 200 \text{ GeV}^2$.

Figure 12.1: $-0.2 < t < -0.1 \text{ (GeV/c)}^2$

Figure 12.2: $-0.3 < t < -0.2 \text{ (GeV/c)}^2$

Figure 12.3: $-0.4 < t < -0.3 \text{ (GeV/c)}^2$

Figure 12.4: $-0.5 < t < -0.4 \text{ (GeV/c)}^2$

Figure 12.5: $-0.6 < t < -0.5 \text{ (GeV/c)}^2$

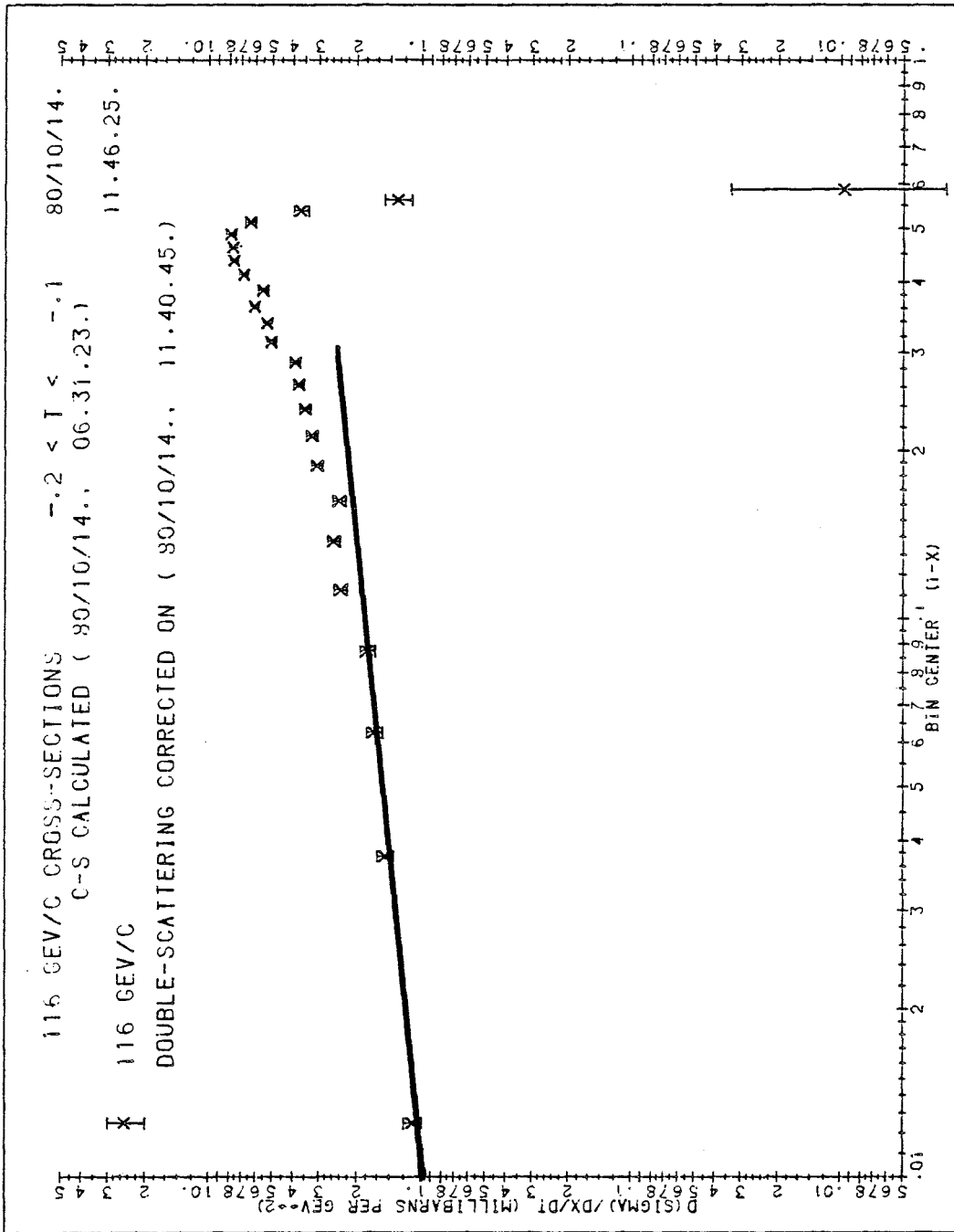


Figure 12.1: $-0.2 < t < -0.1 \text{ (GeV/c)}^2$

Figure 12.2: $-0.3 < t < -0.2$ (GeV/c)²

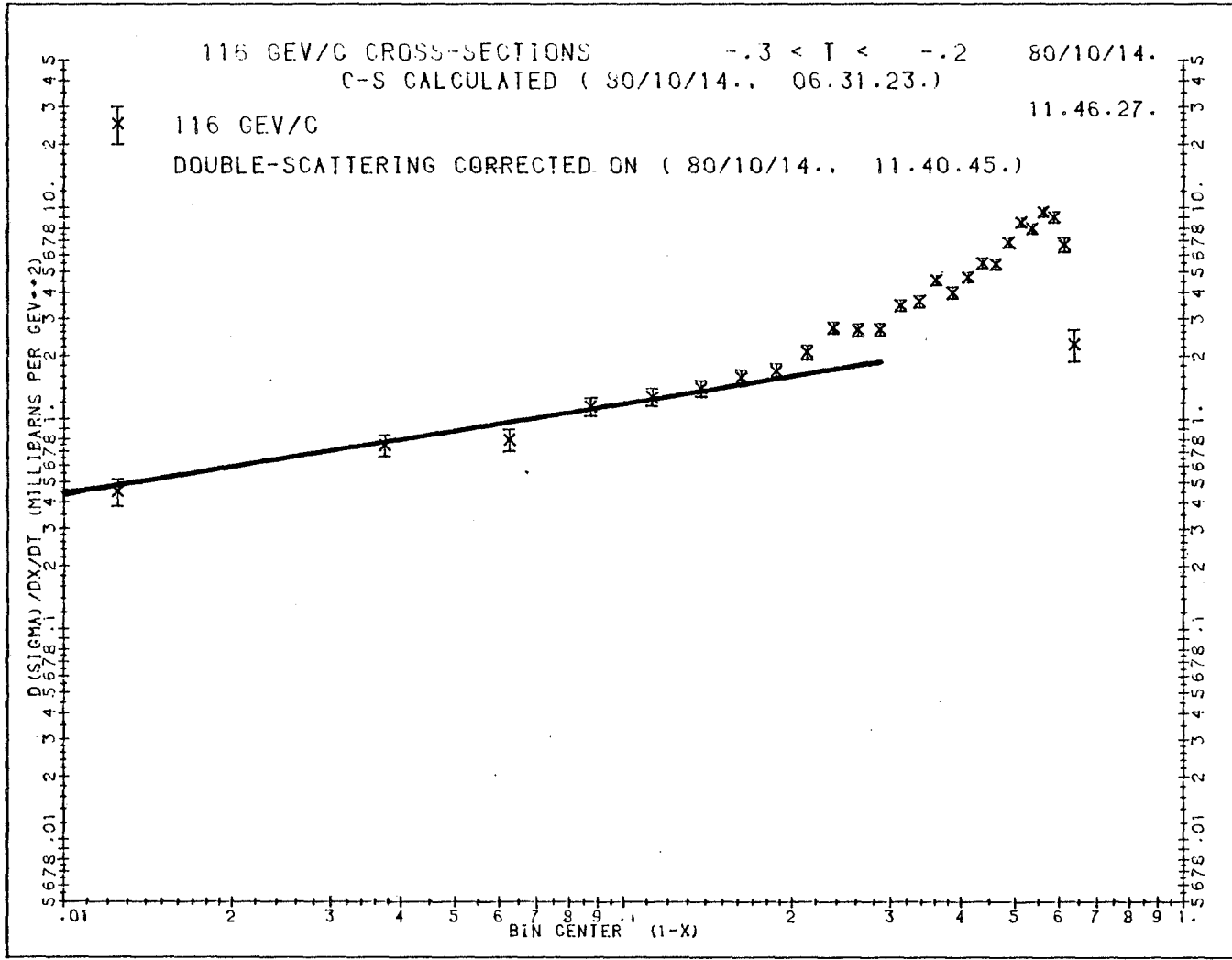


Figure 12.3: $-0.4 < t < -0.3$ (GeV/c)²

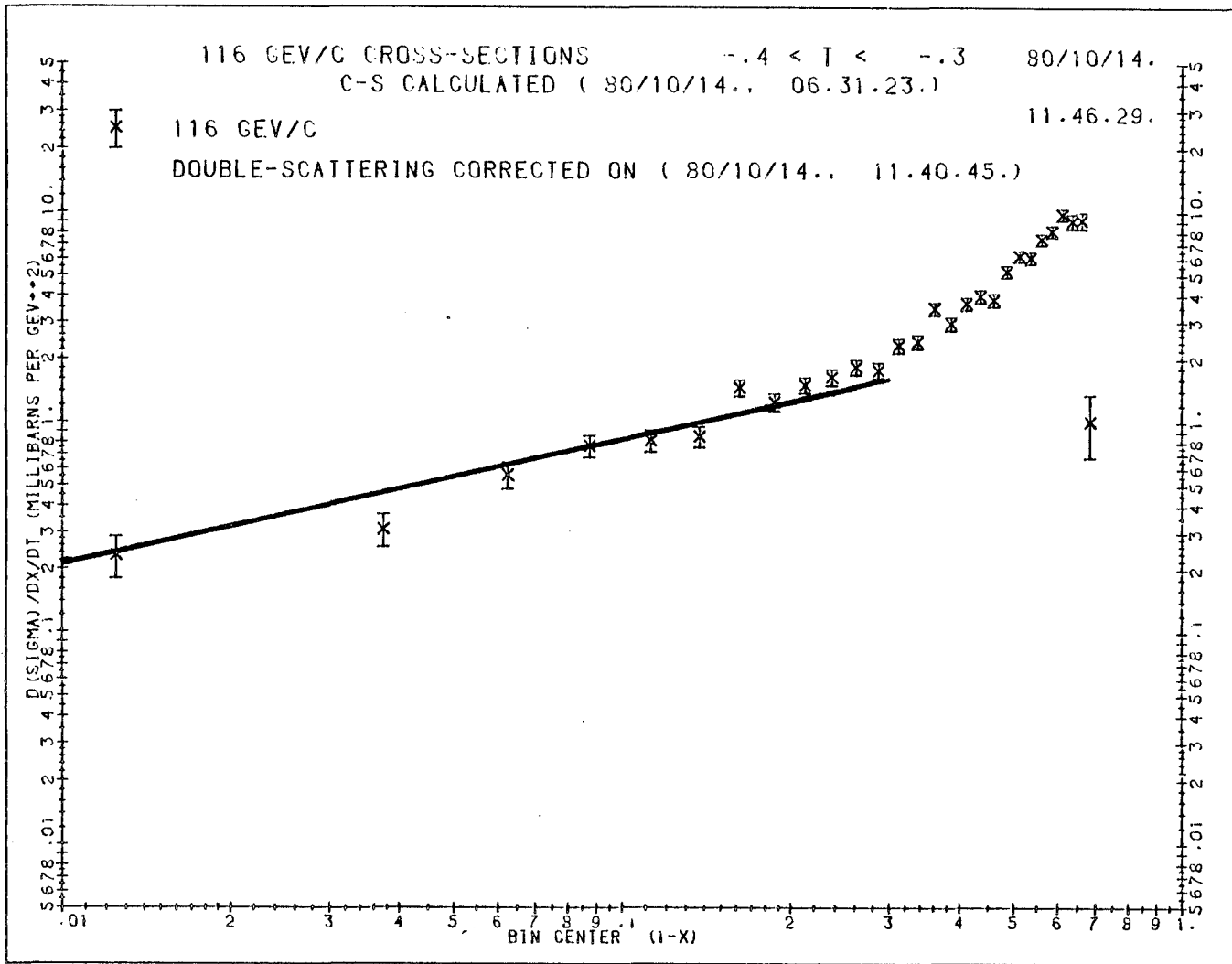


Figure 12.4: $-0.5 < t < -0.4$ (GeV/c)²

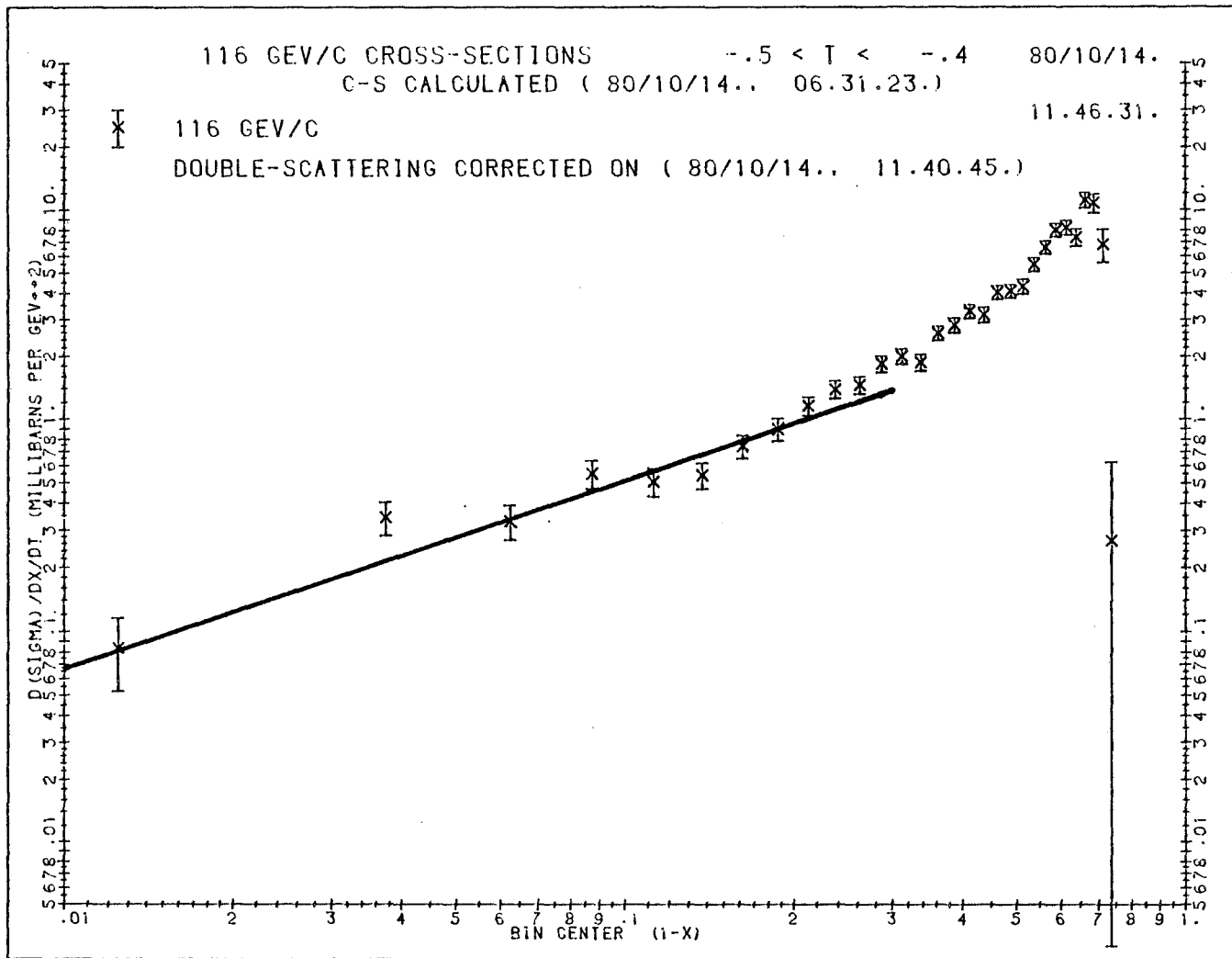
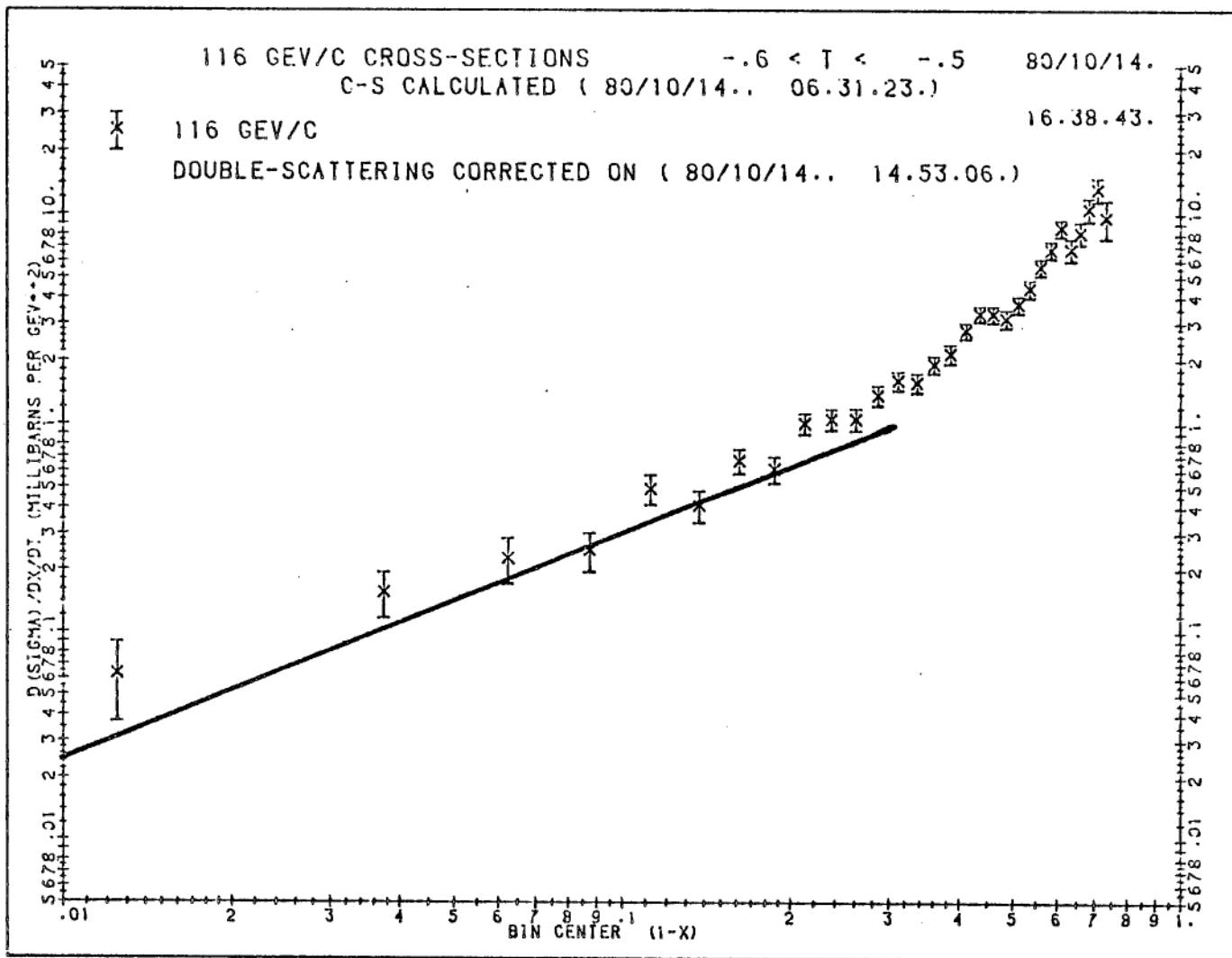


Figure 12.5: $-0.6 < t < -0.5$ (GeV/c)²



REFERENCES

1. A comprehensive study of all facets of Regge theory with references is contained in P. D. B. Collins, An Introduction to Regge Theory and High Energy Physics (Cambridge University Press, New York, 1977).
2. R. E. Hendrick, Phys. Rev. D11, 536 (1975).
3. J. Roehig et al., Phys. Rev. Lett. 38, 1116 (1977);
G. J. Bock et al., Phys. Rev. Lett. 42, 350 (1979).
4. A. V. Barnes et al., Phys. Rev. Lett. 37, 76 (1976);
O. I. Dahl et al., Phys. Rev. Lett. 37, 80 (1976).
5. A. Mueller, Phys. Rev. D2, 2963 (1970).
6. C. E. de Tar et al., Phys. Rev. Lett. 26, 675 (1971).
7. R. G. Kennett, "Experimental Tests of Triple Regge Theory," Ph.D. thesis, CALT-68-742 (1979).
8. A. Borg et al., Nuovo Cimento 22A, 559 (1974);
J. V. Beaupre et al., Nuc. Phys. B30, 381 (1971);
E. Simopovlov et al., Nuc. Phys. B96, 413 (1975);
R. Blokzijl et al., Nuc. Phys. B39, 141 (1972);
P. Bosetti et al., Nuc. Phys. B60, 307 (1973);
M. Deutschland et al., Nuc. Phys. B70, 189 (1974);
C. Cochet et al., Nuc. Phys. B124, 61 (1977).
9. P. Chliapnikov et al., Phys. Lett. 35B, 581 (1971);
A. Vayaki et al., Nuc. Phys. B58, 178 (1973);
K. Paler et al., Phys. Lett. 43B, 437 (1973);
P. Beilliere et al., Nuc. Phys. B90, 20 (1975).
10. From experiments, the effect of such cuts is known to be small. For a review of the theoretical and experimental evidence for cuts, see A. C. Irving and R. P. Worden, Physics Reports 34, 117 (1977).
11. Assuming that $B_n(t)$ factorizes, it can be rewritten

$$B_n(t) = \gamma_{AC}^n(t) \gamma_{BD}^n(t)$$

where γ_{AC}^i is the coupling constant for the ACi vertex, etc.

12. In the cross channel, s and t are evaluated using the negative of the physical 4-momenta of \bar{B} and \bar{C} .
13. R. D. Field and G. C. Fox, Nuc. Phys. B80, 367 (1974).
14. V. Barger and D. Cline, Phys. Rev. 156, 1522 (1967).
15. F. James and M. Roos, computer code MINUIT (CERN, 1971).
16. For a review of the experimental evidence concerning the Regge treatment of inclusive reactions, see S. N. Ganguli and D. P. Roy, Regge Phenomenology of Inclusive Reactions (Tata Institute of Fundamental Research, Bombay, India), 1980. (Preprint).

Appendix I

HADRON BEAM

When the kaon charge exchange experiments were first proposed, the Fermilab M4 line was operated as a neutral beam line, i. e. a straight line of collimators which selected a solid angle interval from the production target. The line also contained sweeping magnets to remove charged particles. Conversion of the M4 line was preferable to using existing charged hadron beams because the need to identify kaons and to tag phase space coordinates sets an upper limit on total flux at 10^6 to 10^7 particles per one second spill. The 7.25 milliradian production angle of the M4 line yields lower total hadron flux, but a higher fraction of kaons and antiprotons than existing beams produced at smaller angles.

The design of the beam was largely determined by physical constraints of the existing M4 line. The hadrons emerged from a beryllium target, $1.5 \text{ mm} \times 1.5 \text{ mm} \times 203 \text{ mm}$, which was in the extracted 400 GeV proton beam. The accepted solid angle and maximum momentum were determined by the strongest wide aperture quadrupole doublet which would fit in the pit in the Front End Hall. The image formed by the doublet was dispersed by a dipole. A slit collimator at the first image selected a 15% momentum spread; a second quadrupole doublet imaged the slit near the hydrogen target. Additional

dipoles steered the beam so as to result in zero transverse momentum dispersion at the final focus, and corrected for minor misalignments of quadrupoles. All elements following the first doublet were arranged so that no further aperture limitation occurred, at least at the design momentum. The behavior at the design momentum is only a guide; the longitudinal dispersion is such that at the highest transmitted momentum, the intermediate focus has moved downstream to the vicinity of the hydrogen target.

Figure 1 shows the optic axis and limiting rays from the Be target for both transverse axes. Table I gives the location of beam elements, fields, and the numerical data for Fig. 1.

TABLE I
The Charged M4 Beam

Z Distance in meters from production target
 $\int Bdz$ Field integral in kgauss·m in dipole or at 3.81 mm from quad axis
 Polarity Dipoles: + Negative particles are bent to beam left
 Quads: + Negative particles are focussed horizontally
 X Distance in cm from 'neutral beam line,' X > 0 → beam left
 θ_x, θ_y Half angle of envelope (x → horizontal, y → vertical) in milliradians
 $\Delta x, \Delta y$ Half width in cm of envelope

Fields are for 200 GeV/c particles.

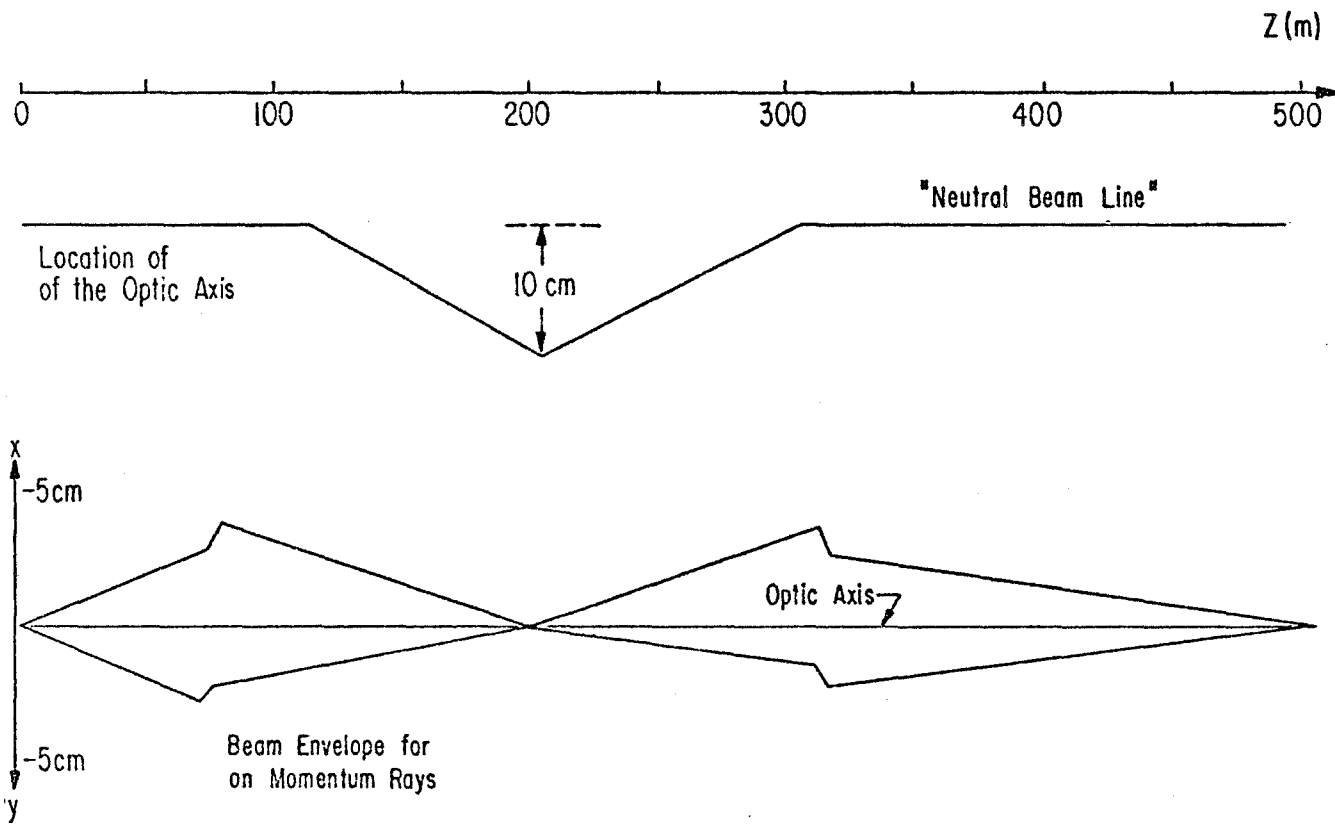
The envelope is determined by the C4 collimator (for "on momentum" particles).

The magnifications are:

	$\frac{x}{y}$	$\frac{y}{x}$
Target to Focus 1	1.16	2.26
Focus 1 to Focus 2	2.27	1.35

Z(m)	Name	$\int Bdz$	Polar	X	Δx	θ_x	Δy	θ_y
0	meson target				0.0	0.375	0.0	0.325
74.85	4Q1	24.43	-	0.0	3.28	3.21	2.14	1.90
78.32	4Q2	24.02	+	0.0	3.87	0.321	1.75	0.144
113.41	4B1	7.56	-	0.0	2.74	0.321	1.25	0.144
116.00	T4V1V	0.0		-0.34	2.69	0.321	1.23	0.144
117.86	4BS4							
200.16	S4C5			-9.83	0.0	0.321	0.02	0.144
201.68	S4C6			-10.0	0.05	0.321	0.0	0.144
204.72	4B2	7.56	+	-10.35	0.20	0.321	0.07	0.144
208.15	4B3	7.56	+	-10.17	0.31	0.321	0.12	0.144
210.60	T4V2H	0.65	-	-10.03	0.35	0.321	0.13	0.144
308.12	4B4	7.56	-	0.0	3.52	0.321	1.55	0.144
310.97	4Q3	8.91	+	0.0	3.49	0.916	1.63	0.700
312.95	4Q3A	8.91	+	0.0	3.22	2.090	1.810	1.305
315.19	4Q4	8.77	-	0.0	2.83	1.076	2.05	0.620
317.16	4Q4A	8.77	-	0.0	2.69	0.136	2.12	0.107
318.79	T4V3H	0.65	+	0.0	2.67	0.136	2.10	0.107
320.05	T4V4V	0.0		0.0	2.65	0.136	2.09	0.107
485.29	4B5	36.2	+	0.85	0.56	0.136	0.28	0.107
511.89	4B6	36.2	-	0.13	0.04	0.136	0.03	0.107
516.11	H2 target			0.13	0.0	0.136	0.0	0.107

Figure I. 1. The M4 Beam Line.



Appendix II

ČERENKOV COUNTER

Identification of kaons in an incident beam which also contains pions and antiprotons was accomplished with a differential Čerenkov counter. Table I gives some useful relations for such counters.

Our counter, patterned after a design by S. Pruss of Fermilab, uses a 2.5 meter focal length primary mirror to image the Čerenkov ring off of the beam line. The ring image is formed on a secondary mirror which has a circular hole concentric with the reflected beam axis. The radius of the hole provides a velocity discrimination level; particles whose velocity is above the Čerenkov threshold but below the hole threshold (kaons) radiate light to a phototube (PM1) located behind the hole, while particles whose velocity is above the hole threshold radiate light onto the secondary mirror. The secondary mirror is a field optic to reflect light into a second phototube (PM2). (See Fig. 1.)

In principle, such a counter can be operated at any radiator density (index of refraction) for which the kaons radiate Čerenkov light. In practice, a lower bound is set by the requirement that the counter be efficient (we require at least six photoelectrons for the kaons). An upper bound results from the reduced angular separation of pion and kaon light as the radiator density is increased. One loses the ability to discriminate particle type as this difference approaches the Čerenkov light angular spread resulting from angular and momentum spread of the particle beam, spherical aberration of the primary mirror, dispersion of the radiator, and thermal stability of the radiator density. In practice, an optimum density was at about twice the threshold for kaons. Table II summarizes some typical operating parameters.

The counter had some special design features to enhance its operation.

1) The radiator was always below atmospheric pressure. Oxygen leaks destroy the counter efficiency by ultraviolet absorption long before a significant density change occurs. We therefore used double O ring seals and maintained a vacuum between the two seals.

2) The A parameter was kept high by using quartz windows, C31000M phototubes, and an MgF_2 coat on the mirrors.

3) At high energies the radiator is He. The phototubes were behind double windows with vacuum in between to prevent He diffusion into the phototubes.

Most of the radiator was contained in a 75 meter beam pipe. At most energies, the effective radiator length was determined by the Čerenkov angle and the 15 cm radius of the primary mirror.

As used in the experiment; the counter was easily tuned to give excellent discrimination between kaons and pions. The pulse height distributions were consistent with about six photoelectrons; the discrimination of pions and kaons can be judged from the scatter plot of kaon pulse height vs pion pulse height in Fig. 2. The few events representing a signal in both phototubes are legitimate two particle traversals.

TABLE I
Useful Relations

Čerenkov angle

$$\theta^2 = 2(n-1) - m^2 c^2 / p^2$$

Index of refraction vs pressure (20°C)

$$n-1 = 33 \times 10^{-6} P(\text{atm}) \text{ (He)}$$

$$= 287 \times 10^{-6} P(\text{atm}) \text{ (N}_2\text{)}$$

Number of photoelectrons

$$N = AL \theta^2 \quad A \sim 100 \text{ to } 150 \text{ cm}^{-1} \text{ for good phototubes and optics}$$

TABLE II
Operating Parameters

Momentum (GeV/c)	175	125	75
$n-1 (\times 10^6)$	7.0	12.8	45.3
Pressure (atm)	0.21 He	0.39 He	0.16 N ₂
θ_k (mr)	2.4	3.1	6.8
θ_π (mr)	3.6	4.9	9.3
$\Delta \theta$ (mr)	1.2	1.8	2.5
N (kaons)	5.4	7.0	11.0
For 5% pressure shift			
$\Delta \theta_k$ (mr)	0.15	0.21	0.33
$\Delta \theta_\pi$ (mr)	0.10	0.13	0.24
For 10% momentum shift			
$\Delta \theta_k$ (mr)	0.34	0.51	0.65
$\Delta \theta_\pi$ (mr)	0.18	0.25	0.37
Multiple scattering (μr)	4.7	8.9	18

Figure II. 1. Details of the Cherenkov Counter Optics.

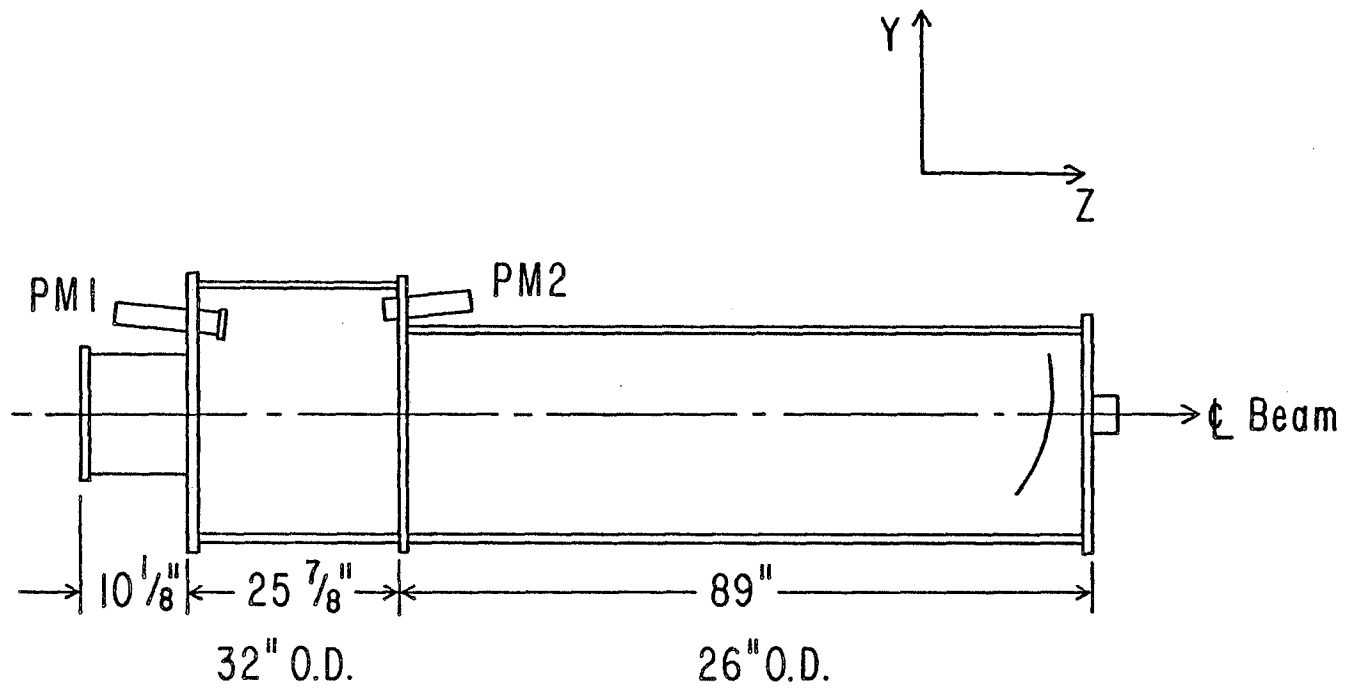
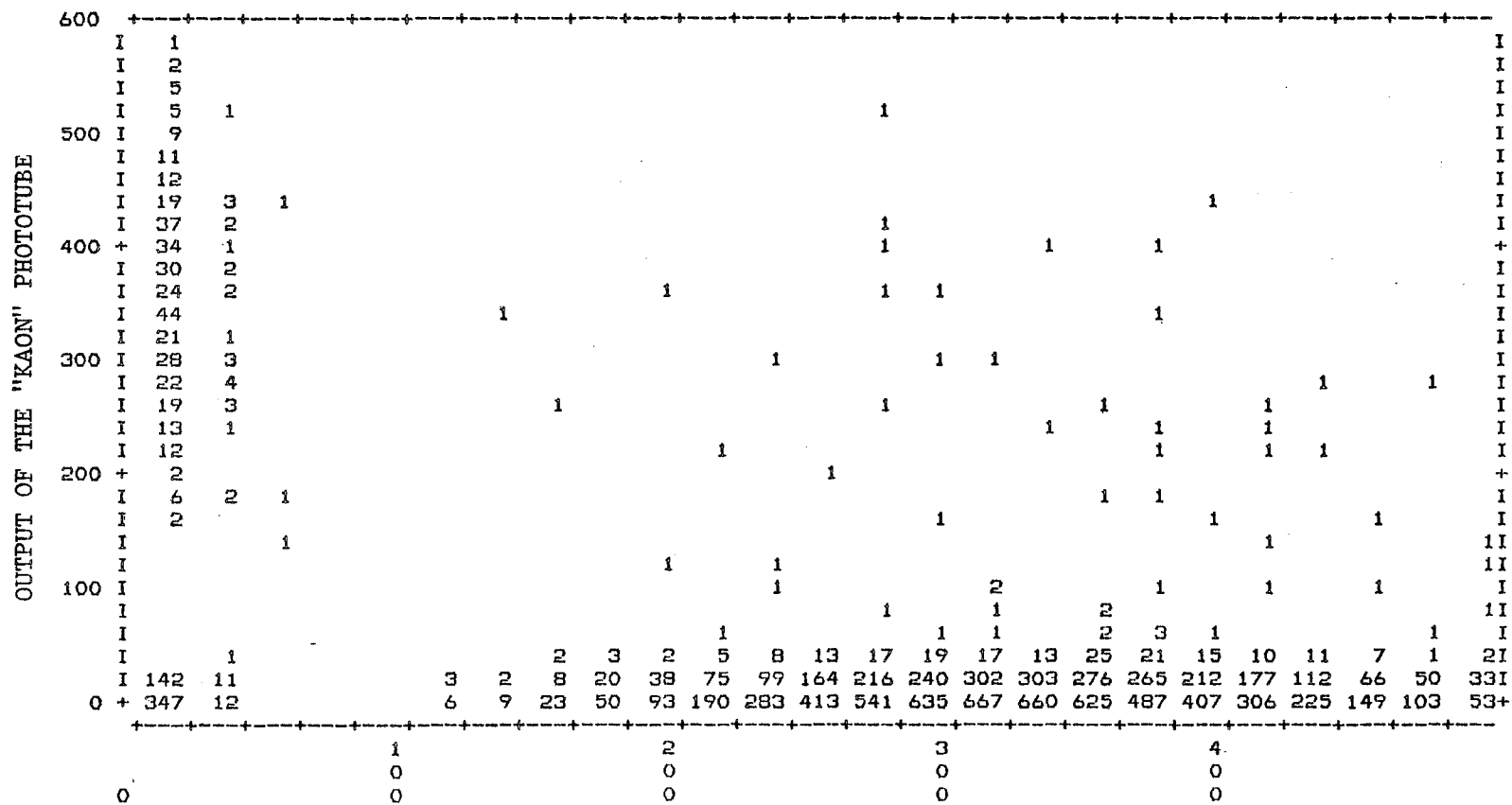


Figure II. 2. Response of the Cherenkov Counter to the M4 Beam.

Plotted is the pulse height in the PION tube versus the pulse height in the KAON tube.

The lower, right hand cluster is due to pions. The upper, left hand cluster is due to kaons. The lower, left hand cluster is due to anti-protons.

Total number of entries: 9,735.



OUTPUT OF THE "PION" PHOTOTUBE

Appendix III

BEAM SPECTROMETER

To determine the presence of a beam particle, as well as to measure its momentum and to ascertain that it was kaon, we used a spectrometer consisting of a differential Cerenkov counter (see Appendix II),, scintillation counters and a magnetic spectrometer (Figure 1).

Three small scintillation counters in coincidence registered the fact that a charged particle went down the beam line. A large ($10 \times 31 \text{ cm}^2$) scintillator with a hole surrounding the beam was used to suppress beam particles accompanied by halo particles. (See Appendix VII).

To determine the vector momentum of each beam particle we used a set of eight proportional wire chamber planes (four (x, y) pairs) and two bending magnets.

The two magnets were excited in series with opposite and equal field integrals. Thus the overall effect of the pair of magnets on the beam was to displace it parallel to itself by 150 mm to beam left.

The wire chambers, deployed in four (x, y) pairs, two upstream and two downstream of the first magnet, were used to determine particle trajectories. These chambers (type A beam chambers,

built by the Fermilab Research Services Department) had an anode plane of 64 wires, spaced 1 mm apart, and two cathode planes of aluminum foil. The wires were 12 micron gold plated tungsten and the anode to cathode spacing was 3 mm. We used a gas mixture of 20% CO₂, 0.15% Freon 13B1 and argon to balance. Under those conditions the standard operating voltage was 5.8 kV.

The signal on a wire, after amplification, was shaped by a one-shot whose output width was 300 ns. The output of the 64 one-shots in one plane were processed by an address encoder as follows. The presence of a signal from at least one wire (the OR of all the channels) started the encoding process and temporarily disabled all the inputs. Logic circuits constructed from MECL priority encoding chips determined the address of the first hit encountered in a search from either end of the bit pattern which represented the state of the wires. The larger of the two addresses together with three status bits were latched into a coincidence register. If status bit 1, 2 or 3 was set, we had, respectively, a hit on a single wire, hits on two adjacent wires or other multiwire hit combinations. Events without a set status bit, with multiply-set status bits or with bit 3 set were rejected. Consequently we did not accept events with more than one recorded beam particle. Appropriate corrections were made to the normalization in the cross section determinations. At the end of the encoding process the input to the encoder was reenabled. The dead time for each

encoding process was 400 ns, hence the experiment as a whole was disabled for 450 ns every time a beam particle was detected.

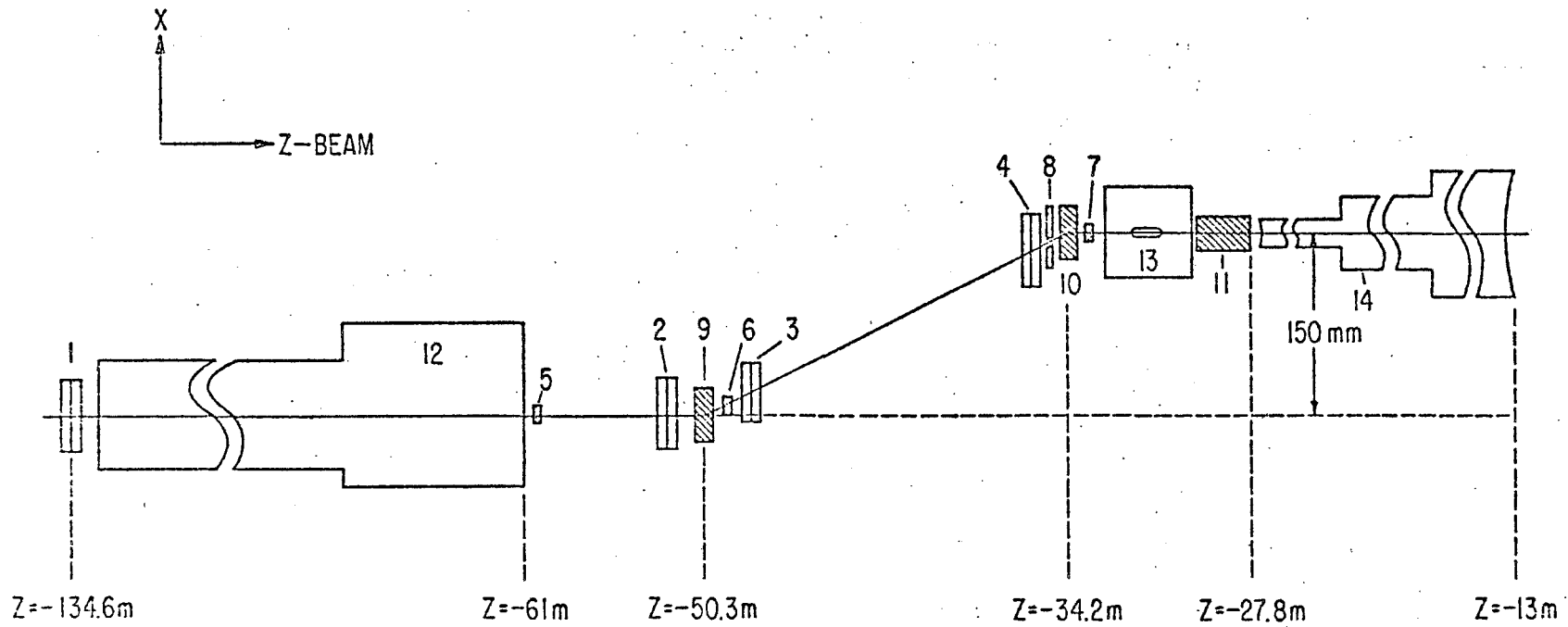
On Table I we give the typical performance parameters of this system. The efficiency quoted here is a result of both the performance of the wire chambers and the characteristics of the encoders. The chambers and their encoders were built and maintained by M. Haldeman, W. Haynes and T. Soszynski of the Fermilab Research Services Department. We gratefully acknowledge their contribution to this experiment. Further details of the M4 beam can be found in Appendix I.

TABLE I
Beam Chamber Spectrometer Resolutions

P	X'(rad)	Y'(rad)	$\delta P/P$
68	51.5	52.1	0.0047
116	31.7	31.1	0.0038
176	20.7	20.3	0.0036

Figure III.1. Beam Spectrometer.

- 1-4 (X, Y) proportional wire chambers
- 5 B1 counter
- 6 B2 counter
- 7 B3 counter
- 8 Halo counter
- 9, 10 EPB magnets
- 11 Sweeping magnet
- 12 Cherenkov counter
- 13 Hydrogen target
- 14 Vacuum decay pipe



BEAM SPECTROMETER (Plan View)

Appendix IV

LIQUID HYDROGEN TARGET

This experiment used a liquid hydrogen target built by the Hydrogen Target Group at Fermilab. The target consisted of two flasks, a reservoir and a refrigerator; all in a vacuum vessel (see Figure 1). Table I gives the target specifications of interest to this analysis.

TABLE I

Flask lengths	25.4 and 45.7 cm (at STP)
Flask diameter	5.1 cm
Flask material	0.127 mm Mylar
Upstream vacuum window	0.127 mm Mylar
Foam vacuum vessel	1.91 cm foam and 0.254 mm Mylar on the side tapering to 1.27 cm foam and 0.127 mm Mylar on the ends

When cold, with the vacuum vessel evacuated, the flasks contracted by 0.3%. During the run, the target vapor pressure was 15 psi, implying a density of 0.0708 gm/cm.

Figure IV.1. Liquid Hydrogen Target.

Appendix V

MULTIWIRE PROPORTIONAL CHAMBER

Construction

The proportional wire chamber part of the downstream spectrometer consisted of three stations, each with two separate modules. The sense wires of one module were oriented at ninety degrees to the sense wires of the other module in the same station.

The characteristics of each module were:

1. It had a separate gas enclosure. The windows were 0.051 mm thick Aclar (type 3C). The seals along the edges were RTV.
2. It consisted of one sense wire (anode) plane located between two high voltage (cathode) planes. The spacing between sense wires was 2.0 mm. The spacing between the high voltage wires was 1.0 mm. The sense wires were 20 or 25 micron gold-plated tungsten stretched to 45 gram tension. The high voltage wires were 0.064 mm phosphor-bronze stretched to 150 gram tension. The spacing between the anode and each of the cathode planes was 6 mm. The high voltage wires were oriented at ninety degrees to the sense wires.
3. The high voltage wires were soldered to a common pad which extended through the gas seal to the outside.
4. The sense wires were imbedded inside an epoxy pad (Epon 815, V40 hardener). This pad provided the support for the wires as well as the gas seal. Once on the outside, the wires were soldered to individual pads on a printed circuit board which was part of the mechanical structure of the module.
5. There were four different types of chamber module:

		<u>Sense wire diameter</u>	<u>Total number of wires</u>
upstream	X	25 microns	576
upstream	Y	25 microns	384
downstream	X	20 microns	768
downstream	Y	20 microns	576

The upstream modules had a support wire (AWG 30 wire-wrap wire) located along the center line perpendicular to the sense wires. The support wire was glued with Humiseal type 1A27 to each sense wire and was brought to the outside. The 576-wire module had two such wires located 1/3 of the sense wire length from the edge of the plane. The 768-wire module had three such wires, one located in the center, and the others each 1/4 of the sense wire length from the edge of the plane.

To eliminate electromechanical instabilities, the sense wire planes were "terminated" by grading the radii of the outside wires in each plane as shown in Figure 1.

Each module was set up approximately centered on the beamline. For each station, the X and Y modules had their sense wires oriented at right angles to each other, accurate to about 100 microradians. In E-383, the first station (P1U, P1V) was rotated as a unit so that the Y module wires were at 45 degrees to the vertical, with their upper end to beam left. Again, this alignment was accurate to about 100 microradians. All other stations had their modules aligned such that their Y wires were vertical to within 100 microradians.

Gas and High Voltage

The gas used in these chambers was the mixture:

CO₂:20%, Freon 13B1: 0.15%, Argon: balance

We bought this mixture from Matheson, without requesting a special analysis, for \$51 per 200 cubic foot container (1980 price). We had some

problems with defective valves. The gas for each chamber was monitored by a separate flowmeter. The gas pressure for all chambers was regulated to 3.5 psi at the input to the flowmeter valve. A small back pressure was developed in each module by a "drag line" (3 feet of 1/4" tubing). Except under testing conditions, bubblers were not used. The gas consumption appears to have been determined by macroscopic leaks along the chamber edges. The set of proportional chambers used in E-383 had a total volume of about 12 cubic feet and was operated at a gas flow of about 1.7 cubic feet per hour during normal running conditions.

Under these conditions, the upstream chambers (25 micron sense wires) would plateau at 4.7-4.8 KV and the downstream chambers (20 micron sense wires) at 3.9-4.0 KV. Each module was powered by a Fermilab No. ES-7109 power supply through a 10 megohm resistor. These supplies were protected against fast and slow current excursions. Between beam spills each module would draw between 20 and 100 nanoamperes. During the beam spill, at one million particles per second through the chambers, the average current drawn from the supply was 1-3 microamperes.

Design problems caused the current drawn from the supply to rise to several milliamperes during conditions of high humidity. Flowing warm air over the exposed high voltage surfaces reduced the leakage current to its normal value.

Read-out System

The information about the coordinates of the point of traversal of a particle through the chamber was processed as follows (see Figure 2).

A particle generated a few ionization electrons in the gas. The electric field between the wire planes swept those electrons towards the closest sense wire. When the particle traversed the chamber "about half way" between two adjacent wires, the ionization electrons were shared between those two wires. Depending on operating conditions, this "central area" constituted 10-20% of the space between wires. In the region

within about 100 microns from the center of the wire the field was large enough to cause further ionization (gas amplification). These electrons generated a signal at the input to the amplifier A. Inputs in excess of about 10-30 fC gave a standard output (+3.5 V, 60 ns wide) which would trigger the one-shot B. This one-shot was used as an adjustable delay. This delay allowed the particle which generated the signal on the wire, to be processed by a fast trigger logic system to decide whether the wire signal should be stored for further processing. The delayed wire signal (trailing edge of the one-shot output) and the trigger logic output were processed by a coincidence gate whose output was latched. The latches for all the wires were arranged into one long shift register chain.

The output of the trigger logic, used to latch the wire signal, was also used to start further processing of the latched data and to send an interrupt to the interface of the data acquisition computer, thus initiating the transfer of the data to magnetic tape.

When the number of hits was small compared to the number of wires in the detector, it was more economical to transmit addresses of hit clusters rather than a binary image of the wire system. This conversion was done by the "scanner module."

A 5 MHz clock train was generated in the scanner and transmitted to the far end of the detector. From there, two transmission lines (part of one physical cable) went as a "daisy chain" from detector module to detector module and eventually back to the scanner. One line ("clock line") transmitted the clock train which stepped the shift registers, the other ("data line") connected the shift registers from one module to those from the next one and eventually the output of the "last" shift register to the scanner. Thus, at the input to the scanner, we received, in synchronism, the Nth pulse of the returning clock train and the original state of the Nth latch in the shift register (i.e. the output of the shift register chain after N steps). The cumulative count of the clock pulses at the input to the scanner was the address of the wire whose state was currently on the data

line. The scanner contained a 64 word memory. At the end of this procedure ("the scan") this memory contained the address of the last wire of each hit cluster together with the cluster length.

The interrupt, generated by the output of the trigger logic, initiated the transfer of the data stored in the scanner, as well as data stored in other modules (scalers, ADC's, spark chamber digitizers, etc.), to the computer memory, using standard CAMAC protocol.

The proportional chambers were built at the Carleton University Physical Sciences Shop under the direction of Louis Raffner. The readout electronics was designed by Thomas Nunamaker and was purchased from Nanometric Systems, Inc.

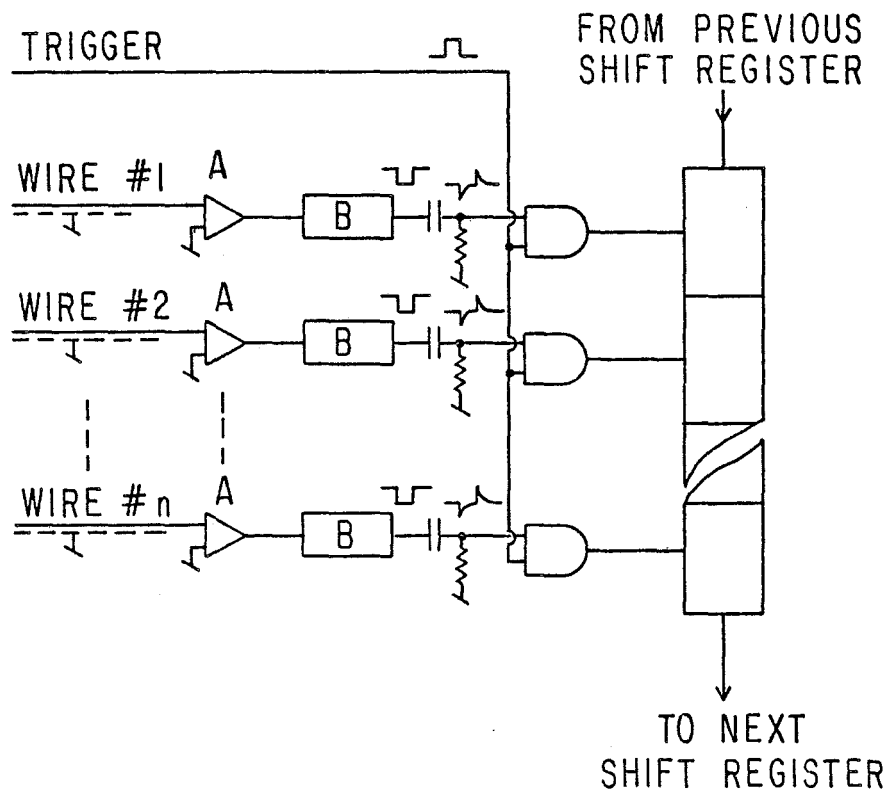
Figure V.1. "Termination" of Sense Wire Planes.



- - 250μ BERYLLIUM COPPER, 1000 g TENSION
- - 125μ BERYLLIUM COPPER, 600 g TENSION
- - $20/25\mu$ GOLD PLATED TUNGSTEN, 45 g TENSION
(STANDARD ANODE WIRE)

Figure V.2. Proportional Wire Chamber Readout Logic.

- A. Amplifier
- B. One-shot



Appendix VI
WIRE SPARK CHAMBERS

The downstream spectrometer included 24 planes of spark chambers, mounted in five stations (see Fig. 1). The upstream three chamber stations each had two smaller modules. The first station downstream of the analysis magnet had two larger modules; the last station had one module. The upstream chambers had two mutually orthogonal wire planes in one gas enclosure. The downstream chambers had two mutually orthogonal wire planes in one gas enclosure (X,Y) and two planes at a relative angle of 60° in another gas enclosure (U,V). All chambers were mounted so that the mutually orthogonal wires were horizontal and vertical. In this orientation, the downstream (U,V) planes were oriented at $\pm 30^{\circ}$ from vertical.

Spark Chamber Specifications

	<u>Upstream</u>	<u>Downstream</u>
Active area	123 by 59 cm	150 by 100 cm
Wire spacing	1 mm	1 mm
Wire diameter	0.027 mm	0.229 mm
Gap	1 cm	1 cm

Note: The downstream wires were woven with 0.229 mm. nylon in a "window screen" mesh.

All wires were embedded in an epoxy pad on the frame which also served as a gas seal. At one end the wires came through the pad and were soldered to

a copper bus. Each pair of planes had one bus at ground and one bus pulsed to negative high voltage.

The high voltage pulse was produced by discharging coaxial lines through a thyratron (See Fig. 2). This produced a 200 ns pulse. In the upstream chambers, each gap had an impedance of 5Ω and was driven by three lines. In the downstream chambers, each gap had an impedance of 4Ω and was driven by four lines. The lines were charged to 9.5 kV, giving a peak of approximately 4.7 kV on each gap. The shape and peak value of the high voltage pulse could be adjusted by varying the termination resistance on each gap. We kept the high voltage pulse repetition rate at or below 100 Hz with a duty cycle at or below 10%. (1 sec. on, 9 secs. off).

After each pulse, a -400 V, 2 ms long pulse was applied to the chamber to sweep out residual ions. This pulse was superimposed on a D.C. clearing voltage of -75 V.

The chambers used a standard mixture of 90% Neon/10% Helium. Flow to each chamber was monitored by a flowmeter. The gas was bubbled through a flask of ethanol (kept at $4^{\circ}\text{C}.$) to inhibit the formation of secondary sparks caused by ultraviolet emission from the primary sparks. The chambers needed a substantial gas flow for proper operation; there was evidence that this was due to contamination produced by sparks. We used one 220 cubic feet cylinder of gas in a normal day.

These chambers used a magnetostrictive read-out system. Magnetostriction is the phenomenon in which a change in the magnetization of a substance changes its physical dimensions.¹ Each chamber had a magnetostrictive wire "ribbon", supported by an aluminum "wand", insulated, and clamped on the chamber wires between the bus and the epoxy pad. The current along a chamber wire from a spark formed a magnetic pulse which caused a

mechanical deformation, an "acoustic pulse", which propagated along the ribbon in both directions at a velocity of about 6 cm/ μ s. At each end, the pulse was absorbed to prevent reflections. At one end, a small pick-up coil detected the change in flux as the pulse caused a change in the magnetization of the ribbon. At each end of each wire plane, a fiducial wire was installed. This wire was located between the wand and the chamber frame. Each high voltage pulse produced a current pulse in each fiducial wire.

The output of each pick-up coil was amplified and sent to a digitizing system designed and built by F. Kirsten at Lawrence Berkeley Laboratory.² This system consisted of a clock module, discriminator and digitizing modules. The clock module produced a 25 MHz pulse train. Each amplified wand signal was input to a discriminator which produced an output pulse at the time of arrival of the peak of the input signal. The digitized spark (or fiducial) coordinate, equal to the number of clock pulses between a common start and the time of arrival of the discriminator output at the digitizer input, was stored in a memory. Each channel could record as many as sixteen coordinates.

Using the known distance between fiducial wires and the time difference between the arrival of the fiducial pulses, the ribbon propagation velocity was calculated. The time difference between a spark pulse and a fiducial pulse could thus be converted to the distance of the spark from the fiducial wire.

The contents of the memories were transferred, along with the rest of the event information, to the computer memory, using standard CAMAC protocol.

Some "typical" chamber efficiencies are shown in Table I.

References

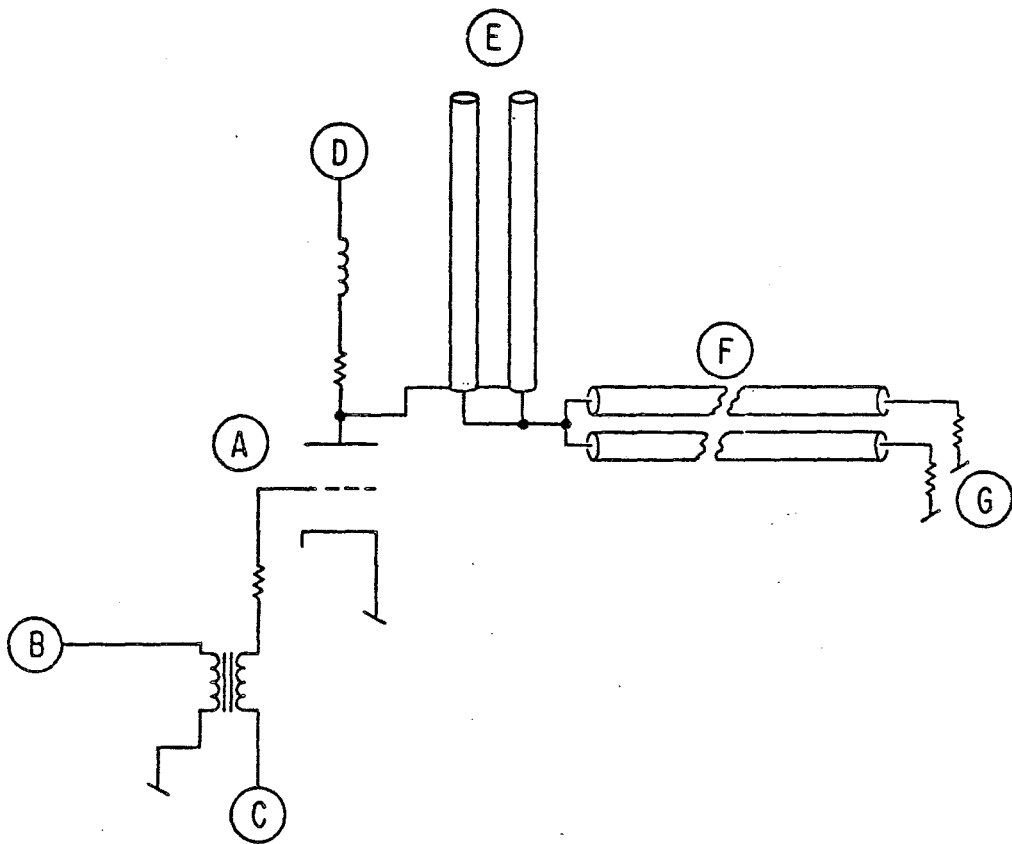
1. P. Rice-Evans, Spark, Streamer, Proportional and Drift Chambers, (Richelieu, London, 1974), pp. 149-155.
2. F. A. Kirsten, LBL Engineering, Note No. EET-1394, 1972.

TABLE I
Spark Chamber Efficiencies

Plane	Run 79	Run 273	Run 40B
1	.88	.91	.84
2	.93	.94	.85
3	.96	.94	.89
4	.78	.78	.84
5	.97	.98	.96
6	.95	.96	.96
8	.92	.98	.96
9	.96	.98	.97
10	.94	.97	.96
11	.87	.89	.90
13	.83	.95	.93
14	.94	.93	.96
15	.83	.79	.89
16	.98	.99	.98
17	.97	.96	.97
19	.95	.98	.97
20	.99	.98	.99
21	.90	.93	.90

Figure VI. 1. High Voltage Pulser for the Spark Chamber.

- A. Thyratron
- B. Trigger signal
- C. Bias voltage supply
- D. High voltage supply
- E. Energy storage and pulse forming cables
- F. Transmission line
- G. Effective termination provided by the spark chamber



Appendix VII
TRIGGER COUNTERS AND LOGIC

The scintillation counters and wire chambers, the sources of signals for the trigger logic, are shown in Fig. 1. In this Appendix we use the following notation for these sources:

B_1, B_2, B_3 Three small scintillation counters mounted along the incident beam line.

K Output of the Cherenkov counter (Appendix II) when traversed by a kaon.

H Scintillation counter surrounding the beam, which indicated the presence of a particle(s) outside the beam phase space ("halo").

I_1, \dots, I_{16} Sixteen scintillation counters, mounted to form a 1.5 m. by 1.2 m. wall which covered the downstream aperture of the detector, except the beam region ("I-counters")

$I = \sum_{i=1}^{16} I_i$: Logical sum of the signals from all the I-counters. I indicated that there was at least one charged particle outside the beam region

B5 Small scintillation counter covering the region where the beam intersected the first chamber station. A hit on this counter was either a non-interacting beam particle or a beam particle which had undergone elastic scattering or diffractive dissociation.

- P_1, \dots, P_6 Analog counting circuits which processed the outputs of the proportional chamber amplifiers, in groups of four. Its output was a pulse, 100 ns wide, whose amplitude was proportional to the number of groups struck. Excluded from this logic were wires in the beam region.
- P Logical combination of P_1, \dots, P_6 which indicates that there were at least two "hits" in at least one of the two planes of each station.
- V "Veto" level, which inhibited the trigger during the periods when the experiment was not "live". Examples of "dead" periods are: data acquisition periods, times when the beam chamber encoders were active, settling periods for ADC's after clearing, etc.

The logical combination of these signals to form a trigger is illustrated in Fig. 2 and can be described as taking place in the following stages:

1. Is there a beam kaon while the experiment was "live"? If so, then count it (beam flux normalization) and proceed to the next state. The beam flux can be expressed:

$$\phi_K = B_1 \cdot B_2 \cdot B_3 \cdot \bar{H} \cdot \bar{V} \cdot K$$

2. Has the beam kaon interacted in the target in what could be the desired charge exchange interaction, i.e., is there at least one charged track outside and no charged track inside the beam region? If so, latch the ADC's and coincidence registers and proceed to the next stage. The interaction signal can be expressed:

$$IT = \phi_K \cdot I \cdot \bar{B5}$$

3. Given an interaction signal, is it consistent with a $(K_S \rightarrow \pi^+ + \pi^-)$ decay in the detector, i.e., are there at least two hits at each PWC station? If so, then trigger the spark chambers and the data acquisition system. If not, then clear the ADC's and the coincidence registers. The final trigger can be expressed:

$$FT = P \cdot IT$$

To monitor the operation of the detector and to acquire the data needed to estimate losses due to accidental vetoes, signal rates at all stages of the logic circuits were continuously monitored. Table I shows the cumulative signal counts at representative stages in the logic.

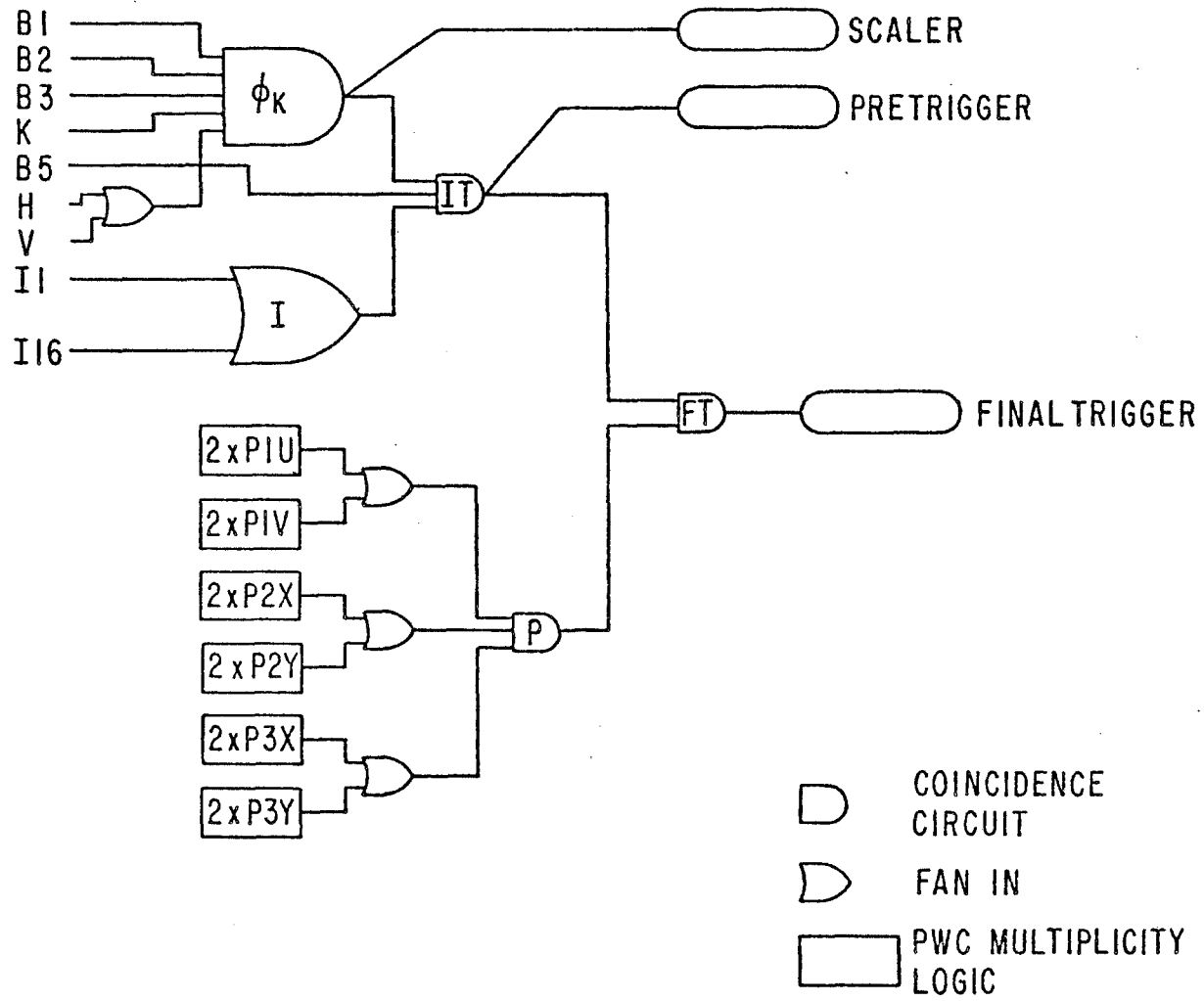
TABLE I

Cumulative Signal Counts

<u>Signal</u>	<u>68 GeV/c</u>	<u>116 GeV/c</u>	<u>176 GeV/c</u>
Beam	11,150 M	9,880 M	6,330 M
Φ_K	286 M	251 M	201 M
IT	22,700 K	15,800 K	12,100 K
FT	785 K	1,710 K	2,550 K
Raw K	11,141	49,747	115,057
Good K	8,335	34,213	68,987

Figure VII. 1. Trigger Logic.

See text for definition of symbols.



Appendix VIII

PATTERN RECOGNITION/TRACK FITTING

The final trigger logic signal (FT), initiates the recording of the state of all detector modules on magnetic tape. From this information, the off-line analysis system must sift out, with high and accurately known efficiency, the events which show a $K_S \rightarrow \pi^+ + \pi^-$ decay and determine its kinematic parameters. This is done in two major steps:

1. Using only the information from the wire chambers, we reconstruct straight-line track segments in each of the (upstream/downstream) parts of the two spectrometers. Details of this procedure are given below.
2. Given the track segments and the stored information from the non-chamber part of the detector, we sift out the desired process ($K^- + p \rightarrow \overline{K^0} + X$) from triggers resulting from other processes. Details for this procedure are given in Appendix IX.

The search for the track in the beam spectrometer is simplified by the fact (see Appendix III) that only one hit (or hit cluster) per plane could be recorded. The reconstruction of the vector momentum of the particle which generated such a track is straightforward. Consistency checks between the redundant pieces of information are detailed in Appendix XII.

In the forward spectrometer, we have the possibilities of

1. Several tracks, not necessarily with recorded hits in all wire planes, associated with the event which generated the trigger.
2. Tracks, usually recorded rather inefficiently, from particles not associated with the event which generated the trigger.
3. Hits not associated in any obvious manner with a track.

The track-finding procedure uses a computer algorithm which finds the combinations of hits which form tracks. It is important to locate all the tracks regardless of the kinematic configuration of the event and of the number of extraneous hits and tracks present (extraneous information changes in amount and character with the beam energy). While inefficiencies of this algorithm due to failures of the wire chambers to record the passage of a particle (chamber inefficiency) can be handled with our simulation studies (see Appendix X), no attempt has been made to determine the inefficiency of the algorithm due to confusion by extraneous hits and/or tracks. Very detailed inspection of the performance of the algorithm under a large number of simulated test conditions, has convinced us that this type of inefficiency can be neglected.

We can summarize the structure of the algorithm as follows:

1. We search for a straight line track in the elevation view ("Y-track"), all the way through the spectrometer. The small vertical bend in the analysis magnet is not significant at this stage.
2. As shown in Fig. 9 , there is one "X,Y,U,V," station upstream and two such stations downstream of the analysis magnet. These stations, which allow us to correlate hits in the elevation view ("Y-view") with those in the plan view ("X-view"), give us the anchor points for the search of track segments in the X-view. In this view, particle tracks are bent in the analysis magnet. These segments will be straight lines on each side of the magnet, which should intersect at its magnetic center. The transverse momentum kick of 200 MeV/c gives a typical particle of 50 GeV/c a bend of 4 milliradians.

The recognized hit patterns for these track segments and the kinematic variables of the associated tracks are recorded on magnetic tape. This information is the input to the final event selection described in Appendix IX .

In what follows we describe, in detail, the pattern-recognition algorithm. This description is intended to be the repository of a rather complex set of procedures to form the basis for any more detailed discussion. It is not intended for the reader primarily interested in an overall description of this experiment.

PATTERN RECOGNITION ALGORITHM

Y-track Pattern Recognition

1. Y-view trackfinding is controlled by subroutine PATREC.
2. Use all pairs of sparks as seeds to define search roads, subject only to these conditions:
 - A. Sparks are on opposite sides of the analysis magnet.
 - B. Sparks in OSU 5, OSU 6, or PWC 1Y are not allowed to form seed pairs with sparks in SLAC 3 or PWC 3Y. This allows the use of fixed-width roads and sets a minimum to errors in Y-track slopes and intercepts.
 - C. The pair must not belong to a Y-road already found.
 - D. The line defined by this pair must pass through the active area of OSU 1.

This procedure is extremely conservative and time-consuming, but also extremely safe. It could be made much faster by reducing the number of seed planes. The present specifications are part of the code in PATREC.

3. Search a road along the line defined by the seed sparks.

- A. Find the closest spark, if any, within ± 3 mm. This road width is taken from array RD in COMMON/GEOM/. It is currently set in a data statement in SREAD. This is very conservative; the spark chamber resolution is known to be about 0.4 mm.
 - B. If a total of 6 (IPCUT (2)) or more sparks (including the seed pair) are found, this is a track candidate. The pattern is stored.
 - C. No more than 40 such roads are presently allowed. This is limited only by dimensions of certain arrays and by index limit tests in PATREC and RDSRCH.
4. The track candidates are examined in detail:
- A. The spark number is tested.
 - B. The Z-separation of contributing stations is tested. A call to NYSEP returns the number of stations contributing to this candidate. This number is required to be greater than 3 (IPCUT (4)). Roads with greater than 6 sparks automatically pass this cut.
 - C. The sparks are fit to a straight line.
 - D. All contributing planes are checked for sparks which are closer to the fit line. If found, the pattern is changed and the sparks refit. If a spark does not lie within the road, it is removed and the pattern is refit. If a plane did not contribute, but now has a spark within the road, it is added to the pattern and the pattern refit. If changes were made, this checking is repeated. No more than a second checking is allowed.

- E. If changes were made in the pattern in step D, go back to Step A above, skipping step D on the second pass.
- F. Make a cut on the confidence level of the fit. This cut is at 0.01. Note that because of G below, this does not mean that 1 percent of the tracks are lost, but that 1 percent of the 11-spark tracks (for example) are forced into the 10-spark category. The variances of spark measurement are set in a data statement in the program SREAD. The current value is 1×10^7 .
- G. If the candidate fails the confidence level cut, we call subroutine REFIT which removes the spark with the largest contribution to the chi-square and refits. It internally applies the spark number and separation cuts. It will loop, removing sparks until the resulting track does pass the cuts. This procedure is probably good for tracks which have a large number (hopefully 6) of good sparks and only a few (hopefully 1) bad sparks. It is certainly a bad procedure if the numbers of good and bad sparks are similar.
- H. Before moving on to step I below, we remove an obvious objection by making sure that no candidate is a subset of another. Typically, (I have never seen an exception) at this point in the program, if any are removed it is because they are identical.
- I. If the track candidate fails to pass these cuts, it is labelled a failure by setting $IRD > 80$.

5. Check spark sharing.
 - A. Subroutine YSQUEZ is called to remove failures from the list. They are gone forever.
 - B. No tracks are allowed to share a spark. Subroutine BESTY examines all candidates for spark sharing. If it is detected, the spark is awarded to the track with the higher confidence level. The candidate from which the spark has been removed is reconsidered with regard to all the Y-track cuts listed in 3 above.
 - C. If necessary, YSQUEZ is called again to remove new failures.
 - D. Candidates making it this far are declared good Y-tracks and will be written onto the output tape, even if no matching X-track is found.

Correlation Finding

1. Correlation finding is controlled by subroutine CSEEK which is called by PATREC when a good Y-track has been found.
2. Here I discuss combining coordinate pairs (U-V, X-U, and/or X-V pairs) to associate sparks in these other views with the Y-track already found. This sort of correlation finding is possible in four separate places: the upstream tilted PWC station and the three downstream SLAC chamber modules. For each of these four places, limits are calculated based on the track-finding road widths and the tilt angles involved in the calculation of Y. These cuts are labelled RUV, RXU, and RXV in the program. With 3 mm. road widths, RUV is 6 mm. for the 3 SLAC stations and 4.24 mm. for the tilted PWC's. There is also defined a much smaller window within which most of the real correlations are expected to appear, RLO (RLO = 1.5 mm.).

3. The search for correlated sparks proceeds in each of the four correlation stations as follows:
 - A. Each U-V pair is examined to see if it is within RUV of the Y-coordinate calculated from the Y-track. If it is, this pair is stored and the limit parameter RUV is decreased (but not below RLO).
 - B. If a second U-V pair is discovered within the RUV window (but not within the RLO window), closer to the Y-track than the first pair, it will replace the first pair.
 - C. If any pair is found within the RLO window, no pair outside the RLO window is recorded.
 - D. If more than one pair is discovered within the RLO window, they are all recorded up to a limit of four. No priority ordering is done for such multiple pairs.
 - E. If a U-V pair is found with a deviation within the RLO window, no search of X-U and X-V pairs is made. Otherwise a search of both X-U and X-V pairs is made using the same sort of procedure as detailed above for the U-V pair searching. In particular, a better X-U pair will replace a U-V pair; a better X-V pair can replace a X-U pair, etc. It is possible to finish with a good X-U pair and a good X-V pair only if both are within the tight RLO window.

Downstream Track-finding

1. Since there is an upstream-downstream asymmetry in the number of possible correlation stations with three downstream and only one upstream, the pattern recognition looks first for a downstream space track. If none is found, an upstream search is not attempted.

2. If there are two or three stations with at least one possible correlated pair, the program DNSEEK does the following:
 - A. All possible combinations of the correlated pairs are investigated in the same way. In principle, there could be up to $4 \times 4 \times 4 = 64$ such combinations, although the number is usually one, two or four. The program could handle only forty such combinations because of certain array sizes.
 - B. A simultaneous fit is made to these new pairs and the old Y-sparks from the previously-found Y-track. A loose cut is made on the probability of the fit.
 - C. If a combination passes this cut, the result of this fit is projected into all downstream planes not already contributing to the space track. Any sparks within the plane road width (3 mm.) are added to the track. The track is then refit and the process repeated only once more, making sure that these new sparks are the closest ones in the plane in question. The sparks forming the initial correlation combination are not allowed to change during this process, of course, nor are the Y-sparks allowed to change.
 - D. In a perfect track, all the X-sparks will be picked up in step C above, since in the correlation hunting we quit after finding a good U-V pair.
 - E. If new sparks were round, the track is refit and its quality of fit re-considered. If it now fails (because of the addition of these new sparks), the new sparks are removed one by one in the order of their residuals, until an acceptable track remains. Again, none of the original sparks can be removed at this stage, no matter how hit its residual.

- F. This track is now stored, and the next combination of correlated pairs is considered.
 - G. After all pair combinations have been tested, it is possible to have duplicate tracks. The list of possible tracks is checked to make sure that no track is a subset of any other.
 - H. At this point, we allow no two track candidates to share even a single spark. If such sharing is detected, the spark in question is awarded to the track with the better probability of fit.
 - I. If no acceptable track candidate has been found by combining the pairs, one drops down a class and repeats, in detail, the procedure. For example, if three stations have a single correlation pair, this gives a single triplet to test. If this triplet fails to yield a track candidate, we investigate the three possible doublets which could be formed from this triplet. If the doublets also fail, we still try to salvage the track by treating each single correlation pair separately as detailed below.
3. If only a single correlation pair is found, we:
- A. We look first for three or four X-sparks which point through the X-position calculated from the single correlated pair.
 - B. If such an X-track is found, its sparks are added to those of the singlet pair and a fit is made. The resulting track candidate is treated just like candidates from double and triple correlation pairs described above.
 - C. If no X-track of this type is found, we continue to look for three U-sparks or three V-sparks and proceed as above if any are found.

4. The final result of the downstream space track finding is usually a single track, but because the cuts are so loose, it is possible to have multiple downstream track candidates each corresponding to the same Y-sparks. The correct will be chosen in the end by selecting the track which matches its upstream partner best at the magnet center.

Upstream Track finding

1. If there exists a correlated pair in the upstream PWC station, the following is done:
 - A. A search for X-sparks is made along the road connecting the intercept of the downstream track segment at the center of the analysis magnet with an X-position calculated from the PWC U-V pair. If three X-sparks are found (out of six planes) this is declared a potential track and a fit is made to all upstream X- and Y-sparks. No constraint is made on the intercept of this track at the center of the magnet.
 - B. If the probability of the fit is good enough, the planes not contributing are searched to make sure that we have not missed any sparks.
 - C. If any sparks are added, the fit quality is checked again with the usual actions taken if the track is now judged bad; namely, the new sparks are removed one at a time until an acceptable track results.
2. If the PWC pair fails to yield an acceptable track candidate, the track is treated as having no correlation information.
 - A. The intercept of the downstream track with the analysis magnet center defines a pseudo-plane with one spark at the center of the magnet.
 - B. This pseudo-plane and the most upstream four X-chambers are used to define a road which is searched for sparks. If three sparks are found,

including the one real spark used as a seed, it is considered a track candidate. The track is fit, as before, also searching the upstream PWC's for sparks.

- C. If this pseudo-plane direct road search fails to yield a candidate, we try one more time in the following way. We use as seed planes the two most upstream X-planes (still in the upstream arm). Search roads are defined for these tracks. If such a road points to within 1 cm. of the downstream intercept, it is treated according to the procedures outlines above.
3. The end result of all this is usually one upstream and one downstream track segment. It is possible to have multiple segments. In that case, the pair with the smallest separation at the center of the analysis magnet is selected. All others are discarded.

Appendix IX
EVENT SELECTION

We selected events consistent with decays of known long-lived neutral particles (kaons, lambdas and anti-lambdas) produced in the target by an interaction of the beam particle. First we eliminate events:

1. without at least one track of each charge,
2. without a reconstructable beam track.¹

Tracks in events passing these cuts were required to be reconstructable, in-time, and inside the aperture of the experiment. After each cut, criterion 1 above was applied to the event.

We rejected tracks:

3. without a valid momentum,²
4. with upstream and downstream segments failing to meet at the magnetic center of the analysis magnet,
5. with fewer than two PWC hits,
6. without at least one hit in both the X and Y views at the last chamber station,³
7. with tracks passing inside the software B5 veto counter,⁴
8. without a corresponding I-counter hit.⁵

Remaining pairs of oppositely-charged particles were rejected if they were not consistent with the above neutral "vee" hypothesis. We rejected pairs with:

9. decay vertex distance-of-closest-approach too large,
10. Z coordinate of the decay outside a fiducial volume,
11. X and Y coordinate of the decay outside a fiducial volume,⁶
12. mass inconsistent with the kaon, lambda or anti-lambda hypothesis.

We rejected pairs where the calculated intercept between the beam track and the reconstructed neutral track had

13. had too large a distance-of-closest-approach,

14. had too large an intercept difference, in either projection, at the target center,⁷
15. lay outside the target fiducial volume.

Events with two accepted pairs sharing a track were rejected as "ambiguous." For events with more than one pair passing the kaon mass cut, the pair with the largest diparticle momentum was passed on to the final cuts.

The final cuts were made to eliminate pion-induced events and events which might be lambdas. Also cuts were made to simplify some acceptance calculations.

16. Events where the pion momentum component normal to the neutral track was less than 0.11 GeV/c were eliminated. In this kinematic region, lambdas could be mistaken for kaons.
17. Events with a 'KAON' Cherenkov counter signal below threshold were rejected to eliminate pion-induced events.
18. A software PWC logic cut was made.⁸
19. Events with tracks too close in either projection at the first spark chamber plane were rejected.⁹

Pairs passing all nineteen of the above criteria were considered "good kaons" and included in the final analysis.

FOOTNOTES

1. A beam track was considered reconstructable if all the following were true.
 1. In the X view, only 2X or 3X (but not both) was not hit.
 2. In the Y view, 1Y had a hit as did at least two of the remaining planes.
 3. The track was inside the fiducial volume in X, X', Y, Y', and P defined at the middle of the target.
 4. The intercepts of the upstream and downstream X track segments at the center of the 4B5 magnet were sufficiently close together.
2. A track had a valid momentum if it had enough hits to allow reconstruction of track segments on each side of the analysis magnet, and if its reconstructed momentum was below the upper limit for beam particles.
3. While tracks were reconstructed with an upstream segment and hits in only the first downstream station, these were rejected as having too large an uncertainty in momentum.
4. To compute the effect of the B5 veto counter on the acceptance, the fiducial region was enlarged, centered on the B5 counter.
5. The (X, Y) intercept of the track at the I-counter wall ($Z = 14.0$ m) was calculated. The predicted counter (and its neighbor if the intercept was within 1 cm of the counter edge) was checked. Tracks with a pulse height above threshold were accepted. This requirement was not made on tracks passing through the beam opening in the I-counter wall.
6. The decay vertex was required to lie inside a cone centered on the Z axis with a radius of 2.54 cm at the upstream end of the target and 45.4 cm at the downstream end of the decay pipe ($z = -13.0$ m).

7. This cut was made to reject kaons from interactions in the upstream vacuum window. Since the beam was deflected by the sweeping magnet before these interactions, the projection of the kaon to the target center tended to be to one side of the target.
8. To compute the effect of the PWC logic on the acceptance, the regions in each chamber which were not included in the trigger (to deaden the beam area) were enlarged and the PWC logic signal recalculated.
9. Events with both tracks too close in either projection could only have one spark in the first chamber, moving the calculated decay vertex position downstream.

TABLE I

Variable Names

CD	Distance of closest approach of the charged tracks at the decay vertex
XD, YD, ZD	(X, Y, Z) coordinates of the center point of closest approach of the charged tracks at the decay vertex
QCA	Fractional Q-value discrepancy for the kaon hypothesis
QLA(QALA)	Fractional Q-value discrepancy for the lambda (antilambda) hypothesis
	$QCA = \frac{m(\text{diparticle}) - m(\text{kaon})}{m(\text{kaon}) - 2 m(\text{pion})}$ $QLA = \frac{m(\text{diparticle}) - m(\text{lambda})}{m(\text{lambda}) - m(\text{proton}) - m(\text{pion})}$
CP	Distance of closest approach between the beam track and the reconstructed diparticle "track"
DXP	(X(diparticle) - X(K)) at Z = -31.2 m (target center)
DYP	(Y(diparticle) - y(K)) at z = -31.2 m (target center)
XP, YP, ZP	(X, Y, Z) coordinate of the center point of closest approach between the beam track and the reconstructed diparticle "track"

TABLE II

Event Selection Criteria
(low limit, high limit)

Parameter	68 GeV/c	116 GeV/c	176 GeV/c
CD (m)	0.0, 0.01	0.0, 0.01	0.0, 0.01
ZD (m)	-27.25, -13.0	-27.25, -13.0	-27.25, -13.0
QCA	-0.12, 0.12	-0.12, 0.12	-0.12, 0.12
QLA	-0.2, 0.2	-0.2, 0.2	-0.2, 0.2
QALA	-0.2, 0.2	-0.2, 0.2	-0.2, 0.2
CP (m)	0.0, 0.008	0.0, 0.01	0.0, 0.01
DXP (m)	-0.008, 0.008	-0.01, 0.01	-0.01, 0.01
DYP (m)	-0.01, 0.01	-0.01, 0.01	-0.01, 0.01
XP (m)	-0.02, 0.02	-0.02, 0.02	-0.02, 0.02
YP (m)	-0.02, 0.02	-0.02, 0.02	-0.02, 0.02
ZP (m)	-33.2, -29.2	-33.2, -20.2	-33.2, -29.2

TABLE III
Event Selection History

Beam Momentum	68 GeV/c	116 GeV/c	176 GeV/c
Triggers recorded	784,505	1,709,536	2,553,830
Triggers with at least one track of each charge	251,915	682,195	1,144,484
Remaining events with good beam track	212,101	569,103	1,050,443
Remaining events with at least one "good" track of each charge	66,163	251,236	566,346
Events with at least one kaon	<u>11,141</u>	<u>49,747</u>	<u>115,057</u>
Events lost due to the final cuts			
1.) P_1 (criterion 16)	1,181	7,537	20,003
2.) Cherenkov signal (criterion 17)	65	0	0
3.) P-Logic (criterion 18)	1,091	4,491	15,517
4.) Pions too close (criterion 19)	<u>469</u>	<u>3,556</u>	<u>10,520</u>
Accepted kaons	8,335	34,213	68,987

Figures IX. 1 - IX. 10. Geometric and Kinematical Acceptance
Criteria for 116 GeV/c Data.

Arrows indicate acceptance limits.

Figure IX. 1. Distance of closest approach at the production vertex
(CP).

Figure IX. 2. Difference between the X-intercepts of the K^- -track
and \bar{K}^0 -track at the target center plane (DXP).

Figure IX. 3. Difference between the Y-intercepts of the K^- -track
and \bar{K}^0 -track at the target center plane (DYP).

Figure IX. 4. Z-coordinate of the production vertex.

Figure IX. 5. Distance of closest approach at the decay vertex (CD).

Figure IX. 6. Momentum component of the decay particle transverse
to the diparticle momentum.

Figure IX. 7. Z-coordinate of the decay vertex.

Figure IX. 8. Diparticle mass for the kaon hypothesis (QCA)

$$QCA = \frac{m(\text{diparticle}) - 2m(\text{pion})}{m(\text{kaon}) - 2m(\text{pion})}$$

Figure IX. 9. Diparticle mass for the lambda hypothesis (QLA).

$$QLA = \frac{m(\text{diparticle}) - m(\text{proton}) - m(\text{pion})}{m(\text{lambda}) - m(\text{proton}) - m(\text{pion})}$$

Figure IX. 10. Diparticle mass for the anti-lambda hypothesis
(QALA) (QALA = QLA).

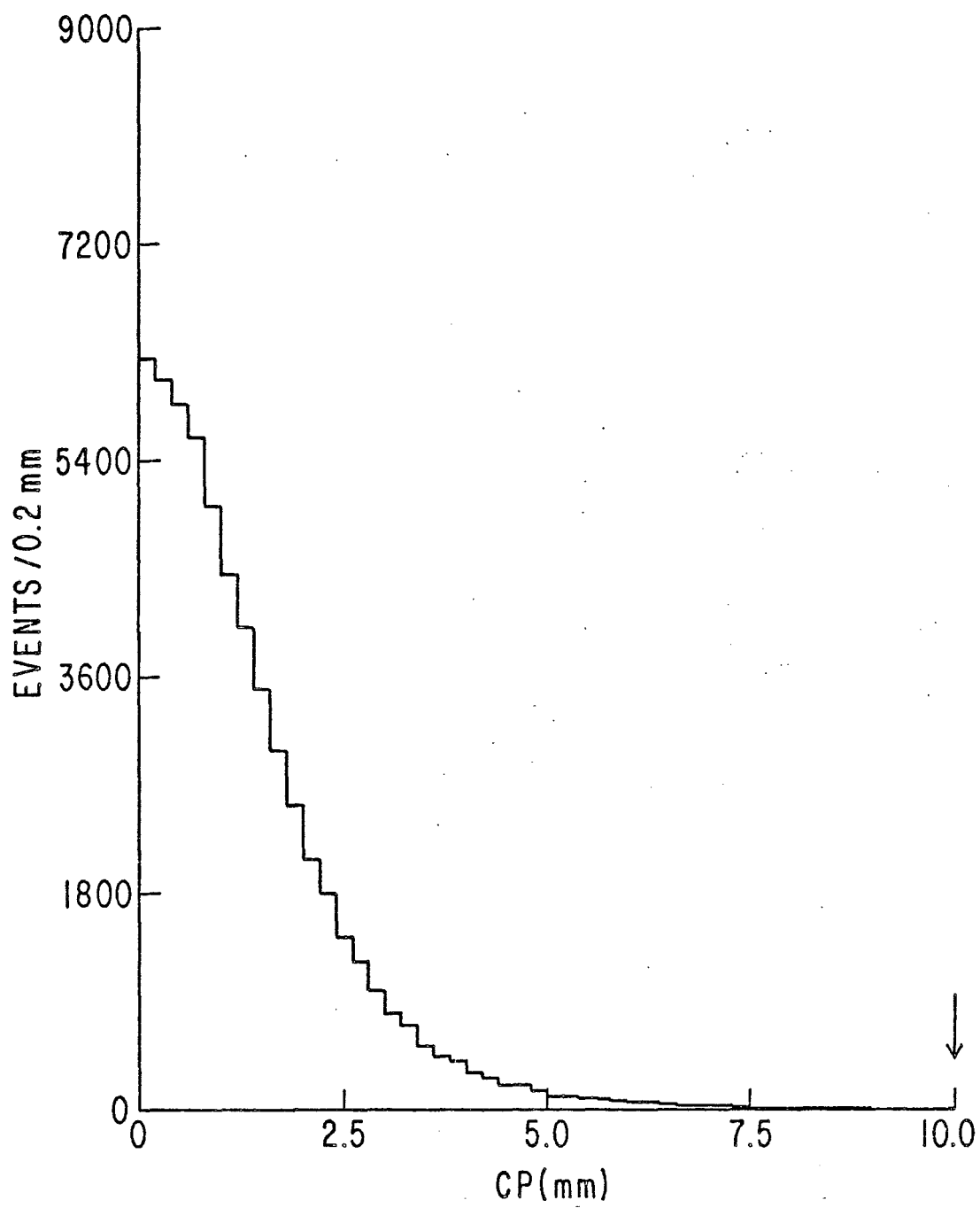


Figure IX. 1

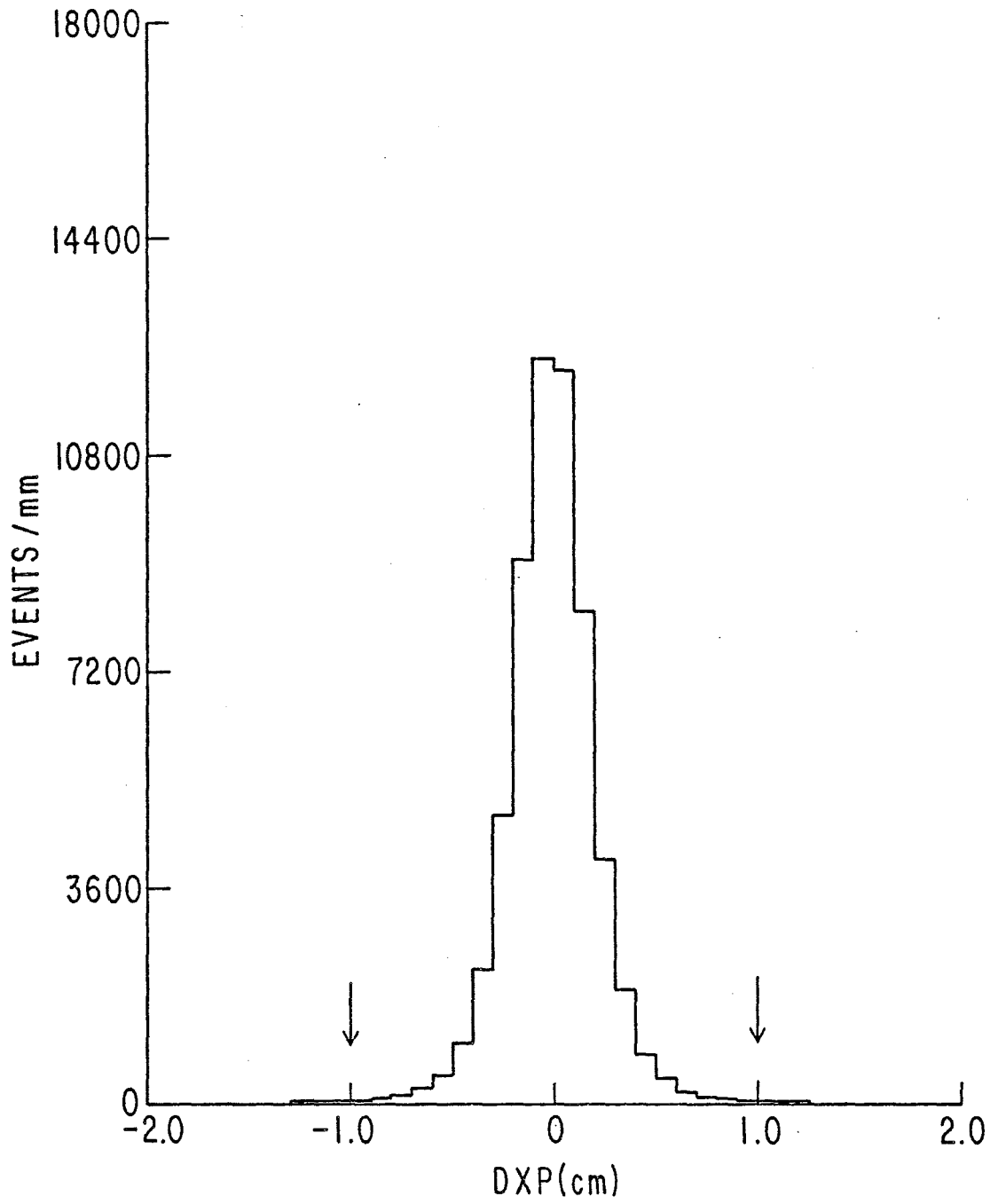


Figure IX. 2

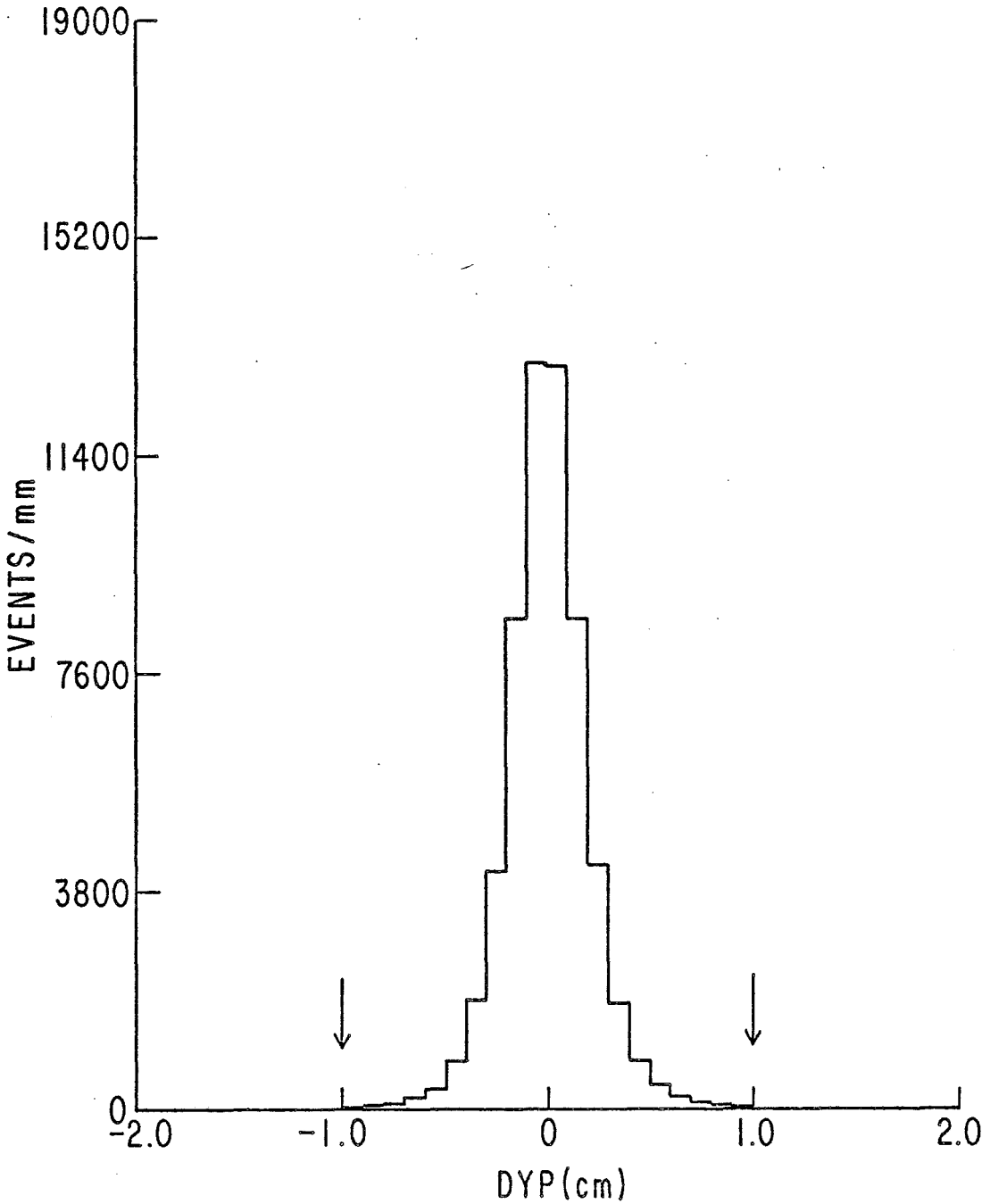


Figure IX. 3

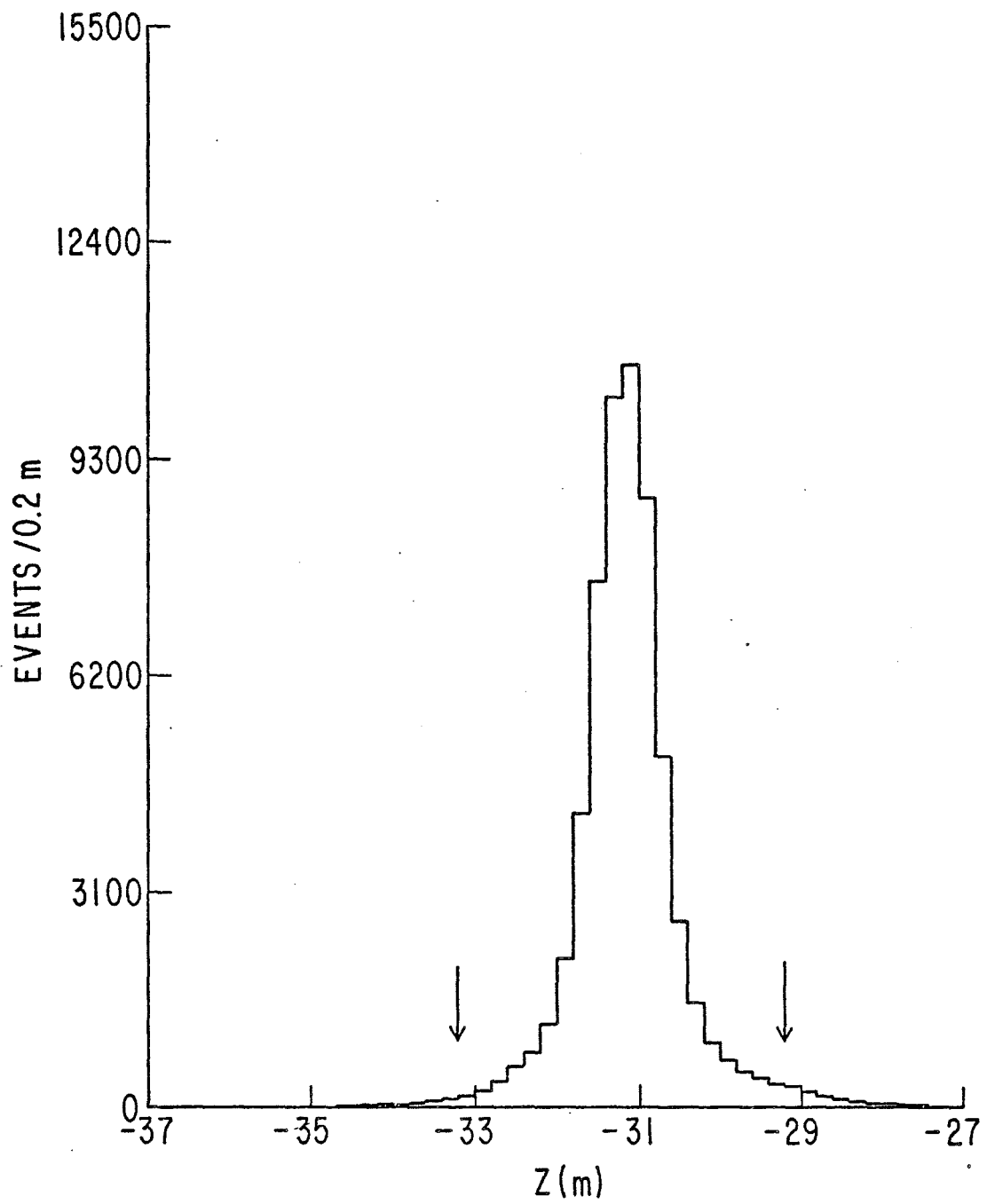


Figure IX. 4

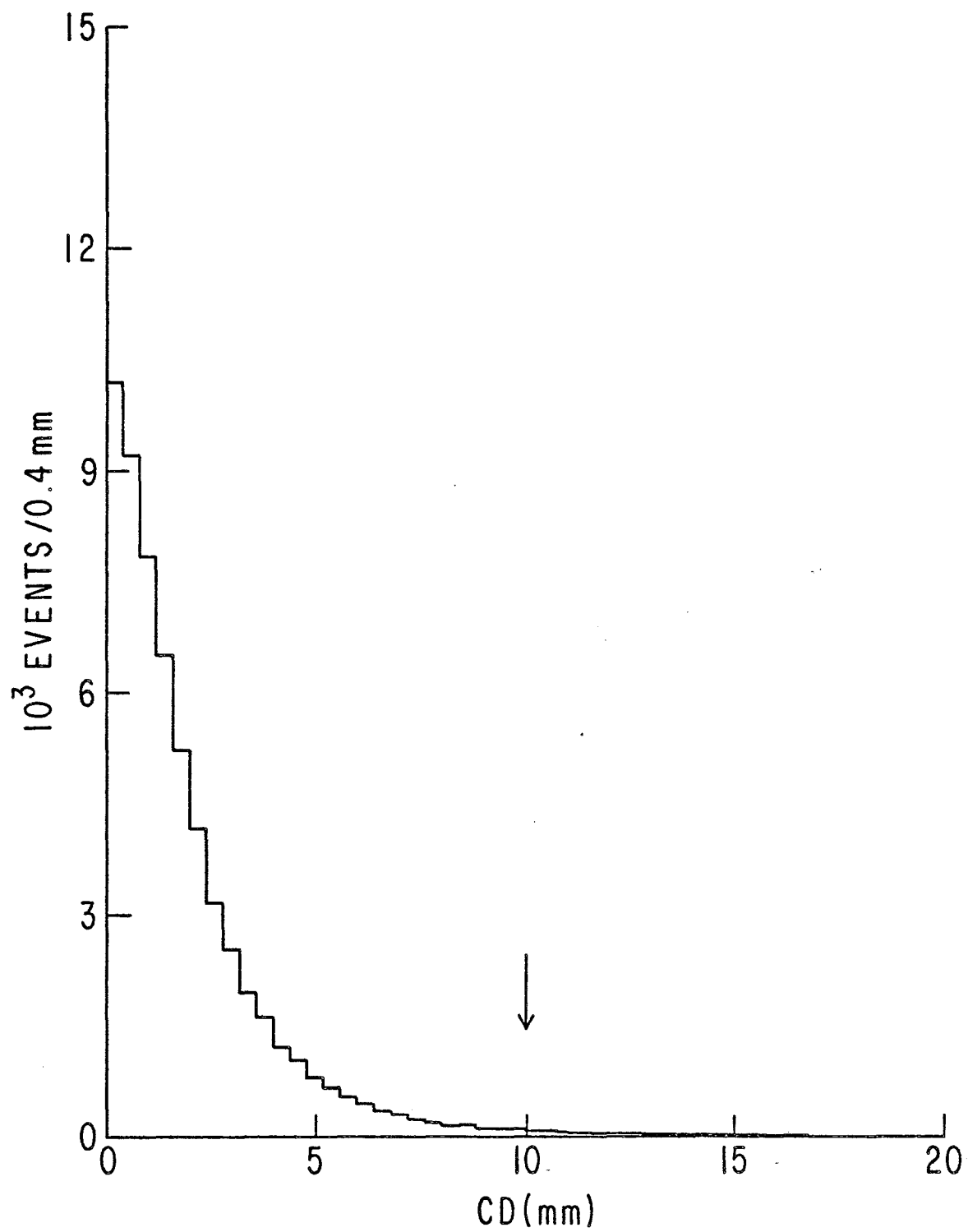


Figure IX. 5

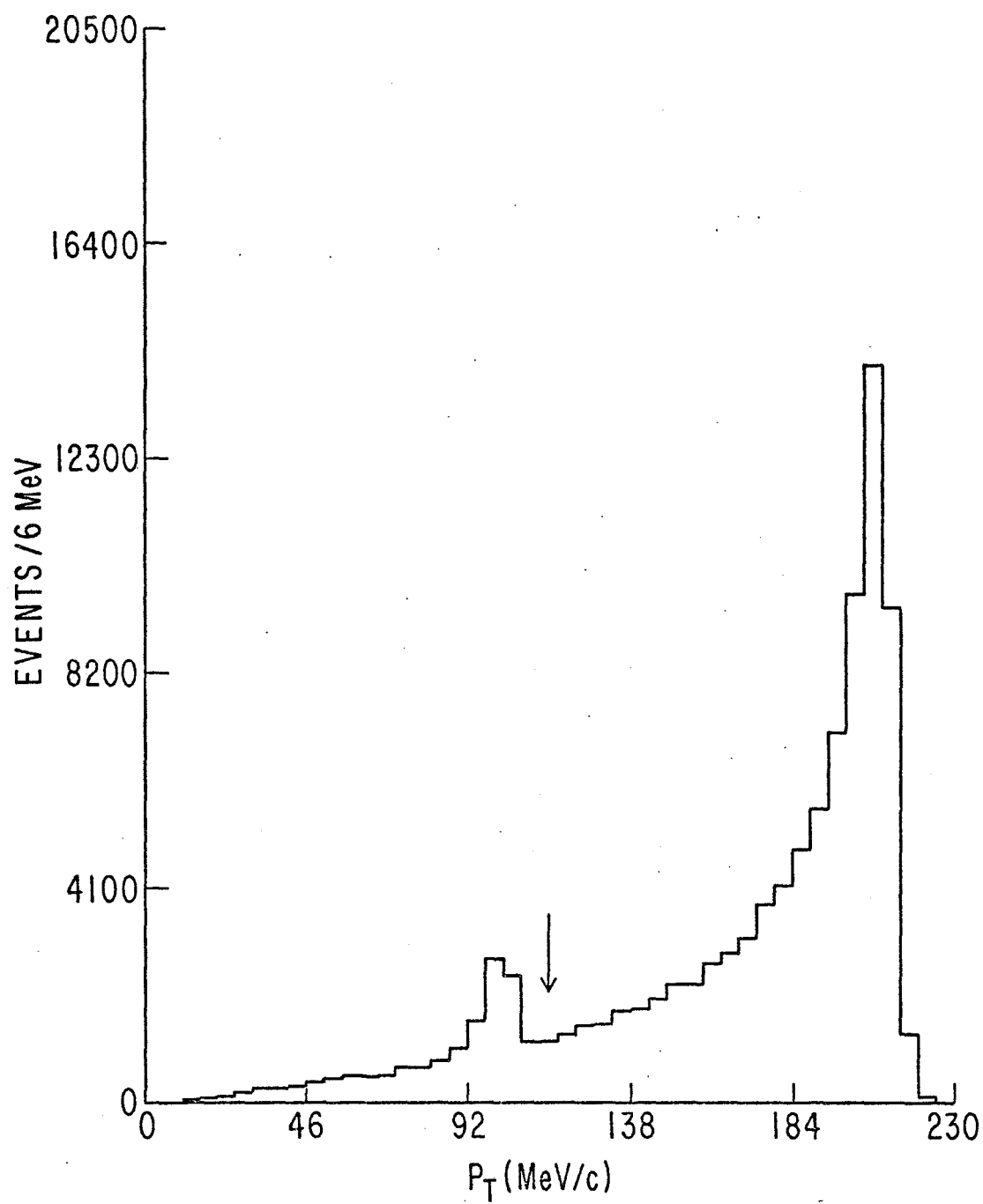
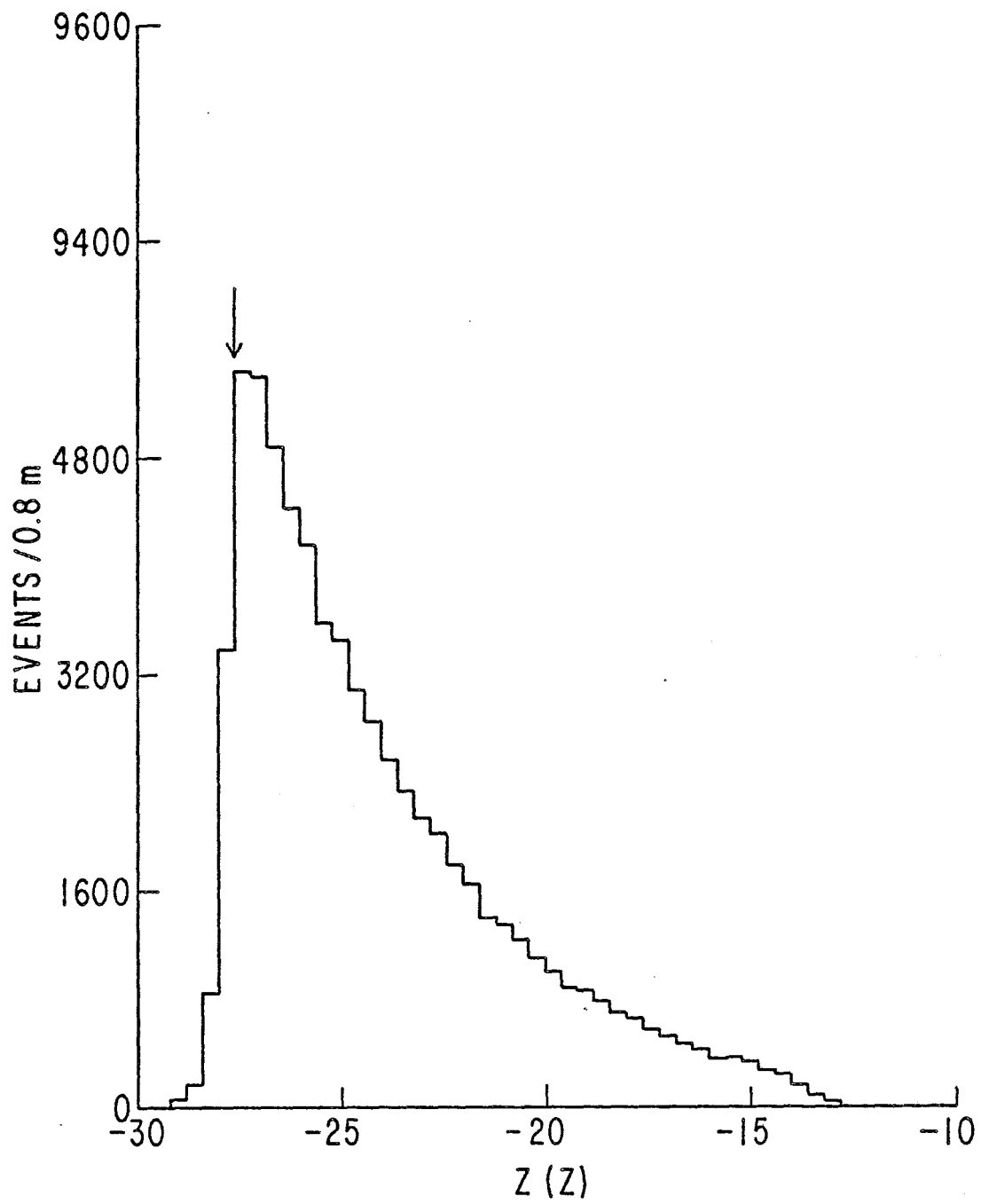


Figure IX. 6



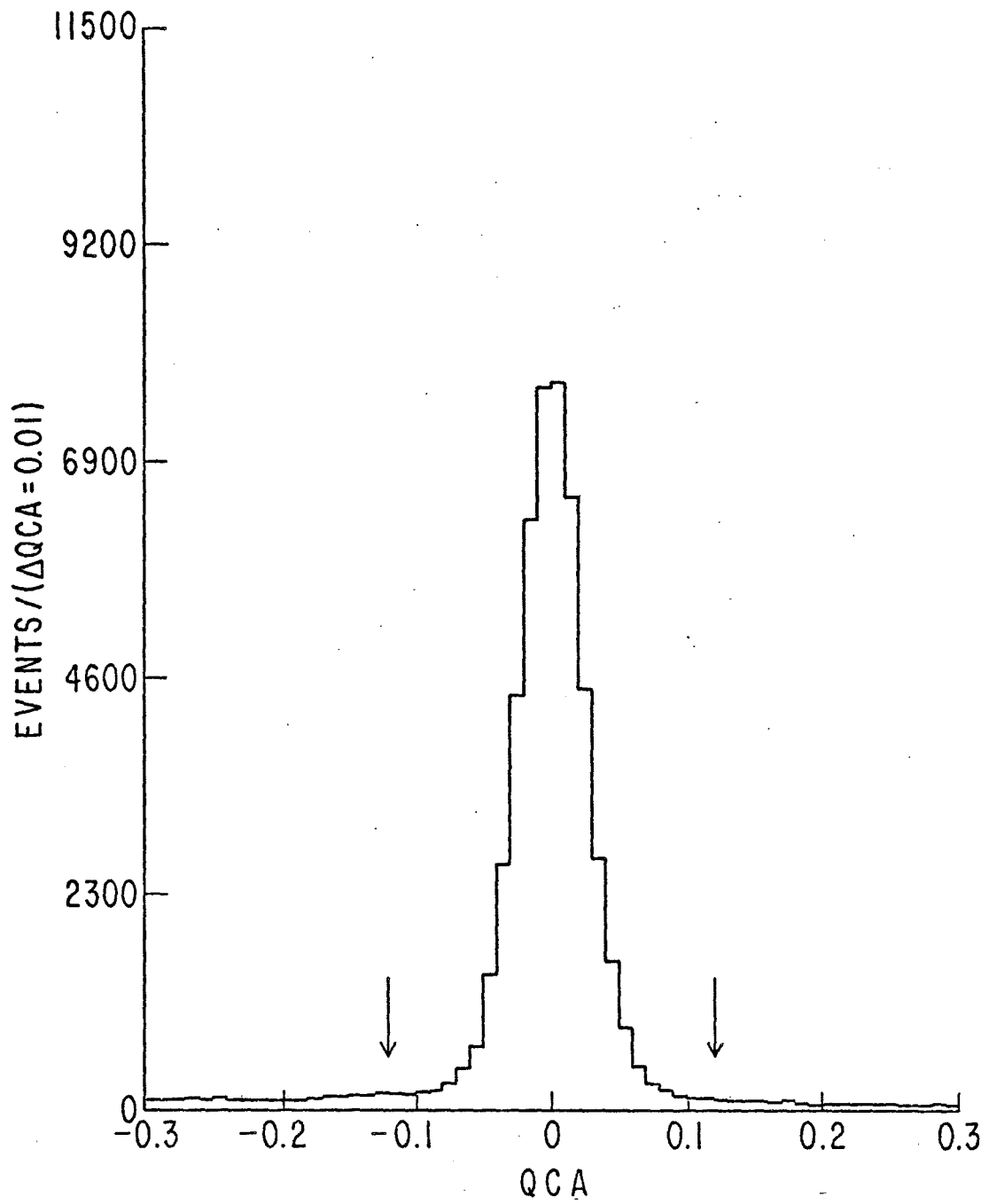


Figure IX.8

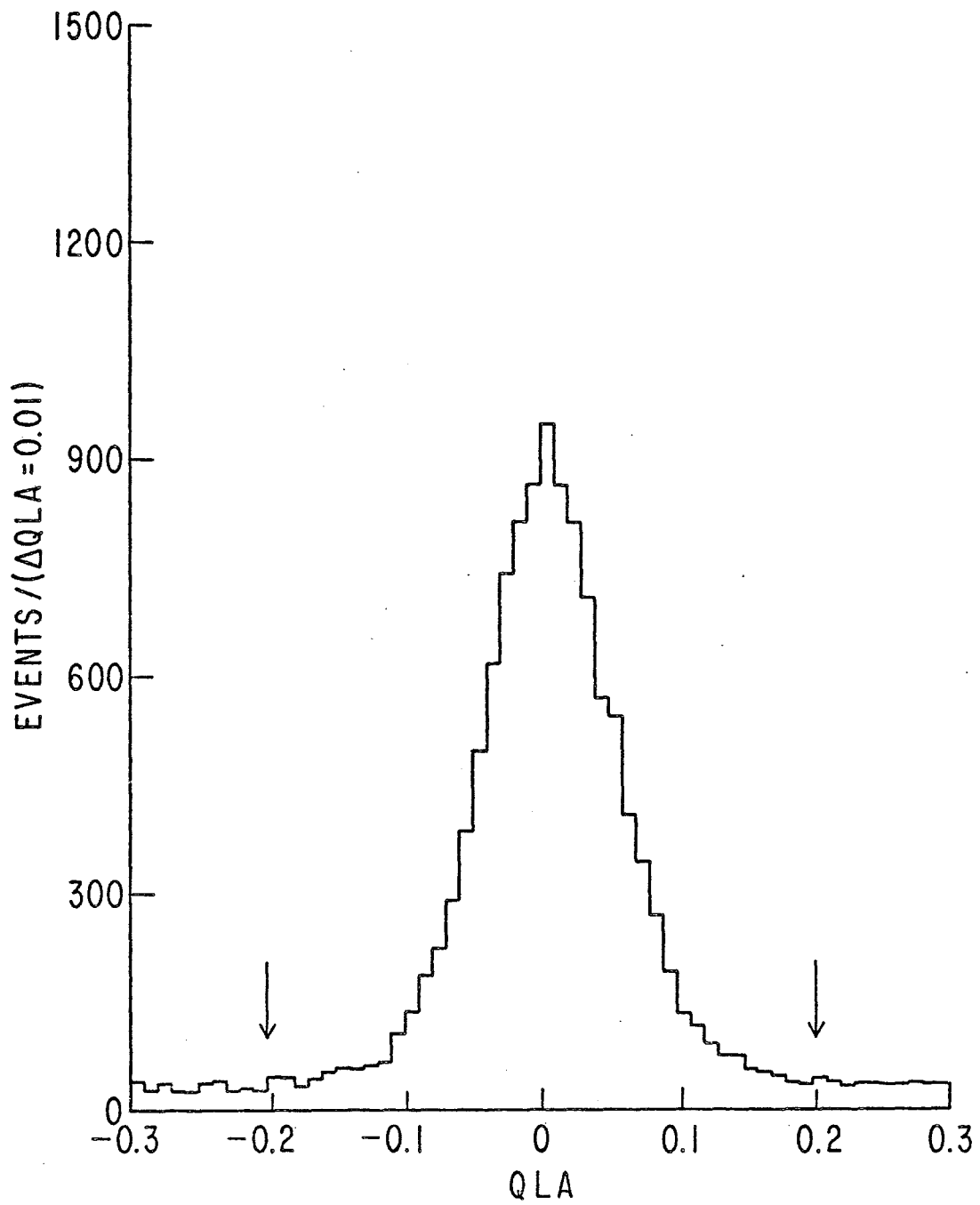


Figure IX. 9

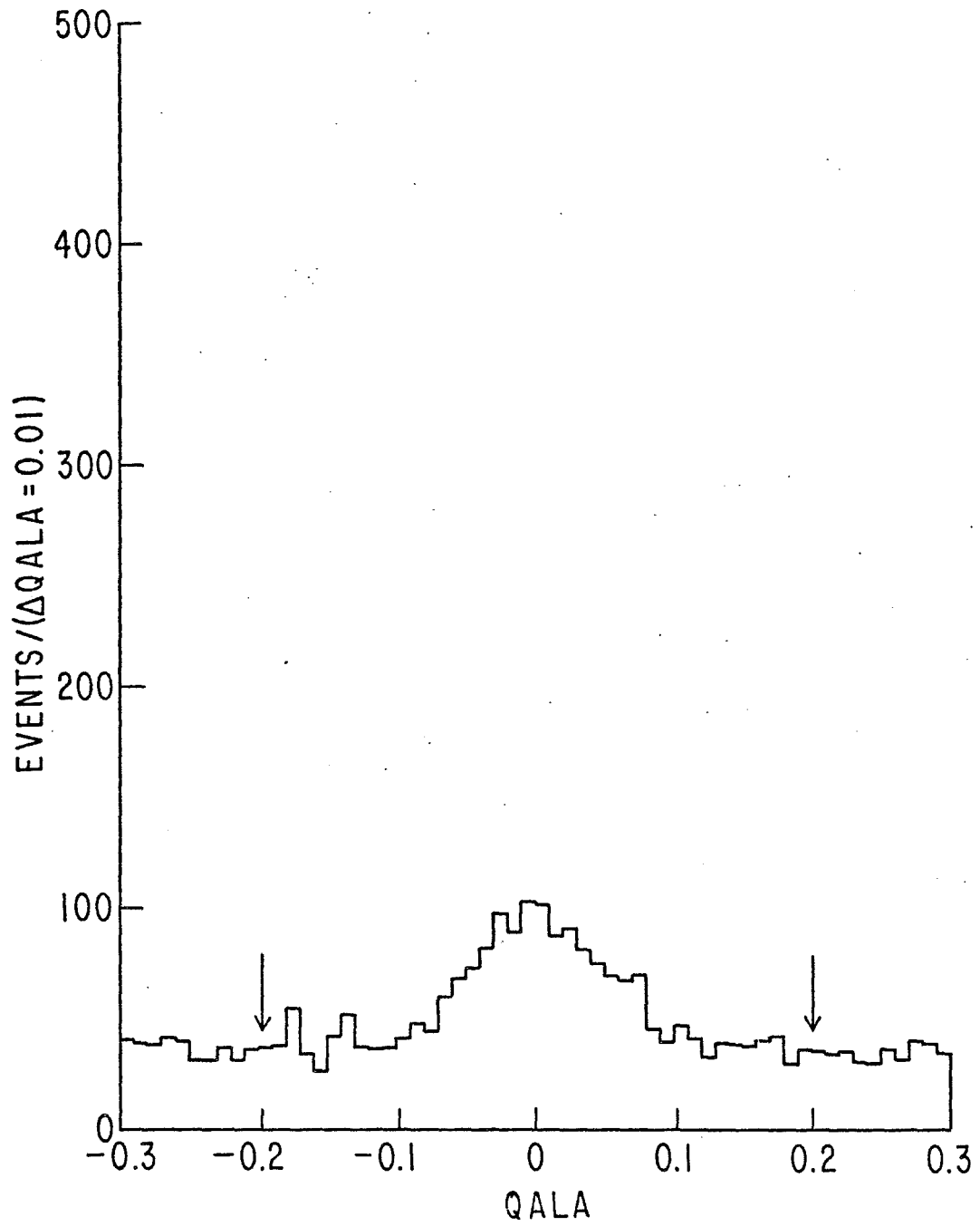


Figure IX.10

Appendix X

MONTE CARLO

We describe the simulation of the data by Monte Carlo methods and compare distributions, in several kinematic variables, of data and simulated events.¹

The Monte Carlo modelled the incident K^- beam, the K^- -proton interaction, the K short (K_s) decay and followed the resulting pions through the spectrometer.

The phase space parameters of the incident K^- were gaussian-distributed with X and X' selected at an X -focus; Y and Y' were selected at a Y -focus. The K^- momentum distribution from the data was used for the Monte Carlo. The K^- was traced through the beam spectrometer to an interaction point in the target. This beam track was multiply-scattered² and its position in the eight beam chambers calculated.

The distribution of kinematic parameters (x and t) for the $K^- \rightarrow K_s$ interaction matched that of the data. A random polar angle was picked and the K_s momentum vector in the K^- coordinate system was calculated.³ This vector was then transformed to the experiment coordinate system.

The interaction point was distributed throughout the target to reflect beam attenuation.

The Z -coordinate of the $K_s \rightarrow \pi^+ + \pi^-$ decay was selected according to the decay distribution for K_s 's generated at the production point, including the effects of K_l - K_s interference.

x , s , t , Z (production) and Z (decay) were encoded into one computer word in the "generated event" file used for efficiency calculations.

To model the K_s decay, the π^+ momentum was isotropically distributed in the K_s rest frame, with the $\vec{p}(\pi^-) = -\vec{p}(\pi^+)$ in that frame. The pion momenta were then Lorentz-transformed to the K -short laboratory frame⁴ and then transformed to the experiment coordinate system.

If the K-short decay occurred before or inside the sweeping magnet, the pions were traced through the magnet. All pions were traced through the spectrometer.

A pion decay Z-coordinate was picked for each pion. If the decay occurred inside the experiment, a momentum vector for the muon was calculated (isotropic in the pion rest frame), and the muon was traced through the rest of the experiment.

Simulated events which passed two loose aperture cuts entered the final section of the Monte Carlo program.

The pion and muon tracks were multiply-scattered and the track positions in each chamber calculated. These "spark" positions were perturbed, plane-by-plane, by a gaussian whose width was determined from the spark residuals measured in the data. Sparks were thrown out to simulate the chamber inefficiencies measured in the data.⁵ The remaining sparks were formatted to be input to the pattern recognition program used for the data. Into the word which contains ADC information for data events, we encoded the production and decay coordinates as well as the slopes, intercepts and momentum of each unperturbed track. This enabled us to measure our resolution by comparing the generated value of a parameter, decoded from the ADC words, with the value for that parameter found by analysis of the simulated sparks.

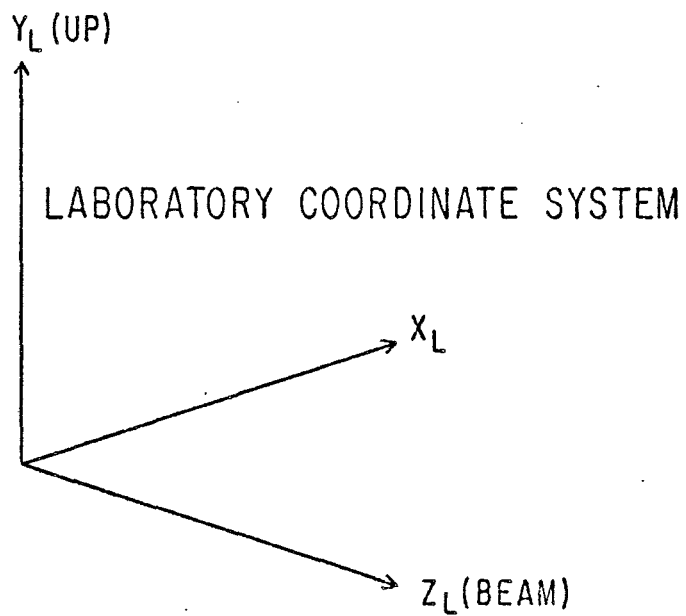
These simulated events were then processed by the same pattern-recognition/track fitting and event selection programs as were the data.

To check that the Monte Carlo program accurately simulated the data, comparisons were made between real and simulated data in several kinematic variables (see Figures X.2 - X.11).

FOOTNOTES

1. The laboratory system referred to in this Appendix is that of Figure 1.
2. Moliere theory (6) was used to calculate a scattering angle distribution for four values of scattering thickness (measured in radiation length). At each scattering center, the Moliere distribution for the thickness nearest that of the current scatterer was selected and broadened or narrowed by a factor $\sqrt{L_s/L_d}$ where L_s is the thickness of the scatter (in radiation lengths) and L_d is the thickness (in radiation lengths) for which the distribution was calculated.
3. See Figure 1.
4. See Figure 1.
5. Chamber efficiencies for each data run were encoded on a disk file with the number of accepted data events from the run. The fraction of the total Monte Carlo sample calculated using the efficiencies from a given run was the same as the fraction of the total accepted kaon sample contained in the run.
6. H.A. Bethe, Phys.Rev. 89, 1256 (1953).

Figure X. 1. Coordinate Systems used in the Analysis of
this Experiment.



KAON BASED COORDINATE SYSTEM

$$\hat{X}_K = \frac{\hat{P}_K \times \hat{Z}_L}{\sqrt{1 - (\hat{P}_K \cdot \hat{Z}_L)^2}}$$

$$\hat{Z}_K = \hat{P}_K$$

$$\hat{Y}_K = \hat{Z}_K \times \hat{X}_K$$

WHERE \hat{P}_K UNIT VECTOR ALONG KAON MOMENTUM

$\hat{X}_L, \hat{Y}_L, \hat{Z}_L$ UNIT VECTORS ALONG LABORATORY
COORDINATE AXES

Figures X. 2 - X. 15. Comparison between Our Data and the Predictions from the Monte Carlo Computations for the Same Total Number of Events.

———— Computed Prediction



Experimental Data

	<u>68 GeV/c</u>	<u>116 GeV/c</u>	<u>176 GeV/c</u>
Distance of closest approach at production (CP)	X. 2	X. 3	X. 4
Distance of closest approach at decay (CD)	X. 5	X. 6	X. 7
Z-coordinate of decay vertex	X. 8	X. 9	X. 10
Difference between intercepts of K^- and K^0 at target center plane (DXP)	X. 11	X. 12	
Mass of Neutral Kaon			
$\Delta QCA = \frac{m(\text{diparticle}) - 2m(\text{pion})}{m(\text{kaon}) - 2m(\text{pion})}$	X. 13	X. 14	X. 15

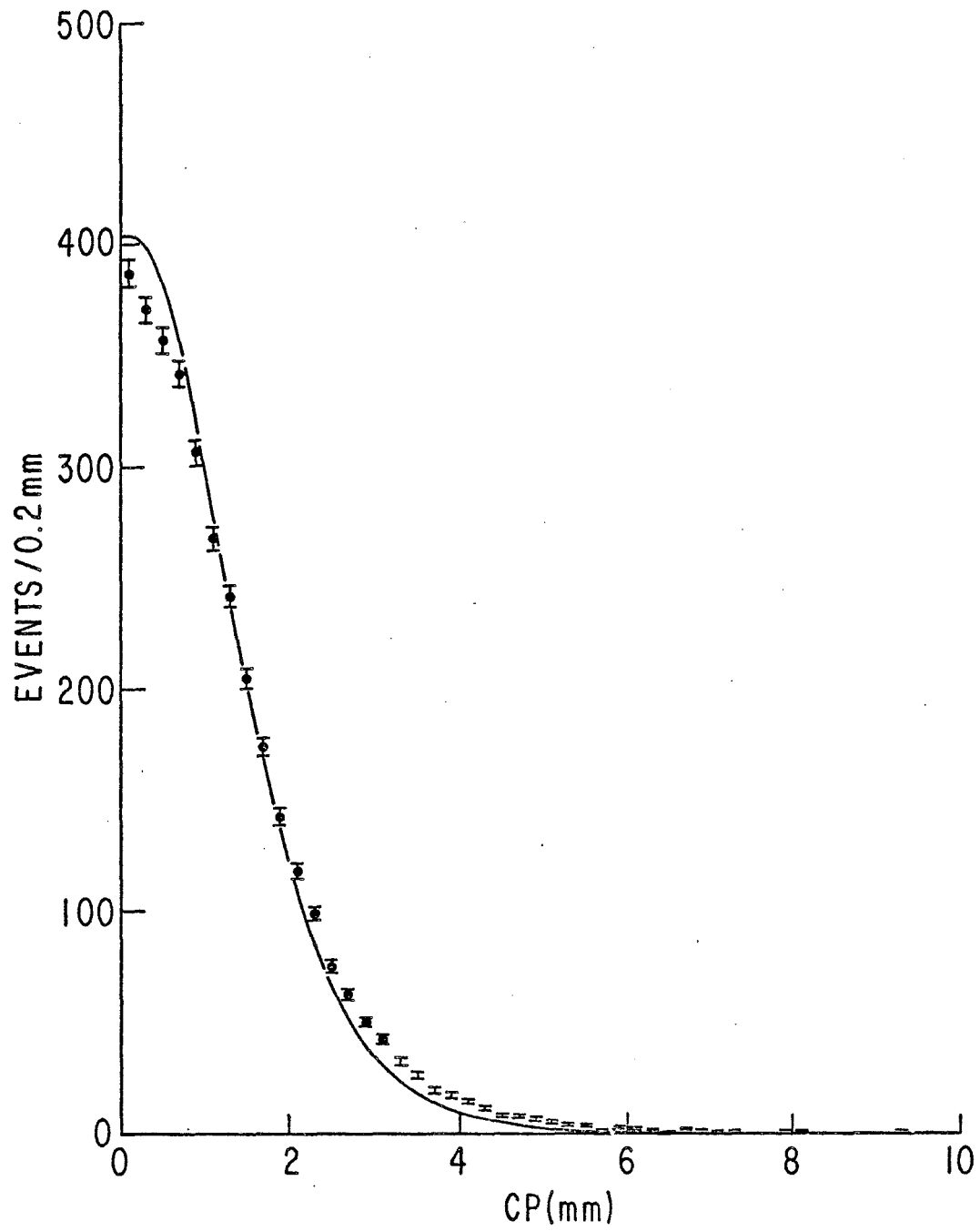


Figure X.2

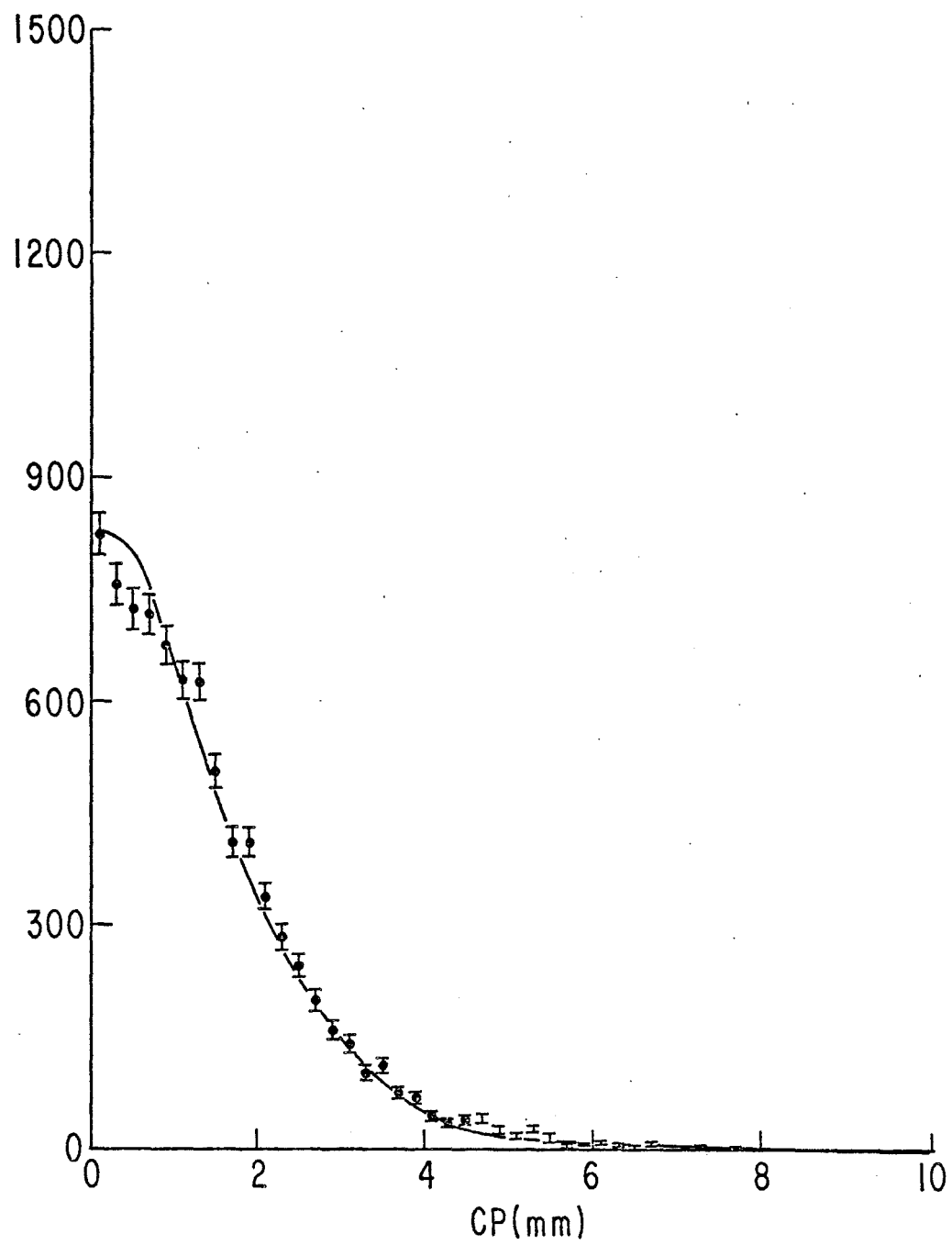


Figure X. 3

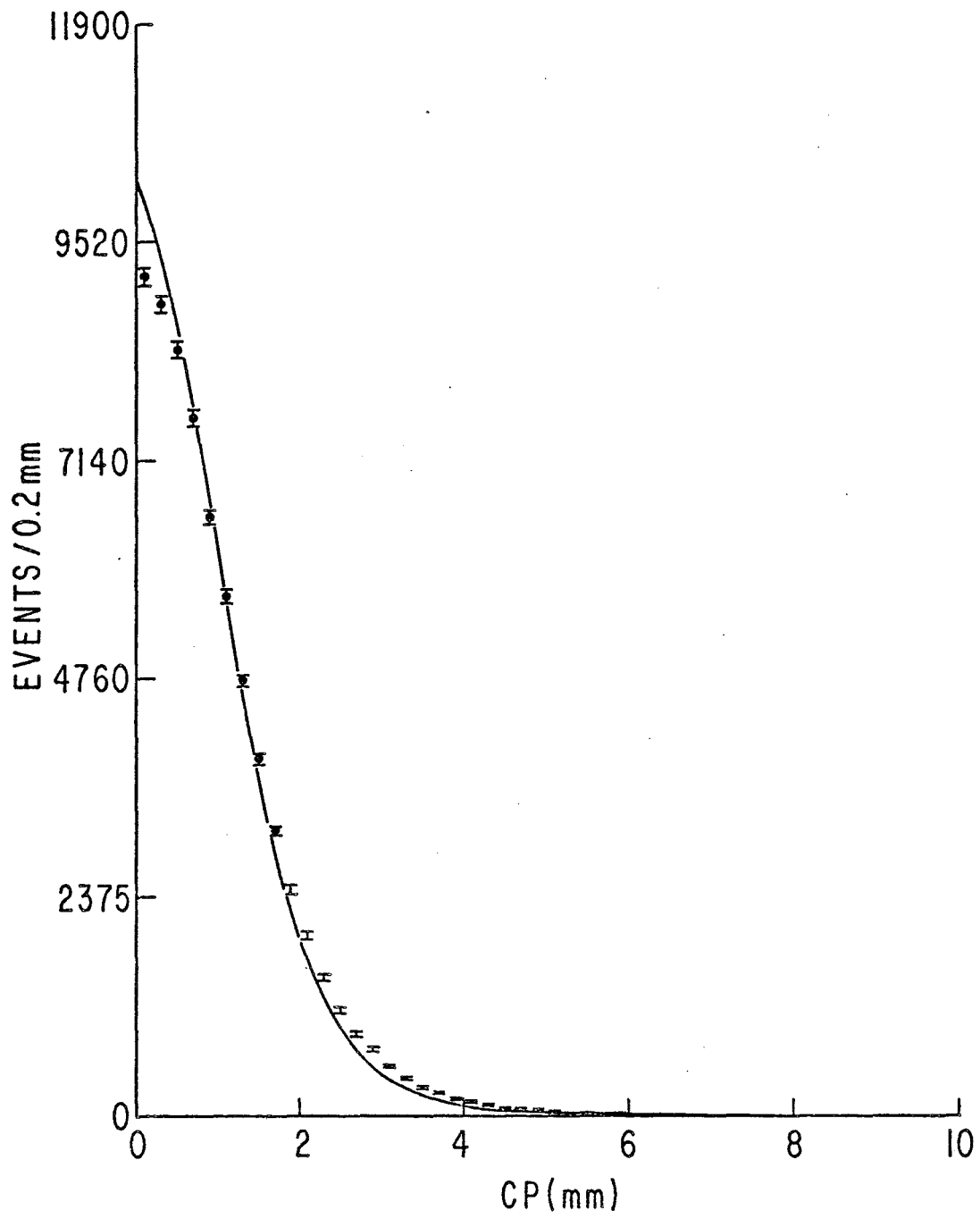


Figure X. 4

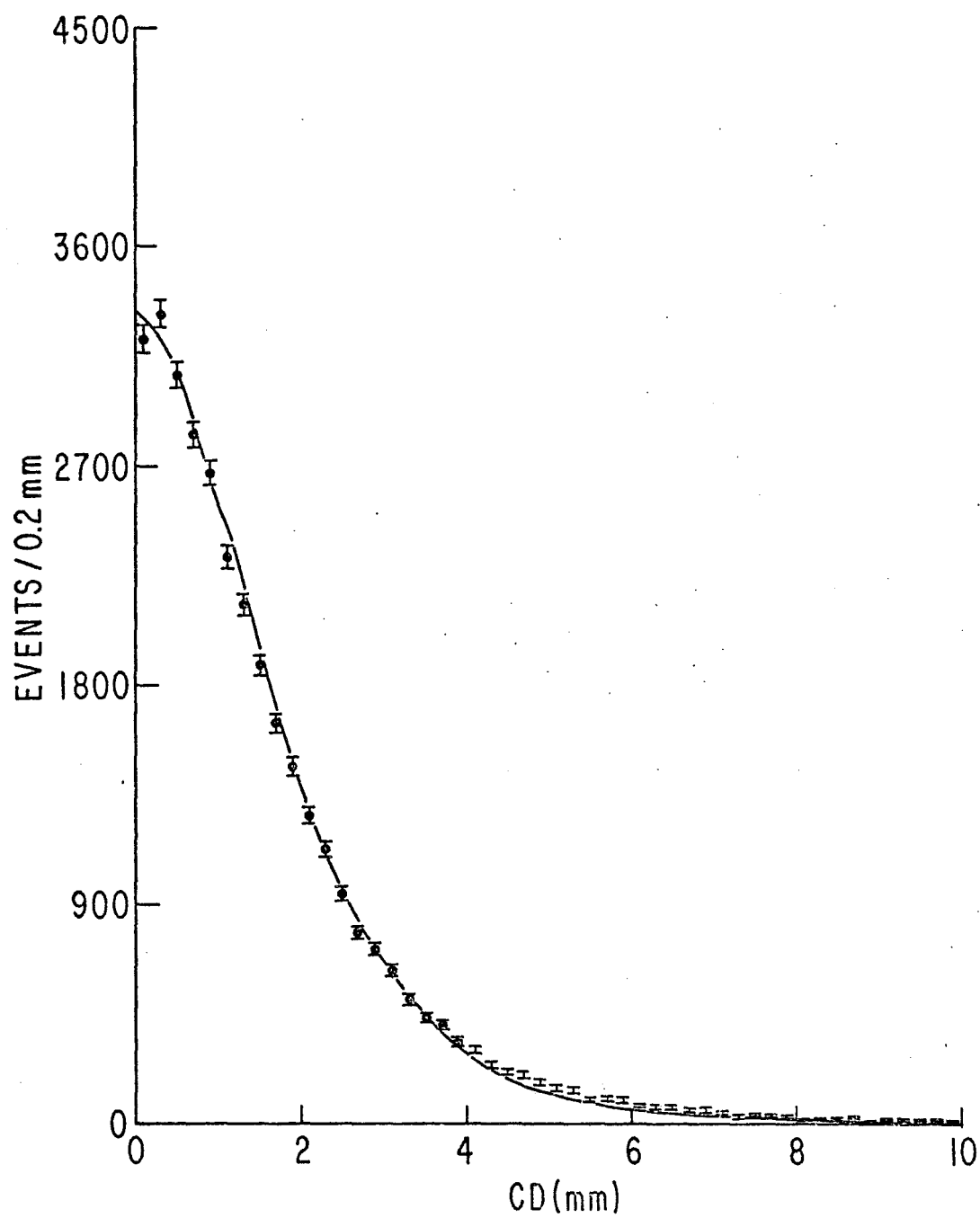


Figure X.5

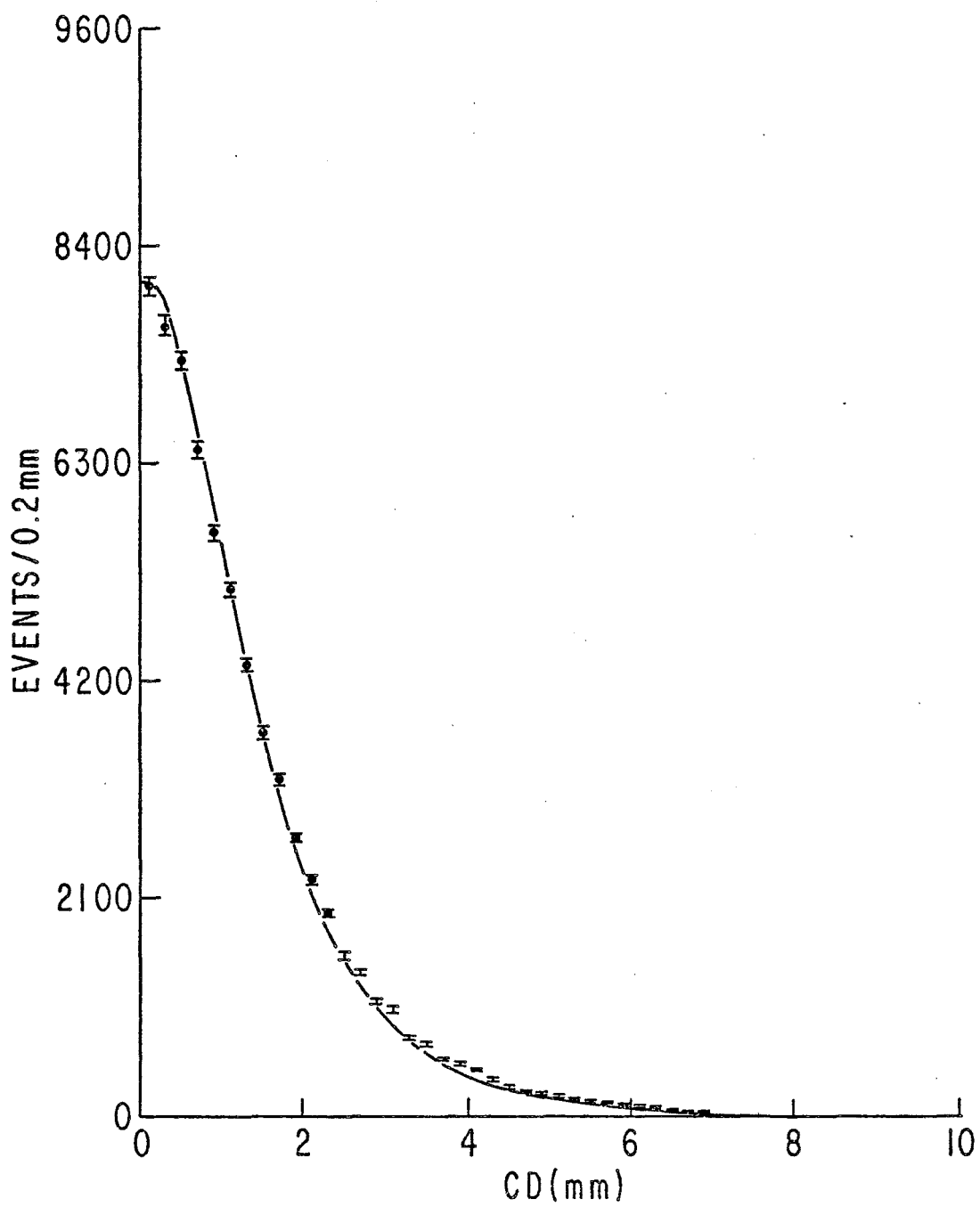


Figure X.6

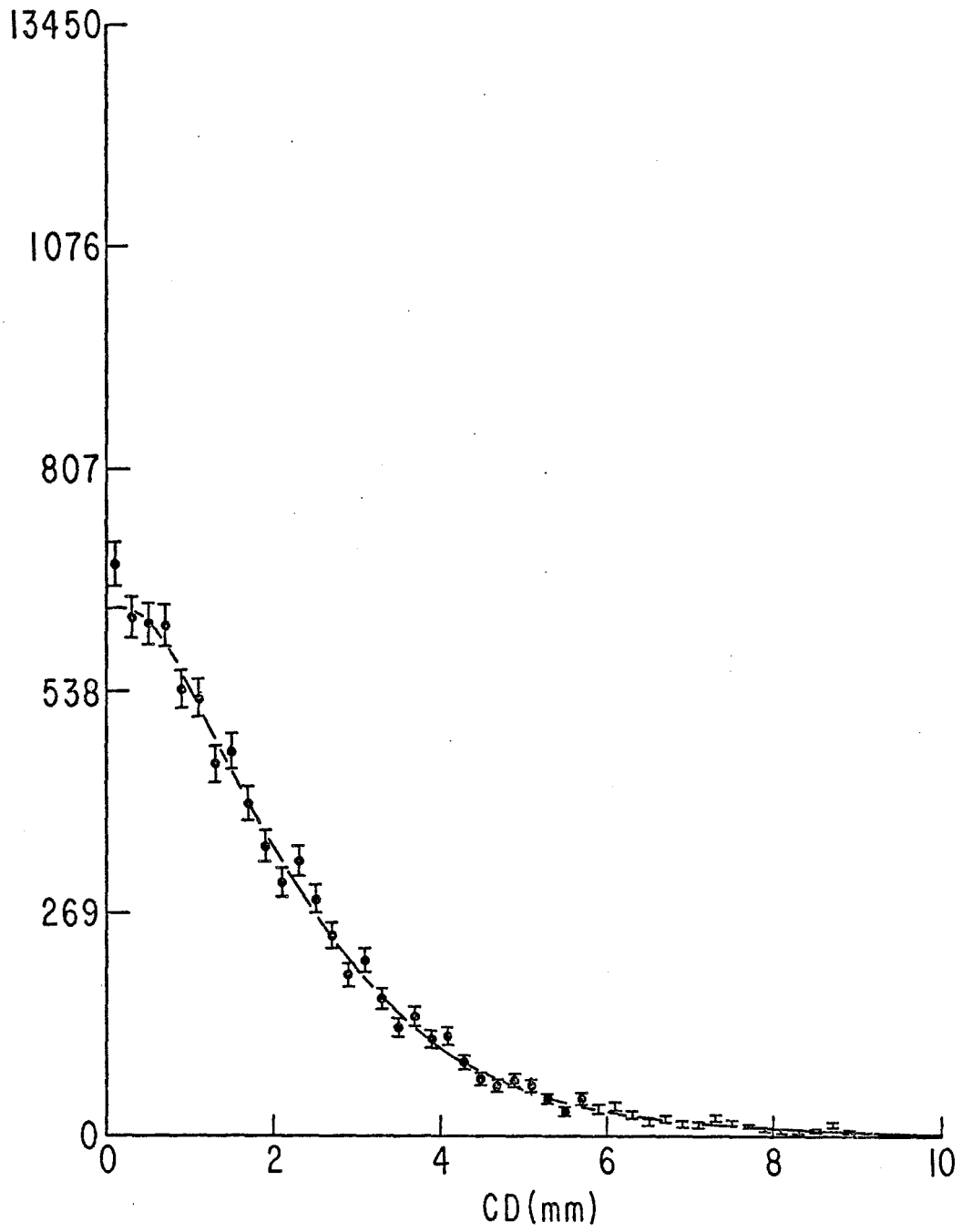


Figure X.7

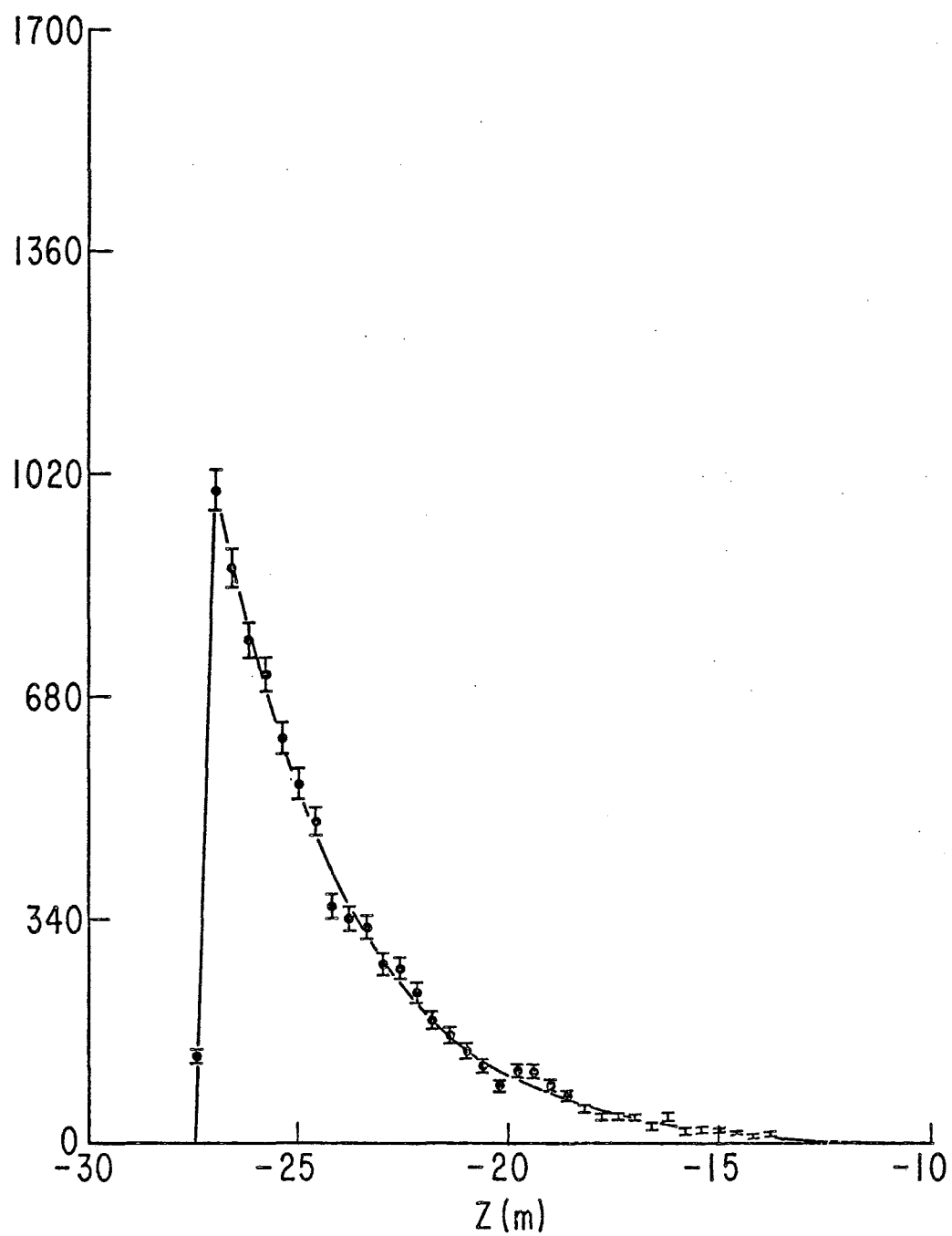
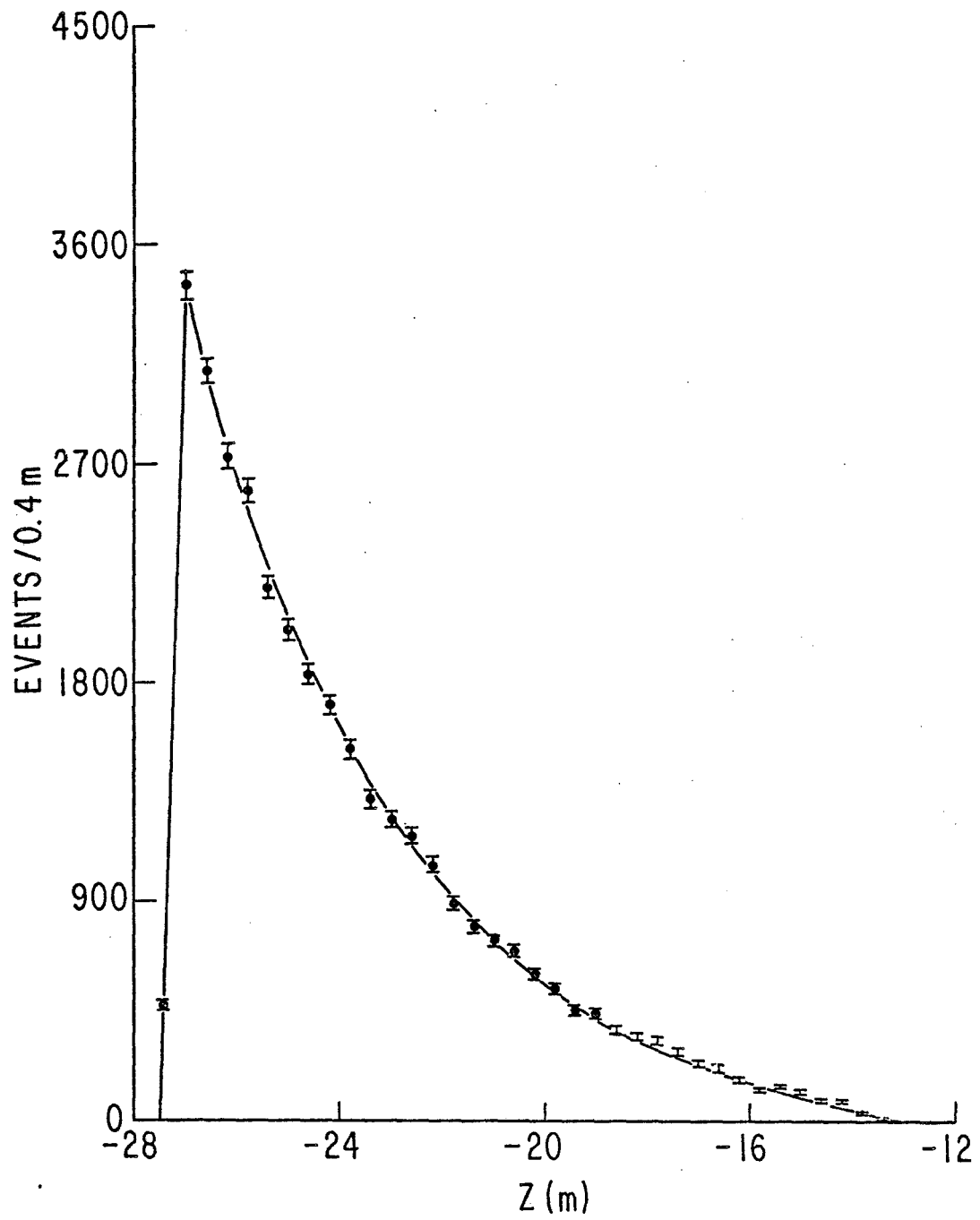


Figure X.8



Figuré X-19

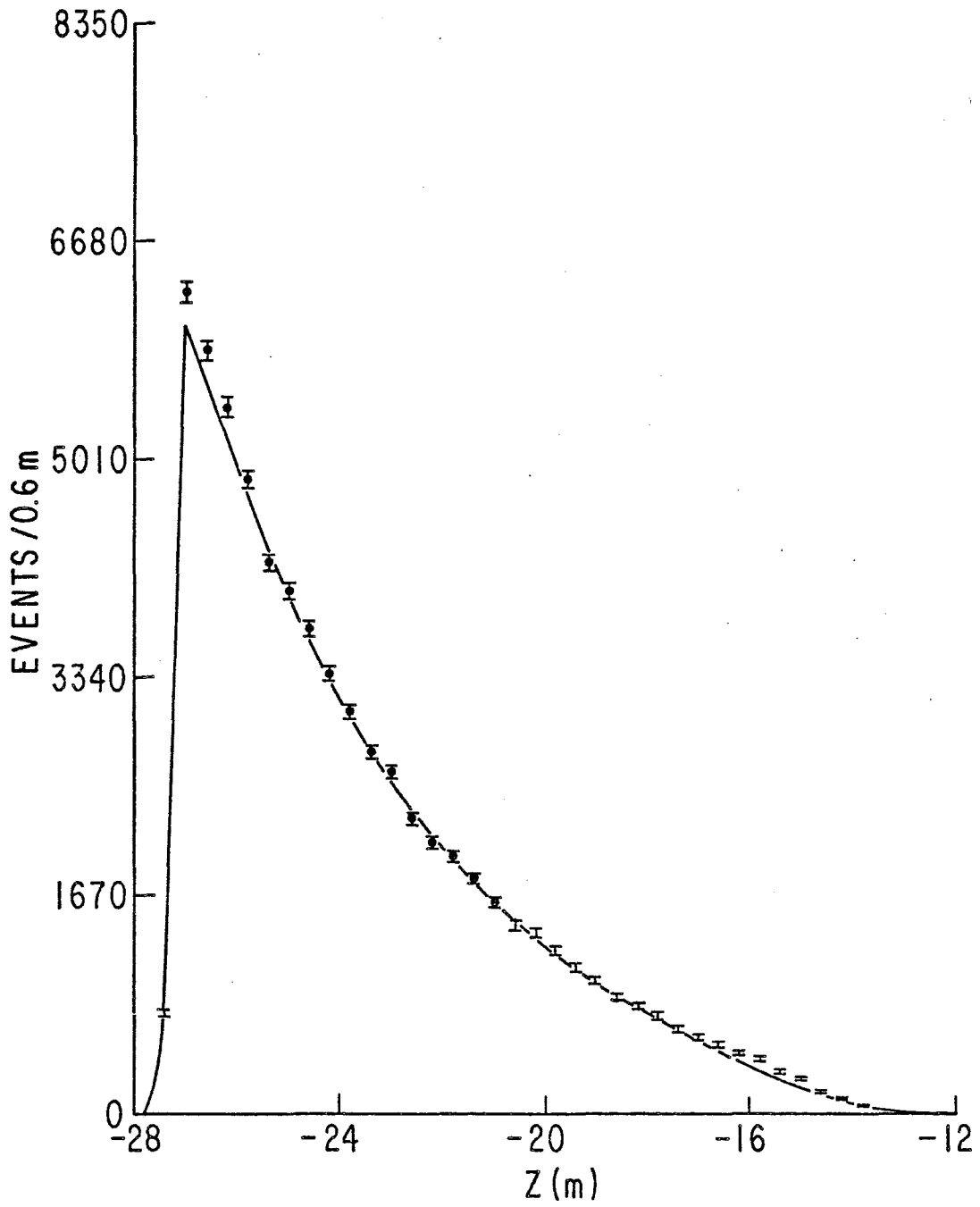


Figure X.10

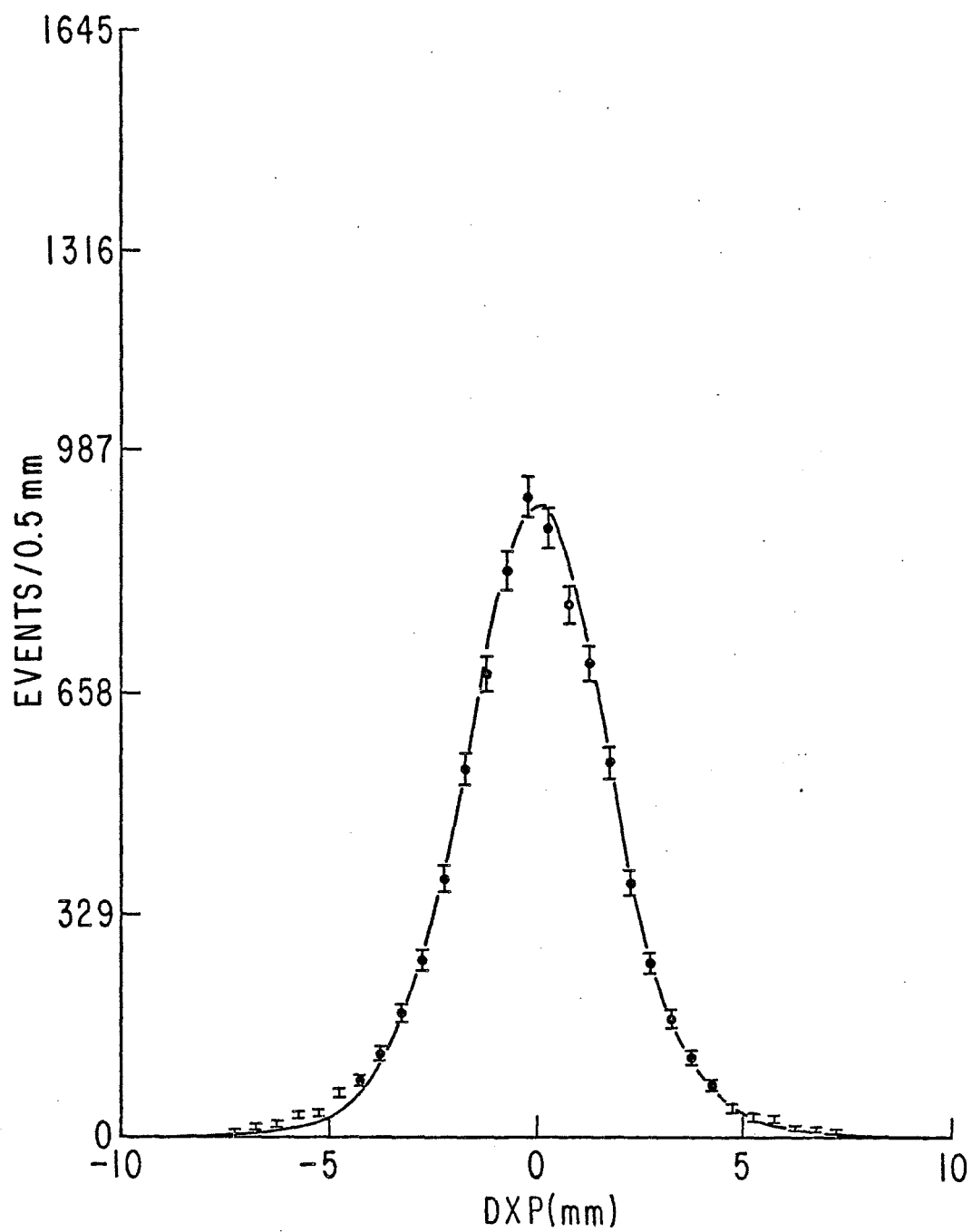


Figure X.11

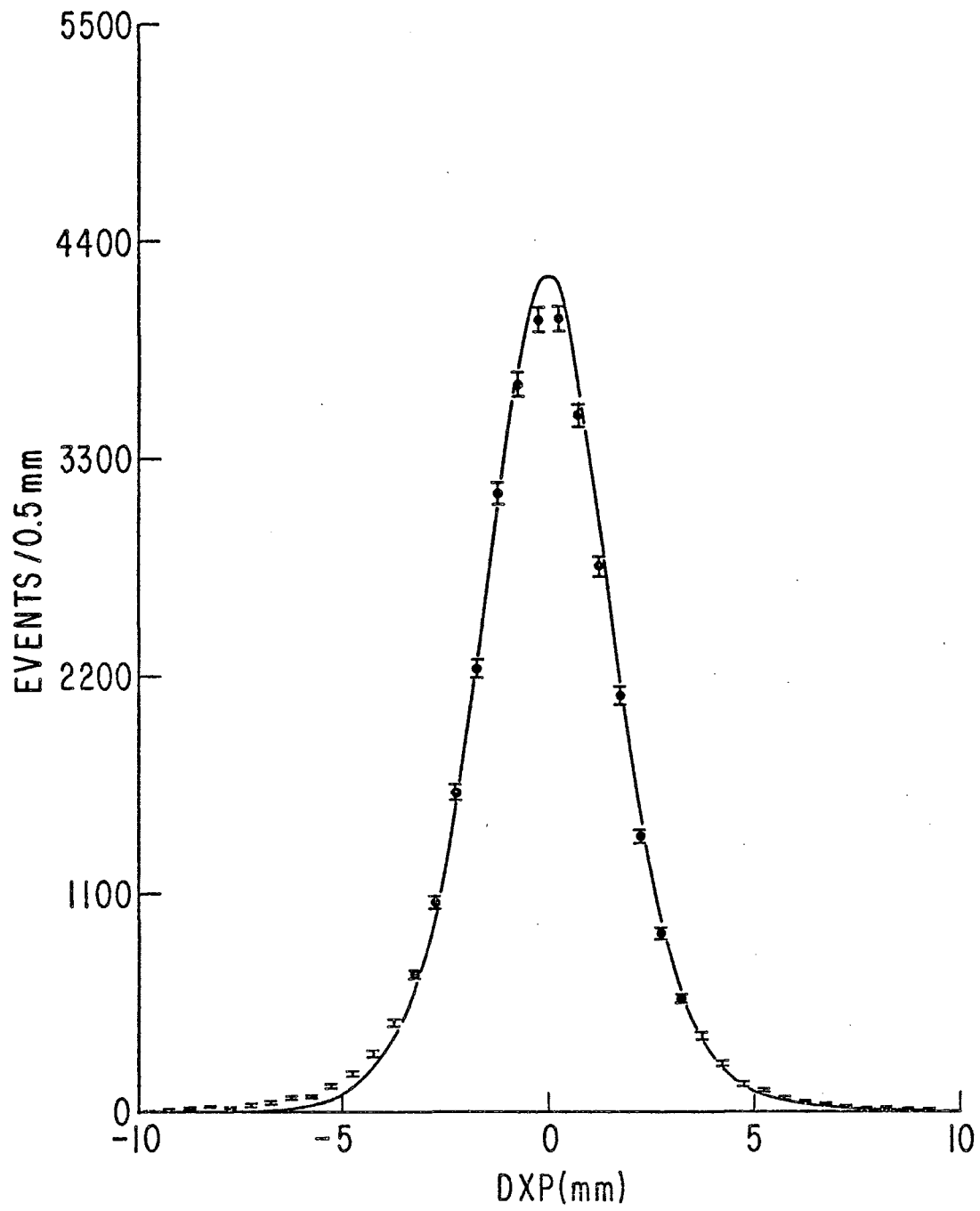


Figure X. 12

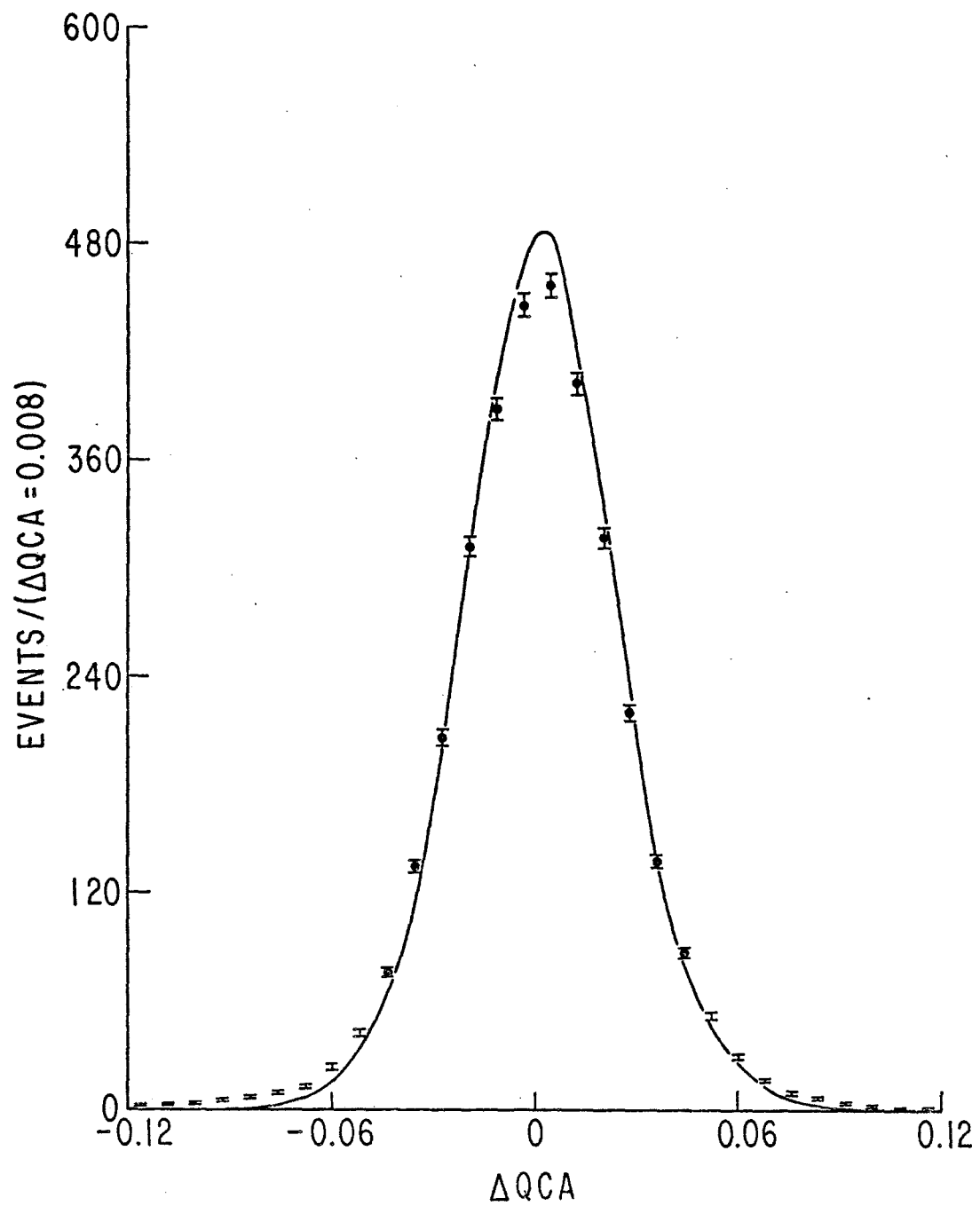


Figure X: 13

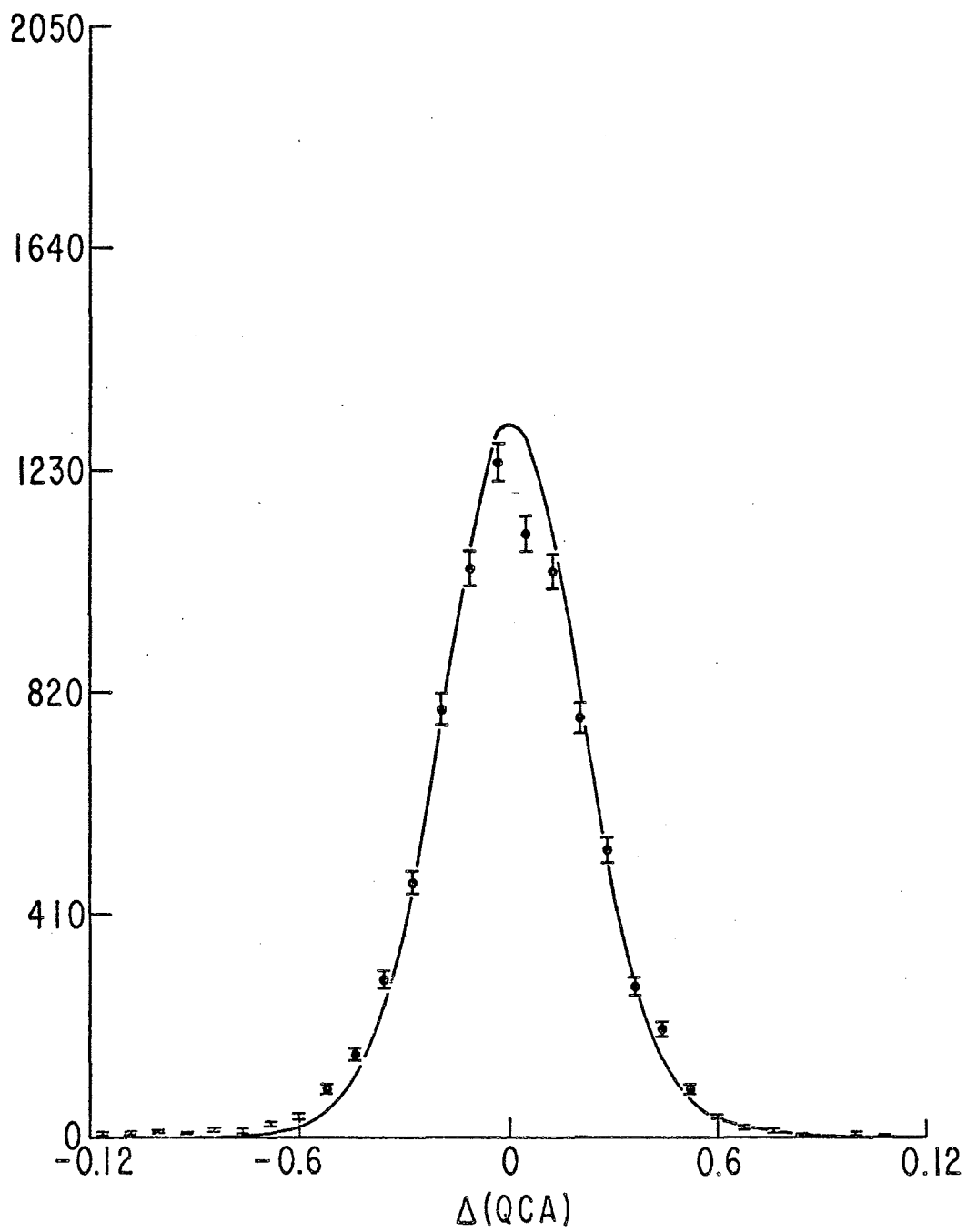


Figure X.14

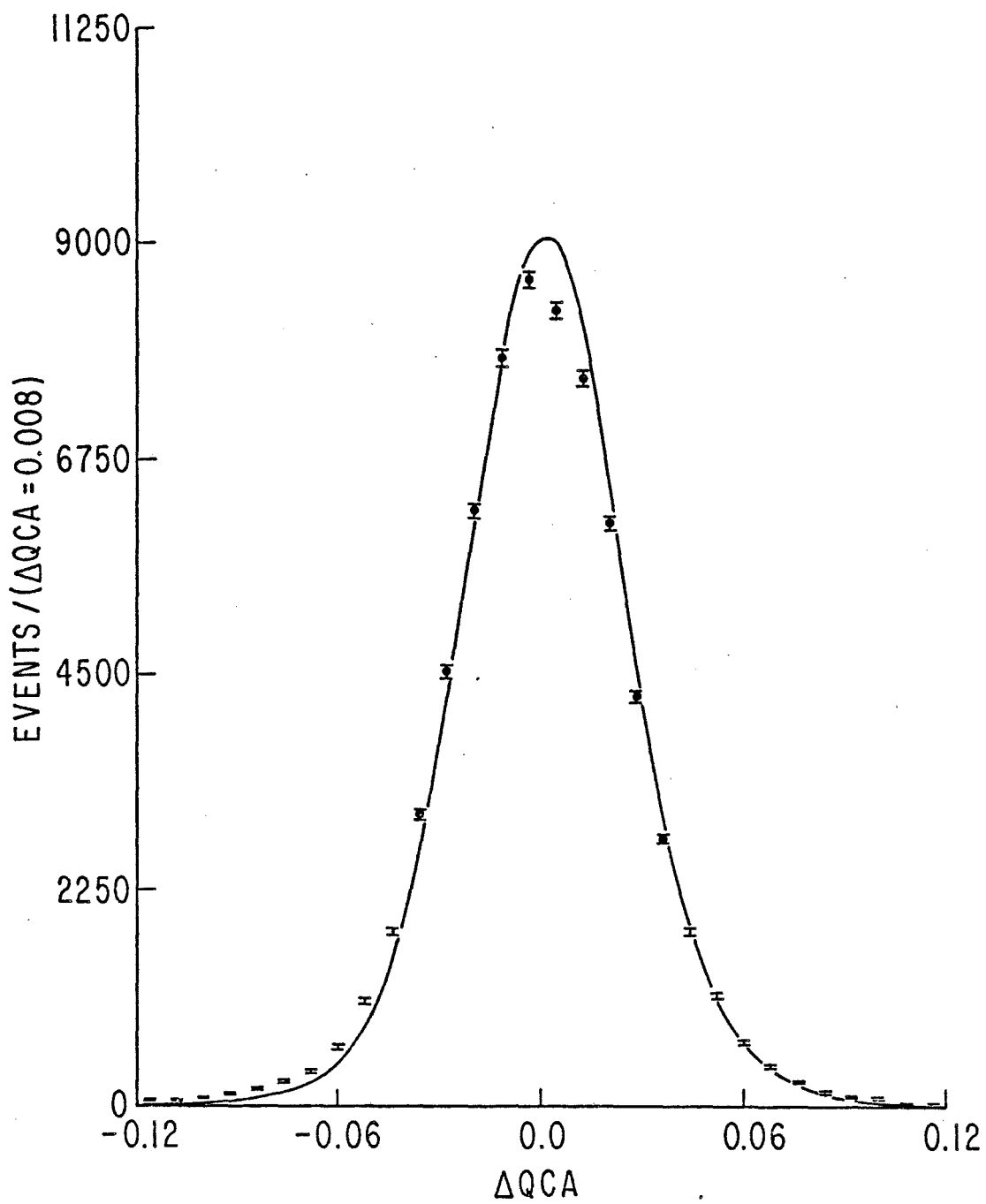
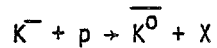


Figure X. 15

Appendix XI

CALCULATION OF THE CROSS-SECTION

This appendix describes our calculation of the cross-section for the reaction:



While the cross-section for each of the three beam tunes (68, 116, 176 GeV/c) is calculated separately, we assume that the s-dependence is weak enough to justify averaging our results over the 10% spread of incident K^- . So, for each beam tune, we assume that the cross-section is a function of x and t only.

We use the following notation in this appendix:

Accepted events	data or simulated events which satisfy all the criteria detailed in Appendix IX.
(x,t) bin	Region in the (x,t) plane of widths ($\Delta x, \Delta t$). (x,t) refers to the values of those variables at the center of bin.
Reconstructed values	Values of the variables (both for data and simulated events) calculated by the analysis program. These values are "incorrect" to the extent of the experimental errors.
Generated values of x and t	"Correct" values of x and t for the simulated events.
Target full	Condition of the target when filled with liquid hydrogen at a vapor pressure of 1 atmosphere.

Target empty	Condition of the target when filled with gaseous hydrogen at 1 atmosphere and 27 ⁰ K.
$N_F(x,t), N_E(x,t)$	Number of accepted data events for target (full, empty) in an (x,t) bin.
ϕ_F, ϕ_E	Numbers of incident K^- arriving while the experiment was active, for target (full, empty) corrected for beam chamber inefficiencies.
$\epsilon(x,t)$	Average detection efficiency of the forward spectrometer for $\overline{K^0}$'s in an (x,t) bin. If it takes N_1 trials into an (x,t) bin (generated values) to obtain N_2 accepted events, $\epsilon = N_2/N_1$.
ρ	Density of liquid hydrogen in equilibrium with its vapor phase at 1 atmosphere ($\rho = 0.0708 \text{ gm/cm}^3$).
L	Target length (L = 70.9 cm).
N	Avogadro's number ($N = 6.022 \times 10^{23}$).
Δx	Bin size in x ($\Delta x = 0.025$).
Δt	Bin size in t ($\Delta t = 0.1 \text{ (GeV/c)}^2$).
C	Correction factor (see Table I).
B	$\overline{K^0} \rightarrow \pi^+ \pi^-$ Branching ratio (B = 0.3434)

We define the average cross-section in (x,t)

$$\frac{d^2\sigma(x,t)}{dxdt} = \frac{1}{\Delta x \Delta t} \left[\frac{N_F(x,t)}{\phi_F} - \frac{N_E(x,t)}{\phi_E} \right] \cdot \frac{1}{\epsilon(x,t)} \frac{C}{\rho L N B}$$

TABLE I
Corrections to Cross-Section

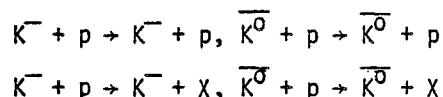
	68 GeV/c	116 GeV/c	176 GeV/c
1) B5 counter hit by track other than kaon decay products	1.0013	1.0013	1.0017
2) Beam phase space cuts	1.0110	1.0130	1.0062
3) Pions labelled as kaons	1.0290	1.0000	1.0000
4) K^- decay between Cherenkov counter and target	1.0105	1.0077	1.0070
5) $\overline{K^0}$ absorption downstream of target	1.0060	1.0060	1.0060
6) K^- and $\overline{K^0}$ absorption in target	1.0550	1.0550	1.0560
7) Pion absorption in spectrometer	1.0440	1.0430	1.0430
C (product of 1-7)	1.166	1.132	1.125

1. The B5 correction was calculated by looking at the (X,Y) impact of in-time tracks which were not part of reconstructed neutral "vee's". The B5 veto in the trigger eliminated all tracks inside the counter itself, so the number of hits was estimated by extrapolating from the track density around the counter.

2. The beam phase space correction was needed because the event selection program rejected events with beam tracks on the wings of the phase space distributions.
3. During the 68 GeV/c running, the threshold of the discriminator for the K signal from the Cherenkov counter was too low, allowing some pions to trigger the experiment. Studying the Cherenkov counter ADC's enabled us to correct for this.
4. Kaon decay between the Cherenkov counter and the target was modelled by the program DECAY TURTLE (1) which uses Monte Carlo techniques to give beam phase space distributions for a given set of magnets and apertures. Given the location and dimensions of the beam trigger counters, beam chambers and the location and field strength of the beam spectrometer magnets, this program calculated the fraction of K^- 's which decayed between the Cherenkov counter and the target and where the muon from the decay "hit" the counters required to tag it as a "good" beam track.
5. \bar{K}^0 absorption downstream of the target was calculated using the known matter distribution in the experiment and the (K^-, p) inelastic cross-section. The (\bar{K}^0, p) cross-sections were assumed to be equal to the (K^-, p) cross-sections.
6. K^- and \bar{K}^0 absorption in the target was calculated using the (K^-, p) cross-section for producing a kaon with x less than 0.5 or no kaon at all.
7. Pion absorption in the spectrometer was calculated using the $\pi^\pm - p$ total cross-section.

To take into account the redistribution of events between (x,t) bins due to measurement errors in x and t , we multiply the cross-section in each (x,t) bin by the ratio of the number of accepted Monte Carlo events with generated (x,t) over the number of accepted Monte Carlo events with reconstructed (x,t) . This correction was greater than 1% only for $x > 0.90$. The value given below is typical for $x = 0.95$.

Similarly, we took into account the effects of K^- interactions before or \bar{K}^0 interactions after the production of the detected \bar{K}^0 . We considered interactions of the type



K^- and \bar{K}^0 cross-sections were assumed to be equal. The K^- cross-sections and their parameterizations were taken from the results of Fermilab experiments E-7² and E-96³. These interactions caused us to assign incorrect values of t and (for inelastic interactions) of x to our events.

Using the existing sample of events we simulated these interactions, computing the resulting redistribution of events between (x,t) bins. The cross-section was corrected bin by bin.

Typical values for these corrections were:

- 0.984 (measurement error)
- 1.003 (elastic scattering)
- 1.008 (inelastic scattering)

References

1. K. L. Brown and Ch. Iselin, computer code Decay Turtle (CERN, 1974).
2. C. W. Akerlof et al., Phys. Rev. D14, 2864 (1976).
3. R. L. Anderson et al., Phys. Rev. Lett. 38, 880 (1977).

Appendix XII
MEASUREMENT ERRORS

In this experiment, the directly measured quantities fall into four classes:

1. Measurements of the space coordinates of the intercept of a particle trajectory with a wire chamber plane.
2. Measurement of the transverse momentum kick on each of the three bending magnets.
3. Counting of the number of incident kaons which, by interacting in the target, produced the accepted events.
4. Pulse height measurements which were used to ascertain the quality of the logic signals used to trigger the data acquisition.

Scalers which counted logic signals were read out and reset every time an event was acquired. This allowed us to do a statistical analysis of ratios of different rates. In addition, subsidiary measurements of accidental vetoing (of otherwise good signals) were made. We found no indication that our normalization was, at any time, in error by as much as one part in a thousand.

All magnets were mapped with a flip coil which measured the field integral along particle trajectories. The beam spectrometer magnet had field integrals which, at a given current, were equal to within 0.1%. Their uniformity over the aperture occupied by the beam was better than 0.1%. The analysis magnet was less uniform. Most of the events were within a region where the field integral used for each track was interpolated from a table of flip coil measurements.

Measurements of space coordinates depend on the knowledge of the wire spacing and the relative alignment of the planes. High precision survey measurements indicate that the average wire spacing was 1 mm., with an error of less than 1 part per thousand, and that individual wires deviated from this average by less than 0.1 mm. The alignment, with respect to rotations about the normal to the chamber plane, was better than 100 μ r. What remains is the alignment with respect to displacements of the wire planes parallel to themselves. Such alignment is performed by the use of the high energy particles themselves. Alignment of sets of planes in the plan view across the analysis magnet is done in special data taking runs where the magnet is turned off. An analysis of the first and second moments of the mass distribution of reconstructed neutral kaons allows us to continuously monitor this alignment

The results of measurements which use these calibrations can be checked as follows:

1. The mass of the neutral kaon should agree with other measurements.
2. Momenta of beam particles, when measured with both spectrometers, should agree.
3. The hits for every track segment should lie on straight lines.
4. The tracks for the two pions from the $K_S \rightarrow \pi^+ + \pi^-$ decay should intersect at a point in space.
5. The track for the incident kaon and the "track" for the reconstructed K^0 in the interaction $K^- + p \rightarrow \overline{K^0} + X$ should intersect at a point in space.
6. The upstream and downstream segments of a track through a magnet should intersect at its magnetic center.

7. The decay angular distribution of the $K_S^0 \rightarrow \pi^+ + \pi^-$ decay should be isotropic. This is a check on our understanding of the detection efficiency as a whole.

The study of the distribution of the deviations from perfect agreement with the above conditions, (comparing simulated and data events), allows us to:

1. Derive the resolution function for space measurements.
2. From these resolution functions, and other relevant measurements (chamber efficiencies, event distributions in angle and energy, aperture limitations of the detectors, etc.) we can generate the expected distributions of the measured quantities for which we have the above predictions.

The agreement (or lack thereof) between these predictions and the measured distributions (Figs. XII.1 - XII.10) allows us to set limits on the systematic errors which affect our conclusions. Our basic uncertainties can be summarized as shown in Table I. The computed resolution functions (expected distributions of measurement errors) of some of the relevant variables are shown in Figs.

As mentioned in the main text, the cross-sections depend mostly on x and t and only weakly on s . The basic thrust of this experiment is to compare our data with a parametrization predicted by Triple Regge Theory and the results of other experiments. Since, to first approximation

$$x \equiv p_{K^0}/p_{K^-}$$

$$t \equiv (p_{K^0}/p_{K^-}) p_T^2$$

where p_T is the transverse momentum of the $\overline{K^0}$ relative to the K^- .

the possible sources of systematic errors are:

- 1) for x , errors in P_{K^0}/P_{K^-}
- 2) for t , errors in P_{K^0}/P_{K^-} , P_T

We estimate, as an upper limit, a systematic error in P_T of approximately

The systematic error in P_{K^0}/P_{K^-} has as its upper limit the value of 0.5% ($P_{\text{Beam}}/100 \text{ GeV}$) given in Table I.

The resultant systematic error in t does not affect our conclusions in any significant way.

The corresponding systematic error in x causes changes of α considerably smaller than the corresponding statistical errors. In Table I we give the upper limits of the systematic errors estimated for $\alpha(t)$ at a few typical points in (s,t) .

The statistical errors estimated for the cross-sections include effects due to the finite number of observed target full and empty events (these are by far the major sources of these errors) and due to the finite number of simulated events.

TABLE I

Systematic Error in α_E Due to a Mistake of 1% in the
Momentum Calibration of the Beam Spectrometer

Beam Momentum: 176 GeV/c

$-t$	$\delta\alpha$
0.05	0.028
0.15	0.013
0.25	0.037
0.35	0.026
0.45	0.039
0.55	0.069
0.65	0.026
0.75	0.220
0.85	0.081
0.95	0.011

TABLE II
Measurement Errors

X, Y	0.3 mm (each measurement)
Track angle	80 μ r (each track)
Z-coordinate of the decay vertex	32 cm
Z-coordinate of the production vertex	14 cm
Momentum of a decay pion ($\delta p/p$)	0.014 (p(GeV)/100 GeV)
Momentum of a beam kaon ($\delta p/p$)	0.0038
Misalignment of the Z-axis across the analysis magnet	< 10 μ r
Discrepancy of the momentum scales of beam and downstream spectrometers ($\delta p/p$)	< 0.005 (p(beam)/100 GeV)

Figures XII. 1 - XII. 3. Calculated Measurement Resolutions.

Figure XII. 1: Z-coordinate of production vertex (m)

Figure XII. 2: Z-coordinate of decay vertex (cm)

Figure XII. 3: X-coordinate of the pion intercept with the
center plane of the analysis magnet (mm)

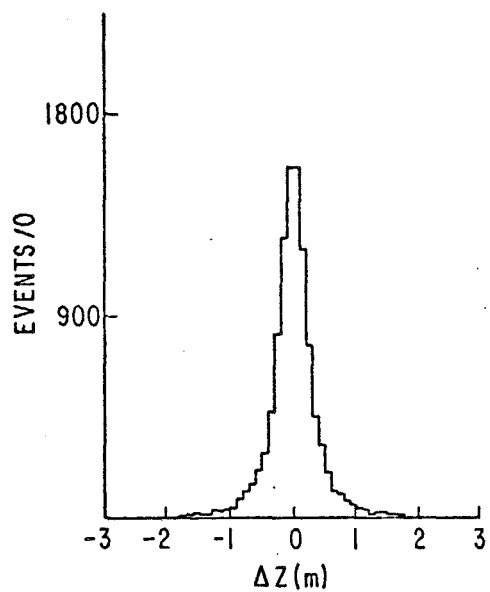


Figure XII. 1

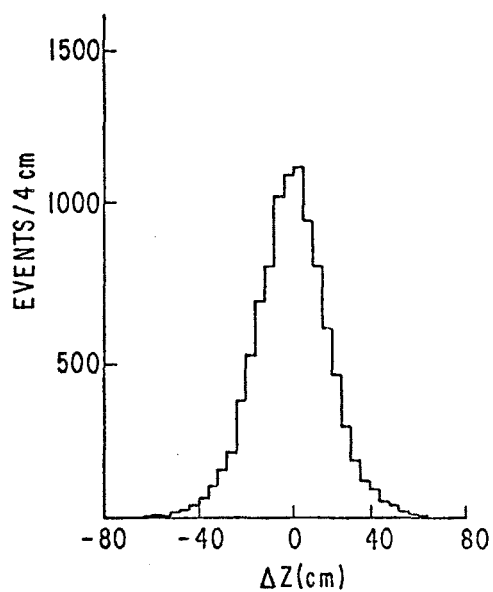


Figure XII. 2

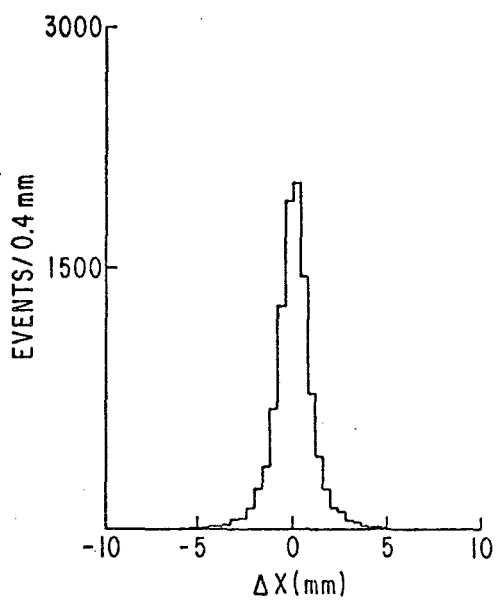


Figure XII. 3

Figures XII. 4 - XII. 7. Calculated Measurement Resolutions.

Figure XII. 4: Momentum of the reconstructed neutral kaon
(fractional)

Figure XII. 5: Momentum of the incident negative kaon
(fractional)

Figure XII. 6: Momentum of the decay pion (fractional)

Figure XII. 7: Angle of the reconstructed neutral kaon
(projection onto the vertical (Y) plane,
microradians)

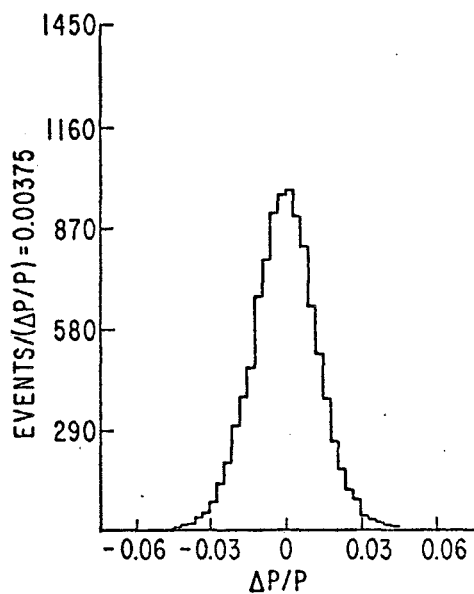


Figure XII. 4

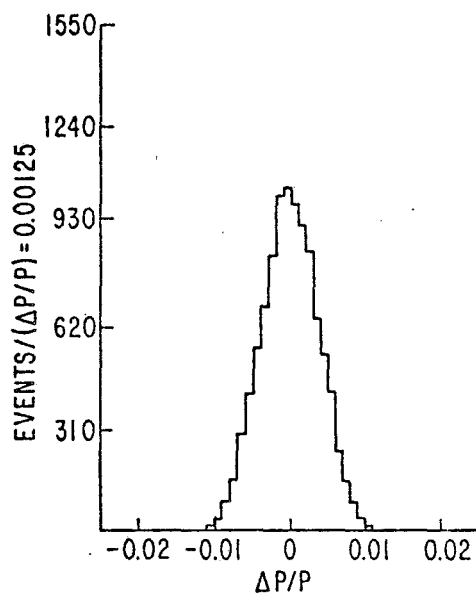


Figure XII. 5

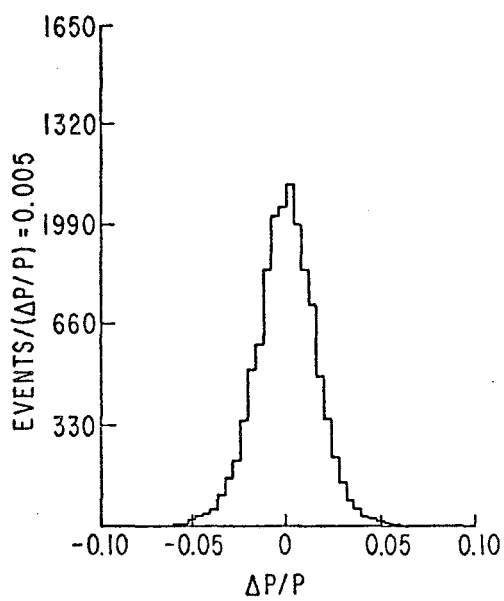


Figure XII. 6

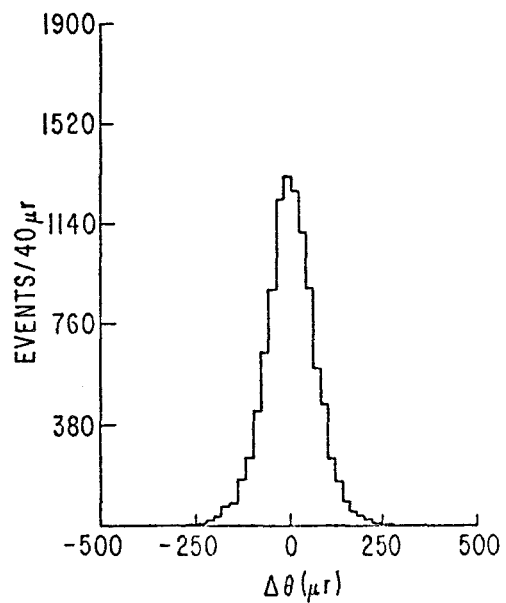


Figure XII. 7

Figures XII. 8 - XII. 10. Calculated Measurement Resolution.
Averaged over the 116 GeV/c data.

Figure XII. 8: Feynman x (absolute)

Figure XII. 9: Four-momentum transfer squared (fractional)

Figure XII.10: Mass of the neutral kaon $(\text{MeV}/c)^2$.

The expected value is $497.7 \text{ MeV}/c^2$.

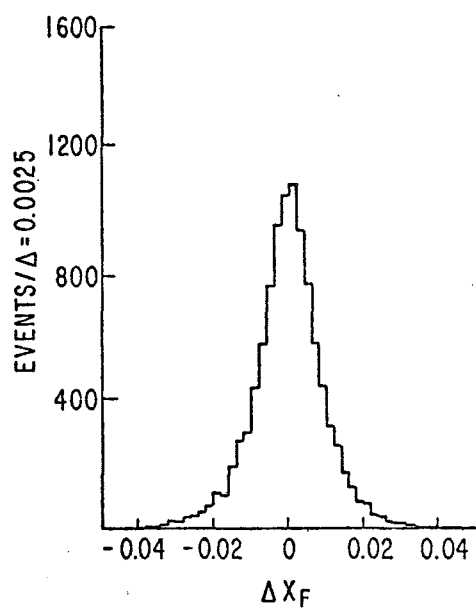


Figure XII. 8

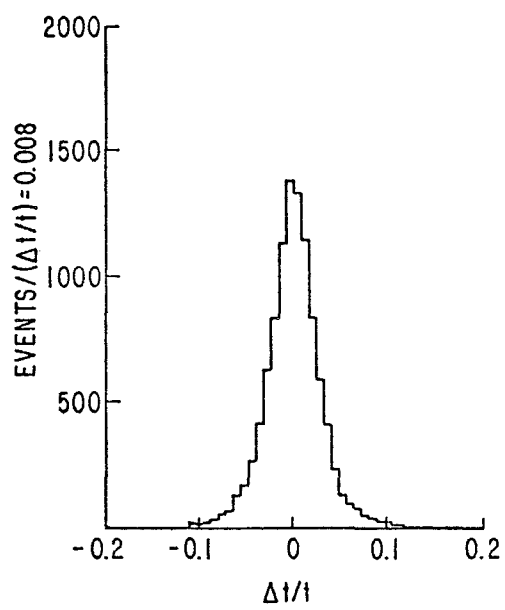


Figure XII. 9

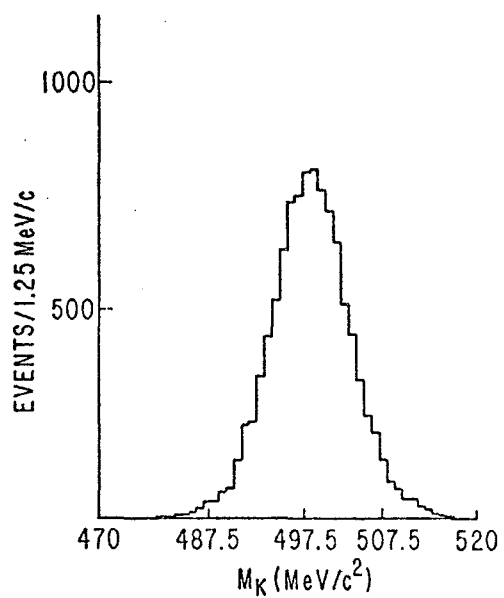


Figure XII. 10

Appendix XIII

DATA ACQUISITION SYSTEM

When the output of the fast logic ("trigger") indicated the occurrence of an event which warranted further ("off-line") analysis, the information generated by the different components of the detector was latched onto local storage modules (scalers, coincidence registers, PWC scanners, ADCs, delay line digitizers for spark chamber read out), and the experiment was suspended ("interrupted"). All the above storage devices were standard CAMAC modules. The crates in which these modules resided were serviced by type A-1 crate controllers. The CAMAC system as a whole was interfaced to a Data General Corp. ECLIPSE S/200 computer by a modified BIRA 1251BD branch driver.

Once the interrupt had been serviced, the modules were read into the computer by using the direct memory access (DMA) features of the CAMAC protocol. The information for each "event" was preceded by a code word ("beginning of event flag") and a sequence number. The events were packed end-to-end into a buffer whose length was 1920 16-bit words ($1920 \times 16 = 30,720$, the number of bits in 512 60-bit words, the natural length for a tape record on a CDC 6600 computer). This buffer was then spooled to disk, while more data was placed into a second 1920-word buffer. Once the data acquisition for one event was completed, the acquisition program went into a

wait loop and the experiment was reenabled. This process continued until the end of the beam spill. At this time another interrupt (the "end of beam" or "EOB") was sent to the interface. The acquisition system then read the data from disk to magnetic tape. At the end of this operation, an analysis program was enabled which processed some (or all) of the event information on the disk, performing the checks needed to ensure the proper functioning of the equipment. This operation (or the subsequent wait loop) continued until the beginning of the next beam spill. Then a third interrupt (the "beginning of beam" or "BOB") was sent to the interface, which caused the analysis activity to stop, the acquisition activity to start and the experiment to be reenabled.

